Department of Polymers and Advanced Materials: Physics, Chemistry and Technology

UNIVERSIDAD DEL PAIS VASCO
THE UNIVERSITY OF THE BASQUE COUNTRY

Probing nanoscale light-matter interactions with fast electrons and near-field optical probes

Thesis by
Carlos Alberto Maciel Escudero

for the degree of
Doctor of Philosophy in Physics

Supervised by
Prof. Javier Aizpurua and
Prof. Rainer Hillenbrand

Donostia-San Sebastian, Spain, December 2023

To my mom, my sister, and Elli,
for encouraging me.

Contents

Laburpena

Mikroskopio optikoari eta argian oinarritutako beste hainbat tresnei esker, objektu ñimiñoak xehetasun handiz aztertzeko gaitasuna lortu du gizakiak historian zehar, begi soilaren ikusmen-ahalmena erabat gaindituz. Hala ere, argi ikusgaia edota infragorria erabiltzen duten mikroskopio optikoek muga garrantzitsu bat daukate, argiaren difrakzio-muga delakoa. Difrakzio-muga Ernst Abbe eta Lord Rayleigh-ek azaldu zuten lehenengoz XIX. mendean eta, horren arabera, bereizi daitekeen bi objekturen arteko distantziarik txikiena ezin da izan mikroskopio optiko arruntetan erabiltzen den argiaren uhin-luzeraren erdia baino txikiagoa [1, 2]. Hortaz, difrakzio-mugak berebiziko garrantzia dauka argia espektro ikusgaian manipulatzeko, bai eta ehunka nanometro baino dimentsio txikiagotan konfinatzeko ere. Gauzak horrela, nanofotonikan geroz eta nanoegitura txikiagoak fabrikatzeko gaitasuna lortzen ari denez, aipatutako difrakzio-muga gainditzeko gai diren teknikak garatzea ezinbestekoa da.

Difrakzioak ezartzen dituen mugak gainditzeko modu bat polaritoiek eskaintzen dute; izan ere, polaritoiak gai dira eremu elektromagnetikoa argiaren uhin-luzeraren erdia baino dimentsio txikiagoetan, nanoeskalan, konfinatzeko; hortaz, oso elementu interesgarriak bilakatu dira argiaren manipulazio eta kontrolerako. Polaritoiak argia osatzen duten fotoien eta materian ematen diren kitzikapen dipolarren (hala nola fonoiak material polarretan, plasmoiak metaletan, edota exzitoiak erdieroaleetan) arteko akoplamenduaren ondorioz sortzen diren uhin elektromagnetiko hibridoak dira [3, 4]. Polaritoiek eragindako eremuaren konfinamendu bortitzaren ondorioz, induzitutako eremu elektromagnetikoaren intentsitatea argi erasotzailearena baino askoz ere handiagoa izatea lor daiteke. Eremuaren intentsitate-areagotze hori hainbat aplikaziotan erabiltzen da, besteak beste molekula bakarraren detekzioan [5], efektu optiko ez-linealen areagotzean [6], edota laginen berotze lokalean [7]. Polaritoien arazo nagusia, ordea, hauen momentu lineala fotoi askeena baino handiagoa dela da, eta beraz, polaritoiak ezin dira eremu urruneko teknika optiko arruntekin kitzikatu. Arazo hori saihesteko tekniken artean, elektroien energia-galeraren espektroskopian (EELS, electron energy-loss spectroscopy ingelesez) oinarritutako ekorketa eta transmisioko mikroskopio elektronikoak (STEM, scanning transmission electron microscopy) edota sakabanatze-motako ekorketako eremu-hurbileko mikroskopio optikoak (s-SNOM, scattering-type scanning near-field optical microscope) oso erabilgarriak dira, polaritoien eremu hurbileko propietateak hautemateko gaitasuna dela-eta.

STEMk estuki enfokatutako elektroi-sorta erabiltzen du material baten propietate optikoak EELS bidez hautemateko, hamarnaka meV-eko energia-bereizme-

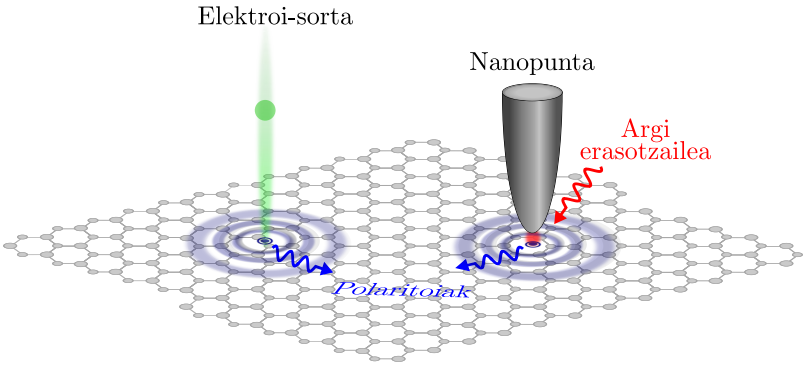

1. Irudia: Argiaren eta materiaren arteko elkarrekintza nanoeskalan, elektroi-sorta azkarrek eta eremu-hurbileko zundek kitzikatuta. Ingurune polaritoniko baten (egitura hexagonal grisa) eta elektroi-sorta azkarraren (izpi berdea) edota nanopuntaren (egitura koniko grisa) arteko elkarrekintza eremu hurbilean. Erermu hurbileko elkarrekintzaren ondorioz, ingurunean zehar polaritoiak kitzikatzen dira (uhin urdinak), hau da, argiaren eta materiaren arteko uhin elektromagnetiko hibridoak. Gezi gorriak nanopunta argiztatzeko erabiltzen den argi erasotzailea adierazten du.

na eta eskala atomikoko bereizmen espaziala erdietsiz. STEMren bidez lortutako informazioa zuzenean erlaziona daiteke laginaren tamaina, forma, eta egitura zehatzarekin [8, 9]. Adibidez, EELS erabilgarria izan da hainbat nanoegituretako plasmoi lokalizatuak karakterizatzeko [10–13], konfigurazio elektronikoak zundatzeko (hala nola exzitoiak trantsizio-metalezko dikalkogenuroetan (TMDC) [14]), zilarrezko heptameroen modu toroidal optikoak iragartzeko [15], edota siliziozko nanobarrunbe dielektrikoen modu fotonikoak hautemateko [16]. Duela gutxi, EELS argiaren eta materiaren arteko elkarrekintza bortitza aztertzeko ere erabili izan da, sekulako bereizmen espazial eta espektralarekin [17–22].

Bestalde, s-SNOMean argia indar atomikoko mikroskopio (AFM, atomic force microscope) baten puntan enfokatzen da, honekin argi erasotzailea puntaren muturrean kontzentratuz eta, beraz, eremu-hurbil oso kontzentratuak lortuz. Punta laginaren gainean jartzean, puntaren muturraren inguruko eremu elektromagnetikoak aldatu egiten dira laginaren erantzun optikoaren ondorioz. Elkarrekintza honek puntatik sakabanatutako argia aldatzen du, eta horrela, sakabanatutako argia aztertuz, laginaren propietate optiko lokalei buruzko informazioa lor daiteke, laginaren gainazalean induzitutako eremu elektromagnetiko lokalak mapatuz [23–25]. Gauzak horrela, s-SNOMek erakutsi du gai dela egitura plasmonikoen [26] eta nanoantena fononikoen [27] eremu hurbileko banaketa modu espazialean mapatzeko. Grafenoan kitzikatutako plasmoiak [28, 29] eta polaritoi anisotropoak [30] irudikatzeko ere eraginkorra dela frogatu da.

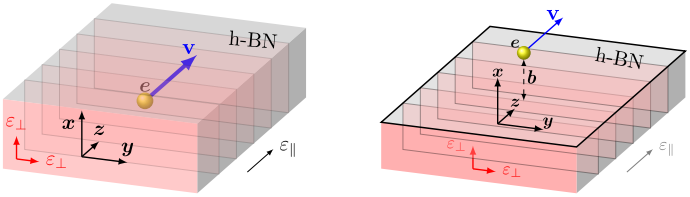

2. Irudia: Elektroi-sorta azkarra h-BN solidoan barrena eta h-BN gainazal erdi-infinitu baten gainean. h-BN solidoan barrena (ezkerreko panela) eta h-BN gainazal erdi-infinituaren gainetik (eskuineko panela) pasarazten den elektroi-sortaren eskema. Elektroi-sorta $\mathbf{v} = v\hat{\mathbf{z}}$ abiaduraz doa h-BNaren ardatz optikoarekiko (z-ardatza) paralelo, eta h-BN gainazal erdi-infinitutik b distantziara. Bi paneletan, plano gorriak z ardatzean pilatuta dauden h-BN geruzak dira.

Hori guztia kontuan izanik, tesi honen helburua elektroi-sorta (electron beam) edota nanopunta (nanotip) bidezko polaritoien eremu hurbileko kitzikapena ikertzea da (ikusi 1. Irudia). Bereziki, ingurune fononiko anisotropoetan sortzen diren polaritoien kitzikapena zein modu elektromagnetiko eta exzitonikoen (edo bibrazio molekularren) arteko akoplamenduaren ondorioz sortzen diren polaritoien kitzikapena izango dugu aztergai. Horretarako, polaritoien eta haien eremu hurbileko ezaugarriei buruzko oinarriak aurkeztuko ditugu, sistema polaritonikoak egoera desberdinetan aztertzeko.

Lehenengo kapituluan, tesi honetan zehar erabiliko ditugun oinarri teorikoa eta metodologia aurkeztuko ditugu. Lehenik eta behin, Maxwell-en ekuazioak berrikusiko ditugu ingurune jarraituetan, erlazio konstitutibo eta oszilatzaile dipolarraren ereduarekin batera. Oszilatzaile dipolarraren eredua tresna baliagarria da eremu polarizagarrietan kitzikapen dipolarrak deskribatzeko. Jarraian, aipatutako eredua erabiliko dugu metaletan kitzikatutako plasmoien eta kristal polarretan kitzikatutako fonoien propietateak ikertzeko. Gure analisia beste zenbait sistematara zabalduko dugu, hala nola, solido, gainazal, geruza mehe eta nanopartikula esferikoetara. Horretaz gain, materiaren eta argiaren arteko akoplamendu bortitza (strong coupling) deskribatuko dugu, oszilatzaile harmonikoetan oinarrituta dauden bi eredu teoriko aurkeztuz. Eredu horiek erabiliz, akoplamendu bortitzeko sistemetan (strongly coupled systems) agertzen diren autoegoera hibridoak (hau da, polaritoiak) deskriba daitezke. Azkenik, behin polaritoien oinarriak azalduta, galera baxuko EELS eta s-SNOMren printzipioak berrikusiko ditugu. Bi teknika horiek berebiziko garrantzia dute tesian zehar aztergai izango diren polaritoien kitzikapenaren ikerketan.

Bigarren, hirugarren eta laugarren kapituluetan, doktoretza-tesi honen emaitza nagusiak aurkeztuko ditugu. 2. kapituluan, EELS erabiliko dugu elektroi azkarren eta polaritoien akoplamendua aztertzeko boro nitruro hexagonalean (h-BN). Ikusiko dugu h-BN materialean bolumeneko eta gainazaleko erreso-

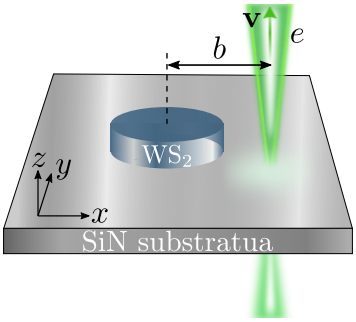

3. Irudia: Elektroi-sorta azkarraren eta wolfram disulfurozko (WS_2) nanodiskoaren arteko elkarrekintza. z norabidean v abiadurarekin eta nanodiskoaren zentrutik b distantziara pasarazten den elektroi-sorta batek kitzikatzen duen WS_2 nanodiskoaren eskema.

nantziak kitzikatu daitezkeela elektroi-sorta azkarrak bi konfigurazio ezberdinetan erabiliz: alde batetik, elektroi-sorta azkarrak h-BN bolumenean barrena pasaraztean eta, bestetik, hutsunearen eta h-BN-aren arteko interfaze infinituan barrena pasaraztean (ikusi 2. Irudia). Material isotropoetan ez bezala, erakutsiko dugu bolumeneko erresonantziak kitzikatu daitezkeela ingurune uniaxialetik kanpo mugitzen diren elektroi-sorta azkarren bidez. Horretaz gain, erakutsiko dugu h-BN azaltzen den bolumen eta gainazaleko fonoi polaritoi kitzikapenek lotura zuzena dutela elektroien abiadurarekin, eta menpekotasun handia dutela elektroi-sortaren eta h-BNaren ardatz optikoaren arteko angeluarekiko.

Hirugarren kapituluan, STEMan EELS erabiliz, teorikoki zein esperimentalki aztertuko dugu anapolo optikoen kitzikapena wolfram disulfuro (WS_2) nanodiskoetan (ikusi 3. Irudia). Errefrakzio-indize altuko disko dielektrikoen EELS profiletan hondoratze (dip) nabarmenak ematen direla erakutsiko dugu, eta hondoratze hauek diskoaren anapolo optikoren kitzikapenarekin erlazionatuta daudela azaldu. Anapoloen kitzikapena eta EELS bidezko detekzioa esperimentalki berresteko, Chalmers University of Technology-ko (Gothenburg, Suedia) gure kolaboratzaileek WS_2 diskoak fabrikatu eta hauetan EELS neurketak egin dituzte. EELS datu esperimentaletan ere anapolo optikoen agerpena ikusiko dugu, eta simulazio numerikoen bidez berretsi. Kapitulu honetan erakutsiko dugu anapolo optikoen maiztasuna diskoaren tamainaren arabera sakabanatzen dela eta, beraz, WS_2 diskoen tamaina aldatuz, anapolo eta WS_2-aren exzitoi trantsizioak gainjarri daitezkeela, anapolo-exzitoi hibridazioa lortuz. Kapituluaren amaieran, WS_2 nanodiskoetan kitzikatutako anapoloen mapa espazialak erakutsiko ditugu (bereizmen azpi-nanometrikoarekin), eta hauen kitzikapena elektroi-sorta posizio desberdinetan kokatuz kontrola daitekeela ondorioztatu.

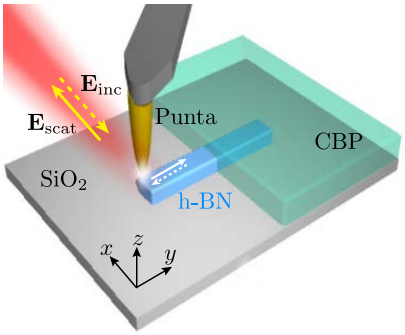

4. Irudia: Molekulaz estalitako h-BN nano-erresonatzailearen eremu-hurbileko zundaketa metalezko punta baten bidez. Laugarren kapituluan aztertutako konfigurazio esperimentalaren eskema. Konfigurazio honetan, h-BN antena geruza molekular batez (egitura berdea) partzialki estalita dago, eta s-SNOM punta (egitura koniko horia) molekularik gabeko h-BN antena zatiaren gainean dago (barra urdina).

Laugarren kapituluan, nano-erresonatzaile fononiko soilen modu lokalizatuen eta geruza organiko erdieroaleen bibrazio-moduen arteko elkarrekintza aztertzeko, CIC Nanoguneko (Donostia-San Sebastian) Nanodevices taldeko kolaboratzaileek eraiki duten eremu-hurbileko espektroskopia infragorria (infrared near-field spectroscopy) erabiliko dugu (ikusi 4. Irudia). Nano-erresonatzailearen eta molekula-geruzaren arteko akoplamendua zuzenean aztertzeko, punta eta erresonatzailearen arteko elkarrekintza minimizatuko dugu erresonantziarik gabeko punta erabiliz. Gainera, puntaren eta molekulen arteko eremu hurbileko elkarrekintza saihestuko dugu honako metodoa jarraituz: nano-erresonatzailearen zati bat molekulaz estaliko dugu, baina beste zatian ez dugu molekularik ipiniko. Ondoren, sistema osoa puntaren bidez kitzikatuko dugu, punta molekularik gabeko zatiaren gainean jarriz. Aipatutako metodo horri urrutiko eremu-hurbileko zundaketa (remote near-field probing) deitu diogu, eta polaritoien mapa espazial eta espektrala sortzeko balioko digu, nano-erresonatzailearen eta molekulen arteko akoplamendua zenbatestea ahalbidetuz. Bestalde, zenbakizko simulazioen bitartez, punta metalikoak (seinalearen demodulazioarekin batera) nano-erresonatzaileaz eta molekulaz osatutako sistema akoplatuaren maiztasun propioen, indargetze-parametroen eta akoplamendu-indarraren gainean duen eragina aztertuko dugu. Tesi honen azken kapituluan, bertan lortutako aurkikuntza nagusiak aurkeztu eta etorkizuneko ikerketarako ildo posibleak proposatuko ditugu.

Introduction

"When light emitted from a tiny sample passes through a series of lenses, the image of the sample is magnified and that, in a nutshell, is the working principle of conventional optical microscopes". This is at least what my high-school teacher of biology told me when we tried to visualize blood cells in the microscope. During that time, I had no doubt that light-based instruments such as optical microscopes have enabled us to study the small in great detail and that throughout history, light has proven useful for expanding our vision beyond what the naked eye can perceive. However, I was not aware of the full story: optical microscopes using visible and infrared light suffer from an important limitation, the diffraction limit of light. Discovered in the 19^{th} century by Ernst Abbe and Lord Rayleigh, the diffraction limit states that the smallest resolvable distance between two objects cannot be smaller than about half the wavelength of the incident illumination used in a conventional optical microscope [1, 2]. This limitation has important consequences on the manipulation of light in the optical range of the spectrum as well as on our ability to guide it in spatial dimensions of less than hundreds of nanometers. However, in the field of nanophotonics, the progress in fabricating progressively smaller nanostructures demands to develop techniques capable of beating the diffraction limit and squeezing light at the nanoscale.

Polaritons provide a way to overcome the limitations imposed by diffraction as they are able to confine the electromagnetic field below this limit, making them promising building blocks for nanoscale light manipulation and control. Polaritons are hybrid light-matter electromagnetic waves that result from the coupling between photons and dipolar excitations in matter, such as phonons in polar materials, plasmons in metals, or excitons in semiconductors [3, 4]. The strong field confinement induced by polaritons can produce electromagnetic fields that are orders of magnitude more intense than the incident field, leading to a variety of applications, including single molecule sensitivity [5], enhancement of non-linear optical effects [6], or local heating of a sample [7]. A major challenge of polariton physics, however, stems from their large momentum mismatch with free-space photons, thus preventing their excitation using conventional far-field optical techniques. Among the variety of techniques to circumvent this limitation, electron energy-loss spectroscopy (EELS) in scanning transmission electron microscopy (STEM) and scattering-type scanning near-field optical microscopy (s-SNOM) are unique techniques for probing polaritons due to their ability to access their near field and provide information not accessible in the far field.

EELS in STEM employs a tightly focused electron beam that allows for mapping the optical properties of a material with tens of meV energy resolution and down to atomic scale spatial resolution while simultaneously relating this information to the samples precise size, shape and structure [8, 9]. For example, EELS has been used to characterize and map localized plasmons in different nanostructures [10–13], to probe electronic excitations such as excitons in transition metal dichalcogenide (TMDC) materials [14], to predict optical toroidal modes in silver heptamer cavities [15], or to map photonic modes of dielectric silicon nanocavities [16]. Recently, EELS has also proven to be a useful technique to resolve strong light-matter interactions with unprecedented spatial and spectral resolution [17–22].

Furthermore, in s-SNOM light is focused on an atomic force microscope (AFM) tip, which acts as an optical antenna that efficiently concentrates the incident illumination at its apex, resulting in strongly concentrated near-fields around it. Upon placing the tip on the sample, the near fields around the apex are modified due to their interaction with the sample's optical response. This near-field interaction also modifies the back-scattered light from the tip, and thus, by recording the tip-scattered light, one can obtain information on the local optical properties of the sample and visualize the local electromagnetic fields induced at the sample surface [23–25]. Notably, s-SNOM has demonstrated its ability to spatially map the near-field distributions of plasmonic structures [26] and phononic nanoantennas [27]. It has also proven effective in imaging graphene plasmons [28, 29] and anisotropic polaritons [30].

Considering all these prospects, this thesis aims at investigating the excitation of polaritons in the near field using a fast electron beam or a metallic tip. Specifically, we focus on the excitation of polaritons arising in anisotropic phononic media as well as polaritons that result from the coupling between electromagnetic modes and excitonic, or molecular vibrational modes. To this end, we introduce the fundamentals of polaritons and their near-field probing and analyze polaritonic systems in different scenarios.

In Chapter 1, we introduce basic concepts, methods, and the theoretical framework that will be used throughout this thesis. We first review Maxwell's equations in continuous media, together with the constitutive relations and the dipole oscillator model. This model serves as a valuable tool for describing dipolar excitation within a polarizable medium. We then apply this model to elucidate the characteristics of plasmons in metals and phonons in polar crystals within the context of the optical properties of solids. Our discussion extends to the manifestation of plasmons and phonon polaritons in various systems, including bulk, surfaces, thin films, and spherical nanoparticles. Furthermore, we review the phenomenon of strong coupling between light and matter, introducing two theoretical frameworks based on harmonic oscillator models. These

frameworks are able to reproduce the appearance of hybrid eigenmodes (polaritons) in strongly coupled systems. Once the basics of polaritons are introduced, we conclude this chapter by reviewing the working principles of low-loss electron energy loss spectroscopy and scattering-type scanning near-field optical microscopy. These two techniques play a crucial role in the investigation of the polaritonic excitations analyzed in this thesis.

In Chapters 2-4, we present the main results obtained in this thesis. In Chapter 2, we theoretically describe how fast electrons couple to polaritonic modes in hexagonal boron nitride (h-BN) by analyzing the electron energy-loss spectra. We show that for h-BN, bulk and surface modes can be excited by a fast electron traveling through the volume or along an infinite interface between h-BN and vacuum. Interestingly, and in strong contrast to excitations in isotropic materials, we show that bulk modes can be excited by fast electrons traveling outside the uniaxial medium. We show that the excitation of bulk and surface phonon polariton modes in h-BN is strongly related to the electron velocity and highly dependent on the angle between the electron beam trajectory and the optical axis of h-BN.

In Chapter 3, we theoretically and experimentally analyze the excitation of optical anapoles in tungsten disulfide (WS_2) nanodisks using EELS in STEM. We identify prominent dips in the EEL spectra of a high-index dielectric disk, and we show that these dips are associated with the excitation of a variety of optical anapoles in the disks. To experimentally verify anapole excitation and detection in EELS, our collaborators at Chalmers University of Technology (Gothenburg, Sweden) fabricate nanodisks made of WS_2 and perform EEL measurements on them. We find the appearance of optical anapoles in the experimental EEL spectra and corroborate them via numerical simulations. Interestingly, we show in this chapter that the optical anapoles frequency (energy loss features) disperse with the disk size, and thus, by varying the WS_2 nanodisk dimensions, an anapole can be tuned to overlap an exciton transition of WS_2, leading to anapole-exciton hybridization. At the end of this chapter, we show spatial maps of the anapoles excited in the WS_2 nanodisks with sub-nanometer resolution and conclude that their excitation can be controlled by placing the electron beam at different positions over the nanodisk.

In Chapter 4, we employ infrared near-field spectroscopy to examine the interaction between the localized modes of individual phononic nanoresonators and the modes of molecular vibrations of organic semiconductor layers, fabricated by our collaborators at the nanodevices group at CIC nanoGUNE (Donostia-San Sebastian). To directly investigate the coupling between the nanoresonator and the moleculer layer, we minimize the tip-resonator coupling by using a non-resonant tip. Additionally, we avoid the direct near-field interactions between the tip and molecules by probing the molecule-free part of

partially molecule-covered nanoresonators, a method we term as *remote* near-field probing. This methodology allows us to generate spatially and spectrally resolved maps of hybrid polariton modes and determine the nanoresonator-molecules coupling strengths. Additionally, we analyze via numerical simulations the potential influence of the metallic tip, together with signal demodulation, on the determination of the eigenfrequencies, damping parameters, and coupling strengths of the nanoresonator-molecules coupled system. In the final chapter of the thesis, we outline the main findings of the thesis and propose possible directions for future research.

1

Basics of polaritons and their near-field probing

We consider first the fictitious bodies called 'quasiparticles'. These arise from the fact that when a real particle moves through the system, it pushes or pulls on its neighbors and thus becomes surrounded by a 'cloud' of agitated particles similar to the dust cloud kicked up by a galloping horse in western.

–Richard D. Mattuck, *A Guide to Feynman diagrams in the many-body problem*

Abstract

In this chapter, we briefly summarize the basic concepts and methods that used throughout this thesis. First, we introduce in Section 1.1 Maxwell's equations in continuous media, the constitutive relations of a polarizable medium, and the dipole oscillator (Lorentz) model. In Section 1.2, we discuss plasmon and phonon polaritons in the context of the optical properties of solids and analyze their emergence in bulk, surface, and structured geometries. At the end of this section, we provide a brief discussion of polaritons in optical anisotropic thin films due to their relevance in this thesis. In Section 1.3, we discuss the phenomenon of strong coupling between light and matter and provide two theoretical frameworks that are able to address the appearance of hybrid eigenmodes (polaritons) in strongly coupled systems. Finally, in Section 1.4, we present some important theoretical concepts underlying low-loss electron energy loss spectroscopy (EELS) and scattering-type scanning near-field optical microscopy (s-SNOM). As it will be shown in the following chapters, the principle of measurement in these two techniques is key to understand many of the results presented in this thesis.

1.1 Electrodynamics in media

1.1.1 Macroscopic Maxwell's equations

From a semi-classical point of view, polaritons can be described as hybrid light-matter electromagnetic waves that originate from the coupling of photons with dipolar excitations in matter such as, plasmons in metals, optical phonons in polar crystals or excitons in semiconductors [3, 4]. Within the classical description, polaritons can be well described by the macroscopic Maxwell's equations [31–34]:

$$\nabla \cdot \mathbf{D}\left(\mathbf{r};t\right) = \rho_{\text{free}}\left(\mathbf{r};t\right), \tag{1.1a}$$

$$\nabla \times \mathbf{E}\left(\mathbf{r};t\right) = -\frac{\partial}{\partial t}\mathbf{B}\left(\mathbf{r};t\right), \tag{1.1b}$$

$$\nabla \cdot \mathbf{B}\left(\mathbf{r};t\right) = 0, \tag{1.1c}$$

$$\nabla \times \mathbf{H}\left(\mathbf{r};\mathbf{t}\right) = \mathbf{J}_{\text{free}}\left(\mathbf{r};t\right) + \frac{\partial}{\partial t}\mathbf{D}\left(\mathbf{r};t\right), \tag{1.1d}$$

which are a set of four coupled partial differential equations that relate, at each point $\mathbf{r}$ in space and time t, the dynamics of the macroscopic electric $\mathbf{E}(\mathbf{r};t)$ and magnetic $\mathbf{B}(\mathbf{r};t)$ fields to the macroscopic (free) charge $\rho_{\text{free}}(\mathbf{r};t)$ and current $\mathbf{J}_{\text{free}}(\mathbf{r};t)$ density distributions. The electric displacement vector $\mathbf{D}(\mathbf{r};t)$ and the auxiliary vector $\mathbf{H}(\mathbf{r};t)$ are related to the macroscopic polarization $\mathbf{P}(\mathbf{r};t)$ and magnetization $\mathbf{M}(\mathbf{r};t)$ of the medium via the following expressions:

$$\mathbf{D}(\mathbf{r};t) = \varepsilon_0\mathbf{E}(\mathbf{r};t) + \mathbf{P}(\mathbf{r};t), \tag{1.2}$$

$$\mathbf{H}(\mathbf{r};t) = \frac{1}{\mu_0}\mathbf{B}(\mathbf{r};t) - \mathbf{M}(\mathbf{r};t), \tag{1.3}$$

where ε_0 and μ_0 are the permittivity and permeability of free space. In this thesis, we will focus on nonmagnetic materials, and thus, throughout the text, it is assumed that $\mathbf{H}(\mathbf{r};t) = \mathbf{B}(\mathbf{r};t)/\mu_0$. To describe dipolar excitations in a material one needs to include in Maxwell's equations relevant information concerning the behavior of the medium under the influence of the electromagnetic field. This information is typically contained in the constitutive relations. As

discussed next, these relations allow us to connect, for example, the polarization of a material with the electric field $\mathbf{E}(\mathbf{r};t)$.

1.1.2 Constitutive relations

If we consider that the response of a medium is linear, one can connect the polarization of the material $\mathbf{P}(\mathbf{r};t)$ induced by the electric field $\mathbf{E}(\mathbf{r};t)$ in the following manner

$$\mathbf{P}(\mathbf{r};t) = \varepsilon_0 \int_{-\infty}^{\infty} \mathrm{d}t' \int \mathrm{d}^3\mathbf{r}' \chi(\mathbf{r}-\mathbf{r}';t-t')\mathbf{E}(\mathbf{r}';t'), \tag{1.4}$$

where $\chi(\mathbf{r}-\mathbf{r}';t-t')$ is the electric susceptibility of the medium and we assume that the material is homogeneous and stationary, meaning that the properties of the medium do not change in space and time [35]. The spatial integration in Eq. (1.4) extends to the entire real space. We will say that $\chi(\mathbf{r}-\mathbf{r}';t-t')$ preserves causality when the polarization of the material is zero in the absence of external illumination. This last condition can be mathematically formulated as follows: for times $t < t'$, the electric susceptibility is $\chi(\mathbf{r}-\mathbf{r}',t-t') = 0$.

Additionally, throughout this thesis, we assume that the response of the material is local, meaning that the value of χ at position $\mathbf{r}$ is independent of its value at any other position $\mathbf{r}' \neq \mathbf{r}$. The electric susceptibility thus takes on the following form: $\chi(\mathbf{r}-\mathbf{r}';t-t') = \chi(t-t')\delta(\mathbf{r}-\mathbf{r}')$, with $\delta(\mathbf{r}-\mathbf{r}')$ the Dirac delta function. Consequently, the constitutive relation changes from Eq. (1.4) to the simpler relation:

$$\mathbf{P}(\mathbf{r};t) = \varepsilon_0 \int_{-\infty}^{\infty} \mathrm{d}t' \chi(t-t')\mathbf{E}(\mathbf{r};t'). \tag{1.5}$$

In order to analyze the spectral response of the material, it is convenient to perform a time-to-frequency Fourier transform to Eq. (1.5) and write the connection between $\mathbf{P}(\mathbf{r};t)$ and $\mathbf{E}(\mathbf{r};t)$ in the frequency domain:

$$\mathbf{P}(\mathbf{r};\omega) = \varepsilon_0 \chi(\omega)\mathbf{E}(\mathbf{r};\omega), \tag{1.6}$$

with ω the angular frequency. We refer the reader to Appendix A for additional details on the Fourier transform. Furthermore, by applying the time-to-frequency Fourier transform to Eq. (1.2), and substituting the result into Eq. (1.6), one finds that the electric displacement field $\mathbf{D}(\mathbf{r};\omega)$ is connected to the

relative permittivity of the material[1] $\varepsilon(\omega) = 1 + \chi(\omega)$ in the following way:

$$\mathbf{D}(\mathbf{r};\omega) = \varepsilon_0 \varepsilon(\omega)\, \mathbf{E}(\mathbf{r};\omega). \tag{1.7}$$

This last expression establishes a connection between the propagation of electromagnetic waves within a medium and the optical response of the medium, which is defined by its dielectric function $\varepsilon(\omega)$. To better understand this connection, we discuss in the following section a simple model that allows us to deduce a mathematical expression of $\varepsilon(\omega)$. This model is known as the dipole (Lorentz) oscillator model.

1.1.3 The dipole (Lorentz) oscillator model

This classical model assumes that a medium is constituted by a group of oscillators, each of which represents for example a negatively charged electron bound to a positively charged nucleus, as illustrated in Fig. 1.1a. Under constant external illumination, of an electric field with amplitude $\mathbf{E}_0$ and angular frequency ω, $\mathbf{E}_{\text{ext}} = \mathbf{E}_0 e^{-i\omega t}$, the displacement of the heavy nucleus remains constant, whereas the displacement $\mathbf{r}(t)$ of the bounded electrons oscillates with natural resonance frequency ω_0, and thus, the electron experiences a restoring force equal to $m_{\text{e}}\,\omega_0^2 \mathbf{r}(t)$, with m_{e} the rest mass of the electron. The dynamics of $\mathbf{r}(t)$ is then determined by the following equation of motion:

$$m_{\text{e}} \frac{\mathrm{d}^2\mathbf{r}(t)}{\mathrm{d}t^2} = -m_{\text{e}}\,\omega_0^2 \mathbf{r}(t) - m_{\text{e}}\gamma \frac{\mathrm{d}\mathbf{r}(t)}{\mathrm{d}t} - e\mathbf{E}_0 e^{-i\omega t}, \tag{1.8}$$

where e is the elementary charge and the parameter γ is the damping constant associated with the energy losses of the electron due to collisions within the medium. The negatively charged electron follows the oscillation of the external illumination and thus, its displacement oscillates harmonically in time as $\mathbf{r}(t) = \mathbf{r}_0 e^{-i\omega t}$. Substituting this last relation into Eq. (1.8), one finds that

$$\mathbf{r}_0(\omega) = -\frac{e}{m_{\text{e}}} \frac{\mathbf{E}_0}{\omega_0^2 - \omega^2 - i\gamma\omega}. \tag{1.9}$$

As we schematically show in Fig. 1.1a, the harmonic motion of the electron bounded to the positive nucleus induces a net dipole moment $\mathbf{p}(t) = -e\mathbf{r}(t) = \mathbf{p}_0 e^{-i\omega t}$ with

$$\mathbf{p}_0(\omega) = -e\mathbf{r}_0(\omega) = \frac{e^2}{m_{\text{e}}} \frac{\mathbf{E}_0}{\omega_0^2 - \omega^2 - i\gamma\omega}. \tag{1.10}$$

[1] Relative permittivity, permittivity or dielectric function all refer to the same quantity: $\varepsilon(\omega)$.

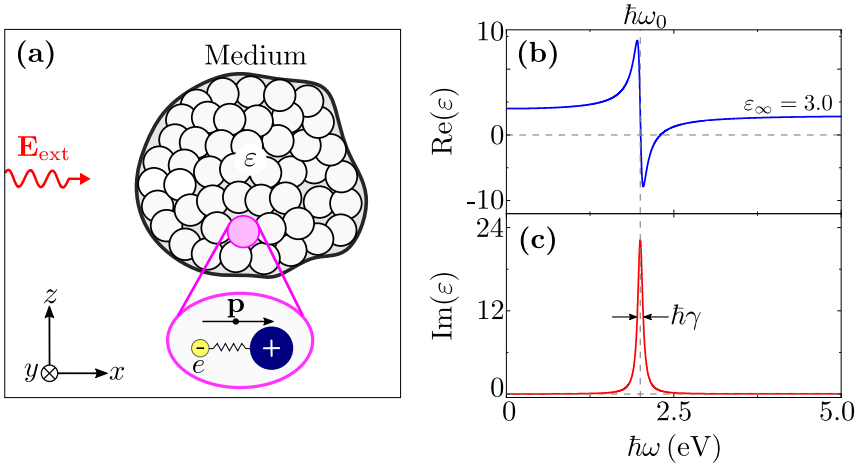

Figure 1.1: Lorentz model. (a) Sketch of the Lorentz model. The external illumination $\mathbf{E}_{\text{ext}}$ (red wavy arrow) polarizes the medium (gray irregular geometry) inducing dipoles (open circles) within the material. The zoom shows that each oscillating dipole $\mathbf{p}(t)$ consists of a negatively charged electron (yellow circle) bounded to a positively charged nucleus (blue circle). (b) Real and (c) imaginary components of $\varepsilon(\omega)$ given by Eq. (1.13). The values were obtained using the following parameters $\hbar\omega_0 = 2.0\,\text{eV}$, $\hbar\gamma = 0.09\,\text{eV}$ and $\varepsilon(0) = 4.0$ and $\varepsilon_\infty = 3.0$. The vertical dashed line indicates the resonant frequency $\hbar\omega_0 = 1.96\,\text{eV}$ and in panel (c) the parameter $\hbar\gamma$ marks the full width at half maximum (FWHM) of Im(ε).

The medium is then composed of several tinny dipoles (oscillators) that collectively produce the macroscopic polarization (dipole moment per unit volume)

$$\mathbf{P}(\omega) = n_0\mathbf{p}_0(\omega) = \frac{n_0 e^2}{m_\text{e}}\frac{\mathbf{E}_0}{\omega_0^2 - \omega^2 - i\gamma\omega}, \tag{1.11}$$

where n_0 is the number of dipoles per unit volume. By comparing Eqs. (1.6) and (1.11), one can deduce the following dielectric function of the medium

$$\varepsilon(\omega) = \varepsilon_\infty + \frac{n_0 e^2}{m_\text{e}\varepsilon_0}\frac{1}{\omega_0^2 - \omega^2 - i\gamma\omega}, \tag{1.12}$$

where we introduce the high-frequency limit $\varepsilon(\infty) = \varepsilon_\infty$. This term represents the polarization of the medium caused by non-resonant processes [36]. Notice that $\varepsilon(0) = n_0^2 e^2/(m_\text{e}\varepsilon_0\omega_0^2)$, and thus, one can rewrite Eq. 1.12 as follows:

$$\varepsilon(\omega) = \varepsilon_\infty + [\varepsilon(0) - \varepsilon_\infty]\frac{\omega_0^2}{\omega_0^2 - \omega^2 - i\gamma\omega}. \tag{1.13}$$

In Figs. 1.1b and 1.1c, we show the real and imaginary components of

$\varepsilon(\omega)$, respectively, for the illustrative values $\hbar\omega_0 = 2.0\,\text{eV}$, $\hbar\gamma = 0.09\,\text{eV}$, $\varepsilon(0) = 4.0$ and $\varepsilon_\infty = 3.0$. We can observe that close to the resonance frequency $\hbar\omega_0 = 2.0\,\text{eV}$ (vertical dashed line) the imaginary component of the dielectric function, $\text{Im}(\varepsilon(\omega))$, exhibits a distinctive peak at $\hbar\omega_0$ and a full width at half maximum (FWHM) equal to $\hbar\gamma$ (see Fig. 1.1c). In contrast, the real component of the dielectric function, $\text{Re}(\varepsilon(\omega))$, reaches its maximum at $\hbar\omega_0 - \hbar\gamma/2$ as we approach $\hbar\omega_0$ (see Fig. 1.1b). The spectrum then decreases sharply, passing through zero until it reaches its minimum at $\hbar\omega_0 + \hbar\gamma/2$ and then increases again until it reaches the high-frequency limit of $\varepsilon(\infty) = \varepsilon_\infty = 3.0$. This characteristic behavior of $\varepsilon(\omega)$ in the Lorentz oscillator model (in particular Eq. (1.12)) accurately describes the optical response of some materials, such as metals, semiconductor and polar crystals at visible and infrared frequencies. Furthermore, this model, based on the description of a material in terms of dipolar excitations, is extremely useful for understanding the propagation of hybrid light-matter electromagnetic waves (polaritons) in such materials. In the next section, we employ the Lorentz oscillator model to describe the optical response of metals and polar crystals and show the importance of Eq. (1.12) in the description of plasmon and phonon polaritons excited in different geometrical arrangements.

1.2 Polaritons in metals and polar crystals

1.2.1 Plasmons and phonons

Metals are excellent heat and electricity conductors due to the high density of free electrons in their conduction band. In a classical description, these free electrons can be considered as a gas moving around in the presence of the potential created by the positive (static) ions of the atomic nuclei of the metal. When the metal is illuminated, this free-electron gas collectively oscillates from its equilibrium position in a similar manner to the motion of bound electrons described in the Lorentz model (see Fig. 1.1a). Thus, the collective oscillation of the free-electron gas can be described by Eqs. (1.8)-(1.11) but setting the natural restoring frequency $\omega_0 = 0$ because the negatively charged particles freely move inside the metal. Using Eq. (1.12), one can deduce that the

dielectric function of metals, $\varepsilon_{\mathrm{m}}(\omega)$, is determined by the following expression (Eq. (1.12)):

$$\varepsilon_{\mathrm{m}}(\omega) = 1 - \frac{\omega_p^2}{\omega^2 + i\gamma\omega}, \tag{1.14}$$

here we introduce the plasma frequency $\omega_p^2 = n_0 e^2/(m_{\mathrm{e}}\varepsilon_0)$. This free-electron gas model, initially proposed by Drude and Sommerfeld [32, 37, 38], accurately captures the optical response of metals at infrared frequencies. At higher frequencies, however, the Drude–Sommerfeld–Lorentz model needs to be modified to account for interband transitions that can occur in metallic materials. In the case of silver or gold, for example one needs to take into consideration interband transitions occurring in the visible range in order to accurately describe the optical response of these metals.

We note that in a classical description, the self-sustained collective oscillations of the free-electron gas inside the metal is referred to as *plasmon* [36, 38]. From a quantum mechanical description, on the other hand, one can write the Hamiltonian of the free-electron gas interacting with the incident electromagnetic field. In appropriate canonical coordinates, one then finds that the electrons collectively oscillate with a frequency of approximately ω_p [39–42]. In this quantum context, the quasiparticle plasmon refers to a quantum of the collective oscillation of the free-electron gas.

Either in the classical or quantum descriptions, plasmons are responsible for the reflection of light at visible frequencies in metals, and for the negative values of the permittivity given by Eq. (1.14). This is clearly shown in Fig. 1.2a, where we plot the real and imaginary components of $\varepsilon_{\mathrm{m}}(\omega)$ given by Eq. (1.14). We use the parameters $\hbar\omega_p = 15.2\,\mathrm{eV}$ and $\hbar\gamma = 0.808\,\mathrm{eV}$ that approximately mimic the optical response of aluminum [43]. From the plots, we see that the real part of the dielectric function (blue line) is negative, and then crosses zero at frequency $\tilde{\omega}_p = \omega_p\sqrt{1-(\gamma/\omega_p)^2}$ (vertical dashed line in Fig. 1.2a). For Al, $\tilde{\omega}_p$ is close to ω_p since $\omega_p >> \gamma$ and thus the term $\sqrt{1-(\gamma/\omega_p)^2} \approx 1$. As we discuss in the next subsection, at frequencies lower than $\tilde{\omega}_p \approx \omega_p$ the electrons oscillate, generating an electric field of opposite sign to the incident field, and thus, electromagnetic waves cannot propagate through the bulk of the metal.

In addition to plasmons, a material can also contain other types of collective excitations. For instance, in polar crystals, *optical phonons* result from the collective vibrations of ions arranged in the well-defined lattice of the crystal[2]. Under external illumination, the motion of the ions is similar to that described by Eq. (1.8). Using this expression, together with Eq. (1.7), one finds that the dielectric function of a polar crystal can be written in the following form

[2]From a quantum mechanical description, the quasiparticle phonon refers to a quantum of the collective vibration of the ions in the crystal lattice [38, 44].

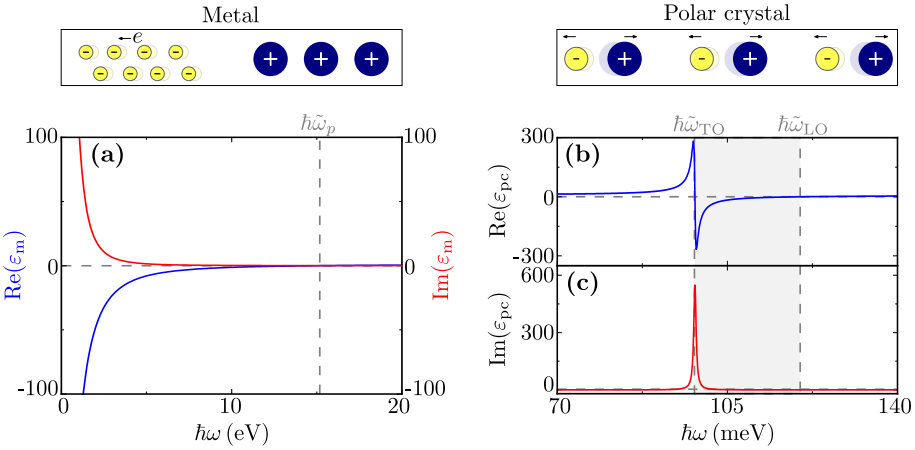

Figure 1.2: Dielectric function of metals and polar crystals. (a) Real (blue line) and imaginary (red line) components of $\varepsilon_{\mathrm{m}}(\omega)$ given by Eq. (1.14). Values are obtained using the following parameters $\hbar\omega_p = 15.2\,\mathrm{eV}$ and $\hbar\gamma = 0.808\,\mathrm{eV}$ typical of aluminium. The vertical dashed line indicates the frequency $\hbar\tilde{\omega}_p = 15.18\,\mathrm{eV}$. (b) Real and (c) imaginary components of $\varepsilon_{\mathrm{pc}}(\omega)$ given by Eq. (1.15). Values are obtained using the following parameters $\varepsilon_\infty = 6.7$, $\hbar\omega_{\mathrm{TO}} = 98.32\,\mathrm{meV}$, $\hbar\omega_{\mathrm{LO}} = 120.14\,\mathrm{meV}$, and $\hbar\gamma_{\mathrm{pc}} = .59\,\mathrm{meV}$ typical of SiC. The shaded gray area marks the Reststrahlen band, with $\hbar\tilde{\omega}_{\mathrm{TO}} = 98.324\,\mathrm{meV}$ and $\hbar\tilde{\omega}_{\mathrm{LO}} = 120.136\,\mathrm{meV}$. Insets above (a) and (b) illustrate the free electrons in the metal and the ions in the polar crystal, respectively.

[38, 45]:

$$\varepsilon_{\mathrm{pc}}(\omega) = \varepsilon_\infty + \frac{\varepsilon_\infty - \varepsilon(0)}{\omega^2/\omega_{\mathrm{TO}}^2 - 1}, \tag{1.15}$$

where ω_{TO} is the transverse optical (TO) phonon frequency and ε_∞ is the high-frequency permittivity. At the longitudinal optical (LO) phonon frequency, ω_{LO}, the dielectric function given by Eq. (1.15) is zero and thus

$$\varepsilon_{\mathrm{pc}}(\omega_{\mathrm{LO}}) = 0 = \varepsilon_\infty + \frac{\varepsilon_\infty - \varepsilon(0)}{\omega_{\mathrm{TO}}^2/\omega_{\mathrm{TO}}^2 - 1} \quad \text{or equivalently,} \quad \frac{\varepsilon(0)}{\varepsilon_\infty} = \frac{\omega_{\mathrm{LO}}^2}{\omega_{\mathrm{TO}}^2}. \tag{1.16}$$

The latter expression is known as the Lydanne-Sachs-Teller relationship, and it allows us to rewrite Eq. (1.15) in the following form:

$$\varepsilon_{\mathrm{pc}}(\omega) = \varepsilon_\infty \left(1 + \frac{\omega_{\mathrm{LO}}^2 - \omega_{\mathrm{TO}}^2}{\omega_{\mathrm{TO}}^2 - \omega^2 - i\omega\gamma_{\mathrm{pc}}}\right), \tag{1.17}$$

where we have introduced the damping constant γ_{pc}, which is associated with the lifetime of the TO phonon. We note that by introducing γ_{pc} into the dielectric function given by Eq. (1.17), $\mathrm{Re}(\varepsilon_{\mathrm{pc}}(\omega))$ is zero at frequencies $\tilde{\omega}_{\mathrm{TO}}$

and $\tilde{\omega}_{\mathrm{LO}}$, determined by the following expressions

$$\tilde{\omega}_{\mathrm{TO}}^2 = \frac{\Delta + \sqrt{\Delta^2 - (2\omega_{\mathrm{TO}}\,\omega_{\mathrm{LO}})^2}}{2}, \tag{1.18}$$

$$\tilde{\omega}_{\mathrm{LO}}^2 = \frac{\Delta - \sqrt{\Delta^2 - (2\omega_{\mathrm{TO}}\,\omega_{\mathrm{LO}})^2}}{2}, \tag{1.19}$$

with

$$\Delta = \omega_{\mathrm{TO}}^2 + \omega_{\mathrm{LO}}^2 - \gamma_{\mathrm{pc}}^2. \tag{1.20}$$

When $\omega_{\mathrm{TO}}, \omega_{\mathrm{LO}} >> \gamma_{\mathrm{pc}}$, one can deduce from Eqs. (1.18)-(1.20) that $\tilde{\omega}_{\mathrm{TO}} \approx \omega_{\mathrm{TO}}$ and $\tilde{\omega}_{\mathrm{LO}} \approx \omega_{\mathrm{LO}}$.

It is worth mentioning that the reduced mass of ions in the polar crystal is greater than that of free electrons in metals, and thus, the natural frequency of optical phonons is generally lower than that of plasmons. For this reason, the excitation of optical phonons in polar materials typically appears at infrared frequencies as observed in Figs. 1.2b-c, where we plot the complex dielectric function described by Eq. (1.17) using the values $\varepsilon_\infty = 6.7$, $\hbar\omega_{\mathrm{TO}} = 98.32\,\mathrm{meV}$, $\hbar\omega_{\mathrm{LO}} = 120.14\,\mathrm{meV}$ and $\hbar\gamma_{\mathrm{pc}} = 0.59\,\mathrm{meV}$. These values approximately mimic the optical response of silicon carbide in the infrared range [46, 47]. For SiC $\omega_{\mathrm{TO}}, \omega_{\mathrm{LO}} >> \gamma_{\mathrm{pc}}$, and thus, $\tilde{\omega}_{\mathrm{TO}} \approx \omega_{\mathrm{TO}}$ and $\tilde{\omega}_{\mathrm{LO}} \approx \omega_{\mathrm{LO}}$. In Fig. 1.2c, we can observe a sharp peak in $\mathrm{Im}(\varepsilon_{\mathrm{pc}}(\omega))$ at around 100 eV, which is associated with the excitation of the transverse optical phonon in SiC. In addition, the real component of $\varepsilon_{\mathrm{pc}}(\omega)$ (blue line in Fig. 1.2b) is negative between the TO and LO phonon frequencies (shaded gray area). This frequency range is known as the Reststrahlen[3] band, and within it, electromagnetic waves cannot propagate through the bulk of the polar crystal, similarly to what occurs with the propagation of EM waves inside metals at energies lower than ω_p.

In the previous discussion, we have illustrated the fact that the Lorentz model describes with accuracy the optical response of plasmonic and phononic materials. This discussion, however, was focused on the material properties and not on the propagation of EM waves in these materials. In the following subsections, we thus analyze in more detail the concepts of plasmon and phonon polaritons by identifying (eigen)solutions of Maxwell's equations in geometrical arrangements such as in bulk, at interfaces, and at finite nanostructures.

[3]The German word "Reststrahlen" means "residual rays".

1.2.2 Bulk polaritons

It is instructive to begin our analysis by considering the propagation of EM waves in the bulk of a metal or a polar crystal. To do so, we consider the following monochromatic transverse wave: $\mathbf{E}(\mathbf{r};t) = \mathbf{E}_0 e^{i(\mathbf{k}\cdot\mathbf{r}-\omega t)}$ with $\mathbf{E}_0$ a complex amplitude vector and $\mathbf{k}(\omega) = (k_x, k_y, k_z)$ the wavevector of the wave. The dynamics of the transverse wave is determined by the Helmholtz equation

$$\left[\nabla^2 + k_0^2 \varepsilon(\omega)\right] \mathbf{E}(\mathbf{r}) = \mathbf{0}, \tag{1.21}$$

with $k_0 = \omega/c$ the magnitude of the wavevector in vacuum and c the speed of light. Inserting the spatial component of the wave, $\mathbf{E}(\mathbf{r}) = \mathbf{E}_0 e^{i\mathbf{k}\cdot\mathbf{r}}$, into Eq. (1.21), we can find the following dispersion relation of the transverse wave

$$k(\omega) = k_0 \sqrt{\varepsilon(\omega)}. \tag{1.22}$$

From this relationship, we immediately see that for frequencies such that the dielectric function acquires negative values, the magnitude of the wavevector is imaginary, that is, $k = i\kappa$. Consequently, the wave, instead of propagating inside the material, will decay as $\mathbf{E}(\mathbf{r}) = \mathbf{E}_0 e^{-\kappa\cdot\mathbf{r}}$. In the case of metals and polar crystals, the real component of their dielectric function has negative values below the plasma frequency and within the Reststrahlen band, respectively (see Fig. 1.2). Thus, for these frequencies, transverse electromagnetic waves cannot propagate inside the materials and rather undergo exponential decay (evanescently decay). This is clearly represented in Fig. 1.3, where we plot the solutions of the dispersion relation (Eq. (1.22)) using the dielectric functions of Al and SiC (Eqs. (1.14) and (1.17)). For illustrative purposes, all the calculations shown in this subsection and in the following are performed considering small losses in the materials ($\gamma \approx 0$ in Eq. (1.14) and $\gamma_{\mathrm{pc}} \approx 0$ in Eq. (1.17)).

Figure 1.3a shows the solution (blue curve) of Eq. (1.22) considering $\varepsilon(\omega) = \varepsilon_{\mathrm{Al}}(\omega)$. We can observe the typical dispersion relation for EM waves propagating inside a metal. This solution is usually referred to as the bulk plasmon polariton (PP) [48]. For small wavenumbers ($k \to 0$), the energy of the bulk PP does not become zero but tends to $\hbar\omega_p$ (gray dashed line). For energies below $\hbar\omega_p$, the real component of the wavenumber is zero, corroborating that EM waves with $\omega < \omega_p$ cannot propagate inside the metal. The differences between the dispersion of the bulk plasmon polariton and that of the bulk phonon polariton (PhP) can be observed in Fig. 1.3b, where the solution (blue curves) of Eq. (1.22) for $\varepsilon(\omega) = \varepsilon_{\mathrm{SiC}}(\omega)$ is plotted. Contrary to the dis-

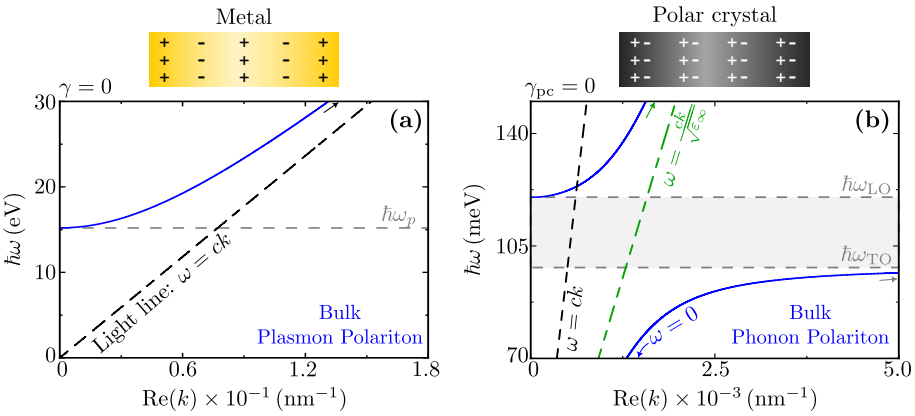

Figure 1.3: Bulk plasmon and phonon polaritons. (a) Dispersion relation of the bulk plasmon polariton (blue curve) determined by Eq. 1.22. The values are obtained considering $\varepsilon(\omega) = \varepsilon_{\mathrm{Al}}(\omega)$ and using the same parameters as the ones employed in Fig. 1.2a. The black dashed line represents the dispersion relation $k = \omega/c$ of a photon in free space, whereas the horizontal gray dashed line indicates the plasma frequency ω_p. (b) Same as (a) but considering $\varepsilon(\omega) = \varepsilon_{\mathrm{SiC}}(\omega)$ and using the parameters employed in Fig. 1.2b. The green dashed line represents the dispersion relation $k = \omega\sqrt{\varepsilon_\infty}/c$ of a photon in a medium with constant permittivity $\varepsilon_\infty = 6.7$. The shaded gray area marks the Reststrahlen band. The arrows in panels (a) and (b) indicate the asymptotic behavior of the dispersions (color code corresponds to the asymptotic line they approximate to), whereas the schematics above the panels provide a visual representation of the bulk of a metal and a polar crystal, respectively. For illustrative purposes, all the calculations in this figure are implemented without considering losses in the materials ($\gamma = 0$ in Eq. (1.14) and $\gamma_{\mathrm{pc}} = 0$ in Eq. (1.17)).

persion of the bulk PP, the dispersion of the bulk PhP exhibits two branches (solutions) for energies that lie outside the Reststrahlen band (shaded gray area). For energies inside this band, the real component of the wavenumber is equal to zero, $\mathrm{Re}(k) = 0$, meaning that transverse waves with these particular energy cannot propagate through the crystal. We provide in the box below an extended mathematical analysis of the asymptotic behavior of the bulk PP and the bulk PhP (indicated by the arrows in Figs. 1.3a and 1.3b).

The bulk polariton is the simplest example of an EM wave propagating in a metal or polar crystal. In the following subsection, we will discuss a special type of EM wave that can propagate at the interface of such materials.

Asymptotic behavior of the dispersion of bulk polaritons considering no losses in the materials

Plasmon polaritons

The asymptotic behavior of the dispersion of the bulk PP can be understood from the following equation (substitute $\varepsilon(\omega) = \varepsilon_{\mathrm{m}}(\omega)$ in Eq. (1.22)):

$$\omega^2 = c^2k^2 + \omega_p^2, \tag{1.23}$$

where we assume that $\gamma = 0$. In the limit of large wavenumbers $ck >> \omega$, one can deduce from Eq. (1.23) that the dispersion approaches to $\omega \approx ck$.

Phonon polaritons

Analogously, one can understand the asymptotic behavior of the dispersion of the bulk PhP by substituting $\varepsilon(\omega) = \varepsilon_{\mathrm{pc}}(\omega)$ in Eq. (1.22). From this substitution, assuming $\gamma_{\mathrm{pc}} = 0$, and solving for ω^2 one obtains the following expression:

$$\omega_{\pm}^2 = \frac{\omega_{\mathrm{LO}}^2}{2} + \frac{c^2k^2}{2\varepsilon_\infty} \pm \frac{c^2k^2}{2\varepsilon_\infty}\sqrt{\left(1 + \frac{\varepsilon_\infty\omega_{\mathrm{LO}}^2}{c^2k^2}\right)^2 - 4\frac{\varepsilon_\infty\omega_{\mathrm{TO}}^2}{c^2k^2}}. \tag{1.24}$$

For large wavenumbers $ck >> \omega$, one can Taylor expand the expression inside the square root of Eq. (1.24) and obtain the following solution:

$$\omega_{\pm}^2 \approx \frac{\omega_{\mathrm{LO}}^2}{2} + \frac{c^2k^2}{2\varepsilon_\infty} \pm \frac{c^2k^2}{2\varepsilon_\infty}\left[1 + \frac{\varepsilon_\infty\omega_{\mathrm{LO}}^2}{c^2k^2} - \frac{2\varepsilon_\infty\omega_{\mathrm{TO}}^2}{c^2k^2} + O(1/ck)^4\right]. \tag{1.25}$$

From the latter equation, one can deduce that the upper branch of the bulk PhP dispersion approaches to $\omega_+ \approx ck/\sqrt{\varepsilon_\infty}$, whereas the lower branch approaches to $\omega_- \approx \omega_{\mathrm{TO}}$.

1.2.3 Surface polaritons

Surface polaritons are hybrid EM waves propagating at the interface between a dielectric and a polaritonic material (in our case, a metal or a polar crystal). These hybrid EM waves evanescently decay in the direction that is perpendicular to the interface separating both media. To elucidate the properties of these waves, we analyze the simplest geometrical arrangement in which they manifest themselves: a planar interface separating two semi-infinite materials.

As illustrated in the insets above Figs. 1.4a and 1.4b, we consider a configuration where at $z > 0$ the material labeled I is air, characterized by a dielectric function $\varepsilon_{\rm I} = 1$, while at $z < 0$, the material labeled II is a metal or a polar crystal characterized by a dielectric function $\varepsilon_{\rm II}(\omega)$, given by Eqs. (1.14) or (1.17), respectively. The surface electromagnetic wave propagating along the x-direction, and polarized with the electric field along the xz-plane (transverse magnetic (TM) polarization), is characterized by the following monochromatic electromagnetic field [48–51]:

$$\mathbf{B}_{\rm I}(\mathbf{r}) = B^o_{\rm I} e^{-\kappa_{\rm I} z + iqx}\,\hat{\mathbf{y}}, \tag{1.26a}$$

$$\mathbf{E}_{\rm I}(\mathbf{r}) = \frac{c^2}{\omega\varepsilon_{\rm I}}\left[i\kappa_{\rm I}\hat{\mathbf{x}} - q\hat{\mathbf{z}}\right] B_{{\rm I},y}(\mathbf{r}), \tag{1.26b}$$

$$\mathbf{B}_{\rm II}(\mathbf{r}) = B^o_{\rm II} e^{\kappa_{\rm II} z + iqx}\,\hat{\mathbf{y}}, \tag{1.26c}$$

$$\mathbf{E}_{\rm II}(\mathbf{r}) = -\frac{c^2}{\omega\varepsilon_{\rm II}}\left[i\kappa_{\rm II}\hat{\mathbf{x}} + q\hat{\mathbf{z}}\right] B_{{\rm II},y}(\mathbf{r}), \tag{1.26d}$$

where $B^o_{\rm I}$, $B^o_{\rm II}$ are amplitude constants that can be determined by using boundary conditions imposed by Maxwell's equations. The EM waves at each medium have wavevectors $\mathbf{k}_{\rm I} = (q, 0, i\kappa_{\rm I})$ and $\mathbf{k}_{\rm II} = (q, 0, -i\kappa_{\rm II})$ with $\kappa_{\rm I}$,$\kappa_{\rm II} > 0$, satisfying the subsequent relationships

$$k^2_{\rm I} = -\kappa^2_{\rm I} + q^2 = \varepsilon_{\rm I}\frac{\omega^2}{c^2}, \tag{1.27a}$$

$$k^2_{\rm II} = -\kappa^2_{\rm II} + q^2 = \varepsilon_{\rm II}\frac{\omega^2}{c^2}. \tag{1.27b}$$

To find the dispersion relation of the surface wave, we apply to Eqs. (1.26)a-d the boundary conditions imposed by Maxwell's equations at the interface between the two media. After doing so, one can obtain the following system of linear equations:

$$\begin{pmatrix} 1 & -1 \\ \varepsilon_{\rm II}\kappa_{\rm I} & \varepsilon_{\rm I}\kappa_{\rm II} \end{pmatrix} \begin{pmatrix} B^o_{\rm I} \\ B^o_{\rm II} \end{pmatrix} = \begin{pmatrix} 0 \\ 0 \end{pmatrix}. \tag{1.28}$$

By solving this system for the non-trivial solution, one finds the condition

$$\kappa_{\rm II}\varepsilon_{\rm I} + \kappa_{\rm I}\varepsilon_{\rm II} = 0, \tag{1.29}$$

which, together with Eqs. (1.27)a-b, allow us to write the dispersion of the surface wave as

$$q(\omega) = \frac{\omega}{c}\sqrt{\frac{\varepsilon_{\rm I}(\omega)\,\varepsilon_{\rm II}(\omega)}{\varepsilon_{\rm I}(\omega) + \varepsilon_{\rm II}(\omega)}}. \tag{1.30}$$

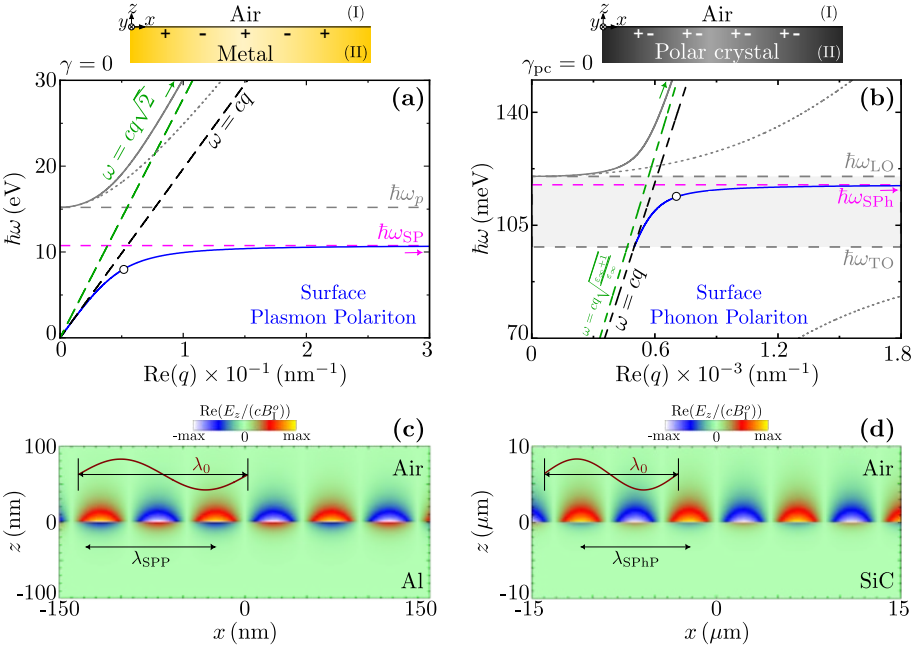

Figure 1.4: Surface plasmon and phonon polaritons. (a) Dispersion relation of surface plasmon polariton (blue curve) and bulk plasmon polariton (gray curve) determined both by Eq. (1.30). The plot was obtained considering $\varepsilon(\omega) = \varepsilon_{\mathrm{Al}}(\omega)$ and using the same parameters as the ones employed in Fig. 1.2a. Black and green dashed lines represent the dispersion relations: $q = \omega/c$ and $q = \omega/(c\sqrt{2})$, respectively. Gray dotted curve represents the dispersion of the bulk plasmon polariton shown in Fig. 1.3a. Horizontal gray and magenta dashed lines indicate the plasma frequency ω_p and the surface plasmon frequency ω_{SP} (Eq. (1.32)), respectively. (b) Same as (a) but considering $\varepsilon(\omega) = \varepsilon_{\mathrm{SiC}}(\omega)$ and using the parameters employed in Fig. 1.2b. Green dashed line represents the dispersion relation $q = (\omega/c)\sqrt{\varepsilon_\infty/(\varepsilon_\infty + 1)}$. Gray dotted curves represent the dispersion of the bulk phonon polariton shown in Fig. 1.3b. Horizontal magenta dashed line indicates the surface phonon frequency ω_{SPh} (Eq. (1.33)). The shaded gray area marks the Reststrahlen band. The arrows in panels (a) and (b) indicate the asymptotic behavior of the dispersions, whereas the insets above the panels provide a visual representation of the systems. Field plots in (c) and (d) show the normalized real part of the z-component of the electric field in the xz-plane for the energies marked by the open circles in panels (a) and (b): (c) 9 eV and (d) 114 meV. The maximum values of the normalized field plots are: (c) 1.62 and (d) 1.70. Double arrow lines mark the wavelength of the SPP (panel (c)) and the SPhP (panel (d)). Insets in the panels show the wavelength of light in free space, λ_0. For illustrative purposes, all the calculations in this figure are implemented without considering losses in the materials ($\gamma = 0$ in Eq. (1.14) and $\gamma_{\mathrm{pc}} = 0$ in Eq. (1.17)).

By comparing Eqs. (1.29) and (1.30), one can deduce that $q(\omega)$ is a real number when $\varepsilon_{\mathrm{II}}(\omega) < 0$ and $|\varepsilon_{\mathrm{II}}(\omega)| > \varepsilon_{\mathrm{I}}(\omega)$. These last conditions can be fulfilled in metals or polar crystals. Indeed, in Fig. 1.4 we plot the evaluation

of Eq. (1.30) using $\varepsilon_{\mathrm{I}}(\omega) = 1$ and $\varepsilon_{\mathrm{II}}(\omega) = \varepsilon_{\mathrm{Al}}(\omega)$ (Fig. 1.4a) or $\varepsilon_{\mathrm{II}}(\omega) = \varepsilon_{\mathrm{SiC}}(\omega)$ (Fig. 1.4b). The most relevant feature of the dispersion relations is the appearance of solutions of electromagnetic modes (blue curves in Figs. 1.4a and 1.4b) below the plasma frequency and within the Restrahlend band. These solutions correspond to surface plasmons (SPP) and surface phonon (SPhP) polaritons, respectively. The gray solid lines in Figs. 1.4a and 1.4b) are electromagnetic modes propagating through the media, similar to the bulk polaritons (gray dotted lines in Figs. 1.4a and 1.4b) discussed in the previous subsection. Note that for small wavenumbers ($q \to 0$) the energy of the SPP becomes zero, whereas the energy of the SPhP is equal to the TO energy. For large wavenumbers ($q >> 1$), on the other hand, the dispersions of the SPP and the SPhP tend to the surface plasmon frequency ω_{SP} and the surface phonon frequency ω_{SPh}, respectively (indicated by the magenta dashed lines in Figs. 1.4a and 1.4b). These large q frequencies can be derived from the poles of Eq. (1.30), that is, from the condition:

$$\varepsilon_{\mathrm{I}} + \varepsilon_{\mathrm{II}} = 0. \tag{1.31}$$

Substituting Eqs. (1.14) and (1.17) into Eq. (1.31), and neglecting losses in the materials, it can be determined that the frequencies ω_{SP} and ω_{SPh} are

$$\omega_{\mathrm{SP}} = \frac{\omega_p}{\sqrt{2}}, \tag{1.32}$$

$$\omega_{\mathrm{SPh}} = \sqrt{\frac{\varepsilon_\infty \omega_{\mathrm{LO}}^2 + \omega_{\mathrm{TO}}^2}{1 + \varepsilon_\infty}}. \tag{1.33}$$

From the dispersion relations, one can notice that for some energies, the surface waves show larger wavenumber than that of a photon with the same energy in free space (compare blue curves with black dashed lines in Figs. 1.4a and 1.4b). This implies that SPP and SPhP have smaller wavelengths than that of light propagating in free space. We emphasize this aspect in Figs. 1.4c and 1.4d, where we show the real part of the z-component of the electric field (Eqs. (1.26)a-b). We clearly observe waves propagating along the interface between the two media, and, more importantly, the polaritons' wavelength, λ_{SPP} and λ_{SPhP}, are smaller than that of light in free space, λ_0 (compare the length of λ_{SPP} and λ_{SPhP} with the length of λ_0 at each panel). This mismatch in wavenumbers between the surface polaritons and light in free space implies that surface polaritons cannot be excited simply using plane-wave illumination.

1.2.4 Surface polaritons in thin films

Many interesting optical materials adopt a layered configuration forming thin films. Examples of these are graphene, hexagonal boron nitride (h-BN) or transition metal dichalcogenides (TMDCs), among others. Surface polaritons also exist in thin films. Their properties depend on the film thickness and the dielectric medium at both sides of the film. In this subsection of the thesis, we explore the properties of surface polaritons confined in films of thickness d made of metal or polar crystal. The film is embedded in air, as schematically illustrated in the insets above Figs. 1.5a and 1.5b. Following the same procedure as in the previous subsection, we can write the (TM-polarized) electromagnetic field of the surface wave in the three media as [50, 51]:

$$\mathbf{B}_{\mathrm{I}}(\mathbf{r}) = B_{\mathrm{I}}^{o}\, e^{-\kappa_{\mathrm{I}} z + iqx}\hat{\mathbf{y}}, \tag{1.34a}$$

$$\mathbf{E}_{\mathrm{I}}(\mathbf{r}) = \frac{c^2}{\omega}\left[i\kappa_{\mathrm{I}}\hat{\mathbf{x}} - q\hat{\mathbf{z}}\right] B_{\mathrm{I},y}(\mathbf{r}), \tag{1.34b}$$

$$\mathbf{B}_{\mathrm{II}}(\mathbf{r}) = \left[B_{\mathrm{II}}^{o} e^{\kappa_{\mathrm{II}} z + iqx} + B_{\mathrm{II}}^{o'} e^{-\kappa_{\mathrm{II}} z + iqx}\right]\hat{\mathbf{y}}, \tag{1.34c}$$

$$\mathbf{E}_{\mathrm{II}}(\mathbf{r}) = -\frac{c^2}{\omega\varepsilon_{\mathrm{II}}}\left[i\kappa_{\mathrm{II}}\left(B_{\mathrm{II}}^{o} e^{\kappa_{\mathrm{II}} z + iqx} - B_{\mathrm{II}}^{o'} e^{-\kappa_{\mathrm{II}} z + iqx}\right)\hat{\mathbf{x}} + qB_{\mathrm{II},y}(\mathbf{r})\hat{\mathbf{z}}\right], \tag{1.34d}$$

$$\mathbf{B}_{\mathrm{III}}(\mathbf{r}) = B_{\mathrm{III}}^{o}\, e^{\kappa_{\mathrm{I}} z + iqx}\hat{\mathbf{y}}, \tag{1.34e}$$

$$\mathbf{E}_{\mathrm{III}}(\mathbf{r}) = -\frac{c^2}{\omega}\left[i\kappa_{\mathrm{I}}\hat{\mathbf{x}} + q\hat{\mathbf{z}}\right] B_{\mathrm{III},y}(\mathbf{r}), \tag{1.34f}$$

with B_{I}^{o}, B_{II}^{o}, $B_{\mathrm{II}}^{o'}$, B_{III}^{o} amplitude constants that can be determined by applying boundary conditions. The wavenumbers κ_{I} and κ_{II} satisfy Eqs. (1.27a) and (1.27b), respectively. Applying boundary conditions to Eqs. (1.34a)-(1.34f) at the interfaces of the film ($z = 0$ and $z = -d$), one obtains the following system of equations:

$$\begin{pmatrix} 1 & -1 & -1 & 0 \\ \kappa_{\mathrm{I}}\varepsilon_{\mathrm{II}} & \kappa_{\mathrm{II}} & -\kappa_{\mathrm{II}} & 0 \\ 0 & e^{-\kappa_{\mathrm{II}} d} & e^{\kappa_{\mathrm{II}} d} & -e^{-\kappa_{\mathrm{I}} d} \\ 0 & \kappa_{\mathrm{II}} e^{-\kappa_{\mathrm{II}} d} & -\kappa_{\mathrm{II}} e^{\kappa_{\mathrm{II}} d} & -\kappa_{\mathrm{I}}\varepsilon_{\mathrm{II}} e^{-\kappa_{\mathrm{I}} d} \end{pmatrix} \begin{pmatrix} B_{\mathrm{I}}^{o} \\ B_{\mathrm{II}}^{o} \\ B_{\mathrm{II}}^{o'} \\ B_{\mathrm{III}}^{o} \end{pmatrix} = \begin{pmatrix} 0 \\ 0 \\ 0 \\ 0 \end{pmatrix}. \tag{1.35}$$

Solving the system for the non-trivial solution, one further finds that the waves confined at the surface of the film are characterized by the following dispersion relation:

$$(\varepsilon_{\mathrm{II}}\kappa_{\mathrm{I}} + \kappa_{\mathrm{II}}) \pm (\varepsilon_{\mathrm{II}}\kappa_{\mathrm{I}} - \kappa_{\mathrm{II}}) e^{-\kappa_{\mathrm{II}} d} = 0. \tag{1.36}$$

The latter relation can be rewritten as the following implicit equations:

$$\omega_+ : \tanh\left(\kappa_{\mathrm{II}}\frac{d}{2}\right) = -\varepsilon_{\mathrm{II}}\frac{\kappa_{\mathrm{I}}}{\kappa_{\mathrm{II}}}, \tag{1.37}$$

and

$$\omega_- : \coth\left(\kappa_{\mathrm{II}}\frac{d}{2}\right) = -\varepsilon_{\mathrm{II}}\frac{\kappa_{\mathrm{I}}}{\kappa_{\mathrm{II}}}. \tag{1.38}$$

Figures 1.5a and 1.5b show the evaluation of the dispersion relations ω_+ (Eq. (1.37)) and ω_- (Eq. (1.38)) for films composed of aluminum and silicon carbide. We can observe that ω_+ describes a high-frequency mode, whereas ω_- describes a low-frequency mode, both approaching either the SP frequency in the case of Al or the SPh frequency in the case of SiC. Indeed, for large wavenumbers ($q >> 1$), $\kappa_{\mathrm{I}} = \kappa_{\mathrm{II}} = q$, and thus, the dispersion relation of surface polaritons propagating in a thin film simplifies from Eq. (1.36) to:

$$\frac{\varepsilon_{\mathrm{II}} + 1}{\varepsilon_{\mathrm{II}} - 1} = \pm e^{-qd}. \tag{1.39}$$

When $q \to \infty$, the right-hand side of Eq. (1.39) approaches zero, and the left-hand side needs to fulfill the condition $\varepsilon_{\mathrm{II}} + 1 = 0$, which is the condition for the excitation of the surface polaritons propagating along a single semi-infinite interface (Eq. (1.31)). In the limit of large wavenumber, ω_+ and ω_- thus both tend assymtotically to the surface frequency.

The appearance of the two polaritonic branches ω_+ and ω_- in the dispersion relation of the thin film can also be understood as a result of the coupling between surface waves generated at each of the interfaces of the film. The electromagnetic fields of the surface polaritons at each surface of the film interact and couple, producing the following two new eigenmodes: (i) a high-frequency mode ω_+ with electric charges distributed at the surfaces of the film antisymmetrically along the z-axis, and (ii) a low-frequency mode ω_- with electric charges distributed at the surfaces of the film symmetrically along the z-axis. We confirm this by plotting in Figs. 1.5c and 1.5d the real part of the z-component of the electric field distributions around the thin films at the energies marked by the open circles in Figs. 1.5a and 1.5b. We can observe surface waves propagating along the interfaces of the film and, more importantly, one can recognize the symmetric and antisymmetric field distributions with respect to the z-axis, which are a direct consequence of the hybrid nature of the two new eigenmodes ω_+ and ω_-. The thin film is one of the simplest geometrical arrangements where coupling between two EM modes gives rise to new hybridized eigenmodes in a system. In Section 1.3 we will study in more detail the physic underlying coupled systems.

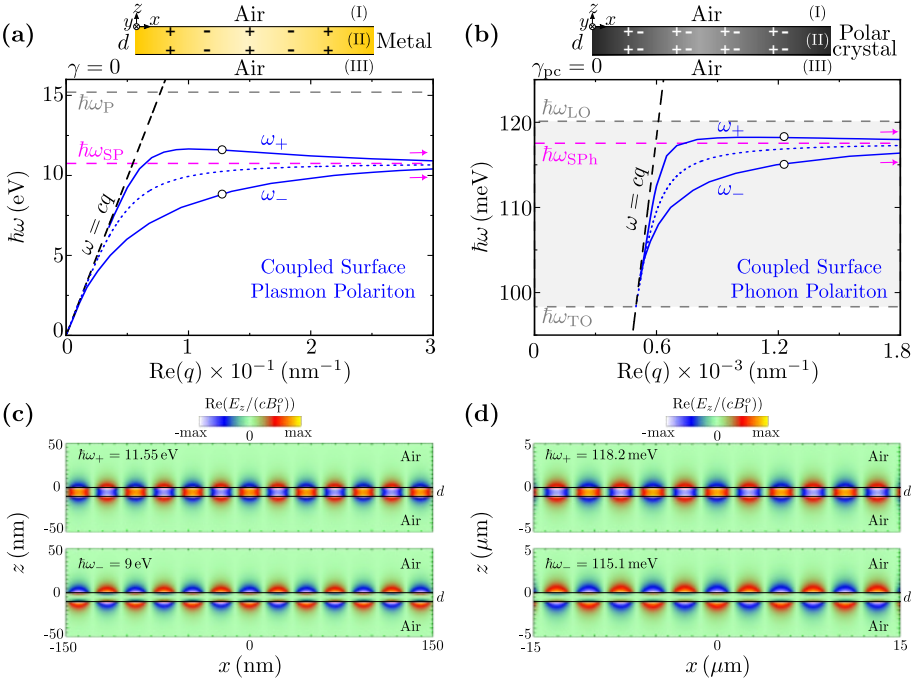

Figure 1.5: Surface plasmon and phonon polaritons in thin films. (a) Dispersion relations ω^+ (Eq. (1.37)) and ω^- (Eq. (1.38)) of surface plasmon polaritons in an Al film of thickness equal to $d = 10$ nm. Blue dotted line shows the dispersion relation of the SPP (same as in Fig. 1.4a). Horizontal gray and magenta dashed lines indicate the plasma frequency ω_p and the surface plasmon frequency ω_{SP}, respectively. (b) Same as (a) but for a SiC film of thickness equal to $d = 1\,\mu$m. The shaded gray area marks the Reststrahlen band, and the blue dotted line shows the dispersion relation of the SPhP (same as in Fig. 1.4b). Black dashed lines in panels (a) and (b) show the dispersion relation of light in free space: $q = \omega/c$. The magenta arrows indicate the asymptotic behavior of the dispersions, whereas the insets above each panel provide a visual representation of the systems. Contour plots in panels (c) and (d) show the normalized real part of the z-component of the electric field in the xz-plane for the energies marked by the open circles in panels (a) and (b): (c) 9 eV (bottom), 11.55 eV (top), and (d) 115.1 meV (bottom), 118.2 meV (top). The maximum values of the normalized field plots are: (c) 2.96 (bottom), 3.15 eV (top), and (d) 2.96 meV (bottom), 2.96 (top). For illustrative purposes, all the calculations in this figure are implemented without considering losses in the materials ($\gamma = 0$ in Eq. (1.14) and $\gamma_{pc} = 0$ in Eq. (1.17)).

1.2.5 Localized surface polaritons

Particles made of metal or polar crystal, such as spherical, square, cubic, or other geometric shapes, can support localized surface plasmon or phonon

modes, which are typically referred to as localized surface plasmon polaritons (LSPP) or localized surface phonon polaritons (LSPhP), respectively. The frequency of these modes depends on the geometrical shape of the particle, and they can be observed in the optical response of the particle [32, 35, 51, 52]. Contrary to the polaritons discussed in the previous subsections, which propagate through the bulk or along the interface of a material, localized surface polaritons are electromagnetic modes spatially confined within the particle and can be excited by plane-wave illumination.

To explore the properties of these localized modes, we show the optical response of a spherical nanoparticle with a radius of 100 nm, characterized by the dielectric function of SiC ($\varepsilon_{\mathrm{SiC}}(\omega)$, given by Eq. (1.17)). Figure (1.6)a displays the electron energy loss, $\Gamma(\omega)$, spectrum of the spherical nanoparticle when a fast electron travels in the vicinity of the nanoparticle, as illustrated in the inset of Fig. 1.6a. In Section 1.4, we will provide an extensive discussion about the numerical calculation of $\Gamma(\omega)$. Intuitively, the fast electron, after interacting with the LSPhP excited at the nanoparticle, loses energy at exactly the LSPhP frequencies ω_ℓ, producing the appearance of peaks in the EEL spectrum at energies $\hbar\omega_\ell$ (see peaks in 1.6a). By plotting the field distribution around the sphere at the energy loss peaks positions, we notice that the electric field is predominantly confined at the surface of the particle (see field plots in Fig. 1.6b). The lowest LSPhP frequency labeled as $\ell = 1$ shows a field distribution with two maxima along the x-direction similar to the field distribution of an electric dipole. For higher frequencies ($\ell = 2, 3, \dots$), the field distribution exhibits additonal maxima around the surface of the sphere, similar to the field distribution of quadrupolar ($\ell = 2$) and octupolar ($\ell = 3$) excitations. For small spherical nanoparticles, within the quasistatic approximation, the localized polariton resonances can be obtained from the following condition [53]:

$$\varepsilon(\omega_\ell) = -\frac{\ell+1}{\ell}. \tag{1.40}$$

By substituting the dielectric function of SiC ($\varepsilon_{\mathrm{SiC}}(\omega)$, given by Eq. (1.17)) into Eq. (1.40), and under the asumption that $\gamma_{\mathrm{pc}} = 0$, one can deduce the following expression for the LSPhP resonances:

$$\omega_\ell = \sqrt{\frac{\ell(\varepsilon_\infty \omega_{\mathrm{LO}}^2 + \omega_{\mathrm{TO}}^2) + \omega_{\mathrm{TO}}^2}{\ell(\varepsilon_\infty + 1) + 1}}. \tag{1.41}$$

One can further deduce from Eq. (1.41) that for high-multipole orders ℓ, the LSPhP resonances approach the SPh frequency (Eq. (1.33)), that is, $\omega_{\ell\to\infty} \approx \omega_{\mathrm{SPh}}$. This particular behavior of the resonances can be traced by plotting the EEL probability spectra as a function of the particle radius a, as shown in

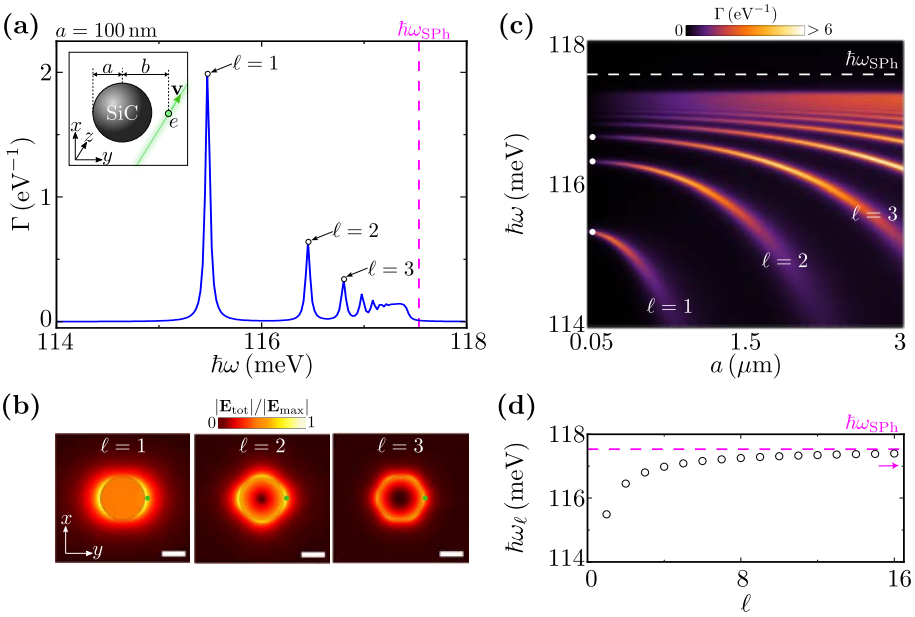

Figure 1.6: Localized surface phonon polaritons. (a) Electron energy-loss probability $\Gamma(\omega)$ of a SiC spherical nanoparticle calculated as a function of the energy loss experienced by a fast electron beam traveling close to the nanoparticle. Inset in the panel shows a sketch of the system under study: spherical nanoparticle (gray sphere) with dielectric function $\varepsilon_{\mathrm{SiC}}(\omega)$ (Eq. (1.17)) and radius $a = 100\,\mathrm{nm}$ excited by a focused electron beam (green ray, e is the elementary charge) traveling along the z-direction with velocity $v = 0.7c$ at a distance $b = 1.01a$ (impact parameter) with respect to the sphere center. Open circles and arrows mark the position of the first three peaks in the EEL spectrum: ($\ell = 1$) 115.47 meV, ($\ell = 2$) 116.45 meV and ($\ell = 3$) 116.80 meV. Vertical magenta dashed line marks the SPh frequency. (b) Amplitude of the total electric field $|\mathbf{E}_{\mathrm{tot}}(\omega)|$ in the xy-plane for energies marked by the open circles in panel (a). The scale bar in the field plots is 100 nm and the green dots indicate the electron beam position. The field plots are normalized to the maximum value in each case (from left to right): 3.17×10^{11} V/m, 2.61×10^{11} V/m and 2.67×10^{11} V/m. (c) EEL probability spectra as function of both the particle radius a and the energy loss experienced by the fast electron traveling with $v = 0.7c$ and $b = 1.01a$. Open circles in the spectra mark the peaks for the particle with radius $a = 100\,\mathrm{nm}$. (d) Localized resonance frequencies ω_ℓ as a function of the multipole order ℓ obtained from Eq. (1.41). Horizontal white and magenta dashed lines in panels (c) and (d) mark the SPh frequency. All calculations were performed using the following parameters for $\varepsilon_{\mathrm{SiC}}(\omega)$: $\varepsilon_\infty = 6.7$, $\hbar\omega_{\mathrm{LO}} = 120.14\,\mathrm{meV}$, $\hbar\omega_{\mathrm{TO}} = 98.32\,\mathrm{meV}$ and $\hbar\gamma_{\mathrm{pc}} = 0.05\,\mathrm{meV}$ typical of SiC. These values are the same as the ones used in Figs. 1.2b-c, but considering a reduced damping constant.

Fig. 1.6c. One can observe that the peaks in the EELS spectra shift to lower energies as the particle radius a increases from 0.05 μm to 3 μm, and, for higher-multipole orders ℓ, the resonances pile up close to the SPh resonance ω_{SPh} (see accumulation of the resonances close to the dashed lines in Figs. 1.6c-d). Indeed, for higher-multipole orders ℓ, the wavelengths of the localized surface

phonon polaritons, $\lambda_{\mathrm{LSPhP}} = 2\pi a/\ell$, are smaller than the local curvature of the spherical particle [54], mimicking the same situation of surface polariton waves propagating along a semi-infinite flat surface (see Fig. 1.4).

The excitation of localized surface polaritons can be also observed in the EEL spectra of a metallic spherical nanoparticle. In Appendix B, Fig. B.1d, we show the EEL spectra of an Al spherical nanoparticle with a radius of $a = 75\,\mathrm{nm}$. The peaks in the spectra are associated with the excitation of localized surface plasmon polaritons at the metallic nanoparticle and, analogue to the tendency of LSPhP resonances, the LSPP resonances with high-multipole order ℓ approach to the SP frequency (Eq. (1.32)).

In addition to spherical nanoparticles, the excitation of localized surface polaritons in plasmonic or phononic materials have been extensively analyzed in different particles including rods [27, 55], ellipsoids [56], cubes [57, 58], triangles [59], among others.

1.2.6 Polaritons in uniaxial thin films

In the previous subsections, we have considered the optical response of a medium to be equal in all directions in the medium. This property is manifested by the isotropic nature of the dielectric function of the materials considered. In addition to isotropic materials, there exists another class of materials whose optical response is strongly dependent on their orientation. These materials are known as anisotropic materials. Their optical response arises from the presence of distinct chemical bonds in different directions within the material. This effect can be modeled by considering the electric susceptibility of the materials as a second-rank tensor $\hat{\chi}(\omega)$. Consequently, the dielectric function of the material is described by a second-rank tensor $\hat{\varepsilon}(\omega)$. This tensor can be diagonalized along the optical axis of the material and can be written in a diagonal representation [60]. In this thesis, we will focus on uniaxial anisotropic materials, meaning that the permittivity tensor $\hat{\varepsilon}(\omega)$ is diagonal, and two of its components are equal. Thus, throughout the thesis, it is always assumed the following form of the permittivity tensor:

$$\hat{\varepsilon}(\omega) = \begin{pmatrix} \varepsilon_{\perp}(\omega) & 0 & 0 \\ 0 & \varepsilon_{\perp}(\omega) & 0 \\ 0 & 0 & \varepsilon_{\parallel}(\omega) \end{pmatrix}. \tag{1.42}$$

We consider that the optical axis of the material is oriented perpendicular to the material surface and the optical response of the material along this direction is usually referred to as the out-of-plane component $\varepsilon_{\parallel}(\omega)$. The other

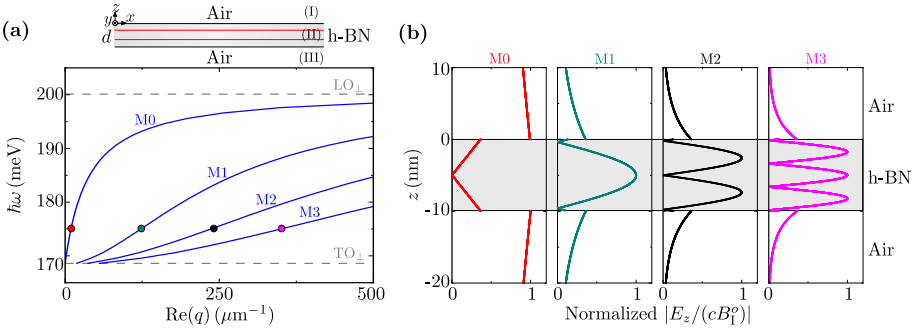

Figure 1.7: Anisotropic polaritons in a h-BN thin film. (a) Dispersion relation (Eq. (1.47)) of the modes in an h-BN film with thickness $d = 10\,\text{nm}$. The h-BN film is surrounded by air, as depicted in the inset above the panel. Gray dashed lines indicate the TO and LO phonon energies in the upper Reststrahlen band. (b) Normalized magnitude of the z-component of the electric field along the z-axis at energy 175 meV and wavenumbers (marked by the color circles in panel (a)): (M0) $9.47\,\mu\text{m}^{-1}$, (M1) $122.91\,\mu\text{m}^{-1}$, (M2) $236.34\,\mu\text{m}^{-1}$ and (M3) $349.78\,\mu\text{m}^{-1}$. The color code of the field plots corresponds to the colors of the circles in panel (a). Gray shaded region in panel (b) marks the h-BN film thickness $d = 10\,\text{nm}$.

relevant direction of the optical response is found in the direction containing the material surface plane, and it is referred to as the in-plane optical component $\varepsilon_\perp(\omega)$. Examples of uniaxial materials are metallic delafossite oxides such as palladium-based delafossite ($PdCoO_2$) [61], multilayer semiconductor transition metal dichlcogenide (TMDC) materials such as tungsten disulfide (WS_2) or molybdenum disulfide (MoS_2) [62, 63] and layered polar crystals such as hexagonal boron nitride (h-BN) [64].

Optical anisotropy can significantly modify the properties of polaritons, as determined by their dispersion relation. To better understand these changes, we analyze in this subsection a thin film made of a representative uniaxial polar material: hexagonal boron nitride. Its optical properties, together with the excitation of bulk and surface polaritons in h-BN, will be discussed in detail in Chapter 2. In brief, hexagonal boron nitride exhibits two Reststrahlen bands within the energy range of $90\,\text{meV} - 200\,\text{meV}$ where phonon polaritons are excitable. We focus in this introduction on the upper Reststrahlen band within the energy range of $168.6\,\text{meV} - 200\,\text{meV}$. In this band, the out-of-plane component $\varepsilon_\parallel(\omega)$ is a positive constant number, while the in-plane component $\varepsilon_\perp(\omega)$ can be described through Eq. (1.17) (see also Chapter 2, Section 2.2).

As illustrated in the inset above Fig. 1.7a, the h-BN film is surrounded by air, and thus, the TM-polarized electromagnetic fields in media (I) and (III) are determined by Eqs. (1.34a)-(1.34b) and (1.34e)-(1.34f), respectively. In medium (II), the electromagnetic field with wavevector $\mathbf{k}_{\text{II}} = (q, 0, i\kappa_e)$ can be

written as [30, 65]:

$$\mathbf{B}_{\mathrm{II}}(\mathbf{r}) = \left[B^{o}_{\mathrm{II}} e^{\kappa_e z + iqx} + B^{o'}_{\mathrm{II}} e^{-\kappa_e z + iqx}\right] \hat{\mathbf{y}}, \tag{1.43a}$$

$$\mathbf{E}_{\mathrm{II}}(\mathbf{r}) = -\frac{c^2}{\omega}\left[i\frac{\kappa_e}{\varepsilon_\perp}\left(B^{o}_{\mathrm{II}} e^{\kappa_e z + iqx} - B^{o'}_{\mathrm{II}} e^{-\kappa_e z + iqx}\right)\hat{\mathbf{x}} + \frac{q}{\varepsilon_\parallel} B_{\mathrm{II},y}(\mathbf{r})\hat{\mathbf{z}}\right], \tag{1.43b}$$

where the wavenumber κ_e of the extraordinary wave in h-BN satisfies the following relationship:

$$k^2_{\mathrm{II}} = \frac{q^2}{\varepsilon_\parallel} - \frac{\kappa_e^2}{\varepsilon_\perp} = \frac{\omega^2}{c^2}. \tag{1.44}$$

Applying the boundary conditions at the interfaces of the anisotropic film ($z = 0$ and $z = -d$), we find the following systems of linear equations:

$$\begin{pmatrix} 1 & -1 & -1 & 0 \\ \kappa_{\mathrm{I}}\varepsilon_\perp & \kappa_e & -\kappa_e & 0 \\ 0 & e^{-\kappa_e d} & e^{\kappa_e d} & -e^{-\kappa d} \\ 0 & \kappa_e e^{-\kappa_e d} & -\kappa_e e^{\kappa_e d} & -\kappa_{\mathrm{I}}\varepsilon_\perp e^{-\kappa_{\mathrm{I}} d} \end{pmatrix} \begin{pmatrix} B^{o}_{\mathrm{I}} \\ B^{o}_{\mathrm{II}} \\ B^{o'}_{\mathrm{II}} \\ B^{o}_{\mathrm{III}} \end{pmatrix} = \begin{pmatrix} 0 \\ 0 \\ 0 \\ 0 \end{pmatrix}. \tag{1.45}$$

Solving this system for the non-trivial solution, one obtains the following dispersion of the modes in the h-BN film:

$$(\varepsilon_\perp \kappa_{\mathrm{I}} + \kappa_e) \pm (\varepsilon_\perp \kappa_{\mathrm{I}} - \kappa_e) e^{-\kappa_e d} = 0, \tag{1.46}$$

which is the analogue to Eq. (1.36) obtained for isotropic films. For large wavenumbers ($q >> 1$), Eq. (1.46) can be simplified as [66]:

$$q(\omega) = \frac{i}{d}\sqrt{\frac{\varepsilon_\parallel(\omega)}{\varepsilon_\perp(\omega)}}\left[2\arctan\left(\frac{i}{\sqrt{\varepsilon_\parallel(\omega)\varepsilon_\perp(\omega)}}\right) + \pi l\right],\ l = 0, 1, 2, 3, \ldots \tag{1.47}$$

with l denoting the mode order. In Fig. 1.7a we plot Eq. (1.47) for an h-BN film of 10 nm thickness. In contrast to the two dispersion branches, ω_+ and ω_-, obtained in isotropic films (Figs. 1.5a-b), we observe in Fig. 1.7a multiple dispersion branches associated with the excitation of hyperbolic phonon polaritons in the h-BN film. Each branch corresponds to a mode whose electric field oscillates inside the film (see gray shaded region in Fig. 1.7b), similarly to guided modes in a dielectric waveguide. Thus, they are labeled using the nomenclature [30, 67]: Ml. The numbers of oscillations of the electric field are equal to the mode order l, and they are a consequence of electric charges being distributed also inside the film and not only at its surface [68].

In Chapter 2, we will investigate the excitation of phonon polaritons in h-BN by fast electron beams, and show that, due to optical anisotropy, their

propagation can be controlled by the velocity and direction of the fast electron.

1.3 Strong light-matter interaction

1.3.1 Overview

Polaritons can be formed through the strong interaction between an electromagnetic mode confined in an optical cavity or resonator (light) and a dipolar excitation (matter). This strong interaction is characterized by a coherent energy exchange rate between light and matter that exceeds the decay rates of both the EM mode and the dipolar excitation. In this context, hybrid light-matter states (polaritons) with inseparable light and matter properties have demonstrated for instance the ability to, modify the chemical reactivity of molecules [69, 70], selectively control phase transitions [71] or manipulate excited states [72].

In Chapters 3 and 4 of the thesis, we analyze the electromagnetic coupling between nanoresonator modes and excitonic or molecular vibrational modes. In particular, in Chapter 3, we investigate the electromagnetic coupling between anapole states and excitons. In Chapter 4, on the other hand, we discuss the electromagnetic coupling between phonon polariton antenna modes and molecular vibrational modes. In both chapters, we use analytical models based on two coupled harmonic oscillators and on coupled mode theory to explain and quantify the electromagnetic coupling between the resonances. Thus, in the following section, we introduce these models as well as key concepts of weakly and strongly coupled systems.

1.3.2 Two-coupled harmonic oscillator model

One of the simplest models that describes the interaction between light and matter is the two-coupled harmonic oscillator model. Figure 1.8a shows an sketch of this model: an electromagnetic mode is represented by an oscillator (EM oscillator) characterized by a displacement $x_{\mathrm{EM}}(t)$, a resonance frequency ω_{EM}, and a damping constant γ_{EM}. The dipolar excitation (an exciton or a

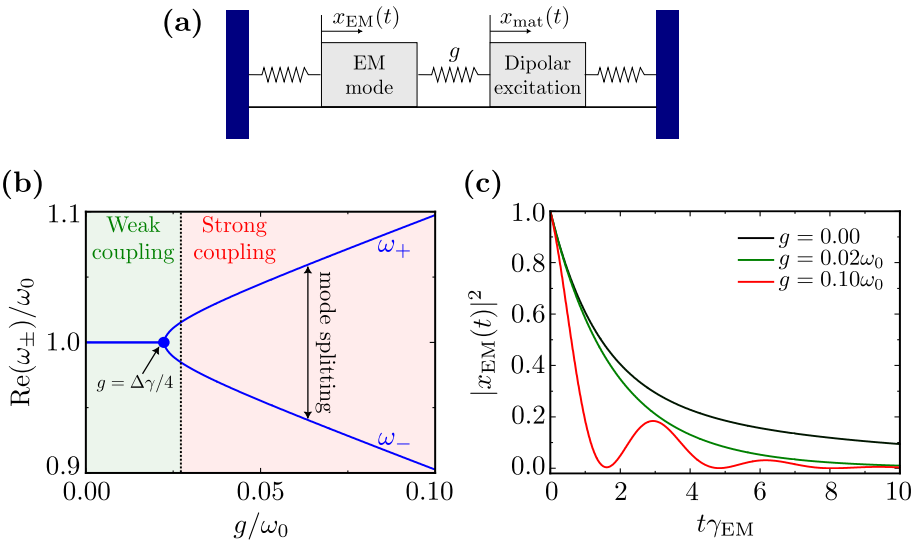

Figure 1.8: Weak and strong light-matter interactions as described by two coupled harmonic oscillators. (a) Illustrative sketch of two oscillators representing the the EM mode and the dipolar excitation resonance. The displacements $x_{\rm EM}$ and $x_{\rm mat}$ of the oscillator are constrained by the springs. (b) Real component of the eigenfrequencies $\omega_\pm$ (Eq. (1.50)) of the hybrid modes as a function of the coupling strength g. The calculations are performed for two oscillators with the same resonant frequency $\omega_{\rm EM} = \omega_{\rm mat} = \omega_0$, and damping constants $\gamma_{\rm EM} = 0.1\omega_0$, $\gamma_{\rm mat} = 0.01\omega_0$. Notice that $\omega_\pm$ and g are normalized to ω_0. The blue point marks the exceptional point and the vertical dashed line marks the value $g = (\gamma_{\rm EM}+\gamma_{\rm mat})/4$. Green and red shaded regions indicate the weak and strong coupling regimes, respectively. (c) Electromagnetic energy $|x_{\rm EM}(t)|^2$ as a function of the parameter $t\gamma_{\rm EM}$, with t the time. Black, green and red lines represent the EM energy for coupling strengths equal to $g = 0$ (uncoupled), $g = 0.02\omega_0$ (weak coupling) and $g = 0.1\omega_0$ (strong coupling), respectively. Figure reproduced from ref. [73].

molecular vibration) resonance, on the other hand, is represented by a second oscillator (matter oscillator) characterized by a displacement $x_{\rm mat}(t)$, a resonance frequency $\omega_{\rm mat}$, and a damping constant $\gamma_{\rm mat}$. The two oscillators are coupled via a coupling strength g. The dynamics of the coupled system is determined by the following system of equations [74, 75]:

$$\ddot{x}_{\rm EM}(t) + \gamma_{\rm EM}\dot{x}_{\rm EM}(t) + \omega_{\rm EM}^2 x_{\rm EM}(t) - 2g\dot{x}_{\rm mat}(t) = 0, \tag{1.48a}$$

$$\ddot{x}_{\rm mat}(t) + \gamma_{\rm mat}\dot{x}_{\rm mat}(t) + \omega_{\rm mat}^2 x_{\rm mat}(t) + 2g\dot{x}_{\rm EM}(t) = 0, \tag{1.48b}$$

where the dots denote time derivatives. This system of two ordinary differential equations can be solved assuming that the displacement of each oscillator is harmonical in time, i.e., $x_{\rm EM}(t) = x_{\rm EM}^o\, e^{-i\omega t}$ and $x_{\rm mat}(t) = x_{\rm mat}^o\, e^{-i\omega t}$. Under this assumption, and substituting these expressions into Eqs. (1.48a)-(1.48b),

one obtains the following system of linear equations:

$$\begin{pmatrix} \omega_{\mathrm{EM}}^2 - \omega^2 - i\omega\gamma_{\mathrm{EM}} & 2gi\omega \\ -2gi\omega & \omega_{\mathrm{mat}}^2 - \omega^2 - i\omega\gamma_{\mathrm{mat}} \end{pmatrix} \begin{pmatrix} x_{\mathrm{EM}}^o \\ x_{\mathrm{mat}}^o \end{pmatrix} = \begin{pmatrix} 0 \\ 0 \end{pmatrix}. \quad (1.49)$$

Furthermore, considering that the value of the resonance frequency ω is similar to the resonance frequencies ω_{EM} and ω_{mat}, the terms $\omega_{\mathrm{EM}}^2 - \omega^2$ and $\omega_{\mathrm{EM}}^2 - \omega^2$ can be approximated as $\omega_{\mathrm{EM}}^2 - \omega^2 \approx 2\omega(\omega_{\mathrm{EM}} - \omega)$ and $\omega_{\mathrm{mat}}^2 - \omega^2 \approx 2\omega(\omega_{\mathrm{mat}} - \omega)$. Using this approximation, one can find the new eigenfrequencies of the coupled system from the non-trivial solution of Eq. (1.49):

$$\omega_{\pm} = \frac{\omega_{\mathrm{EM}} + \omega_{\mathrm{mat}}}{2} - \frac{i}{4}(\gamma_{\mathrm{EM}} + \gamma_{\mathrm{mat}}) \pm \frac{1}{2}\sqrt{4g^2 + \left[\Delta\omega - \frac{i}{2}\Delta\gamma\right]^2}, \quad (1.50)$$

with $\Delta\omega = \omega_{\mathrm{EM}} - \omega_{\mathrm{mat}}$ being the detuning and $\Delta\gamma = \gamma_{\mathrm{EM}} - \gamma_{\mathrm{mat}}$.

The two-coupled harmonic oscillator model can be useful to determine the coupling strength g as well as the polaritonic frequencies of a coupled electromagnetic system, such as a quantum emitter inside a Fabry-Perot (FP) cavity or a metallic nanoparticle dimer. Typically, the determination of these quantities is achieved by fitting the optical response of the electromagnetic system with a physical quantity (observable) derived from the two-coupled harmonic oscillator model. For example, the extinction of the electromagnetic system can be associated with the time-averaged power of the EM oscillator being driven by an external force $F(t) = F_0 e^{-i\omega t}$ [74], i.e.,:

$$\begin{aligned} \mathscr{P}_{\mathrm{EM}}(\omega) &= \frac{1}{2}\mathrm{Re}(-i\omega x_{\mathrm{EM}}^o F_0) \quad (1.51) \\ &= \frac{\omega}{2}\mathrm{Im}\left[\frac{\left(\omega_{\mathrm{mat}}^2 - \omega^2 - i\gamma_{\mathrm{mat}}\omega\right)F_0^2}{(\omega_{\mathrm{EM}}^2 - \omega^2 - i\gamma_{\mathrm{EM}}\omega)(\omega_{\mathrm{mat}}^2 - \omega^2 - i\gamma_{\mathrm{mat}}\omega) - 4g^2\omega^2}\right]. \end{aligned}$$

Thus, by fitting the extinction spectra with with Eq. (1.51), one can obtain the resonance frequencies ω_{EM} and ω_{mat}, as well as the coupling strength g. By substituting these fitting values into Eq. (1.50), one can find the polaritonic frequencies $\omega_{\pm}$. In Chapter 4, we follow a similar fitting procedure to determine the coupling strength and polaritonic frequencies of a vibrational mode coupled to a phononic antenna mode excited by a metallic tip.

To illustrate the solutions that can be obtained from Eq. (1.50), we plot in Fig. 1.8b the real part of $\omega_{\pm}$ (blue curve) as a function of the coupling strength g. We consider that the two oscillators have the same resonance frequency $\omega_{\mathrm{EM}} = \omega_{\mathrm{mat}} = \omega_0$ (zero detuning), but different damping constants $\gamma_{\mathrm{EM}} = 0.1\omega_0$ and $\gamma_{\mathrm{mat}} = 0.01\omega_0$, respectively. When $g < \Delta\gamma/4$, it can be observed in Fig. 1.8b that the frequencies $\omega_{\pm}$ are mathematically degenerate, and thus, the

eigenfrequencies of the coupled and the uncoupled systems are the same. This condition thus establishes the weak coupling regime. By increasing the coupling strength g, the blue curve reaches the critical point $g = \Delta\gamma/4$ (blue point), also referred to as the exceptional point [35]. Beyond this value, the curve splits into two distinct parabolic branches, implying the appearance of two new hybrid modes with different frequencies, ω_+ and ω_-. Therefore, the exceptional point marks the onset of the strong coupling regime. From this analysis, we can conclude that a coupled (two oscillators) system is weakly or strongly coupled if $g > \Delta\gamma/4$. In literature, however, alternative criteria to determine the coupling regime can be found. For example, more restrictive criteria establish that two oscillators are strongly coupled when $g > (\gamma_{\mathrm{EM}} + \gamma_{\mathrm{mat}})/4$ [76, 77], or when the mode splitting $\Omega_{\mathrm{R}} = \sqrt{4g^2 - (\Delta\gamma/2)^2}$ is larger than half the sum of the losses $(\gamma_{\mathrm{EM}} + \gamma_{\mathrm{mat}})/2$ [78–80]. In this thesis, we use the first criterium and consider that two oscillators are strongly coupled when $g > (\gamma_{\mathrm{EM}} + \gamma_{\mathrm{mat}})/4$, which is indicated by the vertical dotted line in Fig. 1.8b.

Weak and strong light-matter interactions have important consequences for the physical properties of a system, as observed in Fig. 1.8c, where we plot the energy of the EM oscillator, proportional to $|x_{\mathrm{EM}}(t)|^2$, as a function of time. When the EM oscillator is uncoupled ($g = 0$, black curve), its energy exponentially decays in time as $|x_{\mathrm{EM}}(t)|^2 = |x^o_{\mathrm{EM}}|^2\, e^{-t\gamma_{\mathrm{EM}}}$ with an exponential time constant (lifetime) equal to $\tau_{\mathrm{EM}} = 1/\gamma_{\mathrm{EM}}$. This lifetime is modified once the EM oscillator is weakly coupled to the matter oscillator. In this case, the energy of the EM oscillator decays as $|x_{\mathrm{EM}}(t)|^2 = |x^o_{\mathrm{EM}}|^2\, e^{-t(\gamma_{\mathrm{EM}}+\gamma_{\mathrm{mat}})/2}$ with an exponential lifetime equal to $\tau_{\mathrm{EM}} = 1/(\gamma_{\mathrm{EM}} + \gamma_{\mathrm{mat}})/2)$, that is, with a smaller lifetime as compared to the case when the EM oscillator is uncoupled (compare black and green lines in Fig. 1.8c). This modification of the oscillator lifetime is known as the Purcell effect [81]. Finally, when the oscillators are strongly coupled, they exchange energy faster than their lifetimes. This leads to a coherent exchange of energy between the two oscillators, as shown by the red dashed line in Fig. 1.8c. It can be observed that the energy of the EM oscillator (represented by the red line) oscillates in time (represented by the gray dashed line). These oscillations are known as Rabi oscillations [75].

It is worth noting that Eqs. (1.48a)-(1.48b) represent a particular way of describing the interaction between light and matter using the model of two-coupled harmonic oscillators. One can show that, in this representation, the displacement $x_{\mathrm{EM}}(t)$ is related to the vector potential $\mathbf{A}_{\mathrm{EM}}(t)$ of the electromagnetic mode, whereas the the displacement $x_{\mathrm{mat}}(t)$ of the matter oscillator is related to the induced dipole moment $\mathbf{p}_{\mathrm{mat}}(t)$ describing the optical response of the dipolar excitation [73].

1.3.3 Temporal coupled-mode theory

Temporal coupled-mode theory (TCMT) offers an alternative approach for modeling the interaction between light and matter. According to this theoretical framework, the optical response of a cavity (resonator) is determined by the transient dynamics of the quasinormal modes (QNMs) excited in the cavity. For example, within TCMT, the equations of motion of two interacting QNMs are [35, 82–86]:

$$\frac{\mathrm{d}a_1(t)}{\mathrm{d}t} = -i\omega_1 a_1(t) - \frac{\gamma_1}{2}a_1(t) - iga_2(t), \tag{1.52a}$$

$$\frac{\mathrm{d}a_2(t)}{\mathrm{d}t} = -i\omega_2 a_2(t) - \frac{\gamma_2}{2}a_2(t) - iga_1(t), \tag{1.52b}$$

where $a_1(t)$, $a_2(t)$ are the amplitudes, ω_1, ω_2 are the resonance frequencies and γ_1, γ_2 are total decay rates of both QNMs. The decay rates are due to the radiative and absorptive losses of the QNM, i. e., $\gamma_1 = \gamma_1^{\mathrm{abs}} + \gamma_1^{\mathrm{rad}}$ and $\gamma_2 = \gamma_2^{\mathrm{abs}} + \gamma_2^{\mathrm{rad}}$. Using matrix notation, Eqs. (1.52a)-(1.52b) can be expressed in the more compact way as:

$$\frac{\mathrm{d}\mathbf{A}_2(t)}{\mathrm{d}t} = -i\begin{pmatrix} \omega_1 - i\gamma_1/2 & g \\ g & \omega_2 - i\gamma_2/2 \end{pmatrix}\begin{pmatrix} a_1(t) \\ a_2(t) \end{pmatrix} = -i\hat{\mathbb{H}}_2\,\mathbf{A}_2(t), \tag{1.53}$$

where $\mathbf{A}_2(t) = (a_1(t), a_2(t))^\top$ is a vector determined by the amplitude of the two QNMs (symbol $\top$ denotes transpose of a matrix) and $\hat{\mathbb{H}}_2$ is a 2×2 matrix describing their evolution in time[4]. With this compact notation, using the ansatz $\mathbf{A}_2(t) = \mathbf{A}_2^o e^{-i\omega t}$ and substituting this expression into Eq. (1.53), one can deduce the following relationship:

$$\left(\hat{\mathbb{H}}_2 - \omega\hat{\mathbb{I}}\right)\mathbf{A}_2^o = \mathbf{0}, \tag{1.54}$$

where $\hat{\mathbb{I}}$ is the identity tensor. The latter relation has non-trivial solution when the determinant of the matrix inside the parenthesis is zero, $\det(\hat{\mathbb{H}}_2 - \omega\hat{\mathbb{I}}) = 0$, or equivalently, when ω is an eigenfrequency of matrix $\hat{\mathbb{H}}_2$. The calculation of such eigenfrequencies, provides solutions of $\omega_\pm$ given by the same mathematical expression as in Eq. (1.50). This shows that the TCMT and the two-coupled harmonic oscillator model provide a similar description of a two-coupled oscillators system.

[4]Note that Eq. (1.53) has a similar form to Schrödinger's equation, hence, $\hat{\mathbb{H}}_2$ is occasionally termed as the effective Hamiltonian [87].

Despite the similarities between TCMT and the two-coupled harmonic oscillator model, TMCT provides an easy way to interpret the extinction power of an object. Indeed, TCMT has been widely used to model the scattered and absorbed power of an object when it is illuminated by a monochromatic plane wave, based on the idea that the incident illumination can be expanded over a set of appropriate scattering (radiation) channels [85]. We employ this theoretical formalism in Chapter 3 to analyze the QNMs, and their coupling to an excitonic resonance, excited in a WS_2 disk by a fast electron beam.

To conclude, we note that the models presented in this section have been widely used to describe many physical systems, including coupled plasmon-exciton systems [74, 75], phonon polaritons coupled to molecular vibrations [88] or a quantum emitter interacting with a single electromagnetic mode of an optical cavity [80]. Although these models are based in purely classical descriptions, under certain circumstances a quantum mechanical approach to the interaction between the dipolar excitation and the EM mode yields similar results. We refer the reader to ref. [73], where a comprehensive analysis of the analogies between classical and quantum models of light-matter interaction is provided.

1.4 Near-field probing of polaritons

As discussed in Section 1.2 and in the Introduction, polaritonic nanostructures show the capability to confine light within subwavelength dimensions, making them unique for controlling and manipulating light beyond the diffraction limit. In addition, the strong field confinement induced by localized surface polaritons can produce electromagnetic fields that are orders of magnitude stronger than the incident field, leading to a variety of applications including single molecule sensitivity [5], enhancement of non-linear effects [6], local heating of a sample [7] or applications where strong light–matter interactions are desired. A major difficulty in polariton physics, however, is the large momentum mismatch between polaritons and free-space photons, which challenges their excitation and probing using conventional far-field optical techniques. In this section, we address how these hybrid light-matter states can be excited and probed with near-field optical techniques. We introduce electron energy loss spectroscopy (EELS) in scanning transmission electron microscopy (STEM) and scattering-type scanning near-field optical microscopy (s-SNOM), as two techniques that

allow for probing polaritons in the near field. While EELS employs fast electron beams, s-SNOM uses elongated metallic or dielectric tips to enable momentum matching with the incident light. In the following subsections, we focus on the theoretical description of the interactions produced in both techniques and briefly discuss their working principle.

1.4.1 EELS

Electron energy loss spectroscopy is a technique based on electron microscopy that allows us to access the near fields induced by an excitation in a sample with subnanometer spatial resolution and tens of meV in energy resolution. Figure 1.9 depicts the fundamental principle of measurement in a scanning-transmission electron microscope. Fast electrons are extracted from an electron gun and accelerated by a voltage typically in the range of $30\,\mathrm{keV} - 300\,\mathrm{keV}$, corresponding to electron velocities of approximately $0.3c$ to $0.8c$. The electron beam is focused and monochromated by a series of lenses that narrow the energy distribution of the fast electron and minimize its size [89]. After being monochromated, the electron beam passes through aberration correctors composed of optical lenses that further reduce the lateral size of the electron beam to the subangstrom scale [90, 91].

By scanning the tightly focused electron beam over a sample, chemical, electronic, and optical information about the sample can be collected [8, 13]. The transmitted electron beam can be analyzed following its passage through post-sample electron optics, such as a high-angle annular dark-field (HAADF) detector, and subsequently examined using an EEL spectrometer. The spectrometer is typically composed of a magnetic prism that disperses incoming electrons based on their energy, a series of spectrometer lenses utilized for magnification and to minimize aberrations, and a CCD camera for recording the resulting spectrum [92].

The spectrum in Fig. 1.9 (see plot at the right of the CCD camera) illustrates a typical low-loss EEL spectrum composed of the following two relevant features: (i) a prominent peak (zero-loss peak) produced from the electrons that experience zero or negligible loss, and (ii) several peaks in the energy range of $0\,\mathrm{eV} - 50\,\mathrm{eV}$ (low-loss region) that are associated with different types of optical excitation in the sample, including bulk and surface polaritons, for instance. The energy range above $50\,\mathrm{eV}$ is known as the core-loss region and the electron energy losses in this spectral range are associated with the interaction of the fast electron and the atomic core electrons of the sample. In this thesis, we focus on the low-loss energy range.

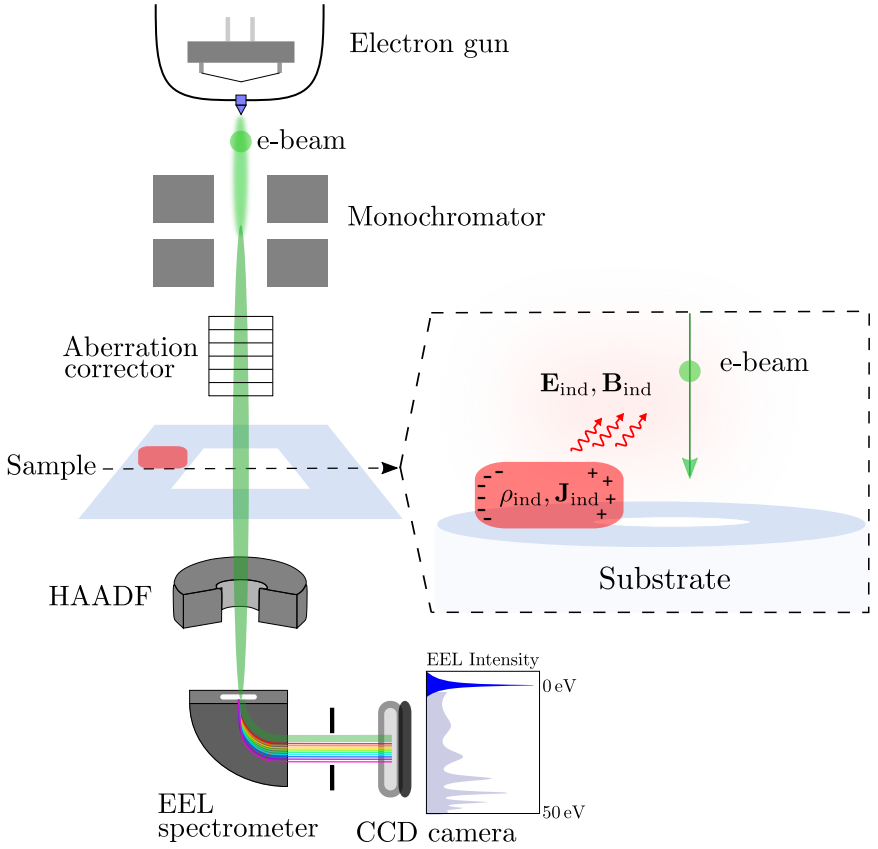

Figure 1.9: Scanning-transmission electron microscope. Schematic representation of the JEOL Mono384 NEO ARM 200F (adapted from https://www.jeol.com/products/scientific/tem/Monochromated_ARM200F.php), which shows a transmission electron microscope equipped with a Schottky field emission gun, double Wien filter monochromator, probe aberration corrector, image aberration corrector and Gatan Imaging Filter continuum high-resolution spectrometer. EELS experiments shown in this thesis were performed with this microscope. The different parts and working principle of the microscope are both explained in the main text. The sketch framed by the dashed lines depicts a representation of the charge and current densities, $\rho_{\mathrm{ind}}(\mathbf{r};t)$ and $\mathbf{J}_{\mathrm{ind}}(\mathbf{r};t)$, respectively, induced by the fast electron in the sample. These densities produce electromagnetic fields $\mathbf{E}_{\mathrm{ind}}(\mathbf{r};t)$ and $\mathbf{B}_{\mathrm{ind}}(\mathbf{r};t)$ that act back on the fast electron.

Within a classical electrodynamics description, the experimental electron energy loss signal coming form the electron-sample interaction can be understood as follows (see the sketch within the dashed line box in Fig. 1.9). The fast electron, represented by a point-like particle with negative electric charge e, travels with constant velocity $\mathbf{v}$ and induces charge and current densities $\rho_{\mathrm{ind}}(\mathbf{r};t)$ and $\mathbf{J}_{\mathrm{ind}}(\mathbf{r};t)$ in the sample. At the same time, these induced densi-

ties produce electromagnetic fields $\mathbf{E}_{\mathrm{ind}}(\mathbf{r};t)$ and $\mathbf{B}_{\mathrm{ind}}(\mathbf{r};t)$ that act back on the probing electron, causing an energy loss that reveals the energy and strength of the excitation induced in the sample. The energy loss ΔE_{EELS} experienced by the electron can be calculated as the work performed by the induced electromagnetic field over the fast electron

$$\Delta E_{\mathrm{EELS}} = e\int_{-\infty}^{\infty} \mathrm{d}t\, \mathbf{v}\cdot\mathbf{E}_{\mathrm{ind}}(\mathbf{r}_{\mathrm{e}};t), \tag{1.55}$$

where $\mathbf{r}_{\mathrm{e}}$ is the electron beam trajectory. Through a time-to-frequency Fourier transform of $\mathbf{E}_{\mathrm{ind}}(\mathbf{r}_{\mathrm{e}};t)$, Eq. (1.55) can be rewritten as:

$$\Delta E_{\mathrm{EELS}} = \int_{0}^{\infty} \mathrm{d}\omega\, \hbar\omega\, \Gamma(\omega), \tag{1.56}$$

where

$$\Gamma(\omega) = \frac{e}{\pi\hbar\omega}\int_{-\infty}^{\infty} \mathrm{d}t\, \mathrm{Re}\left[\mathbf{v}\cdot\mathbf{E}_{\mathrm{ind}}(\mathbf{r}_{\mathrm{e}};\omega)\, e^{-i\omega t}\right], \tag{1.57}$$

is the electron energy-loss probability, which accounts for the probability that an electron loses an energy equal to $\hbar\omega$. The fast electron travels a distance $L = vt$ in a period of time t and thus, from Eq. (1.57), one can identify the electron energy-loss probability per unit length,

$$\Gamma'(\omega) = \frac{\mathrm{d}\Gamma(\omega)}{\mathrm{d}L} = \frac{e}{\pi\hbar\omega}\mathrm{Re}\left[\hat{\mathbf{v}}\cdot\mathbf{E}_{\mathrm{ind}}(\mathbf{r}_{\mathrm{e}};\omega)\, e^{-i\omega L/v}\right], \tag{1.58}$$

where $\hat{\mathbf{v}}$ is the unit vector in the same direction as the electron velocity $\mathbf{v}$. Equations (1.57) and (1.58) provide a way to numerically calculate the EEL spectrum and simulate the EEL signal obtained in EELS experiments.

We note that for many situations addressed in this thesis, the fast electron travels with a trajectory pointing along the z-direction, i.e., $\mathbf{r}_{\mathrm{e}}(t) = (x_{\mathrm{e}}, y_{\mathrm{e}}, z = vt)$. Hence, Eqs. (1.57) and (1.58) are expressed as

$$\Gamma(\omega) = \frac{e}{\pi\hbar\omega}\int_{-\infty}^{\infty} \mathrm{d}z\, \mathrm{Re}\left[\hat{\mathbf{z}}\cdot\mathbf{E}_{\mathrm{ind}}(\mathbf{r}_{\mathrm{e}};\omega)\, e^{-i\omega z/v}\right], \tag{1.59}$$

and

$$\Gamma'(\omega) = \frac{\mathrm{d}\Gamma(\omega)}{\mathrm{d}z} = \frac{e}{\pi\hbar\omega}\mathrm{Re}\left[\hat{\mathbf{z}}\cdot\mathbf{E}_{\mathrm{ind}}(\mathbf{r}_{\mathrm{e}};\omega)\, e^{-i\omega z/v}\right]. \tag{1.60}$$

Electromagnetic fields produced by a fast electron

The evanescent nature of the electromagnetic fields produced by a fast electron offers the capability to investigate different optical excitations in a sample using EELS. To better understand these evanescent fields, we analyze below the EM

fields produced by a fast electron traveling, in free space, along the trajectory $\mathbf{r}_{\mathrm{e}}(t) = (0, 0, z = vt)$.

From Maxwell's equations, one can derive the following mathematical expressions for the EM fields produced by the fast electron [8, 93]:

$$\mathbf{E}_{\mathrm{e}}(\mathbf{r};\omega) = -\frac{e}{2\pi\varepsilon_0}\frac{\omega}{v^2\gamma_{\mathrm{L}}}e^{i\omega z/v}\left\{\mathrm{sign}(\omega)K_1\left(\frac{|\omega|}{\gamma_{\mathrm{L}}v}R\right)\hat{\mathbf{R}} - \frac{i}{\gamma_{\mathrm{L}}}K_0\left(\frac{|\omega|}{\gamma_{\mathrm{L}}v}R\right)\hat{\mathbf{z}}\right\}, \tag{1.61}$$

$$\mathbf{B}_{\mathrm{e}}(\mathbf{r};\omega) = -\frac{e}{2\pi\varepsilon_0}\frac{|\omega|}{cv\gamma_{\mathrm{L}}}e^{i\omega z/v}K_1\left(\frac{|\omega|}{\gamma_{\mathrm{L}}v}R\right)\hat{\boldsymbol{\phi}}, \tag{1.62}$$

where $\gamma_{\mathrm{L}} = 1/\sqrt{1 - v^2\varepsilon(\omega)/c^2}$ is the Lorentz factor, $\mathbf{r} = (\mathbf{R}, z) = (x, y, z)$, $R = \sqrt{x^2 + y^2}$, $\hat{\boldsymbol{\phi}}$ is the unit vector in the azimuthal direction in cylindrical coordinates, $K_0(x)$, $K_1(x)$ are the zero and first order modified Bessel functions of the second kind, respectively, and sgn stands for the sign function. Figures 1.10a-b show the evaluation of the electric (Eq. (1.61)) and magnetic (Eq. (1.62)) fields of an electron traveling with velocity $v = 0.7c$ (approximately 200 keV). We can observe that the fields exponentially decay as a function of the distance R, and, the amplitude of the radial component of the electric field, $|E_{\mathrm{e},R}|$, is larger than that of $|E_{\mathrm{e},z}|$ (compare blue and red solid lines in Fig. 1.10a). This is a consequence of the Lorentz contraction experienced by the fields produced by the fast electron traveling at a constant velocity, compared to the fields produced by the same electron when it is at rest ($v = 0$). Indeed, by decreasing the velocity of the electron to 5 % the speed of light, the Lorentz contraction reduces, and thus, one can observe that $|E_{\mathrm{e},R}|$ approaches $|E_{\mathrm{e},z}|$ (compare blue and red dashed lines in Fig. 1.10a).

Bulk polaritons and Cherenkov radiation

The EEL probability (Eqs. (1.57)-(1.60)) provides valuable information which reveals, for example, the optical excitation produced at a sample. To show an example of this, we consider the following situation: a fast electron traveling with constant velocity $\mathbf{v}$ through the bulk of SiC, as illustrated in the inset of Fig. 1.11a. The EEL probability per unit path is given by [8]:

$$\Gamma'_{\mathrm{bulk}}(\omega) = \frac{e^2}{(2\pi)^2\omega^2\hbar\varepsilon_0}\mathrm{Im}\left\{\left[k_0^2 - \frac{\omega^2}{\varepsilon_{\mathrm{SiC}}\,v^2}\right]\ln\left[\frac{\varepsilon_{\mathrm{SiC}}\,k_0^2 - \omega^2/v^2 - (k_\perp^{\mathrm{c}})^2}{\varepsilon_{\mathrm{SiC}}\,k_0^2 - \omega^2/v^2}\right]\right\}, \tag{1.63}$$

with $\hbar k_\perp^{\mathrm{c}}$ the maximum value of the perpendicular component of the momentum transfer of the electrons selected by the collection aperture of the EELS spectrometer.

Figure 1.11a shows the evaluation of Eq. (1.63) (blue curve) for the energy

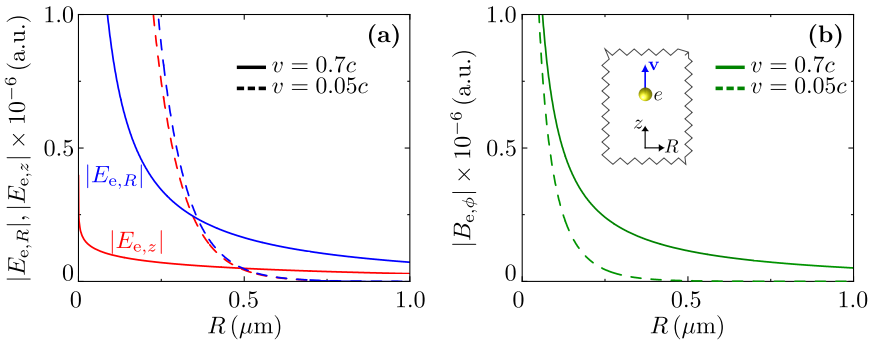

Figure 1.10: Electromagnetic fields produced by a fast electron. (a) Amplitude of the radial component (solid blue line) and the z-component (solid red line) of the electric fields produced by a fast electron traveling in free space with velocity $v = 0.7c$. Dashed lines correspond to the evaluation of the field amplitudes considering that the electron is traveling with $v = 0.05c$. (b) Same as in panel (a) but for the components of the magnetic field. The inset in (b) illustrates the electron beam trajectory. For the calculation we use Eqs. (1.61)-(1.62) and choose $\hbar\omega = 100\,\text{meV}$ as a representative energy in the infrared range.

range of $80\,\text{eV} - 160\,\text{eV}$, which includes the Reststrahlen of SiC. The electron travels with velocity $v = 0.7c$. We recognize in the EEL spectrum the appearance of a peak at the LO phonon energy, demonstrating that the electron energy losses in the Reststrahlen band (shaded gray area) are due to bulk phonon polariton excitations. Interestingly, outside the Reststrahlen band, we can also observe the appearance of small electron energy losses, as shown in the zoomed view in Fig. 1.11b. These losses are a consequence of the fast electron traveling faster than the speed of light in SiC, i.e., $v > c/\sqrt{\varepsilon_{\text{SiC}}}$. In this case, the field distribution (Eq. (1.61)) produced by the fast electron traveling through SiC exhibits wake patterns (see field plot in Fig. 1.11c). This physical phenomenon is known as Vavilov-Cherenkov radiation [94–101] . When the fast electron travels slower than the speed of light in SiC, it does not radiate, and thus no wake patterns are formed. This is evident in Fig. 1.11d, where we plot the field distribution produced by the electron traveling with a reduced velocity of 20% the speed of light. This analysis reveals that a fast electron, interacting with a sample, can lose energy through different mechanisms. In Chapters 2 and 3, we will thoroughly analyze the electron energy losses obtained from the interaction of fast electron beams with anisotropic polaritonic media and high-index dielectric disks.

It is worth mentioning that for a structure with an arbitrary geometrical shape, it is not always possible to find analytical solutions for $\Gamma(\omega)$. In Appendix B.1, we thus describe a methodology based on the Finite Element Method (FEM) to solve Maxwell's equations and to calculate the EEL proba-

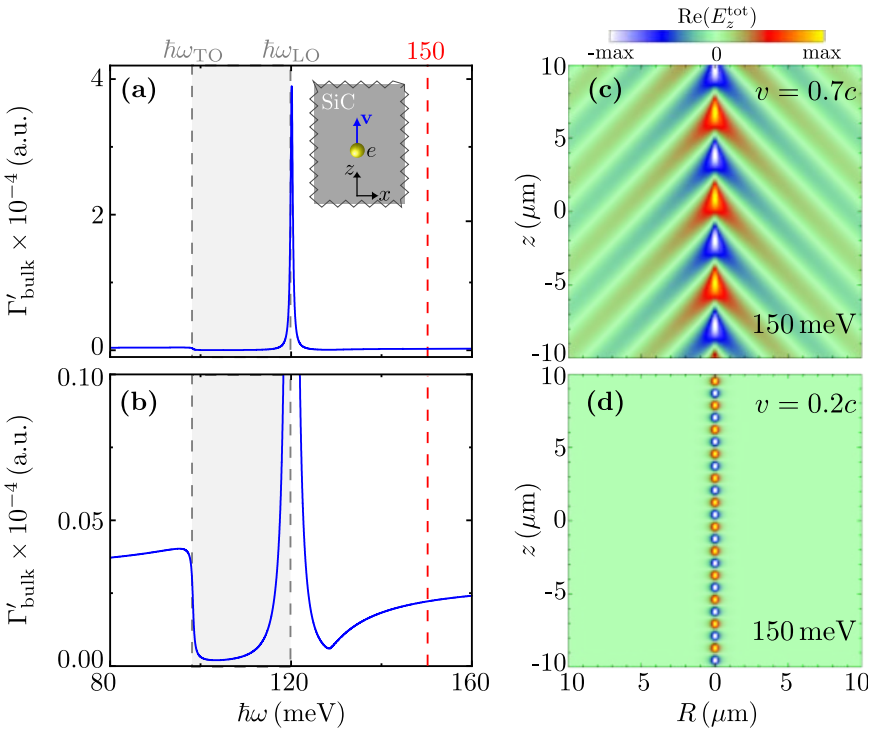

Figure 1.11: Excitation of bulk PhPs and Cherenkov radiation by a fast electron. (a) Electron energy-loss probability $\Gamma'_{\mathrm{bulk}}(\omega)$ in SiC obtained with Eq. (1.63). The shaded gray area marks the Reststrahlen band and $\hbar\omega_{\mathrm{TO}}$, $\hbar\omega_{\mathrm{LO}}$ mark the position of the TO and LO phonon energies, respectively. As depicted by the inset in panel (a), the electron is traveling through SiC characterized by a dielectric function $\varepsilon_{\mathrm{SiC}}(\omega)$ (Eq. (1.63)). The calculation is performed assuming $v = 0.7c$ and $k_{\perp}^{c} = 0.1\,\text{Å}^{-1}$. Panel (b) shows a zoom into panel (a). The contour plot in panel (c) depicts the real part of the z-component of the total electric field induced by the fast electron along the cylindrical coordinates (R, z) for an energy loss of 150 meV (marked by the red dashed line in panels (a) and (b)) and $v = 0.7c$. Panel (d) shows the same as panel (c) but considering an electron velocity $v = 0.2c$. The field plots are normalized to the maximum value in each case: (c) 8.0×10^{-8} a.u. and (d) 5.0×10^{-7} a.u. All calculations were performed using the same values for the dielectric function of SiC, $\varepsilon_{\mathrm{SiC}}(\omega)$, as the ones used in Figs. 1.2b-c.

bility $\Gamma(\omega)$.

1.4.2 s-SNOM in the infrared range

Scattering-type scanning near-field optical microscopy (s-SNOM) is an alternative technique for probing and exciting polaritons [27, 28, 30, 67]. In this

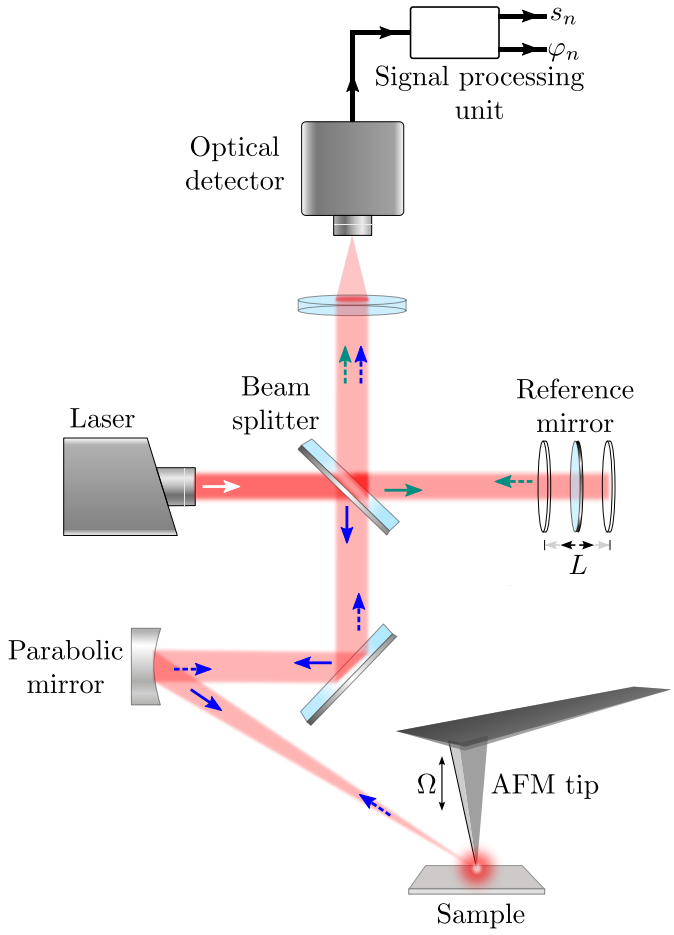

Figure 1.12: llustration of a typical nano-FTIR spectroscopy setup based on s-SNOM (reproduced from https://www.attocube.com/en/products/microscopes/nanoscale-imaging-spectroscopy/technology/s-SNOM). A broadband mid-infrared laser beam is split into two distinct beams by a beam splitter. One of these beams is focused onto the AFM tip oscillating at a frequency Ω, whereas the other beam is directed to a reference mirror. The back-scattered light from the AFM tip is directed to a mid-infrared detector, where it interferes with the light reflected at the reference mirror. The detector measures the intensity of the light that results from this interference. This detector signal is demodulated at the frequency $n\Omega$ and recorded as a function of the position L of the reference mirror, yielding interferograms. A subsequent Fourier Transform of these interferograms yields near-field amplitude and phase spectra, $s_n(\omega)$ and $\varphi_n(\omega)$, respectively.

technique, a metallic atomic force microscope tip is illuminated by a focused laser beam (see Fig. 1.12). Owing to the the lighting rod effect, the incident illumination is strongly confined at the tip apex, producing strong near fields

around it. By placing the tip above a sample, the near-field interaction between tip and sample modifies the tip-scattered light. Thus, by recording the back-scattered light from the tip as a function of the tip position, one can obtain images of the dielectric properties or the electromagnetic fields of a sample [23–25]. In such a way, s-SNOM enables sub-wavelength optical imaging with a spatial resolution that is usually determined by the tip apex radius (around $10\,\mathrm{nm} - 50\,\mathrm{nm}$).

S-SNOM has shown great potential for probing and mapping polaritons in different structures. For example, s-SNOM has been used to map the near-field distributions of phononic and plasmonic nanoantennas [27], as well as to imaging graphene plasmons [28, 29] and in-plane and out-of-plane anisotropic polaritons [102, 103].

The concept of this technique is illustrated in Figure 1.13. The infrared illumination $\mathbf{E}_{\mathrm{inc}}$ (yellow wavy arrow) polarizes the tip, resulting in an induced net dipole moment $\mathbf{p}_0$ at the tip (vertical blue arrow in Fig. 1.13a). By placing the tip in close proximity to the sample, the near-field interaction between tip and sample induces an additional dipole moment $\mathbf{p}_{\mathrm{NF}}$ at the tip (vertical red arrow in Fig. 1.13a). The induced dipole $\mathbf{p}_{\mathrm{NF}}$ produces a radiated field $\mathbf{E}_{\mathrm{NF}}$ (depicted by the red wavy arrow), containing the dielectric properties of the sample. Simultaneously, the induced dipole $\mathbf{p}_0$ produces the radiated field $\mathbf{E}_{\mathrm{BG}}$ (depicted by the blue wavy arrow), which is the predominant contribution to the tip-scattered field and provides negligible information about the sample.

Tip modulation and signal demodulation

To obtain the background-free near-field contribution $\mathbf{E}_{\mathrm{NF}}$ and to suppress the background field $\mathbf{E}_{\mathrm{BG}}$, the AFM works in tapping mode and thus the tip oscillates normal to the sample at a frequency Ω (see Fig. 1.13b). This allows to perform amplitude and phase-resolved detection of the tip-scattered field at a frequency $n\Omega$ ($n \geq 2$). We illustrate this procedure in Figs. 1.13c-d. The near fields at the tip exponentially decay in space, and thus, the tip-scattered near field $\mathbf{E}_{\mathrm{NF}}$ increases non-linearly when decreasing the tip-sample distance h_{tip}. The background-scattered field $\mathbf{E}_{\mathrm{BG}}$, on the other hand, increases approximately linearly when decreasing h_{tip}. Due these spatial dependency, when the tip oscillates harmonically in time, $\mathbf{E}_{\mathrm{NF}}(t)$ generates a strongly anharmonic time-dependent scattered field (blue curve in Fig. 1.13c), whereas $\mathbf{E}_{\mathrm{BG}}(t)$ yields a nearly time-harmonic background scattered field (red curve in Fig. 1.13c)). These behaviors can be clearly recognized by expressing the tip-scattered field,

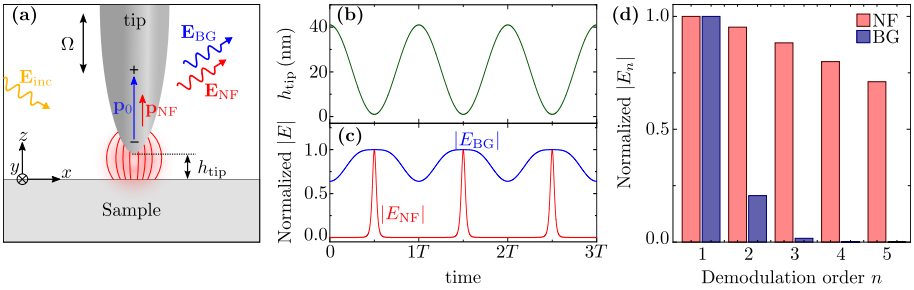

Figure 1.13: Suppression of the background-scattered field by tip modulation and signal demodulation. (a) Schematic representation of the AFM tip positioned at a height of h_{tip} with respect to the sample surface. The tip oscillates along the z-direction at frequency Ω, and it is illuminated by far-field illumination $\mathbf{E}_{\mathrm{inc}}$ (yellow wavy arrow). This illumination induces a dipole moment $\mathbf{p}_0(t)$ (blue arrow) at the tip strongly concentrated at the tip appex. By placing the tip close to the sample, an additional polarization $\mathbf{p}_{\mathrm{NF}}$ (red arrow) is induced at the tip due to the near-field interaction (red spot) between tip and sample. The corresponding dipoles $\mathbf{p}_0$ and $\mathbf{p}_{\mathrm{NF}}$ give rise to the tip-scattered fields $\mathbf{E}_{\mathrm{BG}}$ (blue wavy arrow) and $\mathbf{E}_{\mathrm{NF}}$ (red wavy arrow), respectively. (b) Height of the tip as a function of the tip-oscillation period $T = 2\pi/\Omega$. (c) Amplitudes of the tip-scattered background field E_{BG} (blue curve) and tip-scattered near-field E_{NF} (red curve) as a function of T. The curves are obtained assuming that: $E_{\mathrm{BG}}(t) = [\cos(2\pi h_{\mathrm{tip}}(t)/\lambda) + 1]/2$ and $E_{\mathrm{NF}}(t) = [h_{\mathrm{tip}}(T/2)]^3/[h_{\mathrm{tip}}(t)]^3$, $\lambda = 200\,\mathrm{nm}$. (d) Amplitude of the demodulated background field (blue bars) and demodulated near-field (red bars) for the first five demodulation orders n. The Fourier transform of $E_{\mathrm{BG}}(t)$ and $E_{\mathrm{NF}}(t)$ are performed using the Fourier package of Wolfram Mathematica software. Plots in panels (b)-(d) are normalized to the maximum value in each case.

$E_{\mathrm{scat}}(t)$, as the following Fourier series:

$$E_{\mathrm{scat}}(t) = E_{\mathrm{BG}}(t) + E_{\mathrm{NF}}(t) = \sum_{n=-\infty}^{\infty} (E_{\mathrm{BG},n} + E_{\mathrm{NF},n})\, e^{-in\Omega t}, \tag{1.64}$$

where $E_{\mathrm{BG},n}$ and $E_{\mathrm{NF},n}$ are the n^{th} complex Fourier coefficients of $E_{\mathrm{BG}}(t)$ and $E_{\mathrm{NF}}(t)$, respectively. Importantly, for high frequencies $n\Omega$ with $n \geq 2$, the Fourier coeffcients $E_{\mathrm{BG},n}$ of $E_{\mathrm{BG}}(t)$ are strongly suppressed, while the Fourier coeffcients $E_{\mathrm{NF},n}$ of $E_{\mathrm{NF}}(t)$ still contribute to $E_{\mathrm{scat}}(t)$ for $n \geq 3$ (see Fig. 1.13d). This analysis thus shows that demodulation of the tip-scattered field $E_{\mathrm{scat}}(t)$ at $n \geq 2$ yields the desired near-field contribution $E_{\mathrm{NF}}(t)$.

Therefore, measuring the field, for instance, through interferometric detection as illustrated in Fig. 1.12, which is proportional to the tip-scattered field, $E_{\mathrm{scat}}(t) = E_{\mathrm{BG}}(t) + E_{\mathrm{NF}}(t)$, in combination with demodulation of the detector signal at a frequency $n\Omega$ where $n \geq 2$, produces the background-free near-field amplitude and phase signals:

$$s_n \propto |E_{\mathrm{NF},n}| \quad \text{and,} \tag{1.65a}$$

$$\varphi_n \propto \arg(E_{\mathrm{NF},n}). \tag{1.65b}$$

To implement this in the experiment, amplitude and phase resolved measurements are performed in combination with higher harmonic demodulation [104]. This procedure gives amplitude and phase signals which are proportional to s_n and φ_n. S-SNOM utilizes a monochromatic laser beam for sample illumination to acquire its dielectric properties. In contrast, nanoscale Fourier transform infrared (nano-FTIR) spectroscopy employs broadband illumination to yield spectral information about the sample [105, 106].

Tip-sample near-field interaction: Lippmann-Schwinger equation

To theoretically simulate the detected signal obtained in s-SNOM experiments, we perform numerical simulations using the commercial package COMSOL Multiphysics (see Appendix B), where we model the tip as a conical platinum structure of 1 μm length and a semispherical apex of 25 nm radius. We assume that the tip-scattered light $\mathbf{E}_{\mathrm{scat}}$ arriving to the detector in the s-SNOM experiments is proportional to the net dipole moment $\mathbf{p}_{\mathrm{tip}}$ induced at the tip. This induced dipole moment is given as a sum of the dipole moment $\mathbf{p}_0$ induced by the incident illumination plus the dipole moment $\mathbf{p}_{\mathrm{NF}}$ induced by the near-field interaction with the sample, as we demonstrate below.

The tip-scattered field $\mathbf{E}_{\mathrm{scat}}(\mathbf{r})$ can be described as a series of multiple scattering events occurring between the tip and the sample. From a mathematical point of view, this series can be formulated in terms of the following Lippmann-Schwinger equation [35, 107–109]:

$$\begin{aligned}\mathbf{E}(\mathbf{r}) = \mathbf{E}_{\mathrm{inc}}(\mathbf{r}) + k_0^2 \int_{V_{\mathrm{T}}'} \mathrm{d}^3\mathbf{r}_{\mathrm{T}}'\, \hat{\mathbb{G}}_0(\mathbf{r},\mathbf{r}_{\mathrm{T}}') \cdot \hat{\chi}_{\mathrm{T}}(\mathbf{r}_{\mathrm{T}}') \cdot \mathbf{E}(\mathbf{r}_{\mathrm{T}}') + \\ + k_0^2 \int_{V_{\mathrm{S}}'} \mathrm{d}^3\mathbf{r}_{\mathrm{S}}'\, \hat{\mathbb{G}}_0(\mathbf{r},\mathbf{r}_{\mathrm{S}}') \cdot \hat{\chi}_{\mathrm{S}}(\mathbf{r}_{\mathrm{S}}') \cdot \mathbf{E}(\mathbf{r}_{\mathrm{S}}'),\end{aligned} \tag{1.66}$$

which establishes that the electric field $\mathbf{E}(\mathrm{r})$ at each point $\mathbf{r}$ in space is a sum of the incident electric field $\mathbf{E}_{\mathrm{inc}}(\mathbf{r})$ plus the electric fields scattered by the tip (labeled as T) and by the sample (labeled as S). The integrations in Eq. (1.66) extend over the volume of the tip, V_{T}', and the volume of the sample, V_{S}', with volume elements $\mathrm{d}^3\mathbf{r}_{\mathrm{T}}'$ and $\mathrm{d}^3\mathbf{r}_{\mathrm{S}}'$, respectively. The volume elements are located at $\mathbf{r}_{\mathrm{T}}'$ and $\mathbf{r}_{\mathrm{S}}'$. The tip and sample are characterized by their electric susceptibility tensors, $\hat{\chi}_{\mathrm{T}}(\mathbf{r})$ and $\hat{\chi}_{\mathrm{S}}(\mathbf{r})$, respectively, and $\hat{\mathbb{G}}_0(\mathbf{r},\mathbf{r}')$ is the Green's tensor in free space satisfying the wave equation [110]

$$\nabla \times \nabla \times \hat{\mathbb{G}}_0(\mathbf{r},\mathbf{r}') - k_0^2\, \hat{\mathbb{G}}_0(\mathbf{r},\mathbf{r}') = \hat{\mathbb{I}}\, \delta(\mathbf{r}-\mathbf{r}'). \tag{1.67}$$

By introducing the operators:

$$\hat{\mathbb{T}}(\mathbf{r}) = k_0^2 \int_{V_\mathrm{T}'} \mathrm{d}^3\mathbf{r}_\mathrm{T}'\, \hat{\mathbb{G}}_0(\mathbf{r}, \mathbf{r}_\mathrm{T}') \cdot \hat{\chi}_\mathrm{T}(\mathbf{r}_\mathrm{T}')\cdot, \tag{1.68}$$

and

$$\hat{\mathbb{S}}(\mathbf{r}) = k_0^2 \int_{V_\mathrm{S}'} \mathrm{d}^3\mathbf{r}_\mathrm{S}'\, \hat{\mathbb{G}}_0(\mathbf{r}, \mathbf{r}_\mathrm{S}') \cdot \hat{\chi}_\mathrm{S}(\mathbf{r}_\mathrm{S}')\cdot, \tag{1.69}$$

the Lippmann-Schwinger equation can be written in simpler notation:

$$\mathbf{E}(\mathbf{r}) = \mathbf{E}_\mathrm{inc}(\mathbf{r}) + \hat{\mathbb{T}}(\mathbf{r})\mathbf{E}(\mathbf{r}_\mathrm{T}') + \hat{\mathbb{S}}(\mathbf{r})\mathbf{E}(\mathbf{r}_\mathrm{S}'). \tag{1.70}$$

In this compact expression, it is evident that the unknown variable in the Lippmann-Schwinger equation is the electric field $\mathbf{E}(\mathbf{r})$, appearing at the left and right sides of the equality in Eq. (1.70). In general, it is not possible to find an analytical solution for $\mathbf{E}(\mathbf{r})$ and thus different methods need to be employed in order to find a solution. One possible method is an iterative approach, i.e., substituting the expression of $\mathbf{E}(\mathbf{r})$ into the terms on the right side of Eq. (1.70). This approach provides valuable information of the scattered field produced by the tip and the sample. For example, by examining the first two iterations and appropriately reorganizing terms, it can be deduced that the electric field $\mathbf{E}(\mathbf{r})$ can be calculated from the following expansion[5]:

$$\begin{aligned}\mathbf{E}(\mathbf{r}) = \mathbf{E}_\mathrm{inc}(\mathbf{r}) + \hat{\mathbb{T}}(\mathbf{r})\mathbf{E}_\mathrm{inc}(\mathbf{r}_\mathrm{T}') + \hat{\mathbb{S}}(\mathbf{r})\mathbf{E}_\mathrm{inc}(\mathbf{r}_\mathrm{S}') + \\ + \hat{\mathbb{T}}(\mathbf{r})\hat{\mathbb{S}}(\mathbf{r}_\mathrm{T}')\mathbf{E}_\mathrm{inc}(\mathbf{r}_\mathrm{S}') + \hat{\mathbb{S}}(\mathbf{r})\hat{\mathbb{T}}(\mathbf{r}_\mathrm{S}')\mathbf{E}_\mathrm{inc}(\mathbf{r}_\mathrm{T}') + \cdots\end{aligned} \tag{1.71}$$

This expansion can be interpreted as a series of multiple scattering events between the tip and sample. This can be recognized by assuming that the tip and the sample are two point-like electric dipoles with electric susceptibility tensors $\hat{\chi}_\mathrm{T}(\mathbf{r}) = \hat{\alpha}_\mathrm{T}\delta(\mathbf{r} - \mathbf{r}_\mathrm{T})$ and $\hat{\chi}_\mathrm{S}(\mathbf{r}) = \hat{\alpha}_\mathrm{S}\delta(\mathbf{r} - \mathbf{r}_\mathrm{S})$, respectively. The two point-like dipoles are located at positions $\mathbf{r}_\mathrm{T}$, $\mathbf{r}_\mathrm{S}$ and they are characterized by their electric polarizability tensors $\hat{\alpha}_\mathrm{T}$ and $\hat{\alpha}_\mathrm{S}$. By illuminating the point-like dipoles with a local electric field $\mathbf{E}_\mathrm{loc}(\mathbf{r})$, the dipoles polarize and scatter electric fields which can be obtained using the following expressions

$$\mathbf{E}_\mathrm{T}(\mathbf{r}) = k_0^2\, \hat{\mathbb{G}}_0(\mathbf{r}, \mathbf{r}_\mathrm{T}) \cdot \mathbf{p}_\mathrm{T}, \tag{1.72}$$

$$\mathbf{E}_\mathrm{S}(\mathbf{r}) = k_0^2\, \hat{\mathbb{G}}_0(\mathbf{r}, \mathbf{r}_\mathrm{S}) \cdot \mathbf{p}_\mathrm{S}, \tag{1.73}$$

where $\mathbf{p}_\mathrm{T} = \hat{\alpha}_\mathrm{T} \cdot \mathbf{E}_\mathrm{loc}(\mathbf{r}_\mathrm{T})$ and $\mathbf{p}_\mathrm{S} = \hat{\alpha}_\mathrm{S} \cdot \mathbf{E}_\mathrm{loc}(\mathbf{r}_\mathrm{S})$ are the dipole moments induced by $\mathbf{E}_\mathrm{loc}(\mathbf{r})$ at the tip and sample, respectively.

[5]Due to its similarity with the expansion obtained in quantum scattering theory, Eq. (1.71) is sometimes referred to as the Born series.

Under the assumption that the tip and sample are point-like electric dipoles, the operators $\hat{\mathbb{T}}(\mathbf{r})$ (Eq. (1.68)) and $\hat{\mathbb{S}}(\mathbf{r})$ (Eq. (1.69)) can be rewritten as

$$\hat{\mathbb{T}}(\mathbf{r}) = k_0^2\, \hat{\mathbb{G}}_0(\mathbf{r}, \mathbf{r}_\mathrm{T}) \cdot \hat{\alpha}_\mathrm{T} \cdot, \tag{1.74}$$

$$\hat{\mathbb{S}}(\mathbf{r}) = k_0^2\, \hat{\mathbb{G}}_0(\mathbf{r}, \mathbf{r}_\mathrm{S}) \cdot \hat{\alpha}_\mathrm{S} \cdot . \tag{1.75}$$

Substituting the latter expressions into Eq. (1.71), one finds that the Born series (Eq. (1.71), describing the multiple scattering events occurring between the two point-like dipoles, is

$$\begin{aligned} \mathbf{E}(\mathbf{r}) - \mathbf{E}_\mathrm{inc}(\mathbf{r}) = {} & k_0^2\, \hat{\mathbb{G}}_0(\mathbf{r}, \mathbf{r}_\mathrm{T}) \cdot \hat{\alpha}_\mathrm{T} \cdot \mathbf{E}_\mathrm{inc}(\mathbf{r}_\mathrm{T}) + k_0^2\, \hat{\mathbb{G}}_0(\mathbf{r}, \mathbf{r}_\mathrm{S}) \cdot \hat{\alpha}_\mathrm{S} \cdot \mathbf{E}_\mathrm{inc}(\mathbf{r}_\mathrm{S}) + \\ & + k_0^2\, \hat{\mathbb{G}}_0(\mathbf{r}, \mathbf{r}_\mathrm{T}) \cdot \hat{\alpha}_\mathrm{T} \cdot k_0^2\, \hat{\mathbb{G}}_0(\mathbf{r}_\mathrm{T}, \mathbf{r}_\mathrm{S}) \cdot \hat{\alpha}_\mathrm{S} \cdot \mathbf{E}_\mathrm{inc}(\mathbf{r}_\mathrm{S}) + \\ & + k_0^2\, \hat{\mathbb{G}}_0(\mathbf{r}, \mathbf{r}_\mathrm{S}) \cdot \hat{\alpha}_\mathrm{S} \cdot k_0^2\, \hat{\mathbb{G}}_0(\mathbf{r}_\mathrm{S}, \mathbf{r}_\mathrm{T}) \cdot \hat{\alpha}_\mathrm{T} \cdot \mathbf{E}_\mathrm{inc}(\mathbf{r}_\mathrm{T}) + \cdots \end{aligned} \tag{1.76}$$

According to Eqs. (1.72) and (1.73), the first two terms on the right side of Eq. (1.76) represent the electric fields scattered by the tip and the sample, both of which are polarized by the incident field:

$$\mathbf{E}^\mathrm{T}_\mathrm{BG}(\mathbf{r}) \equiv k_0^2\, \hat{\mathbb{G}}_0(\mathbf{r}, \mathbf{r}_\mathrm{T}) \cdot \hat{\alpha}_\mathrm{T} \cdot \mathbf{E}_\mathrm{inc}(\mathbf{r}_\mathrm{T}), \tag{1.77}$$

$$\mathbf{E}^\mathrm{S}_\mathrm{BG}(\mathbf{r}) \equiv k_0^2\, \hat{\mathbb{G}}_0(\mathbf{r}, \mathbf{r}_\mathrm{S}) \cdot \hat{\alpha}_\mathrm{S} \cdot \mathbf{E}_\mathrm{inc}(\mathbf{r}_\mathrm{S}). \tag{1.78}$$

We label these fields as BG because they contribute to the background field, $\mathbf{E}_\mathrm{BG}(\mathbf{r})$, as discussed in Fig. 1.13. In addition, using Eq. (1.78), the third term in Eq. (1.76) can be rewritten as

$$\begin{aligned} \mathbf{E}^\mathrm{TS}_\mathrm{NF}(\mathbf{r}) &\equiv k_0^2\, \hat{\mathbb{G}}_0(\mathbf{r}, \mathbf{r}_\mathrm{T}) \cdot \hat{\alpha}_\mathrm{T} \cdot k_0^2\, \hat{\mathbb{G}}_0(\mathbf{r}_\mathrm{T}, \mathbf{r}_\mathrm{S}) \cdot \hat{\alpha}_\mathrm{S} \cdot \mathbf{E}_\mathrm{inc}(\mathbf{r}_\mathrm{S}) \\ &= k_0^2\, \hat{\mathbb{G}}_0(\mathbf{r}, \mathbf{r}_\mathrm{T}) \cdot \hat{\alpha}_\mathrm{T} \cdot \mathbf{E}^\mathrm{S}_\mathrm{BG}(\mathbf{r}_\mathrm{T}). \end{aligned} \tag{1.79}$$

Upon examination of the latter expression, one realizes that the third term in Eq. (1.76) represents the field scattered by the tip when it is polarized by the near fields produced by the sample. Similarly, using Eq. (1.72), one can rewrite the fourth term in Eq. (1.76) as

$$\begin{aligned} \mathbf{E}^\mathrm{ST}_\mathrm{NF}(\mathbf{r}) &\equiv k_0^2\, \hat{\mathbb{G}}_0(\mathbf{r}, \mathbf{r}_\mathrm{S}) \cdot \hat{\alpha}_\mathrm{S} \cdot k_0^2\, \hat{\mathbb{G}}_0(\mathbf{r}_\mathrm{S}, \mathbf{r}_\mathrm{T}) \cdot \hat{\alpha}_\mathrm{T} \cdot \mathbf{E}_\mathrm{inc}(\mathbf{r}_\mathrm{T}) \\ &= k_0^2\, \hat{\mathbb{G}}_0(\mathbf{r}, \mathbf{r}_\mathrm{S}) \cdot \hat{\alpha}_\mathrm{S} \cdot \mathbf{E}^\mathrm{T}_\mathrm{BG}(\mathbf{r}_\mathrm{S}), \end{aligned} \tag{1.80}$$

which represents the field scattered by the sample when it is polarized by the near fields produced by the tip. These first four terms of the Born series of the scattering process (Eq. (1.76)) are schematically illustrated in Fig. 1.14.

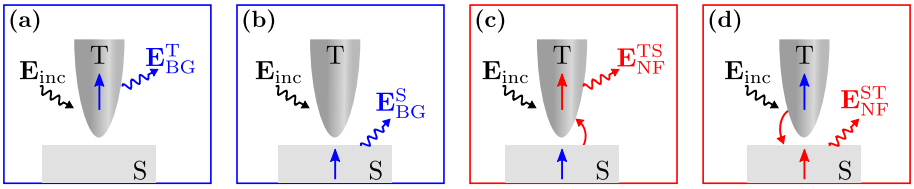

Figure 1.14: Born series of the tip-sample interaction. Schematic representation of the first four terms in the Born series given by Eq. (1.76). The incident illumination $\mathbf{E}_{\mathrm{inc}}$ polarizes the tip and sample, inducing a dipole at (a) the tip (blue arrow) and (b) the sample (blue arrow). Each dipole scatters fields given by $\mathbf{E}^{\mathrm{T}}_{\mathrm{BG}}(\mathbf{r})$ (Eq. (1.77)) and $\mathbf{E}^{\mathrm{S}}_{\mathrm{BG}}(\mathbf{r})$ (Eq. (1.78)). (c) The near fields produced by the dipole induced at the sample (blue arrow) induce an additional polarization at the tip that modifies its dipole moment (red arrow). Thus, the tip scatters fields given by $\mathbf{E}^{\mathrm{TS}}_{\mathrm{NF}}(\mathbf{r})$ (Eq. (1.79)). (d) The near fields produced by the dipole induced at the tip (blue arrow) induce an additional polarization at the sample that modifies its dipole moment (red arrow), and thus, the sample scatters fields give by $\mathbf{E}^{\mathrm{ST}}_{\mathrm{NF}}(\mathbf{r})$ (Eq. (1.80)). The blue color of the box in panels (a) and (b) emphasizes that the scattered field contributes to the background field, whereas the red color of the box in panels (c) and (d) emphasizes that the scattered field is a result of the near-field tip-sample interaction.

From this analysis, one can expect that subsequent terms of the Born series (indicated by the three dots in Eq. (1.76)) represent further scattering events of the tip and sample, both being polarized by their near-fields. For example, one of the subsequent terms in the Born series is

$$\begin{aligned}\mathbf{E}^{\mathrm{TST}}_{\mathrm{NF}}(\mathbf{r}) &\equiv k_0^2\,\hat{\mathbb{G}}_0(\mathbf{r},\mathbf{r}_{\mathrm{T}})\cdot\hat{\alpha}_{\mathrm{T}}\cdot k_0^2\,\hat{\mathbb{G}}_0(\mathbf{r}_{\mathrm{T}},\mathbf{r}_{\mathrm{S}})\cdot\hat{\alpha}_{\mathrm{S}}\cdot k_0^2\,\hat{\mathbb{G}}_0(\mathbf{r}_{\mathrm{S}},\mathbf{r}_{\mathrm{T}})\cdot\hat{\alpha}_{\mathrm{T}}\cdot\mathbf{E}_{\mathrm{inc}}(\mathbf{r}_{\mathrm{T}})\\ &= k_0^2\,\hat{\mathbb{G}}_0(\mathbf{r},\mathbf{r}_1\mathrm{T})\cdot\hat{\alpha}_{\mathrm{T}}\cdot\mathbf{E}^{\mathrm{ST}}_{\mathrm{NF}}(\mathbf{r}_{\mathrm{T}}),\end{aligned} \tag{1.81}$$

which represents the following scattering event: the incident field polarizes the tip, causing a net dipole moment at the tip. This net dipole moment produced near field that polarizes the sample, inducing a dipole moment at the sample, whose near field polarize the tip again, changing the induced dipole moment at the tip and thus changing the tip-scattered field.

Induced dipole moment and s-SNOM signal

When the scattering of the sample is much smaller than the scattering of the tip, the term $\mathbf{E}(\mathbf{r})-\mathbf{E}_{\mathrm{inc}}(\mathbf{r})$ in Eq. (1.76) is approximately equal to the tip-scattered field $\mathbf{E}_{\mathrm{scat}}(\mathbf{r})$. Under this approximation, using Eqs. (1.77)-(1.81) and substituting them into the Born series (Eq. (1.76)), one finds that the

tip-scattered field can be expressed as follows

$$\mathbf{E}_{\text{scat}}(\mathbf{r}) = k_0^2\,\hat{\mathbb{G}}_0(\mathbf{r},\mathbf{r}_{\text{T}})\cdot[\underbrace{\hat{\alpha}_{\text{T}}\cdot\mathbf{E}_{\text{inc}}(\mathbf{r}_{\text{T}})}_{\mathbf{p}_0}+\underbrace{\hat{\alpha}_{\text{T}}\cdot\mathbf{E}^{\text{S}}_{\text{BG}}(\mathbf{r}_{\text{T}})+\hat{\alpha}_{\text{T}}\cdot\mathbf{E}^{\text{ST}}_{\text{NF}}(\mathbf{r}_{\text{T}})+\cdots}_{\mathbf{p}_{\text{NF}}}] \tag{1.82}$$

In this form, one can identify that the tip-scattered field arriving at the detector in the far field, $\mathbf{E}_{\text{scat}}$, is proportional to the dipole moment $\mathbf{p}_0$ induced by the incident illumination plus the dipole moment $\mathbf{p}_{\text{NF}}$ induced by the near-field interactions with the sample, i.e., $\mathbf{E}_{\text{scat}} \propto \mathbf{p}_{\text{tip}} = \mathbf{p}_0 + \mathbf{p}_{\text{NF}}$. The latter relationship provides a way to calculate the tip-scattered field and simulate the detected signal in s-SNOM experiments. Indeed, by assuming tip modulation, the dipole moment induced at the tip changes in time accordingly and, demodulation of $\mathbf{p}_{\text{tip}}(t)$ yields n^{th}-order demodulated scattered field $p_{\text{tip},n}$, which can be associated with the experimental demodulated signal (Eqs. (1.65a)-(1.65b)) as:

$$s_n \propto |p_{\text{NF},n}| \quad \text{and,} \tag{1.83a}$$

$$\varphi_n \propto \arg(p_{\text{NF},n}). \tag{1.83b}$$

In Appendix B.2, we provide a methodology based on the FEM to calculate the dipole moment $\mathbf{p}_{\text{tip}} = \mathbf{p}_0 + \mathbf{p}_{\text{NF}}$ induced at the conical tip and we provide a procedure to demodulate $\mathbf{p}_{\text{tip}}(t)$. These methodologies, together with the concepts discussed in this section, will be used in Chapter 4 to investigate the near-field spectroscopy of phononic nanoantennas.

1.5 Summary

In this chapter, we have presented a classical description of polaritons in metals and polar crystals using Maxwell's equations, and we have introduced two different techniques for probing polaritons. First, we revised Maxwell's equation in continuous media, as well as the constitutive relations and the Lorentz model to describe dipolar excitations in matter. Second, we introduced the concept of plasmons in metals and optical phonons in polar crystals in the context of the optical properties of solids. We also analyzed the propagation and dispersion of plasmons and phonon polaritons in bulk, semi-infinite surfaces, thin films, and

spherical nanoparticles. We exemplified the role of optical anisotropy by analyzing the optical response of a uniaxial anisotropic film made of h-BN. Third, we introduced the concepts of weak and strong light-matter interactions and presented two models that allow us to quantify the coupling strength between two coupled resonators. Finally, we discussed EELS and s-SNOM as two techniques capable of probing polaritons in the near field. We briefly discussed their working principles and provided some of the basic mathematical framework necessary to understand and interpret the experimental results obtained with both techniques. The concepts and mathematical derivations discussed in this chapter are key to understanding the results presented in the following chapters of this thesis.

2

Probing hyperbolic phonon polaritons in h-BN with fast electron beams

Great, this is what I wanted to see! The angle of the wake is exactly the same as for the bulk polariton.

– Javier's email (May 20, 2020)

Abstract

In this chapter, we theoretically describe how fast electrons couple to polaritonic modes in uniaxial materials by analyzing the EEL spectra. We show that for a uniaxial medium with hyperbolic dispersion, bulk and surface modes can be excited by a fast electron traveling through the volume or along an infinite interface between the material and vacuum. Interestingly, and in contrast to excitations in isotropic materials, we show that bulk modes can be excited by fast electrons traveling outside the uniaxial medium. We demonstrate our findings with the representative uniaxial material hexagonal boron nitride (h-BN). We show that the excitation of bulk and surface phonon polariton modes is strongly related to the electron velocity and highly dependent on the angle between the electron beam trajectory and the optical axis of the material. The results discussed in this chapter have been published in the following publication: C. Maciel-Escudero et al. "Probing and steering bulk and surface phonon polaritons in uniaxial materials using fast electrons: Hexagonal boron nitride", Physical Review B **102**, 115431 (2020).

2.1 Introduction

Polar materials have become of high interest in the field of nanophotonics due to their ability to support phonon polaritons. As discussed in the Chapter 1, these are quasi–particles which result from the coupling between electromagnetic waves and crystal lattice vibrations [3, 111] with a characteristic wavelength lying in the mid–infrared region. They can enhance the electromagnetic field deep below the diffraction limit with large quality factors compared to infrared plasmons [4, 112, 113], making them promising building blocks for infrared nanophotonics applications [64, 114–116].

An interesting two-dimensional (2D) polar material is hexagonal boron nitride (h-BN) because of its high quality phonon polaritons and the easy preparation of the single atomic layers made by exfoliation [27, 30, 117–120]. Aside from being widely used in heterostructures [121], h-BN is emerging by itself as a versatile material offering novel optical and electro-optical functionalities. The crystal layer structure that constitues h-BN, mediated via interlayer van der Waals forces, produces a uniaxial optical response of the material which provides a possibility to excite hyperbolic phonon polaritons.

Hyperbolic phonon polaritons excitable on h-BN within the range of $90\,\mathrm{meV} - 200\,\mathrm{meV}$ might be a key to many novel photonic technologies relying on the nanoscale confinement of light and its manipulation. As a result, efficient design and utilization of h-BN structures require spectroscopic studies with adequate spatial resolution. This can be provided, for instance, by EELS using electrons as localized electromagnetic probes. Recently, instrumental improvements in EELS performed in a scanning transmission electron microscope allowed for spatially mapping phonon polaritons [122] and also hyperbolic phonon polaritons in h-BN [123, 124]. The focused electron beam of an electron microscope has thus become a suitable probe to access the spectral information of low-energy excitations in technologically relevant materials, with nanoscale spatial resolution. Thus, EEL spectra in phononic materials can be of paramount importance to reveal the properties of phonon polariton excitations.

In this chapter, we first discuss in Section 2.2 the dielectric properties of h-BN. In Subsections 2.3.1-2.3.4, we show that a fast electron traveling through volume h-BN in a trajectory parallel to the stacking direction (optical axis) of the h-BN layers can excite volume (bulk) phonon polaritons inside and outside

the h-BN Reststrahlen bands. Our analysis reveals that the excitation of the volume polariton modes is strongly dependent on the electron velocity and also on the orientation between the electron beam trajectory and the h-BN optical axis. We study in Subsection 2.3.5 the formation of wake patterns in the field distribution induced by the electron beam at h-BN. The methodology implemented here allows us to connect the excitation of these wake fields with the different electron energy loss mechanisms experienced by the fast electron in the medium: (i) excitation of phonon polaritons or (ii) Cherenkov radiation. We also discuss in Subsection 2.3.6 the emergence of asymmetric wake patterns exhibited by the induced electromagnetic field when the electron beam trajectory sustains an angle relative to the h-BN optical axis. In Section 2.4 we show that a fast electron beam interacting with a semi-infinite h-BN interface excite Dyakonov surface phonon polaritons within the h-BN upper Reststrahlen band. Finally, we demonstrate in Section 2.5 that the probing electron traveling above the h-BN in aloof trajectories excites volume phonon polaritons thus allowing for remote activation of these type of polaritons.

2.2 Dielectric properties of h-BN

We first review the optical properties of h-BN that will be used in this chapter to theoretically analyze the energy losses suffered by fast electrons traveling inside the bulk of h-BN, or traveling in aloof trajectories above h-BN. As mentioned in the introduction to this chapter, the atomic arrangement that constitutes h-BN produces an anisotropic optical response of the material. This implies that the dielectric function of h-BN need to be described by the following diagonal tensor [117, 118]:

$$\hat{\varepsilon}_{\text{h-BN}} = \begin{pmatrix} \varepsilon_{\perp} & 0 & 0 \\ 0 & \varepsilon_{\perp} & 0 \\ 0 & 0 & \varepsilon_{\parallel} \end{pmatrix}, \tag{2.1}$$

where we assumed that the stacking direction of the h-BN layers, defined as the optical axis, is along the z-axis. Thus, $\varepsilon_x = \varepsilon_y = \varepsilon_{\perp}$ is the in-plane component of the tensor and $\varepsilon_z = \varepsilon_{\parallel}$ is the out-of-plane component, parallel to the optical axis of h-BN (see caption in Fig. 2.1a). Since h-BN is a polar crystal, one can further assume that both diagonal components of the h-BN permittivity tensor

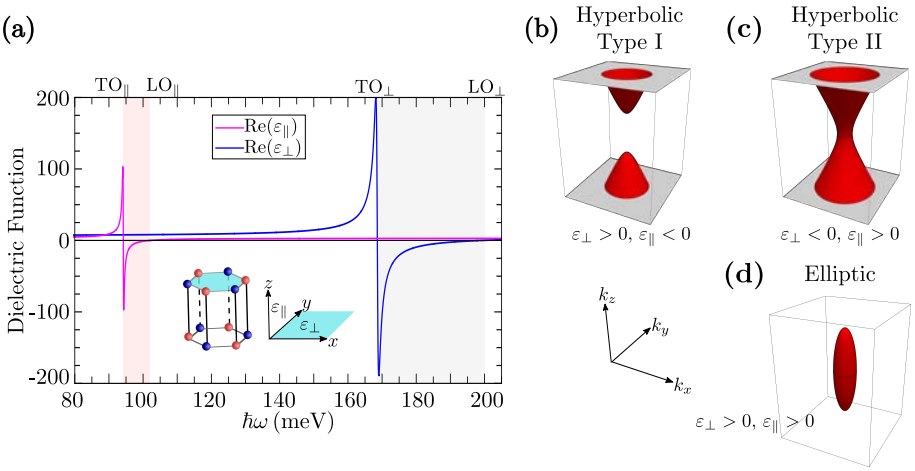

Figure 2.1: Dielectric properties of h-BN. (a) Real parts of the components of the h-BN dielectric function. The shaded red area marks the lower Reststrahlen band and the gray area the upper Reststrahlen band. Inset illustrates the crystal lattice structure of h-BN. Isofrequency surface for an energy in the (b) lower Reststrahlen band (hyperbolic Type I), (c) upper Reststrahlen band (hyperbolic Type II) and (c) outside the Reststrahlen bands (elliptic region). The isofrequency surfaces are obtained using Eq. (2.5) together with the parameters presented in Table 2.1.

can be well described with Eq. (1.17) as (see ref. [117])

$$\varepsilon(\omega) = \varepsilon_\infty \left(1 + \frac{\omega_{\mathrm{LO}}^2 - \omega_{\mathrm{TO}}^2}{\omega_{\mathrm{TO}}^2 - \omega^2 - i\omega\gamma_{\mathrm{pc}}}\right). \tag{2.2}$$

The values used for each constant are presented in Table 2.1.

When $\mathrm{Re}(\varepsilon_\parallel) \cdot \mathrm{Re}(\varepsilon_\perp) < 0$, phonon polaritons can propagate inside the material. As we will show in the next section, bulk phonon polaritons in h-BN exhibit a hyperbolic dispersion [114, 125], that is, the relationship between the different components of the polariton wavevector $\mathbf{k}(\omega) = (k_x, k_y, k_z)$ traces a surface in momentum space which corresponds to a hyperboloid. For h-BN, one can find two energy bands (Reststrahlen bands) where one of the principal components of the permittivity tensor is negative. Each Reststrahlen band is defined by the energy region between the transverse and longitudinal optical phonon energy, TO and LO, respectively ($\mathrm{TO}_\perp$ and $\mathrm{LO}_\perp$ for the upper Reststrahlen band and $\mathrm{TO}_\parallel$ and $\mathrm{LO}_\parallel$ for the lower Reststrahlen band, see Fig. 2.1a).

Figure 2.1a depicts the in- and out-of-plane permittivities of h-BN, $\varepsilon_\perp$ and $\varepsilon_\parallel$, respectively. The energy range in Fig. 2.1a shaded in red corresponds to the lower Reststrahlen band (94.2 meV − 102.3 meV) where the real part of

the out-of-plane permittivity is ($\mathrm{Re}(\varepsilon_{\parallel})$) negative, leading to a isofrequency surface in the form of a two-sheet hyperboloid (Type I), as shown in Fig. 2.1b. The energy region shaded in gray corresponds to the upper Reststrahlen band (168.6 meV − 200.1 meV), where the real part of the in-plane permittivity ($\mathrm{Re}(\varepsilon_{\perp})$) is negative and the isofrequency surface corresponds to a one-sheet hyperboloid (Type II), as shown in Fig. 2.1c. On the other hand, when $\mathrm{Re}(\varepsilon_{\parallel}) \cdot \mathrm{Re}(\varepsilon_{\perp}) > 0$, the isofrequency surfaces traced by the polariton wavevector in momentum space adopt the shape of an ellipsoid (see Fig. 2.1d). The hyperbolic or elliptic geometrical shape of the isofrequency surface determines the properties of propagation of the polaritonic waves in bulk h-BN, and also, as we explore in the following sections, leads to different physical phenomena as compared to a conventional isotropic material.

	In-plane ($\varepsilon_{\perp}$)	Out-of-plane ($\varepsilon_{\parallel}$)
ε_{∞}	4.90	2.95
$\hbar\omega_{\mathrm{TO}}$	168.6 meV	94.2 meV
$\hbar\omega_{\mathrm{LO}}$	200.1 meV	102.3 meV
$\hbar\gamma_{\mathrm{pc}}$	0.87 meV	0.25 meV

Table 2.1: Parameters of the components of permittivity tensor of h-BN. Parameters used for the in-plane and out-of-plane permittivities of h-BN taken from ref. 27.

2.3 Excitation of IR bulk modes in h-BN

2.3.1 Bulk modes in h-BN

According to Maxwell's equations in momentum-frequency $(\mathbf{k}, \omega)$ space, the dispersion relation for a wave propagating in the volume of an anisotropic material can be found from the following equation [126, 127]:

$$\det\left[\hat{\mathbb{G}}^{-1}(\mathbf{k};\omega)\right] = \det\left[\mathbf{k}\otimes\mathbf{k} - k^2\,\hat{\mathbb{I}} + k_0^2\,\hat{\varepsilon}\right] = 0, \tag{2.3}$$

where $\hat{\mathbb{G}}^{-1}$ is the inverse of the Green's tensor, $\mathbf{k}(\omega) = (k_x, k_y, k_z)$ is the wavevector of the wave, $k_0 = \omega/c$ is the magnitude of the wavevector in vacuum, c is the speed of light, $\det[x]$ stands for the determinant of a ma-

trix, $\otimes$ is the tensor product, and $\hat{\mathbb{I}}$ is the identity tensor. Particularly, for a uniaxial medium, the dielectric response can be described in tensor form as $\hat{\varepsilon}(\omega) = \mathrm{diag}[\varepsilon_\perp, \varepsilon_\perp, \varepsilon_\parallel]$. In this case, two solutions (modes) arise from Eq. (2.3), yielding the dispersion relation for ordinary waves:

$$k^2 = k_0^2 \varepsilon_\perp, \tag{2.4}$$

and the dispersion relation for extraordinary waves:

$$\frac{k_x^2 + k_y^2}{\varepsilon_\parallel} + \frac{k_z^2}{\varepsilon_\perp} = k_0^2. \tag{2.5}$$

Equation (2.4) represents concentric spheres in $\mathbf{k}$ space for a given energy $\hbar\omega$ (with $\varepsilon_\perp > 0$), while Eq. (2.5) represents hyperboloids or ellipsoids in the reciprocal space depending on the sign of the permittivity components $\varepsilon_\parallel$ and $\varepsilon_\perp$. Altogether the isofrequency surfaces of the polariton wavevector $\mathbf{k}(\omega)$ in momentum space (for a uniaxial medium) constitute the dispersion relation of the phonon-polariton modes and, as observed in Eqs. (2.4) and (2.5), are represented geometrically by spheres, ellipsoids or hyperboloids. Note that these modes are independent of the exciting probe used. In Figs. 2.1b-d we depict the isofrequency surfaces for h-BN for each energy region, inside and outside the Reststrahlen bands. As we will show in the following subsections, fast electron beams are effective probes capable of exciting the different phonon-polariton modes sustained in h-BN.

2.3.2 Electron energy-loss probability in bulk h-BN

Fast electron beams can couple to bulk polaritonic modes sustained in anisotropic media. We can observe this by analyzing the energy losses experienced by the probing electron when traveling in such media. As discussed in Chapter 1, electron energy losses, ΔE_{EELS}, can be calculated within classical electrodynamics as

$$\begin{aligned} \Delta E_{\mathrm{EELS}} &= \frac{e}{2\pi} \int \mathrm{d}t\, \mathbf{v} \cdot \int_{-\infty}^{\infty} \mathrm{d}\omega\, \mathbf{E}_{\mathrm{ind}}(\mathbf{r}_e; \omega)\, e^{-i\omega t} \\ &= \int_0^{\infty} \mathrm{d}\omega \int_0^{L_e} \mathrm{d}L\, \hbar\omega\, \Gamma'(\omega), \end{aligned} \tag{2.6}$$

where L_e is the distance traveled by the fast electron, and, one identifies the electron energy-loss (EEL) probability per unit length, $\Gamma'(\omega)$, as

$$\Gamma'(\omega) = \frac{e}{\pi\hbar\omega}\mathrm{Re}\left[\hat{\mathbf{v}}\cdot\mathbf{E}_{\mathrm{ind}}(\mathbf{r}_e;\omega)\,e^{-i\omega L/v}\right], \tag{2.7}$$

with $\hat{\mathbf{v}}$ the unit vector in the same direction as the electron velocity $\mathbf{v}$, and $L = vt$ is the distance traveled by the fast electron in a period of time t. Hence, to calculate $\Gamma'(\omega)$ one needs to know the induced electric field $\mathbf{E}_{\mathrm{ind}}(\mathbf{r}_e;\omega)$. We derive below the expressions of the total electric field $\mathbf{E}_{\mathrm{tot}}(\mathbf{r};\omega)$ and $\Gamma'(\omega)$ for an electron beam trajectory inside h-BN parallel to its optical axis, as depicted in Fig. 2.2.

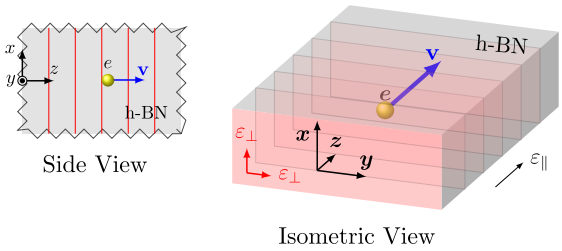

Figure 2.2: Electron traveling through the bulk of h-BN. Schematics of the electron traveling through h-BN with velocity $\mathbf{v} = v\hat{\mathbf{z}}$ parallel to the h-BN optical axis (z-direction). In the side view, the red lines represent the single h-BN layers that are stacked along the z-axis. In the isometric perspective, the red planes depict the h-BN layers.

It follows from Maxwell's equations that the field produced by the fast electron plus the induced electric field, namely the total electric field ($\mathbf{E}_{\mathrm{tot}}(\mathbf{r};\omega)$) is given by

$$\mathbf{E}_{\mathrm{tot}}(\mathbf{r};\omega) = -i\frac{\omega}{(2\pi)^3 c^2\varepsilon_0}\int_{\mathbb{K}^3}\mathrm{d}^3\mathbf{k}\;\rho_e(\mathbf{k};\omega)\,\hat{\mathbb{G}}(\mathbf{k};\omega)\cdot\mathbf{v}\,e^{i\mathbf{k}\cdot\mathbf{r}}, \tag{2.8}$$

with ε_0 the vacuum permittivity and $\rho_e(\mathbf{k};\omega) = -2\pi e\delta(\omega - \mathbf{k}\cdot\mathbf{v})$ the charge density of the probing electron with e the electron charge. The integration in Eq. (2.8) extends over the whole reciprocal space $\mathbb{K}^3$ and the delta function introduced by the charge density ensures conservation of energy and momentum. Indeed, one finds that in the non-relativistic limit the energy that the electron with initial velocity $\mathbf{v}$ transfers to the medium upon loosing momentum $\hbar\mathbf{k}$ is

$$\hbar\omega = \frac{|\mathbf{p}_e + \hbar\mathbf{k}|^2}{2m_e} - \frac{|\mathbf{p}_e|^2}{2m_e} = \hbar\mathbf{v}\cdot\mathbf{k} + \frac{\hbar^2}{2m_e}k^2, \tag{2.9}$$

with $\mathbf{p}_e = m_e\mathbf{v}$ the initial momentum of the fast electron and m_e the mass of the electron. By neglecting recoil of the incident electron, from Eq. (2.9)

one can obtain the so-called nonrecoil approximation where $\omega = \mathbf{k}\cdot\mathbf{v}$. Note that the z-component of the wavevector is fixed by $k_z = \omega/v$ when the electron travels in the z-direction.

To calculate the energy loss probability in the bulk, $\Gamma'_{\mathrm{bulk}}(\omega)$, experienced by the fast electron in anisotropic medium, we substitute Eq. (2.8) into Eq. (2.7). Notice that a fast electron traveling in vacuum loses no energy, thus we can use $\mathbf{E}_{\mathrm{tot}}(\mathbf{r};\omega)$ instead of $\mathbf{E}_{\mathrm{ind}}(\mathbf{r};\omega)$ in Eq. (2.7). Using the cylindrical symmetry of the field produced by the fast electron one finds that

$$\Gamma'_{\mathrm{bulk}}(\omega) = \int_0^{k_\perp^{\mathrm{c}}} \mathrm{d}k_\perp \, P_{\mathrm{bulk}}(k_\perp;\omega), \tag{2.10}$$

where

$$P_{\mathrm{bulk}}(k_\perp;\omega) = -\frac{2e^2 k_\perp v}{(2\pi)^3 \hbar c^2 \varepsilon_0 v_z} \int_0^{2\pi} \mathrm{d}\phi \, \mathrm{Im}\left[\hat{\mathbf{v}}\cdot\hat{\mathbb{G}}_{k_z}\cdot\hat{\mathbf{v}}\right], \tag{2.11}$$

is the probability for the electron to transfer a transverse momentum $\hbar k_\perp$ (to the electron trajectory) upon losing energy $\hbar\omega$. We will refer to this quantity as momentum-resolved energy loss probability. In Eq. (2.11) $\hat{\mathbb{G}}_{k_z} = \hat{\mathbb{G}}(k_\perp, \phi, k_z = \omega/v_z - \mathbf{k}_\perp\cdot\mathbf{v}/v_z)$, and ϕ is the angle between $\mathbf{k}_\perp$ and the k_x-axis, with $\hbar k_\perp^{\mathrm{c}}$ the maximum value of the modulus of perpendicular momentum of the electrons selected by the collection aperture of the EELS spectrometer. Particularly, when the electron beam trajectory points out in the same direction as the h-BN optical axis ($\mathbf{v} = v\hat{\mathbf{z}}$), expressions for $\mathbf{E}_{\mathrm{tot}}(\mathbf{r};\omega)$ and thus for $\Gamma'_{\mathrm{bulk}}(\omega)$ can be found in a closed form (see the box in the next page for the analytical formula of the Green's tensor in uniaxial anisotropic media):

$$\mathbf{E}_{\mathrm{tot}}(\mathbf{r};\omega) = \frac{e}{2\pi\varepsilon_0}\frac{\omega}{v^2\gamma_{\mathrm{L}}\varepsilon_\perp}\mathbf{g}(\mathbf{r};\omega), \tag{2.12}$$

where $\gamma_{\mathrm{L}} = 1/\sqrt{1 - v^2\varepsilon_\perp/c^2}$ is the Lorentz factor and

$$\begin{aligned}\mathbf{g}(\mathbf{r};\omega) = e^{i\omega z/v}\Bigg[&\frac{i}{\gamma_{\mathrm{L}}}K_0\left(\sqrt{\frac{\varepsilon_\parallel}{\varepsilon_\perp}}\frac{|\omega|}{\gamma_{\mathrm{L}}v}R\right)\hat{\mathbf{z}} \\ &- \mathrm{sgn}(\omega)\sqrt{\frac{\varepsilon_\parallel}{\varepsilon_\perp}}K_1\left(\sqrt{\frac{\varepsilon_\parallel}{\varepsilon_\perp}}\frac{|\omega|}{\gamma_{\mathrm{L}}v}R\right)\hat{\mathbf{R}}\Bigg],\end{aligned} \tag{2.13}$$

is written in cylindrical coordinates $\mathbf{r} = (\mathbf{R}, z) = (x, y, z)$, $R = \sqrt{x^2 + y^2}$, $K_0(x)$, $K_1(x)$ are the zero and first order modified Bessel functions of the second kind and sgn stands for the sign function.

Green's tensor decomposition in a uniaxial medium

The Green's tensor satisfying the wave equation [32, 128–130]

$$\nabla^2\hat{\mathbb{G}}(\mathbf{r};\omega) + k_0^2\,\hat{\varepsilon}\,\hat{\mathbb{G}}(\mathbf{r};\omega) - \nabla[\nabla\cdot\hat{\mathbb{G}}(\mathbf{r};\omega)] = \hat{\mathbb{I}}\,\delta(\mathbf{r}), \tag{2.14}$$

can be expressed in $(\mathbf{k},\omega)$ space as follows

$$\hat{\mathbb{G}}(\mathbf{k};\omega) = \left[\mathbf{k}\otimes\mathbf{k} - k^2\,\hat{\mathbb{I}} + k_0^2\,\hat{\varepsilon}\right]^{-1}. \tag{2.15}$$

From Eq. (2.15) one can deduce that the inverse of the Green's tensor for a uniaxial medium can be decomposed in the form $\hat{\mathbb{G}}^{-1} = (k_0^2\varepsilon_\perp - k^2)\,\hat{\mathbb{I}} + \mathbf{k}\otimes\mathbf{k} + k_0^2(\varepsilon_\parallel - \varepsilon_\perp)\,\hat{\mathbf{z}}\otimes\hat{\mathbf{z}}$ where $\varepsilon_\perp = \varepsilon_x = \varepsilon_y$ and $\varepsilon_\parallel = \varepsilon_z$. This tensor decomposition allows us to find the following expression for $\hat{\mathbb{G}}(\mathbf{k};\omega)$ [126, 127]:

$$\begin{aligned}\hat{\mathbb{G}}(\mathbf{k};\omega) = \frac{1}{k_0^2\varepsilon_\parallel\varepsilon_\perp - \mathbf{k}\cdot\hat{\varepsilon}\cdot\mathbf{k}}\Bigg[&\varepsilon_\parallel\hat{\mathbb{I}} - (\varepsilon_\parallel-\varepsilon_\perp)\hat{\mathbf{z}}\otimes\hat{\mathbf{z}} \\ &-\frac{\mathbf{k}\otimes\mathbf{k}}{k_0^2} + \frac{\varepsilon_\parallel-\varepsilon_\perp}{k_0^2\varepsilon_\perp - k^2}(\mathbf{k}\times\hat{\mathbf{z}})\otimes(\mathbf{k}\times\hat{\mathbf{z}})\Bigg],\end{aligned} \tag{2.16}$$

where we used that the inverse of the Green's tensor can be obtained as $\hat{\mathbb{G}}^{-1} = \mathrm{adj}[\hat{\mathbb{G}}]/\det[\hat{\mathbb{G}}]$, with $\mathrm{adj}[\hat{\mathbb{G}}]$ the adjoint of $\hat{\mathbb{G}}$.

The momentum-resolved energy loss probability becomes

$$\begin{aligned}P_{\mathrm{bulk}}(k_\perp;\omega) = -\frac{2e^2}{(2\pi)^2\omega^2\hbar\varepsilon_0}\mathrm{Im}\Bigg\{&\left[k_0^2\varepsilon_\perp - \frac{\omega^2}{v^2}\right] \\ &\times\frac{k_\perp}{\varepsilon_\parallel[\varepsilon_\perp k_0^2 - \omega^2/v^2] - \varepsilon_\perp k_\perp^2}\Bigg\},\end{aligned} \tag{2.17}$$

and, substituting Eq. (2.17) into Eq. (2.10), one finds that

$$\begin{aligned}\Gamma'_{\mathrm{bulk}}(\omega) = \frac{e^2}{(2\pi)^2\omega^2\hbar\varepsilon_0}\mathrm{Im}\Bigg\{&\left[k_0^2 - \frac{\omega^2}{\varepsilon_\perp v^2}\right] \\ &\times\ln\left[\frac{\varepsilon_\parallel\varepsilon_\perp k_0^2 - \varepsilon_\parallel\omega^2/v^2 - \varepsilon_\perp(k_\perp^c)^2}{\varepsilon_\parallel\varepsilon_\perp k_0^2 - \varepsilon_\parallel\omega^2/v^2}\right]\Bigg\}.\end{aligned} \tag{2.18}$$

The non-retarded versions of $P_{\mathrm{bulk}}(k_\perp;\omega)$ and $\Gamma'_{\mathrm{bulk}}(\omega)$ can be obtained by setting k_0 equal to zero in Eqs. (2.17) and (2.18).

The spectrum of the momentum-resolved energy loss probability and the

EEL probability provide valuable information which reveals the properties of the modes of the anisotropic material. We thus explore in the following the connection between the dispersion relation of the h-BN excitations in the upper Reststrahlen band with these two quantities.

2.3.3 Excitation in the upper Reststrahlen band

In the following we address the electron energy losses in h-BN and the connection of these losses with the isofrequency surfaces of the material. We first show in Fig. 2.3a the isofrequency curve of a h-BN phonon polariton for an energy in the upper Reststrahlen band (red curve). We chose 195 meV as a representative value of this band. When a fast electron beam is used to probe these excitations in the medium, the velocity of the electron determines the momentum transfer, as $\mathbf{k} \cdot \mathbf{v} = \omega$ (Eq. (2.9) in the nonrecoil approximation). If the electron is traveling along the z-direction, then $k_z = \omega/v$ (blue horizontal line in Fig. 2.3a). Following Eq. (2.5), this also sets the value of the $\hbar k_\perp$ momentum component ($k_\perp^2 = \varepsilon_\parallel k_0^2 - \varepsilon_\parallel k_z^2/\varepsilon_\perp$) of the excited phonon polariton.

The intersections between $k_z = \omega/v$ and the isofrequency curves in the upper Reststrahlen band establish a relationship between the energy $\hbar\omega$ of the hyperbolic phonon polariton and its perpendicular momentum component $\hbar k_\perp$. In the left panel of Fig. 2.3b we plot this relationship (blue dashed line) and the momentum-resolved energy loss probability $P_{\text{bulk}}(k_\perp;\omega)$ (light blue-yellow contour plot) for $v = 0.1c$. We note that the highest values of $P_{\text{bulk}}(k_\perp;\omega)$ coincide with the blue dashed line and its asymptotic behavior approaches the $\text{LO}_\perp$ phonon energy for large $k_\perp$. This demonstrates that electron energy losses in the upper band are due to phonon polariton excitations. We confirm this by integrating $P_{\text{bulk}}(k_\perp;\omega)$ over $k_\perp$ up to a cutoff momentum $\hbar k_\perp^c$, which yields the EEL probability $\Gamma'_{\text{bulk}}(\omega)$ (right panel of Fig. 2.3b). A clear peak can be observed at the longitudinal optical phonon. This energy loss peak is slightly asymmetric with a broader tail inside the Reststrahlen band compared to that outside the band. Importantly, at energies above the $\text{LO}_\perp$ phonon energy no losses are found. This can be understood with the help of the isofrecuency curves in Fig. 2.3a. For instance, at energy 205 meV (black dashed line, above the upper Reststrahlen band) the ellipse does not intersect the blue horizontal line and therefore there is no excitation above the upper band. For energies below the $\text{TO}_\perp$ phonon energy, the ellipses may intersect or not the blue horizontal line of k_z depending on the particular energy. For instance, at an energy of 160 meV (green dashed line, below the upper Reststrahlen band in Fig. 2.3a) the ellipse does not cut $k_z = \omega/(0.1c)$ and therefore there is no excitation in-

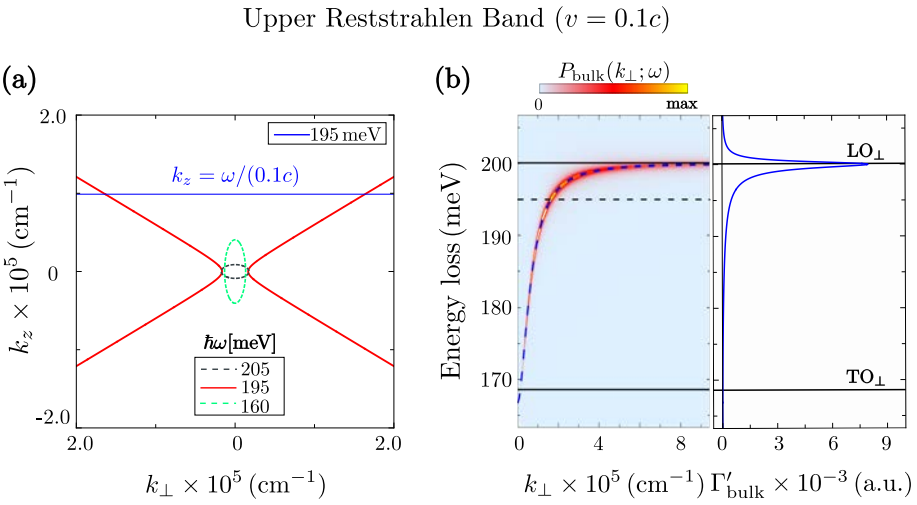

Figure 2.3: Excitation of hyperbolic PhPs in the Upper Restrahlen band. (a) Isofrequency curves for energies inside (195 meV, red solid line) and outside (160 meV and 205 meV, green and black dashed lines) the upper Reststrahlen band plotted for the wavevector k_z versus $k_\perp = \sqrt{k_x^2 + k_y^2}$. The horizontal blue line represents the momentum $\hbar k_z = \hbar\omega/(0.1c)$ transferred by the fast electron to the polaritons when it travels along the z-direction with $v = 0.1c$. The blue line is evaluated at energy 195 meV (caption at the top right of the figure). The contour plot (left panel) in (b) shows the momentum-resolved energy loss probability $P_{\rm bulk}(k_\perp;\omega)$ normalized to the maximum value (3 a.u.) for $v = 0.1c$. The right panel in (b) shows the energy loss probability $\Gamma'_{\rm bulk}(\omega)$ obtained by integrating $P_{\rm bulk}(k_\perp;\omega)$ over $k_\perp$ up to $k_\perp^c = 0.05\,\text{Å}^{-1}$. LO$_\perp$ and TO$_\perp$ label the position of the energy of the LO$_\perp$ and TO$_\perp$ phonon energies, respectively.

duced in that case. However, for other energies the isofrequency surfaces can cut the k_z line, and therefore an anisotropic dielectric mode can be excited (tail below 170 meV in Fig. 2.3b). We learn from this analysis that the excitation of the phonon polariton modes close to the upper Reststrahlen band is highly dependent on the topology (hyperbolic or elliptic) of the isofrequency surfaces.

The dependency of phonon polariton excitation on the isofrequency surface allows to control the polaritonic modes as we discuss now in Fig. 2.4b, where we show the real part of the z-component of the total electric field at $\hbar\omega = 195$ meV (representing the energy within the hyperbolic dispersion regime in the upper Reststrahlen band), induced by a fast electron with velocity $v = 0.1c$. A schematic representation of such electron beam trajectory is displayed in the inset of Fig. 2.4b. We observe two important features: the formation of a wake pattern and an oscillatory behavior of the field in the z-direction. This spatial periodicity is connected with the parallel momentum component ($\hbar k_z = \hbar\omega/v$) transferred by the electron since the observed wavelength along the z-axis is

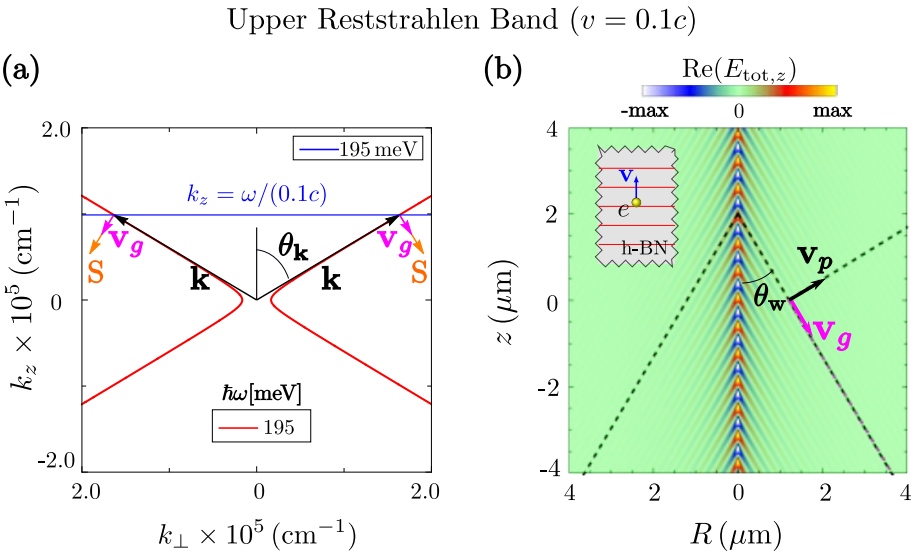

Figure 2.4: Propagation of hyperbolic PhPs in the Upper Restrahlen band. (a) Isofrequency curve for the energy 195 meV (red solid line, same isofrequency curve as in Fig. 2.3a). The black arrows represent the polariton wavevector $\mathbf{k}(\omega)$, $\theta_\mathbf{k}$ is the angle between $\mathbf{k}(\omega)$ and the k_z-axis, the magenta arrows represent the group velocity $\mathbf{v}_g$ and the orange arrows the Poynting vector $\mathbf{S}$. The contour plot in panel (b) depicts the real part of the z-component of the total electric field induced by the fast electron along the cylindrical coordinates (R, z) for an energy of 195 meV. The field plot is normalized to the maximum value 1×10^{-5} a.u. The black arrow in panel (b) represents the phase velocity $\mathbf{v}_p$ (parallel to $\mathbf{k}(\omega)$), and θ_w is the angle between the wake patterns and electron beam trajectory. The inset in (b) illustrates the electron beam trajectory and orientation of the h-BN crystal planes.

$\lambda_z = 2\pi/k_z$. This implies that the wavelength λ_z decreases with increasing energy of the phonon polariton. Furthermore, the direction of the wake pattern is governed by the polariton phase velocity ($\mathbf{v}_p$ parallel to $\mathbf{k}(\omega)$, black arrow).

The outward direction (relative to the electron beam trajectory) of the wavefronts is determined by the sign of the radial component of $\mathbf{v}_p$ relative to the radial component of the energy flow (given by the Poynting vector $\mathbf{S} = \mathbf{E} \times \mathbf{H}$ parallel to the group velocity $\mathbf{v}_g = \nabla_\mathbf{k}\omega$ [67, 131–134], magenta arrow). We recognize in Fig. 2.4a that the group and the phase velocities are nearly perpendicular, and their projection onto the radial axis are parallel, leading to a wave propagating away from the electron beam trajectory (positive phase and positive group velocity with respect to the energy propagation direction). It is worth noting that the projection of the group and the phase velocities onto the beam trajectory direction (z-direction) leads to negative phase and positive group velocities relative to S_z (Fig. 2.4b).

Changing the velocity of the electron

As pointed out, for each energy $\hbar\omega$, the velocity of the fast electron determines (primarily) the polariton wavevector parallel to the beam trajectory, k_z, and consequently the perpendicular wavevector $k_\perp$ (according to Eq. (2.5)). To emphasize the velocity dependency, we perform the same analysis (Fig. 2.5a-b) as in Fig. 2.3a-b but increasing the electron velocity to $v = 0.5c$. In Fig. 2.5a a zoom into the isofrequency curve of Fig. 2.3a is presented, together with the value k_z (horizontal blue line) determined by the electron velocity $v = 0.5c$. The increase of the electron velocity leads to the excitation of 195 meV polaritons with reduced momentum (determined by the intersection of the blue horizontal line and the red isofrequency curve). By calculating the momentum-resolved energy loss probability $P_{\text{bulk}}(k_\perp;\omega)$ (left panel of Fig. 2.5b) and the EEL probability $\Gamma'_{\text{bulk}}(\omega)$ (right panel of Fig 2.5b) we find the same behavior as in Fig. 2.3b for $v = 0.1c$, except for a one order of magnitude reduction in both $k_\perp$ and the magnitude of the energy loss probability.

The differences in the properties of the phonon polaritons launched by the fast electron at both electron velocities are distinguishable in Figs. 2.5d, where we show the real part of the z-component of the total electric field induced by the fast electron with $v = 0.5c$ at energy 195 meV. The spatial period λ_z of the polariton is longer compared to that in Fig. 2.4b as a result of the increase in the electron velocity (smaller $\hbar k_z$ transferred). The direction of the wake field is quite similar to that of panel 2.4b. This behavior is a specific feature of hyperbolic polaritons since the intersection of the blue line both for $v = 0.1c$ and $v = 0.5c$ occur at the asymptote of the hyperbola (compare Figs. 2.4a and 2.5c) which results in polariton wavevectors that have very similar propagation direction but different absolute values.

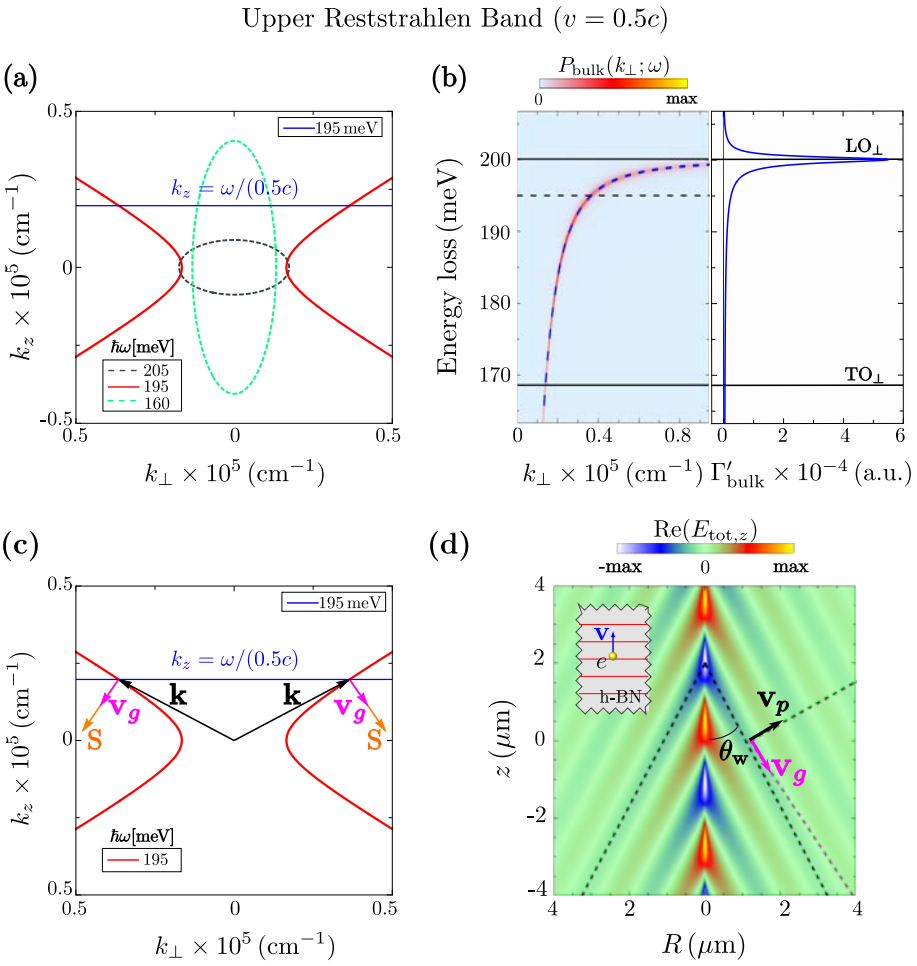

Figure 2.5: Excitation and propagation of hyperbolic PhPs in the Upper Restrahlen band for an electron traveling with velocity $v = 0.5c$. Panel (a) shows a zoom into Fig. 2.3a. The horizontal blue line represents the momentum $\hbar k_z = \hbar\omega/(0.5c)$ transferred by the fast electron to the polaritons when it travels along the z-direction with $v = 0.5c$. The blue line is evaluated at energy 195 meV (caption at the top right of the figure). The contour plot (left panel) in (b) shows the momentum-resolved energy loss probability $P_{\mathrm{bulk}}(k_\perp;\omega)$ normalized to the maximum value (3 a.u.) for $v = 0.5c$. The right panel in (b) shows the energy loss probability $\Gamma'_{\mathrm{bulk}}(\omega)$ obtained by integrating $P_{\mathrm{bulk}}(k_\perp;\omega)$ over $k_\perp$ up to $k_\perp^c = 0.05\,\text{Å}^{-1}$. LO$_\perp$ and TO$_\perp$ label the position of the energy of the LO$_\perp$ and TO$_\perp$ phonon energies, respectively. Panel (c) shows a zoom into Fig. 2.4a. The contour plot in panel (d) depicts the real part of the z-component of the total electric field induced by the fast electron along the cylindrical coordinates (R, z) for an energy of 195 meV. The field plot is normalized to the maximum value 7.5×10^{-7} a.u. The black arrow represents the phase velocity $\mathbf{v}_p$ (parallel to $\mathbf{k}(\omega)$), and θ_{w} is the angle between the wake patterns and electron beam trajectory.

2.3.4 Excitation in the lower Reststrahlen band

In Fig. 2.6a we show the isofrequency curve of h-BN phonon polaritons for an energy in the lower Reststrahlen band (red line). Note that the hyperbolas are rotated by 90° as compared to the upper Reststrahlen band (see Fig. 2.3a and 2.6a). However, the momentum $\hbar k_z$ transferred by the fast electron to the phonon polaritons is still given by the crossing of the hyperbolas with the horizontal blue line (representing $k_z = \omega/v$ for $v = 0.1c$ in Fig. 2.6a). From Eq. (2.5) we obtain the polariton perpendicular momentum $\hbar k_\perp$, which is shown in the left panel of Fig. 2.6b as a function of energy $\hbar\omega$ (dashed blue curve). We also plot the momentum-resolved energy loss probability $P_{\text{bulk}}(k_\perp;\omega)$ for energies within the lower Reststrahlen band. Notice that the highest values of $P_{\text{bulk}}(k_\perp;\omega)$ (red and yellow colors in the contour plot) coincide perfectly with the blue dashed curve, demonstrating that the electron energy losses in the lower band are also governed by polariton excitations. However, in contrast to the upper band, we find that the dashed blue curve has a negative slope, $\mathrm{d}\omega/\mathrm{d}k_\perp < 0$, indicating that the group and the phase velocities are antiparallel (have opposite sign) along the radial direction. We will show below with the information of the total field distribution in Fig. 2.8b that the phase velocity in the radial direction is indeed antiparallel (negative) relative to the Poynting vector (energy flow) while the group velocity in the radial direction is parallel (positive), which is a consequence of the phase and group velocity vectors being perpendicular to each other and rotated by 90° degrees as compared to their configuration in the upper Reststrahlen band.

To obtain spectroscopic information on the excitations in the lower Reststrahlen band, we calculate the EEL probability $\Gamma'_{\text{bulk}}(\omega)$ by integration of $P_{\text{bulk}}(k_\perp;\omega)$ in momentum space (right panel in Fig. 2.6b). Contrary to the case in the upper Reststrahlen band, we observe a uniform and relatively small loss probability between the $\text{TO}_\parallel$ and $\text{LO}_\parallel$ phonon energies without the appearance of a sharp peak around the $\text{LO}_\parallel$ phonon energy. We explain this finding by (i) the large cutoff momenta ($\hbar k_\perp^c$) imposed by the aperture of the microscope detector and (ii) the relationship between the energy and the transverse momentum of the polaritons in the lower band (see Fig. 2.6b left panel). Indeed, we observe in Fig. 2.6b that the asymptotic behavior of the blue dashed line tends to the $\text{TO}_\parallel$ phonon energy for large $k_\perp$. This shows that low energy hyperbolic phonon polaritons, close to $\text{TO}_\parallel$, largely contribute to the energy losses for large $k_\perp^c$ values. Contrary to the case in the upper band, where the high momenta contribution to the electron energy losses comes from polaritons with high energy, close to the $\text{LO}_\perp$ phonon energy (Fig. 2.3b, left panel).

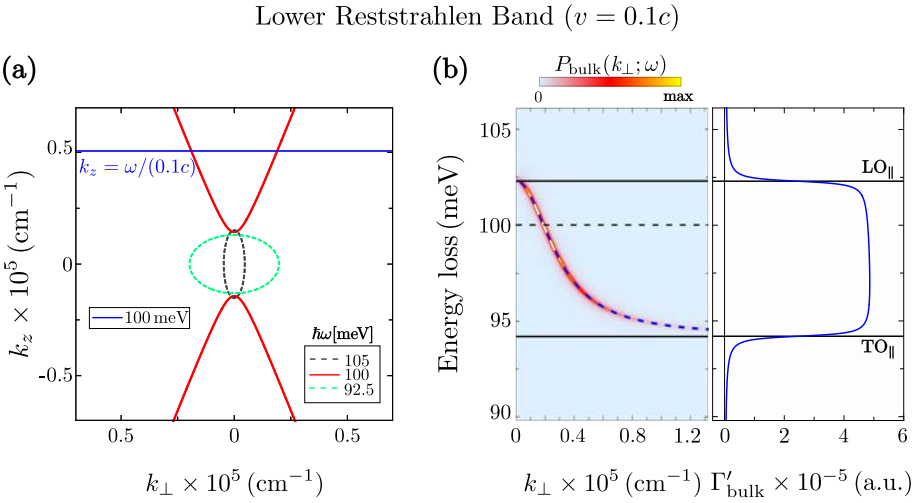

Figure 2.6: Excitation of hyperbolic PhPs in the Lower Restrahlen band. (a) Isofrequency curves for energies inside (100 meV, red solid line) and outside (92.5 meV and 105 meV, green and black dashed lines) the lower Reststrahlen band plotted for the wavevector k_z against $k_\perp = \sqrt{k_x^2 + k_y^2}$. The horizontal blue line represents the momentum $\hbar k_z = \hbar\omega/(0.1c)$ transferred by the fast electron to the polaritons when it travels along the z-direction with velocity $0.1c$. The blue line is evaluated at energy 100 meV. The contour plot (left panel) in (b) shows the momentum-resolved energy loss probability $P_{\rm bulk}(k_\perp;\omega)$ normalized to the maximum value (3 a.u) for $v = 0.1c$. The right panel in (b) shows the energy loss probability $\Gamma'_{\rm bulk}(\omega)$ obtained by integrating $P_{\rm bulk}(k_\perp;\omega)$ over $k_\perp$ up to $k_\perp^c = 0.05$ Å^{-1}. LO$_\parallel$ and TO$_\parallel$ label the position of the energy of the LO$_\parallel$ and TO$_\parallel$ phonon energies, respectively.

To better understand the loss probability in the lower Reststrahlen band as a function of the cutoff momenta $\hbar k_\perp^c$, we show in Figs. 2.7a-d the EEL probability ($\Gamma'_{\rm bulk}(\omega)$, given by Eq. (2.18)) in the vicinity of the lower Reststrahlen band for different cutoff values $k_\perp^c$: (a) 1×10^{-2} Å^{-1}, (b) 1×10^{-3} Å^{-1}, (c) 1×10^{-4} Å^{-1} and (d) 1×10^{-5} Å^{-1}. For the calculation of $\Gamma'_{\rm bulk}(\omega)$ we consider $v = 0.1c$. One can observe that for small cutoff momentum the EEL probability at the LO$_\parallel$ phonon energy is better defined, whereas for large cutoff momenta the sharp peak in Fig. 2.7 broadens. However, cutoff values of 1×10^{-4} Å^{-4} or $\times 10^{-4}$ Å^{-5} are not experimentally feasible, and thus the identification of the LO$_\parallel$ phonon in EELS would be difficult in this configuration.

The excitation of phonon polaritons (within the lower Reststrahlen band) by the probing electron can be observed in Fig. 2.8b, where we show the real part of the z-component of the total electric field induced at energy $\hbar\omega = 100$ meV. Analogously to the upper band, the oscillatory behavior of the field distribution along the z-direction is governed by the transferred momentum $\hbar k_z$. Interest-

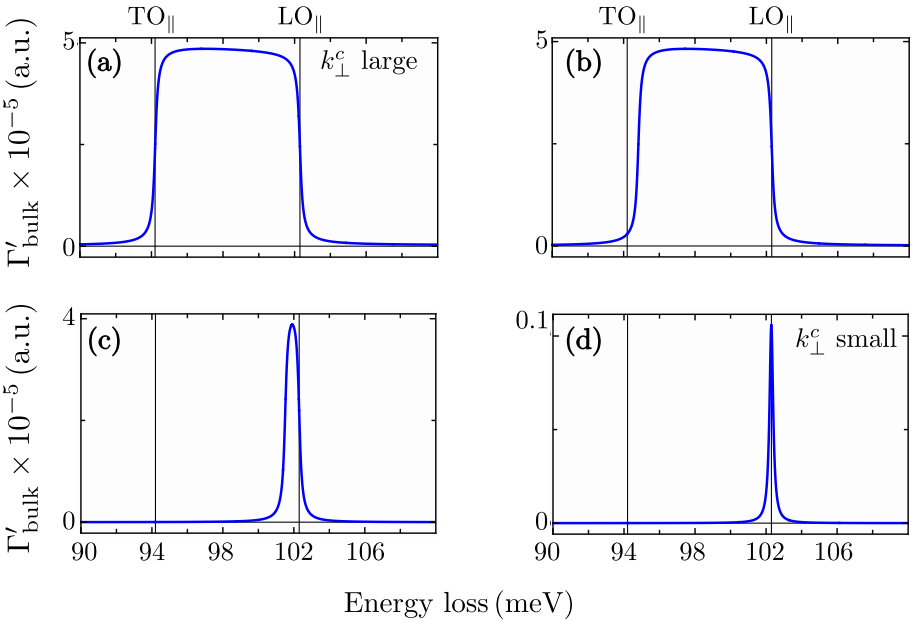

Figure 2.7: Electron energy-loss probability for different cutoff momenta $\hbar k_\perp^c$. Electron energy loss probability, $\Gamma'_{\text{bulk}}(\omega)$, for energies around the lower Reststrahlen band for four different $k_\perp^c$: (a) 1×10^{-2} Å^{-1}, (b) 1×10^{-3} Å^{-1}, (c) 1×10^{-4} Å^{-1} and (d) 1×10^{-5} Å^{-1}. The electron travels through h-BN parallel to the optical axis with velocity $v = 0.1c$.

ingly, the wake pattern is reversed compared to that in the upper Reststrahlen band (compare Figs. 2.4b and 2.8b), i.e., the wavefronts are propagating toward the electron beam [132, 135, 136]. By plotting the group and phase velocity vectors onto the field plots (magenta and black arrows, respectively; also plotted in Fig. 2.8a), we can clearly recognize that the projections of both vectors onto the radial axis (perpendicular to the electron beam trajectory) are antiparallel. This leads to a negative phase and positive group velocity relative to the Poynting vector direction (which points always away from the electron beam to preserve causality) along the radial axis. The negative phase velocity in the radial direction is a direct result of the phase velocity vector being nearly perpendicular to the Poynting vector, both being rotated by 90° as compared to the upper Reststrahlen band (where both phase and group velocities are positive relative to energy propagation in the radial direction, see Figs. 2.4b and 2.5d).

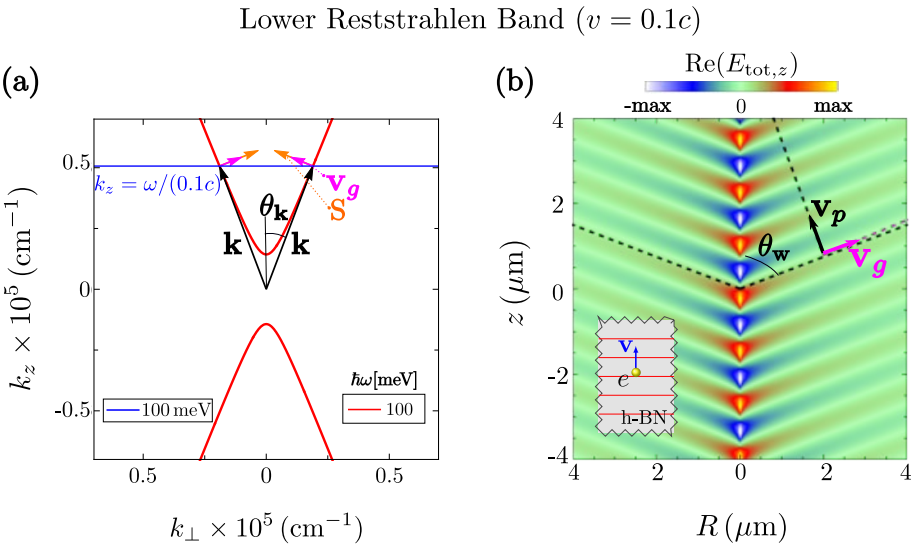

Figure 2.8: Propagation of hyperbolic PhPs in the Lower Restrahlen band. (a) Isofrequency curve for energy 100 meV (red solid line, same isofrequency curve as in Fig. 2.6a). The black arrows represent the polariton wavevector $\mathbf{k}(\omega)$, $\theta_{\mathbf{k}}$ is the angle between $\mathbf{k}(\omega)$ and the k_z-axis, the magenta arrows represent the group velocity $\mathbf{v}_g$ and the orange arrows the Poynting vector $\mathbf{S}$. The contour plot in panel (b) depicts the real part of the z-component of the total electric field induced by the fast electron along the cylindrical coordinates (R, z) for an energy of 100 meV. The field plot is normalized to the maximum value 1×10^{-6} a.u. The black arrow represents the phase velocity $\mathbf{v}_p$ (parallel to $\mathbf{k}(\omega)$), and θ_{w} is the angle between the wake patterns and electron beam trajectory. The inset in (b) illustrates the electron beam trajectory and orientation of the h-BN crystal planes.

Changing the velocity of the electron

When the velocity of the electron is increased up to 50 % the speed of light, the k_z component of the wavevector parallel to the beam trajectory is reduced. In this case, the matching between the red hyperbola and the horizontal blue line is prevented as observed in Fig. 2.9a. This mismatch of energy and momentum forbids the excitation of hyperbolic phonon polaritons. However, the blue line intersects the elliptical isofrequency surface of anisotropic bulk phonon polaritons (dielectric) above and below the lower Reststrahlen band (black and green dashed curves calculated for 105 meV and 92.5 meV, respectively). The matching of energy and momentum at the intersections of the elliptical isofrequency surfaces leads to the excitation of the dielectric modes, as demonstrated by calculating the momentum-resolved energy loss probability $P_{\mathrm{bulk}}(k_\perp; \omega)$ (left panel of Fig. 2.9b).

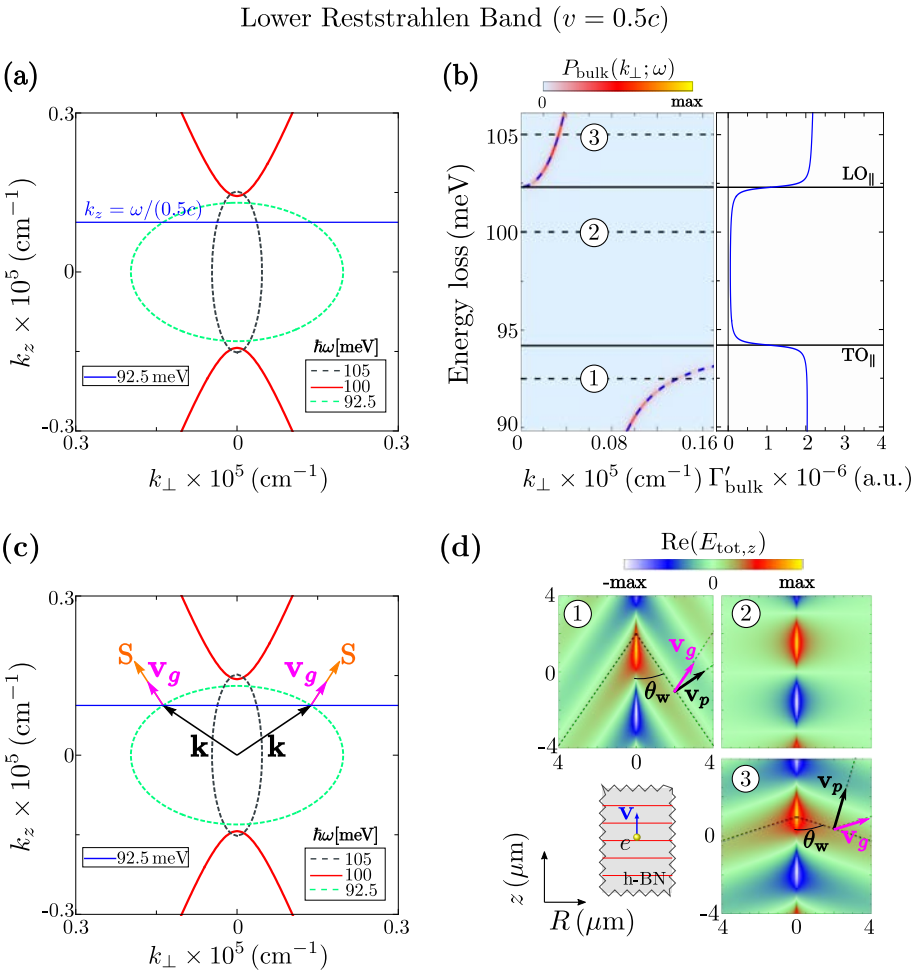

Figure 2.9: Excitation and propagation of hyperbolic PhPs in the Lower Restrahlen band for an electron traveling with velocity $v = 0.5c$. Panel (a) shows a zoom into Fig. 2.6a. The horizontal blue line represents the momentum $\hbar k_z = \hbar\omega/(0.5c)$ transferred by the fast electron to the polaritons when it travels along the z-direction with $v = 0.5c$. The blue line is evaluated at energy 92.5 meV (caption at the bottom left of the figure). The contour plot (left panel) in (b) shows the momentum-resolved energy loss probability $P_{\rm bulk}(k_\perp;\omega)$ normalized to the maximum value (2.5 a.u.) for $v = 0.5c$. The right panel in (b) shows the energy loss probability $\Gamma'_{\rm bulk}(\omega)$ obtained by integrating $P_{\rm bulk}(k_\perp;\omega)$ over $k_\perp$ up to $k_\perp^c = 0.05$ Å^{-1}. LO$_\parallel$ and TO$_\parallel$ label the position of the energy of the LO$_\parallel$ and TO$_\parallel$ phonon energies, respectively. Panel (c) shows a zoom into Fig. 2.8a with the blue line evaluated at an energy of 92.5 meV. The contour plot in panel (d) depicts the real part of the z-component of the total electric field induced by the fast electron along the cylindrical coordinates (R, z) for the energies: 92.5 meV (labeled as 1), 100 meV (labeled as 2) and 105 meV (labeled as 3). The field plots are normalized to the maximum value 7.5×10^{-8} a.u. The black arrow represents the phase velocity $\mathbf{v}_p$ (parallel to $\mathbf{k}(\omega)$), and $\theta_{\rm w}$ is the angle between the wake patterns and electron beam trajectory. The inset in (d) illustrates the electron beam trajectory.

This energy loss probability is determined by the relationship between the energy of the elliptical polaritons and the perpendicular momentum component (dashed blue lines, showing $\omega(k_\perp)$ of the elliptical polaritons). The integration of $P_{\text{bulk}}(k_\perp;\omega)$ in the reciprocal space subsequently yields small energy loss probabilities outside the Reststrahlen band, whereas inside the Reststrahlen band the loss probability is negligible due to absence of polariton excitations.

In Fig. 2.9d we show the z-component of the total electric field induced by the electron beam for energies inside (marked 2) and outside (marked 1 and 3) the lower Reststrahlen band. We can observe the formation of wake patterns only for those energies where the dielectric modes are excited (marked as 1 and 3). Importantly, the wake wavefronts propagate outward the beam trajectory as a consequence of the group ($\mathbf{v}_g$) and phase velocities ($\mathbf{v}_p$ parallel to $\mathbf{k}(\omega)$) being parallel (positive) relative to the Poyting vector in the radial direction (Figs. 2.9c and 2.9d). We can also notice that the projection of these velocity vectors onto the z-direction is positive. This demonstrates that the radial and z projections of $\mathbf{v}_p$ and $\mathbf{v}_g$ for elliptical polaritons are positive, contrary to the hyperbolic regime (Reststrahlen bands) where one of the components of either $\mathbf{v}_p$ or $\mathbf{v}_g$, is negative (Figs. 2.4b, 2.5d and 2.8b).

2.3.5 Induced wake patterns and Cherenkov radiation

We have shown in Subsections 2.3.3 (Figs. 2.4b and 2.5d) and 2.3.4 (Figs. 2.8b and 2.9d) that the field distributions produced by a fast electron traveling through h-BN can exhibit wake patterns. The excitation of these patterns (for energies inside and outside the Reststrahlen bands) is connected to the different mechanisms of energy losses experienced by the fast electron in the h-BN. In the following we discuss this connection.

First, it is worth noting that the excitation of the wake fields inside the Reststrahlen bands occurs in cases where electron energy losses appear (compare Fig. 2.8b with the image in Fig. 2.9d labeled as 2). As we pointed out, the electron energy losses within the Reststrahlen bands correspond to the excitation of hyperbolic phonon polaritons. This implies that the wake fields are associated with the excitation of coherent-charge density fluctuations [136–141] in the h-BN, namely, phonon polaritons.

In contrast to the wake fields inside the Reststrahlen bands, the emergence of the wake patterns outside the bands (see Fig. 2.9d, images labeled as 1 and 3) occur due to a different physical process as compared to that of the excitation of hyperbolic phonon polaritons. Outside the Reststrahlen bands the h-BN permittivity is purely dielectric and thus the electron energy losses correspond

to the radiation emitted by the electron when it passes through the medium with velocity larger than the speed of light (in the h-BN). This mechanism is known as Vavilov-Cherenkov radiation (see Chapter 1). We have confirmed that the losses in this energy range are present even in the absence of damping in the material (not shown), confirming that the losses are due to Cherenkov radiation in this case. This only happens for electron velocities which fulfill

$$v > \frac{c}{\sqrt{\varepsilon_\perp}}, \tag{2.19}$$

being consistent with the condition for excitation of Cherenkov radiation [142, 143].

Finally, one can also note that the excitation of the wake fields in the lower Reststrahlen band depends on the electron velocity (compare Figs. 2.8b and 2.9d label 2). Indeed, for energies in the lower band one can deduce from Eqs. (2.12)-(2.13) that the wake patterns appear under the following condition:

$$\frac{\varepsilon_\parallel}{\varepsilon_\perp} < \frac{v^2}{c^2}\varepsilon_\parallel \text{ or equivalently } v < \frac{c}{\sqrt{\varepsilon_\perp}}, \tag{2.20}$$

where only the real part of the dielectric function is considered. Interestingly, one can observe that the velocity of the fast electron fulfills different conditions for the appearance of wake patterns in different energy ranges (compare Eqs. (2.19) and (2.20)). This difference is a direct consequence of the distinct physical processes in the excitation of the wake fields.

The different nature of the excitation of the wake fields outside and inside the Reststrahlen bands is also reflected in the angle $\theta_w = 90° - \theta_{\mathbf{k}}$ that the wake patterns sustain with respect to the electron beam trajectory. An analysis of this angle and its relationship with the electron beam trajectory is discussed in the following subsection.

2.3.6 Tilted electron beam trajectory

When the electron travels at an angle α relative to the h-BN optical axis (illustrated in Fig. 2.10), the condition for the conservation of energy and momentum given by Eq. (2.9) in the nonrecoil approximation ($\mathbf{k}\cdot\mathbf{v} = k_y v_y + k_z v_z = \omega$) is represented by an inclined plane in momentum space. The magnitude of the momentum transferred by the electron to the phonon polaritons (along the beam trajectory given by $\hat{\mathbf{v}}$) is still given by $\hbar k_{\hat{\mathbf{v}}} = \hbar\omega/v$ and the polariton wavevector can be obtained from the intersection between the plane $\mathbf{k}\cdot\mathbf{v} = \omega$ and the isofrequency surfaces.

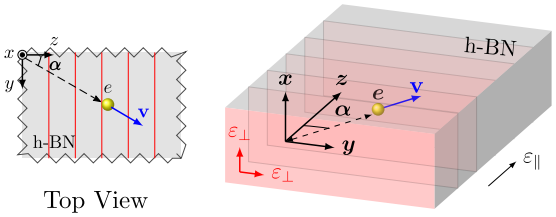

Figure 2.10: Electron traveling at an angle α relative to the h-BN optical axis. Schematics of the electron traveling through h-BN with velocity $\mathbf{v} = v(0, \sin\alpha, \cos\alpha)$ at an angle α with respect to the optical (z)-axis of h-BN.

In Fig. 2.11 we show the intersection between the h-BN isofrequency hyperboloids (red surfaces, Figs. 2.11a and 2.11c) and the plane $\mathbf{k}\cdot\mathbf{v} = \omega$ determined by the electron beam trajectory (blue surfaces, Figs. 2.11a and 2.11c). Notice that the direction of the electron beam trajectory is orthogonal to the blue plane $\mathbf{k}\cdot\mathbf{v} = \omega$. We analyze an electron beam with velocity $v = 0.1c$ and a trajectory angle of $\alpha = 20°$. Finally we chose two representative energies, one in the upper Reststrahlen band at 180 meV (Fig. 2.11a) and the other one in the lower Reststrahlen band at 100 meV (Fig. 2.11c). The gray 2D plots in Figs. 2.11b and 2.11d show the intersection between the red hyperboloid and the blue plane along four different directions determined by the the azimuthal angle of the symmetry axis ϕ: 0°, 60°, 90° and 150°. In the 2D projections the blue dashed lines depict the electron beam trajectory, as viewed from the direction determined by ϕ. The polariton wavevector along each particular direction can be obtained from the intersection between the blue lines and the red hyperbolas. Interestingly, we observe that the intersections are not cylindrically symmetric with respect to the z-axis (Figs. 2.11b and 2.11d). This implies that the polaritonic wave will propagate asymmetrically with respect to the electron beam trajectory. Indeed, depending on the direction of propagation, the intersection between the blue planes and the red hyperboloids in Figs. 2.11a and 2.11c will occur at wavevectors whose z-component can be the same (symmetrical case) or different (asymmetrical case). In the following, we analyze in detail these cases.

The propagation of the polaritonic wave is governed by its phase velocity and thus, by the polariton wavevector $\mathbf{k}(\omega) = (k_x, k_y, k_z)$ which fulfills Eq. (2.5). When the hyperbolic phonon polaritons are excited by an electron beam, the components of $\mathbf{k}(\omega)$ also need to fulfill Eq. (2.9), that is, the components of

$\mathbf{k}(\omega)$ can be obtained from the following two expressions

$$\frac{k_x^2 + k_y^2}{\varepsilon_\parallel} + \frac{k_z^2}{\varepsilon_\perp} = k_0^2, \tag{2.21a}$$

$$k_y \sin\alpha + k_z \cos\alpha = \omega/v, \tag{2.21b}$$

where we assume that the electron velocity is $\mathbf{v} = v(0, \sin\alpha, \cos\alpha)$. Moreover, if we decompose $\mathbf{k}(\omega)$ in cylindrical coordinates as $\mathbf{k}(\omega) = (q\cos\phi, q\sin\phi, k_z)$, and substitute it into Eqs. (2.21a) and (2.21b), we obtain the following system of equations

$$\frac{q^2}{\varepsilon_\parallel} + \frac{k_z^2}{\varepsilon_\perp} = k_0^2, \tag{2.22a}$$

$$q\sin\phi\sin\alpha + k_z\cos\alpha = \omega/v, \tag{2.22b}$$

for q, ϕ and k_z. Notice that the variable q corresponds to $k_\perp$ for trajectories parallel to the h-BN optical axis. However, for the oblique trajectory $\hbar\mathbf{q} = (\hbar k_x, \hbar k_y)$ is no longer orthogonal to the beam trajectory and thus we avoid referring to it as the transverse momentum. One can deduce that the solutions from Eqs. (2.22a) and (2.22b) will show cylindrical symmetry (symmetric with respect to the k_z-axis) when $\alpha = 0°$.

For cases where $\alpha \neq 0°$, this symmetry is broken and the solutions depend on the azimuthal angle ϕ. This dependency is shown in the 2D projections of the relevant curves in Figs. 2.11b and 2.11d, where one recognizes the following:

1. The intersection between the blue line and the red hyperbola is asymmetric with respect to the k_z-axis for $\phi \in (0°, 180°)$, as we observe in Figs. 2.11b and 2.11d for $\phi = 60°$, $90°$, $150°$.

2. The direction of largest asymmetry occurs at $\phi = 90°$ ($k_y k_z$-plane) and the direction of symmetric propagation occurs at $\phi = 0°$ ($k_x k_z$-plane).

3. The intersections between the blue lines and the red hyperbolas are also asymmetric (or symmetric) with respect to the electron beam trajectory (blue dashed line).

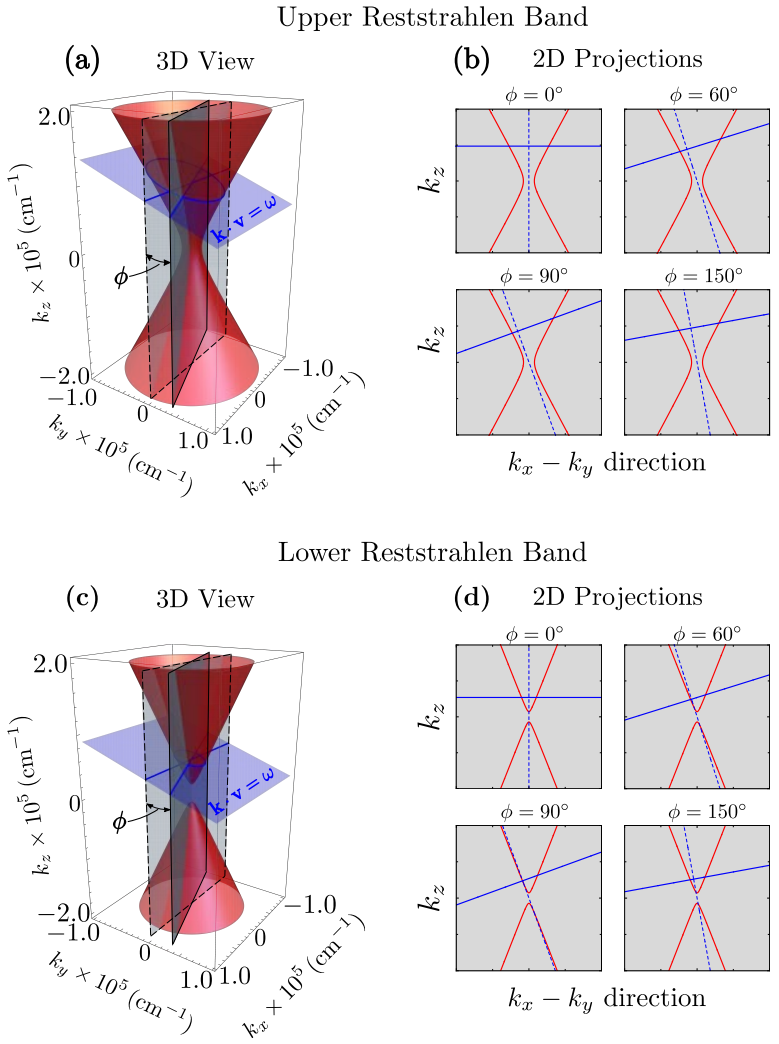

Figure 2.11: Intersection between the isofrequency surfaces of the PhPs dispersion and the plane $\mathbf{k} \cdot \mathbf{v} = \omega$. (a) Isofrequency surface (red hyperboloid) for a representative energy in the upper Reststrahlen band of 180 meV. The blue inclined plane depicts Eq. (2.9) for an electron beam with $v = 0.1c$ and trajectory angle of $\alpha = 20°$. The gray plane represents the different directions set by the azimuthal angle ϕ. The 2D plots in (b) show the intersection between the red hyperboloid and the blue plane in four different directions determined by ϕ: 0°, 60°, 90° and 150°. The blue dashed lines in the 2D projections depict the trajectory of the electron beam, as viewed along each direction determined by the angle ϕ. (c) and (d) are the same as (a) and (b) but for a representative energy in the lower Reststrahlen band of 100 meV.

To better understand the asymmetries in the propagation of the polaritonic waves, we focus on the direction of largest asymmetry: $\phi = 90°$ (equivalently

the $k_y k_z$-plane). From Eqs. (2.21a) and (2.21b) one can obtain the following two solutions for the polariton wavevector in the $k_y k_z$-plane:

$$\mathbf{k}^{(1)} = \frac{\omega}{v}\left[\frac{\varepsilon_\parallel \sin\alpha + \sqrt{\varepsilon_\parallel \varepsilon_\perp \Delta}\cos\alpha}{\varepsilon_\perp \cos^2\alpha + \varepsilon_\parallel \sin^2\alpha}\right]\hat{\mathbf{y}} + \frac{\omega}{v}\left[\frac{\varepsilon_\perp \cos\alpha - \sqrt{\varepsilon_\parallel \varepsilon_\perp \Delta}\sin\alpha}{\varepsilon_\perp \cos^2\alpha + \varepsilon_\parallel \sin^2\alpha}\right]\hat{\mathbf{z}}, \tag{2.23a}$$

$$\mathbf{k}^{(2)} = \frac{\omega}{v}\left[\frac{\varepsilon_\parallel \sin\alpha - \sqrt{\varepsilon_\parallel \varepsilon_\perp \Delta}\cos\alpha}{\varepsilon_\perp \cos^2\alpha + \varepsilon_\parallel \sin^2\alpha}\right]\hat{\mathbf{y}} + \frac{\omega}{v}\left[\frac{\varepsilon_\perp \cos\alpha + \sqrt{\varepsilon_\parallel \varepsilon_\perp \Delta}\sin\alpha}{\varepsilon_\perp \cos^2\alpha + \varepsilon_\parallel \sin^2\alpha}\right]\hat{\mathbf{z}}. \tag{2.23b}$$

with

$$\Delta = \left(\frac{v}{c}\cos\alpha\right)^2 \varepsilon_\perp + \left(\frac{v}{c}\sin\alpha\right)^2 \varepsilon_\parallel - 1. \tag{2.24}$$

From Eqs. (2.23a) and (2.23b) one can recognize that $k_z^{(1)} \neq k_z^{(2)}$, showing the asymmetry in the propagation of the polaritonic wave. Moreover, the angles $\theta_{\mathbf{k}}^{(1)}$ and $\theta_{\mathbf{k}}^{(2)}$ defined by $\mathbf{k}^{(1)}$, $\mathbf{k}^{(2)}$ vectors with respect to the electron beam trajectory (see Figs. 2.12a and 2.12c) satisfy the following relations

$$\tan(\theta_{\mathbf{k}}^{(1)} + \alpha) = \frac{\varepsilon_\parallel \sin\alpha + \sqrt{\varepsilon_\parallel \varepsilon_\perp \Delta}\cos\alpha}{\varepsilon_\perp \cos\alpha - \sqrt{\varepsilon_\parallel \varepsilon_\perp \Delta}\sin\alpha}, \tag{2.25a}$$

$$\tan(\theta_{\mathbf{k}}^{(2)} - \alpha) = \frac{\varepsilon_\parallel \sin\alpha - \sqrt{\varepsilon_\parallel \varepsilon_\perp \Delta}\cos\alpha}{\varepsilon_\perp \cos\alpha + \sqrt{\varepsilon_\parallel \varepsilon_\perp \Delta}\sin\alpha}. \tag{2.25b}$$

When $\alpha = 0°$, one can deduce from Eqs. (2.25a) and (2.25b) that

$$\tan\theta_{\mathbf{k}}^{(1)} = \sqrt{\left(\frac{v}{c}\right)^2 \varepsilon_\parallel - \frac{\varepsilon_\parallel}{\varepsilon_\perp}}, \tag{2.26a}$$

$$\tan\theta_{\mathbf{k}}^{(2)} = -\sqrt{\left(\frac{v}{c}\right)^2 \varepsilon_\parallel - \frac{\varepsilon_\parallel}{\varepsilon_\perp}}. \tag{2.26b}$$

Therefore $\theta_{\mathbf{k}}^{(1)} = \theta_{\mathbf{k}}^{(2)} = \theta_{\mathbf{k}}$ for this particular case of symmetric propagation. Notice that $\theta_{\mathbf{k}}$ is also preserved in any other azimuthal direction. We can observe from Eqs. (2.23a) and (2.23b) that $\mathbf{k}^{(1)}$, $\mathbf{k}^{(2)}$ depend on the electron velocity v. This dependency provides information on the condition that the electron velocity needs to satisfy for the electron beam to excite the polaritonic waves. Indeed, by imposing real value solutions to Eqs. (2.25a) and (2.25b),

one obtains the following condition on v:

$$\frac{v^2}{c^2}\left[\varepsilon_\perp^2\varepsilon_\parallel\cos^2\alpha+\varepsilon_\parallel^2\varepsilon_\perp\sin^2\alpha\right]>\varepsilon_\perp\varepsilon_\parallel. \tag{2.27}$$

This last relationship results in the following inequality $v^2\varepsilon_\parallel/c^2>\varepsilon_\parallel/\varepsilon_\perp$, when $\alpha=0°$, which coincides exactly with the inequality in Eq. (2.20) obtained in Subsection 2.3.5. For the particular case of an isotropic dielectric medium ($\varepsilon_\perp=\varepsilon_\parallel=\varepsilon>0$), this last condition results in the canonical relation for Cherenkov radiation: $v>c/\sqrt{\varepsilon}$. As we discuss in the box below, one can show that the propagation of the wake patterns through the dielectric medium is always cylindrically symmetric with respect to the electron beam trajectory.

Wake patterns in an isotropic dielectric medium

Assuming that the medium has dielectric function characterized by $\varepsilon_\perp=\varepsilon_\parallel=\varepsilon>0$, the two wavevector solutions $\mathbf{k}^{(1)}$, $\mathbf{k}^{(2)}$ given by Eqs. (2.23a) and (2.23b) result in

$$\mathbf{k}^{(1)}=\frac{\omega}{v}\begin{bmatrix}\sin\alpha & -\cos\alpha\\ \cos\alpha & \sin\alpha\end{bmatrix}(\hat{\mathbf{y}}-\sqrt{\Delta}\,\hat{\mathbf{z}})=\frac{\omega}{v}\mathbb{M}\,(\hat{\mathbf{y}}-\sqrt{\Delta}\,\hat{\mathbf{z}}), \tag{2.28a}$$

$$\mathbf{k}^{(2)}=\frac{\omega}{v}\begin{bmatrix}\sin\alpha & -\cos\alpha\\ \cos\alpha & \sin\alpha\end{bmatrix}(\hat{\mathbf{y}}+\sqrt{\Delta}\,\hat{\mathbf{z}})=\frac{\omega}{v}\mathbb{M}\,(\hat{\mathbf{y}}+\sqrt{\Delta}\,\hat{\mathbf{z}}), \tag{2.28b}$$

Note that $\mathbb{M}$ is an orthogonal matrix. This implies that the angles $\theta_{\mathbf{k}}^{(1)}$ and $\theta_{\mathbf{k}}^{(2)}$ are always equal under a rotation of the electron beam trajectory, and thus, the propagation of the wake patterns is always cylindrically symmetric with respect to the electron beam trajectory.

2.3.7 Asymmetric wake patterns

As we pointed out in Sections 2.3.3 and 2.3.4, the excitation of hyperbolic phonon polaritons can be controlled by the velocity of the fast electrons, whereas in the previous section we have shown that the polaritonic wave can propagate asymmetrically with respect to the electron beam trajectory. In this section, we thus study how steering of phonon polaritons can be controlled via the angle α between the electron beam trajectory and the h-BN optical axis. Notice that the symmetric case is similar to the one we discussed in Sections 2.3.3 and 2.3.4. Therefore we will focus here on the analysis of the polariton propagation direction which shows the largest asymmetry, that is,

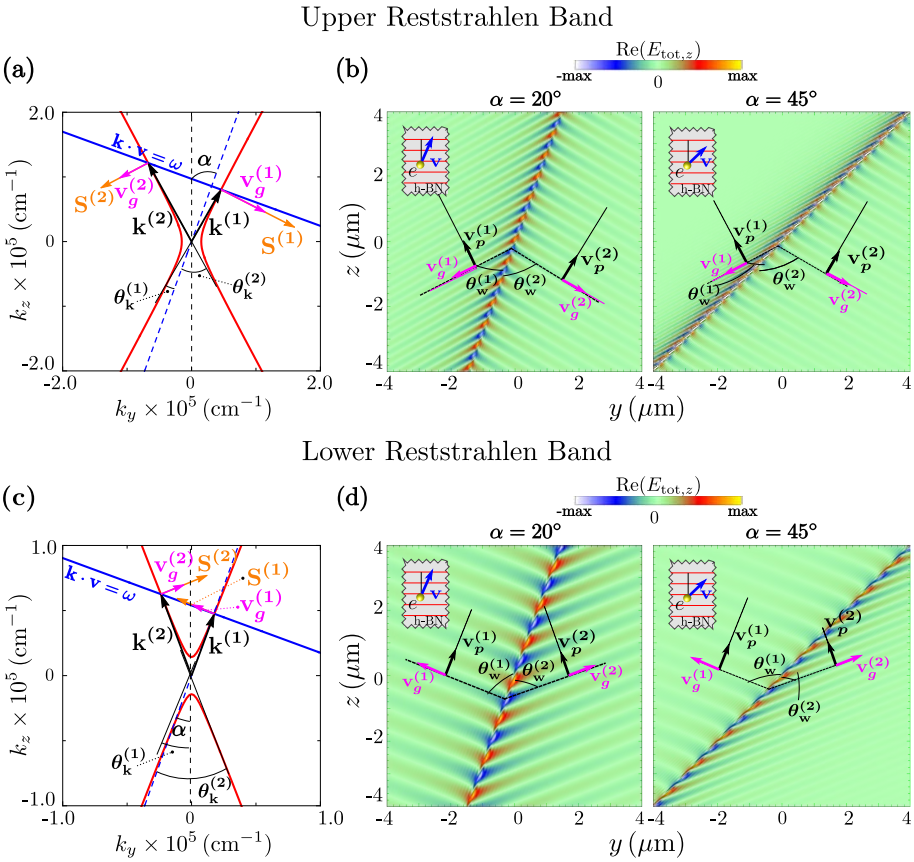

Figure 2.12: Asymmetric wake patterns of PhPs in bulk. Isofrequency curves in the $k_y k_z$-plane for (a) the upper and (c) the lower Reststrahlen bands for representative energies in each band: (a) 180 meV and (c) 100 meV. The blue inclined line represents the condition for the conservation of energy and momentum in the nonrecoil approximation: $\mathbf{k}\cdot\mathbf{v}=\omega$ for an electron with $v = 0.1c$ and $\alpha = 20°$. The black arrows represent the two wavevector solutions $\mathbf{k}^{(1)}$, $\mathbf{k}^{(2)}$ with angles $\theta_{\mathbf{k}}^{(1)}$, $\theta_{\mathbf{k}}^{(2)}$ with respect to the beam trajectory (blue dashed line), the magenta arrows represent the group velocities $\mathbf{v}_g^{(1)}$, $\mathbf{v}_g^{(2)}$ and the orange arrows the Poynting vectors $\mathbf{S}^{(1)}$, $\mathbf{S}^{(2)}$. The contour plots in (b) and (d) show the normalized real part of the z-component of the total electric field in the yz-plane for the energies: (b) 180 meV and (d) 100 meV. We plot the field distributions for two different angles of the electron beam trajectory: 20° (left panels) and 45° (right panels). The maximum values of the field plots are: (b) 4×10^{-6} a.u. and (d) $> 1.5 \times 10^{-6}$ a.u.

the $k_y k_z$-plane.

We show in Fig. 2.12a the line $\mathbf{k}\cdot\mathbf{v} = \omega$ for $v = 0.1c$ (blue line) and the isofrequency hyperbola (red curve) in the $k_y k_z$-plane for a representative energy in the upper Reststrahlen band ($\hbar\omega = 180$ meV). The blue dashed

line represents the electron beam trajectory and the black dashed line the k_z-axis. One can notice that the matching between the blue solid line and the red hyperbola (Fig. 2.12a) occurs at wavevectors $\mathbf{k}^{(1)}$ and $\mathbf{k}^{(2)}$ whose z-component is different. Thus, the projections onto the z-axis of the phase velocities $\mathbf{v}_p^{(1)}$ and $\mathbf{v}_p^{(2)}$ (parallel to $\mathbf{k}^{(1)}$ and $\mathbf{k}^{(2)}$, black arrows) are also different. Due to the hyperbolic shape of the isofrequency curve the z-component of the group velocities $\mathbf{v}_g^{(1)}$ (right orange arrow in Fig. 2.12a) and $\mathbf{v}_g^{(2)}$ (left orange arrow in Fig. 2.12a) parallel to the Poynting vectors $\mathbf{S}^{(1)}$ and $\mathbf{S}^{(2)}$, respectively, are also asymmetric. This difference (asymmetry) in the components of the two phase and group velocities leads to a highly asymmetric propagation of the polaritonic wave with respect to the electron beam trajectory.

The dependency of the polaritonic waves on the angle α can be observed in Fig. 2.12b, where we plot the real part of the z-component of the total electric field produced by the fast electron at energy $\hbar\omega = 180\,\text{meV}$ and $v = 0.1c$ when $\alpha = 20°$ and $\alpha = 45°$. Similar to the parallel trajectory (Sections 2.3.3 and 2.3.4), one can notice the formation of wake patterns and the spatial periodicity of the field along the electron beam trajectory. This periodicity is determined by the momentum transferred along the beam trajectory ($\hbar k_{\hat{\mathbf{v}}} = \hbar\omega/v$) since the corresponding wavelength is $\lambda_{\hat{\mathbf{v}}} = 2\pi/k_{\hat{\mathbf{v}}}$. Thus, the higher the energy of the polariton is, the smaller $\lambda_{\hat{\mathbf{v}}}$ will be. The wake patterns formed by the field distribution are clearly asymmetric with respect to the beam trajectory. We observe (Fig. 2.12b) that the wake fields exhibit largest asymmetry as α is increased from 20° (Fig. 2.12b, left panel) to 45° (Fig. 2.12b, right panel). This is a direct consequence on how the electron transfers different momentum components, $\hbar k_y$ and $\hbar k_z$, to the polaritonic excitation (see Fig. 2.12a). One can notice from Fig. 2.12a that as α is increased, $k_z^{(1)} \approx 0$ and $\mathbf{k}^{(2)}$ tends to the asymptote of the red hyperbola. Therefore, for large angles α the polaritonic wave will propagate relative to the beam trajectory with a phase velocity close to zero on one side of the beam trajectory and with a non-zero phase velocity on the other side of the beam trajectory. These findings explain the tilting of the wavefronts in Fig. 2.12b for $\alpha = 45°$ at the left side of the electron beam. It is worth noting that Fig. 2.12b corresponds to the propagation of the polaritonic wave in the yz-plane. However, for other propagation directions, the field distributions will be different.

In Figs. 2.12c and 2.12d we show the same analysis (electron beam trajectory tilted an angle α with respect to the h-BN optical axis) for a representative energy within the lower Reststrahlen band (100 meV). Importantly, for this case the projections onto the y-axis of the phase velocities $\mathbf{v}_p^{(1)}$ and $\mathbf{v}_p^{(2)}$ are antiparallel (negative) to the y-component of the Poynting vectors $\mathbf{S}^{(1)}$ and $\mathbf{S}^{(2)}$. This yields an asymmetric wave propagating with negative phase velocity (Fig. 2.12d).

Additionally, the electron velocity v allows to control the momentum transfer by the fast electron to the phonon polaritons (Eq. (2.9)). Indeed, as we have shown in Section 2.3.6 (Eq. (2.27)), one can obtain the relationship between v and the excitation of the asymmetric wake patterns by analyzing the wake angles $\theta_{\mathrm{w}}^{(1)} = 90° - \theta_{\mathbf{k}}^{(1)}$ and $\theta_{\mathrm{w}}^{(2)} = 90° - \theta_{\mathbf{k}}^{(2)}$ (Figs. 2.12b and 2.12d).

We have found that the excitation of the polaritonic wave is highly dependent on the orientation of the electron beam trajectory with respect to the h-BN crystallographic arrangement. Thus, while the speed of the electron serves as a means to excite the polaritonic wave or not, the orientation of the electron beam trajectory can serve to control the direction of the polaritonic waves.

2.4 Excitation of Dyakonov surface PhPs in h-BN

In this section, we study the EELS signal when the electron beam is traveling above an h-BN semi-infinite surface. The interface between vacuum and h-BN lies on the yz-plane, as depicted in Fig. 2.13, with the y-axis in the direction of $\varepsilon_\perp$ and the z-axis in the direction of the h-BN optical axis. The electron travels in vacuum at a distance b from the surface (we will refer to this distance as the impact parameter) with velocity v parallel to the optical axis of the h-BN. A schematic representation of the probing electron-surface system is shown in Fig. 2.13.

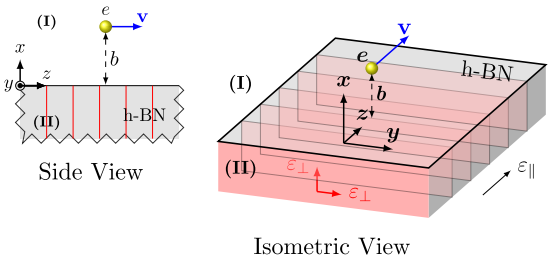

Figure 2.13: Electron traveling above a semi-infinite h-BN surface. Schematics of the probing electron traveling with velocity v at a distance b parallel to a h-BN surface. The optical axis of the h-BN crystal lattice is parallel to the h-BN surface. Label I refers to vacuum, while label II refers to h-BN.

Surfaces of uniaxial materials with optical axis parallel to the surface support

a specific kind of surface waves, the so-called Dyakonov waves [144, 145]. When either $\varepsilon_\perp$ or $\varepsilon_\parallel$ is negative (as in the case of the Reststrahlen bands in h-BN), Dyankonov surface polaritons [146] can propagate along the surface. Recently, Dyakonov surface phonon polaritons have been observed by scattering-type scanning near-field optical microscopy at the edges of h-BN flakes [27, 147] as well as by EELS in STEM [123, 148]. In the latter experiments, the probing electrons were passing outside the flake edge in a perpendicular trajectory. However, the excitation and detection of Dyakonov surface phonon polaritons with an electron beam parallel to an extended surface has not been described yet.

In the following subsections, we first describe the Dyakonov surface phonon polariton modes that exist at the interface between h-BN and vacuum. We then show in Subsections 2.4.2 and 2.4.3 that a localized beam of fast electrons can couple to these polaritons. Particularly, we analyze the corresponding EEL spectra and the polariton wake patterns produced in this configuration. Importantly, we find that surface Dyakonov phonon polaritons are excited only in the upper Reststrahlen band. Therefore, our analysis and calculations are restricted to this energy range.

2.4.1 Surface modes in h-BN

According to Dyakonov's theory [144], the interface described in Fig. 2.13 supports electromagnetic waves that propagate along it and their associated electromagnetic fields decay exponentially perpendicular to the interface [66, 144, 145, 149]. These surface waves can be expressed as a linear superposition of the four following modes propagating along the interface: (i) a transverse electric (TE) mode, (ii) a transverse magnetic (TM) mode (the corresponding fields decay into the vacuum, upper half space in Fig. 2.13 labeled as I), (iii) an ordinary mode, and (iv) an extraordinary mode (the corresponding fields decay exponentially into h-BN, lower half space in Fig. 2.13 labeled as II). Following this scheme the electric field in each media can be written as,

$$\mathbf{E}_{\mathrm{I}}(x>0,y,z) = (\mathbf{A}_{\mathrm{TE}} + \mathbf{A}_{\mathrm{TM}})e^{-\kappa_{\mathrm{I}}x}e^{i(k_y y+k_z z)}, \tag{2.29a}$$

$$\mathbf{E}_{\mathrm{II}}(x<0,y,z) = (\mathbf{A}_{\mathrm{o}}e^{\kappa^{o}_{\mathrm{II}}x} + \mathbf{A}_{\mathrm{e}}e^{\kappa^{e}_{\mathrm{II}}x})e^{i(k_y y+k_z z)}, \tag{2.29b}$$

where harmonic dependency in time has been assumed, and $\mathbf{A}_{\mathrm{TE}}, \mathbf{A}_{\mathrm{TM}}, \mathbf{A}_{\mathrm{o}}, \mathbf{A}_{\mathrm{e}}$ are the amplitudes of each mode. The wavevector of each aforementioned mode is given by

$$\mathbf{k}_d = (i\kappa_{\mathrm{I}}, k_y, k_z) \;\; \mathrm{TE},\; \mathrm{TM}, \tag{2.30a}$$

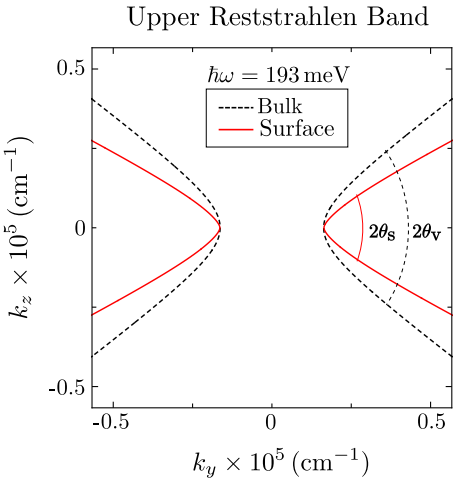

Figure 2.14: Bulk and surface PhPs isofrequency curves. The red solid hyperbola represents the isofrequency curve obtained with Eqs. (2.31a)-(2.31c) and (2.32) for the surface phonon polariton, whereas the black dashed hyperbola represents the isofrequency curve obtained using Eq. (2.5) (setting $k_x = 0$) for the bulk phonon polariton. Both curves are calculated for a representative energy in the upper Reststrahlen band, 193 meV.

$$\mathbf{k}_o = (-i\kappa^o_{\text{II}}, k_y, k_z) \;\; \text{ordinary}, \tag{2.30b}$$
$$\mathbf{k}_e = (-i\kappa^e_{\text{II}}, k_y, k_z) \;\; \text{extraordinary}, \tag{2.30c}$$

where $\kappa_{\text{I}}, \kappa^o_{\text{II}}, \kappa^e_{\text{II}} > 0$ and $k_y, k_z \in \mathbb{C}$ need to fulfill the following conditions:

$$\kappa^2_{\text{I}} = k_y^2 + k_z^2 - (\omega/c)^2 \;\; \text{vacuum}, \tag{2.31a}$$
$$(\kappa^o_{\text{II}})^2 = k_y^2 + k_z^2 - \varepsilon_\perp(\omega/c)^2 \;\; \text{ordinary}, \tag{2.31b}$$
$$(\kappa^e_{\text{II}})^2 = k_y^2 + \frac{\varepsilon_\parallel}{\varepsilon_\perp}k_z^2 - \varepsilon_\parallel(\omega/c)^2 \;\; \text{extraordinary}. \tag{2.31c}$$

Applying boundary conditions imposed by Maxwell's equations at the interface between vacuum and h-BN, one obtains the following relationship [66, 144, 150]

$$(\kappa_{\text{I}} + \kappa^e_{\text{II}})(\kappa_{\text{I}} + \kappa^o_{\text{II}})(\kappa_{\text{I}} + \varepsilon_\perp\kappa^e_{\text{II}}) = (\omega/c)^2(\varepsilon_\parallel - 1)(1 - \varepsilon_\perp)\kappa_{\text{I}}, \tag{2.32}$$

which together with the set of Eqs. (2.31a)-(2.31c) determines the in-plane wavevector (k_y, k_z) of the Dyakonov waves.

It is worth noting that Dyakonov's original work [144] was derived for positive $\varepsilon_\perp$ and $\varepsilon_\parallel$. However Eq. (2.32) is still valid when $\varepsilon_\perp < 0$ and $\varepsilon_\parallel > 0$ [149, 150]. Since negative values in the real part of the permittivity components support the excitation of polaritonic states, Dyakonov surface waves sustained in h-BN

in the mid-infrared region are thus called Dyakonov surface phonon polaritons.

In Fig. 2.14 we plot the isofrequency contour (red curve) of the h-BN surface polariton for an energy within the upper Reststrahlen band (193 meV), obtained from Eqs. (2.31a)-(2.31c) and (2.32). For comparison, we show a cut ($k_y k_z$-plane) of the isofrequency surface of the hyperbolic volume polariton (black dashed line obtained from Eq. (2.5)). We find that the isofrequency curve of the surface polariton is a hyperbola, similar to that of the volume polariton particularly for small momenta. At large momenta, on the other hand, the opening angle of the isofrequency contour of the surface polariton, θ_{s}, is smaller than that of the volume polariton θ_{v}, demonstrating that the dispersion of Dyakonov phonon polaritons is different to the one obtained for the bulk hyperbolic phonon polaritons.

2.4.2 Electron energy-loss probability in surface h-BN

The excitation of Dyakonov surface phonon polaritons by fast electron beams can be revealed in the electron energy loss spectra. In the following, we describe the strategy to obtain the momentum-resolved energy loss probability, $P_{\mathrm{surf}}(k_y;\omega)$, and the EEL probability, $\Gamma'_{\mathrm{surf}}(\omega)$, when the probing electron travels above the h-BN surface (see Fig. 2.13).

To calculate $\Gamma'_{\mathrm{surf}}(\omega)$, following Eq. (2.7), one needs to obtain the induced electric field, $\mathbf{E}_{\mathrm{ind}}(\mathbf{r}_e;\omega)$ along the electron beam trajectory. To that end we obtain $\mathbf{E}_{\mathrm{ind}}(\mathbf{r};\omega)$ by solving Maxwell's equations in the presence of vacuum-h-BN interface, assuming that the electron travels in vacuum with constant velocity v and impact parameter b (Fig. 2.13). Considering the boundary conditions at the interfaces ($x = 0$), one finds the induced electric field in vacuum (region I in Fig. 2.13):

$$\mathbf{E}^{\mathrm{I}}_{\mathrm{ind}}(x,k_y,k_z;\omega) = (b_{\mathrm{I}}, d_{\mathrm{I}}, g_{\mathrm{I}})\,\tilde{\rho}\,e^{-\kappa_{\mathrm{I}}x}, \tag{2.33}$$

with b_{I}, d_{I}, g_{I} being the coefficients involving the dielectric functions at both sides of the interface and $\tilde{\rho} = -2\pi e\delta(\omega - k_z v)e^{-\kappa_{\mathrm{I}}b}/\varepsilon_0$. We refer to Appendix C for a detailed description of the coefficients of the total and induced electric fields at each half space (vacuum and h-BN).

By Fourier transforming (see Appendix A) $\mathbf{E}^{\mathrm{I}}_{\mathrm{ind}}(x,k_y,k_z;\omega) \mapsto \mathbf{E}^{\mathrm{I}}_{\mathrm{ind}}(\mathbf{r};\omega)$ in Eq. (2.33) and inserting its value into Eq. (2.7), we find that $\Gamma'_{\mathrm{surf}}(\omega)$ can be written as

$$\Gamma'_{\mathrm{surf}}(\omega) = \int_0^{k_y^c} \mathrm{d}k_y\, P_{\mathrm{surf}}(k_y;\omega), \tag{2.34}$$

where

$$P_{\text{surf}}(k_y;\omega) = -\frac{e^2}{\pi^2\varepsilon_0\hbar\omega v}\text{Re}\left[g_{\text{I}}\, e^{-2\kappa_{\text{I}}b}\right]\Big|_{k_z=\omega/v}, \tag{2.35}$$

is the probability that the electron transfers a transverse momentum $\hbar k_y$ (y-component of the momentum) upon losing energy $\hbar\omega$. Notice that the z-component of the wavevector in $P_{\text{surf}}(k_y;\omega)$ is fixed by $k_z = \omega/v$, implying that the electron still transfers a momentum parallel to its trajectory equal to $\hbar\omega/v$. The integration of Eq. (2.34) is performed up to the cutoff value k_y^c, which is determined by the aperture of the EELS detector.

As we discussed in Section 2.3, the spectrum of the momentum-resolved energy loss probability and the EEL probability provides information on the properties of the excited modes in the anisotropic medium. We thus show in the following section the relationship between these two quantities and the excitation of Dyakonov surface phonon polaritons.

2.4.3 Excitation of Dyakonov surface PhPs

As pointed out above, the momentum parallel to the trajectory, $\hbar k_z$, transferred by the fast electron to the phonon polaritons is determined by the relation $k_z = \omega/v$. Similarly to the bulk analysis presented in Section 2.3, this relationship represents a horizontal line in the $k_y k_z$ representation of Fig. 2.14. Thus, the transferred momentum can be determined by the crossing between this horizontal line ($k_z = \omega/v$) and the isofrequency hyperbolas obtained from Eqs. (2.31a)-(2.31c) and (2.32). From the latter equations one can further obtain the relationship between the y-component of the polariton wavevector (k_y) and $\hbar\omega$, which is shown in the left panel of Fig. 2.15a (dashed blue curve). We also plot the momentum-resolved energy loss probability $P_{\text{surf}}(k_y;\omega)$ for energies around the upper Reststrahlen band. The probing electron is traveling above the h-BN surface with an impact parameter of 10 nm and velocity $v = 0.1c$. Some similarities between $P_{\text{surf}}(k_y;\omega)$ and $P_{\text{bulk}}(k_\perp;\omega)$ (Fig. 2.3b, left panel) become apparent. For instance, the highest values of $P_{\text{surf}}(k_y;\omega)$ (red and yellow colors in Fig. 2.15a) coincide perfectly with the blue dashed curve, demonstrating that the electron energy losses in the upper band are caused mainly due to the excitation of hyperbolic phonon polaritons. However, by comparing Figs. 2.3b and 2.15a we recognize that the asymptotic behavior (at large momenta) of $P_{\text{surf}}(k_y;\omega)$ occurs at a lower energy compared to the asymptotic behavior of $P_{\text{bulk}}(k_\perp;\omega)$. While $P_{\text{bulk}}(k_\perp;\omega)$ tends to the $\text{LO}_\perp$ phonon energy, $P_{\text{surf}}(k_y;\omega)$ tends to the surface optical ($\text{SO}_\perp$) phonon energy given by the condition $\varepsilon_\perp(\omega_{\text{SO}_\perp}) = -1$ (derived from Eqs. (2.31a)-(2.31c)

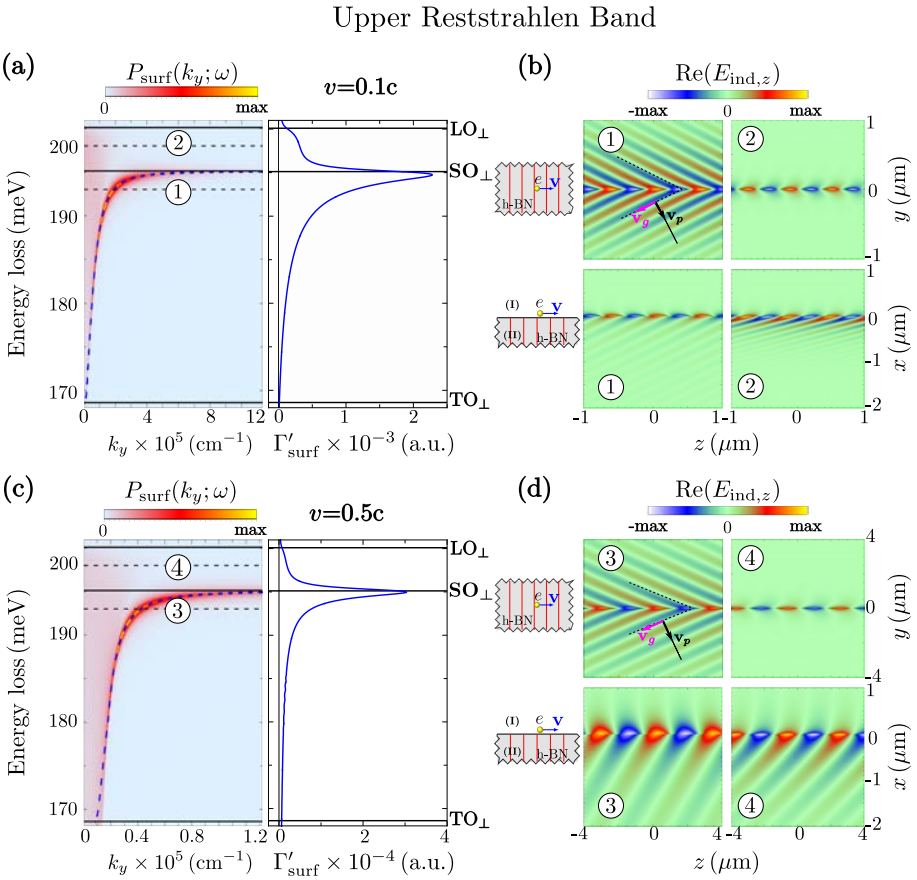

Figure 2.15: Excitation of Dyakonov surface PhPs. The left panel in (a) displays the momentum-resolved energy loss probability $P_{\rm surf}(k_y;\omega)$ normalized to the maximum value (3 a.u.) in the vicinity of the upper Reststrahlen band for $b = 10$ nm and $v = 0.1c$. The right panel in (a) shows the EEL probability $\Gamma'_{\rm surf}(\omega)$ obtained by integrating $P_{\rm surf}(k_y;\omega)$ over k_y up to $k_y^c = 0.09\,\text{Å}^{-1}$. (c) same as in (a) but considering $v = 0.5c$. For this case the maximum value of the momentum-resolved energy loss probability is 1 a.u. The color maps in (b) and (d) show the real part of the z-component of the induced electric field for energies: 193 meV (marked as 1, 3) and 198 meV (marked as 2, 4). The top panels in (b) and (d) correspond to the in-plane views (yz-plane) of the induced field at the interface, while the bottom panels correspond to the out-of-plane views (xz-plane) containing the electron trajectory. The field plots are normalized with respect to the maximum value in each case. For the top panels the maximum values are: (b.1) 1×10^{-4} a.u., (b.2) 7.5×10^{-5} a.u., (d.3) 7.5×10^{-6} a.u. and (d.4) 5×10^{-6} a.u. For the bottom panels the maximum values are: (b.1) 4×10^{-5} a.u., (b.2) 2×10^{-5} a.u. and (d) 1.5×10^{-6} a.u. In panels (b) and (d) the magenta and black arrows represent the group velocity $\mathbf{v}_g$ and phase $\mathbf{v}_p$ velocities, respectively.

and (2.32) for large momenta). Importantly, the latter is a fingerprint of the excitation of surface polariton modes. In our case (electron traveling in vacuum

above the h-BN surface) these surface modes correspond to Dyakonov surface phonon polaritons. We confirm this by integrating $P_{\mathrm{surf}}(k_y;\omega)$ over k_y up to a cutoff momentum $\hbar k_y^c$, which yields the EEL probability $\Gamma'_{\mathrm{surf}}(\omega)$ (right panel of Fig. 2.15a). A clear peak can be observed at the $\mathrm{SO}_\perp$ phonon energy. This loss peak is slightly asymmetric with a broader tail for lower energies in the Reststrahlen band compared to that for larger energies in the band. Notice that for energies above $\mathrm{SO}_\perp$ the loss spectrum displays a shoulder arising from background losses present in the entire upper band at small momentum (red blurred area for small momentum in the left panel of Fig. 2.15a).

The excitation of Dyakonov surface phonon polaritons (within the upper Reststrahlen band) by the probing electron can be observed in real space in Fig. 2.15b, where we show the real part of the z-component of the induced electric field amplitude at energies 193 meV (marked as 1) and 198 meV (marked as 2). The top panels correspond to the evaluation of $\mathrm{Re}(E_z^{\mathrm{ind}}(\mathbf{r};\omega))$ in the yz-plane (in-plane at the interface), and the bottom panels to the evaluation in the xz-plane (lateral view, containing the electron trajectory). One can recognize from the in-plane views (Figs. 2.15b marked as 1) the formation of wake patterns and the oscillatory behavior of the induced field in the z-direction. Similarly to the field distribution shown in Fig. 2.4b, the spatial periodicity along the z-direction is connected with the parallel wavevector component $k_z = \omega/v$, since $\lambda_z = 2\pi/k_z$. Moreover, the wake wavefronts show interesting propagation patterns both in the transverse direction from the beam trajectory as well as into the h-BN.

In the top panel of Fig. 2.15b (image labeled as 1), the wavefronts along the y-direction propagate with positive phase and group velocities relative to the Poynting vector. Indeed, we find that the dashed blue curve in Fig. 2.15a has a positive slope ($\mathrm{d}\omega/\mathrm{d}k_y > 0$), indicating that the projections onto the y-axis of the group and phase velocities are parallel (positive). We also notice that Dyakonov surface phonon polaritons are confined to the interface with penetration of the field into the h-BN interface (Fig. 2.15b, bottom image labeled as 1). For energies larger than that of the $\mathrm{SO}_\perp$ phonon, Dyakonov surface phonon polaritons are not excited (Fig. 2.15b, image labeled as 2). Thus, the induced field distributions for those energies correspond to the reflection of the electron electromagnetic field at the h-BN surface (Fig. 2.15b, top image labeled as 2). We can also notice that the field penetrates into the h-BN (bottom panels of Fig. 2.15b), which is connected with the presence of the red blurred region corresponding to the losses appearing for lower momenta in Fig. 2.15a (left panel).

When the velocity of the probing electron is increased up to 50 % the speed of light, the momentum parallel to the beam trajectory, $\hbar k_z$, is reduced and so does the k_y component of the Dyakonov surface phonon polariton. By

calculating the momentum-resolved energy loss probability $P_{\text{surf}}(k_y;\omega)$ (left panel of Fig. 2.15c) and the EEL probability $\Gamma'_{\text{surf}}(\omega)$ one obtains a similar behavior as in Fig. 2.15a for $v = 0.1c$, except for a one order of magnitude reduction of both k_y and the value of the loss probability.

The differences in the properties of the Dyakonov surface phonon polaritons launched by the fast electron beam can be observed in Fig. 2.15d, where we show the real part of the z-component of the induced electric field amplitude for $v = 0.5c$ at energies 193 meV and 200 meV. Notice that the spatial periodicity λ_z of the polariton is longer in this situation compared to that in Fig. 2.15b as a result of the increased electron velocity. Also, the penetration of the field into the h-BN medium is larger compared to that in Fig. 2.15b. This increase in the penetration depth can be attributed to the increase of the background losses present in the entire upper band (blurred red are in the left panel of Fig. 2.15c). As we will discuss in the next section, these background losses are associated with the excitation of bulk hyperbolic phonon polaritons by the fast electron.

2.5 Remote excitation of bulk PhPs

We have shown in Figs. 2.15b and 2.15d that the electric field penetrates into the bulk of the h-BN semi-infinite surface, which is surprising, as one does not expect the excitation of volume modes in isotropic materials for electron beam trajectories outside the material. By comparing the angles of the wake patterns, we demonstrate that indeed volume modes are excited in h-BN with external beam trajectories.

We first calculated the angle θ_{w} of the wake wavefronts produced by the fast electron traveling through bulk h-BN with $v = 0.5c$ at $\hbar\omega = 193$ meV (Figs. 2.16a and 2.16c), obtaining a value of $\theta_{\text{w}} = 32.35°$. We compare θ_{w} with the angles of the wake wavefronts produced by the fast electron traveling in an aloof trajectory 10 nm above the h-BN surface (Fig. 2.16b and 2.16d). From this comparison we find that: (i) the angle $\theta_{\text{w}_\text{s}} = 24.67°$ of the wake pattern at the h-BN surface (Fig. 2.16b) is different from θ_{w}, and (ii) the angle of the wake pattern excited inside the h-BN is the same as θ_{w} (Fig. 2.16d). This implies that volume modes are excited by the fast electron traveling along trajectories outside the anisotropic medium.

Importantly, these findings open the possibility of remotely exciting volume

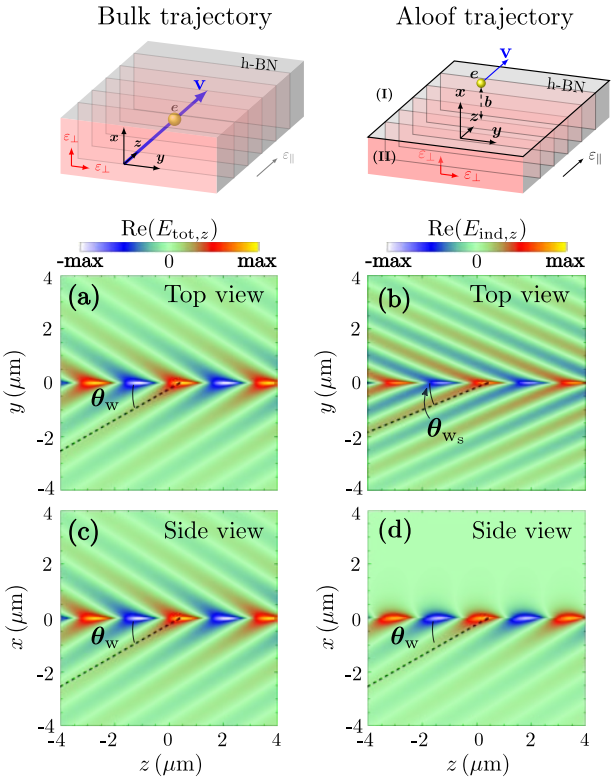

Figure 2.16: Remote excitation of bulk PhPs. (a) Real part of the z-component of the total electric field, $\mathrm{Re}(E_z^{\mathrm{tot}})$ in the yz-plane produced by a fast electron traveling through h-BN parallel to its optical axis. (c) shows $\mathrm{Re}(E_z^{\mathrm{tot}})$ evaluated in the xz-plane. θ_{w} is the angle between the z-axis and the wake patterns formed by the bulk polariton. (b) shows the $\mathrm{Re}(E_z^{\mathrm{tot}})$ in the yz-plane produced by a fast electron traveling in vacuum 10 nm above a semi-infinite h-BN surface. (d) shows $\mathrm{Re}(E_z^{\mathrm{ind}})$ evaluated in the xz-plane. $\theta_{\mathrm{w_s}}$ is the angle between the z-axis and the wake patterns formed by the Dyakonov surface phonon polariton. We used for the calculation of the fields an electron velocity equal to $v = 0.5c$ at energy $\hbar\omega = 193\,\mathrm{meV}$. The field plots are normalized with respect to the maximum value in each case: (a) 5×10^{-7} a.u., (b) 7.5×10^{-6} a.u., (c) 5×10^{-7} a.u. and (d) 1.5×10^{-6} a.u. The insets above (a) and (b) illustrate the geometry under consideration for each case.

phonon polaritons. In contrast to isotropic materials, where an aloof electron beam only couples to surface modes, for anisotropic materials the energy and momentum matching between the electron and the polaritons allows for launching of bulk excitations.

2.6 Summary and conclusions

In this chapter, we have thoroughly analyzed the excitation of optical phonon polaritons in hexagonal boron nitride by focused electron beams for two relevant situations: when the electron travels through the h-BN bulk and when it travels in vacuum above a semi-infinite h-BN surface. For the bulk situation, we observe that the electron couples to volume phonon polaritons when it travels parallel or at an angle α with respect to the h-BN optical axis. We demonstrated that the excitation of these polaritonic modes is strongly dependent on the electron velocity and on the angle α of the trajectory with respect to the optical axis. Furthermore, we have shown that Dyakonov surface phonon polaritons can be excited by a fast electron traveling above the h-BN surface. Interestingly, aloof electron beams are capable of exciting volume polaritons in the h-BN.

By a detailed mode analysis, we show that the electron beam transfers a specific momentum to the material. This momentum transfer determines the properties of the excited phonon polaritons, and thus controls their phase and group velocities, as well as their propagation direction. Importantly, we found that the propagation of polaritonic waves is highly asymmetric with respect to the electron beam trajectory when the trajectory sustains an angle relative to the h-BN optical axis.

Our findings may offer a way to steer and control the propagation of polaritonic waves excited in hyperbolic materials. Although we studied the specific material h-BN, our findings can be generalized and can serve as a guide for the correct interpretation of the different excited modes and loss channels encountered in EELS experiments of uniaxial materials.

3

Probing optical anapoles with fast electron beams

We had some success this week with EELS measurements of the disks. We are seeing multiple very distinct signals between 1 eV and 2.5 eV from disks that are $\sim 550\,nm$ in diameter.

– Andrew's email (October 09, 2020)

Abstract

In this chapter, we theoretically and experimentally analyze the excitation of optical anapoles in tungsten disulfide (WS_2) nanodisks using EELS in STEM. We first identify prominent dips in the EEL spectra of a model high-index dielectric disk. By calculating the electric and toroidal multipole moments of the induced current density produced by the electron beam in the disk, we show that the prominent dips are associated with the excitation of a variety of optical anapoles. To experimentally verify anapole excitation and detection in EELS, we fabricate nanodisks made of WS_2 and compare the experimental EEL signal with numerical calculations. Interestingly, we find that the anapole disperses with the disk size and thus, by varying the WS_2 nanodisk dimensions, the anapole can be tuned to overlap an exciton transition of WS_2 leading to anapole-exciton hybridization. Finally, we show spatial maps of the anapoles excited in the WS_2 nanodisks with subnanometer resolution and conclude that their excitation can be controlled by placing the electron beam at different positions over the nanodisk. The results discussed in this chapter are reported in the following manuscript: C. Maciel-Escudero et al. "Probing optical anapoles with fast electron beams", arXiv:2304.01018.

3.1 Introduction

High-refractive-index dielectric nanostructures have recently emerged as important building blocks for novel photonic devices in the field of nanophotonics and metamaterials [151–156]. They have shown potential for light manipulation at the nanoscale and their fabrication typically involves silicon [152], transition metal dichalcogenide (TMDC) materials [157], and other semiconductors [158, 159] showing small absorption losses compared to plasmonic nanostructures made of gold or silver. An important advantage of dielectric structures is their ability to support electric and magnetic resonances based on the excitation of circular displacement currents within the dielectric structure. The excitation and control of these resonances reveal new physical phenomena that cannot be easily achieved with their plasmonic counterparts. For example, interference between the electric and magnetic resonances can result in simultaneous enhancement of forward scattering and suppression of backward scattering by the structure [160, 161]. Furthermore, the excitation of electric and magnetic resonances can lead to strong field localization inside the structure, and thus, to enhancing nonlinear processes such as the generation of high harmonics [162].

To highlight one intriguing physical phenomenon appearing in the optical response of dielectric nanostructures, we calculate the scattering cross section σ_{scat} and the electric energy E_e of a dielectric disk with different radius R_0 (see Appendix B for details of the simulations). The disk, with $\varepsilon_{\text{d}} = 18$, is illuminated with a plane wave ($\lambda_{\text{inc}} = 1000\,\text{nm}$) traveling along the z-direction and polarized along the x-axis (illustrated in Fig. 3.1a). In Fig. 3.1b we plot the results of the calculations. We observe that σ_{scat} (black line) is close to zero for a disk with $R_0 \approx 250\,\text{nm}$ (gray dashed line) while E_e (blue line) is larger than zero, and thus, the electromagnetic field is confined inside the disk. As we will discuss in this chapter, this optical phenomenon, characterized by vanishing scattering and strong field localization inside the disk, can appear in high-refractive-index dielectric structures and is known as an optical anapole state.

Anapoles are charge-current distributions giving rise to an optical phenomenon characterized by strong suppression of electromagnetic radiation [163, 164]. This phenomenon is typically understood as the interference between the electromagnetic (EM) field produced by a Cartesian electric multipole with the EM field of a toroidal multipole. When this interference is

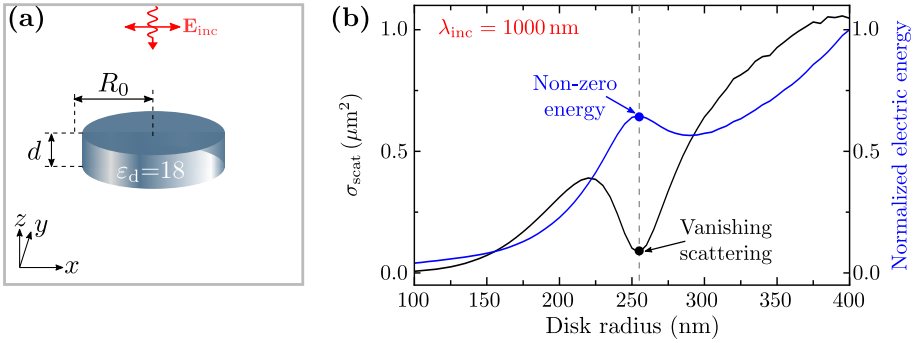

Figure 3.1: Optical anapoles. (a) Sketch of the system under study. The blue cylinder represents the high-index dielectric nanodisk with dielectric function $\varepsilon_{\mathrm{d}} = 18$, thickness $d = 55\,\mathrm{nm}$ and radius R_0. The red arrow represents the incident plane wave polarized along the x-axis with $\lambda_{\mathrm{inc}} = 1000\,\mathrm{nm}$. (b) Scattering cross section σ_{scat} (black line) and electric energy E_e (blue line) of a disk calculated as a function of the radius R_0. The electric energy E_e is normalized to its maximum value. The gray dashed line indicates the nanodisk radius with vanishing σ_{scat}. For simulation details, we refer the reader to Appendix B.

destructive, the system yields a non-radiating current configuration known as the optical anapole state [165, 166]. Excitation of the anapole in a polarizable nanostructure greatly suppresses its scattering cross section thus providing invisibility to nanoobjects [167], which offers promising applications in nanophotonics [168–172]. Additionally, optical anapoles concentrate EM fields inside the nanoresonators serving to enhance nonlinear harmonic generation [173, 174], four-wave mixing [175], Raman scattering [176, 177], and photothermal nonlinearities [178].

Intense experimental and theoretical efforts have been devoted to identifying optical anapole states in different dielectric nanostructures. However, the detection of ideal optical anapoles is complicated and usually requires the suppression of other multipole resonances. Typically, this suppression is achieved by engineering the nanoresonator geometry and by structuring the incident illumination [168, 169, 172]. Complementary to far-field characterization, understanding how anapoles are excited by localized probes can be of paramount importance in order to control and realize the full potential of these non-radiating states. In this context, scanning near-field optical microscopy (SNOM) was applied to study the near-field distribution of Si disks at relevant wavelengths [167, 171]. In this first experiment, the field around the disk was mapped at the anapole wavelength, revealing a maximum in the amplitude of the near field in the middle of the disk [167]. In the second experiment, it was found that the normal component of the electric field induced at the disks is reduced at the anapole wavelength [171]. SNOM offers the advantage of spatially map-

ping both the amplitude and phase of near-field patterns, however, the spatial resolution is limited by the dimensions of the near-field probes (an optical fiber or a metallic tip in the aforementioned cases), which are typically of the order of tens of nanometers. More importantly, the near-field probe itself can couple to the sample [179], leading to spectral shifts of the resonance modes and potential distortions when probing the anapoles. In contrast to SNOM techniques, EELS in STEM is a non-disturbing technique which accesses the clean electromagnetic fields and modes of a sample. At the same time, EELS allows for accessing not only to electric dipole modes but also quadrupoles and higher-order modes that do not, or weakly, couple to far-field radiation.

In this chapter, we present a numerical and experimental analysis of optical anapoles and anapole-exciton hybrids excited in WS_2 nanodisks using fast electron beams. As a proof of concept, we first calculate in Section 3.2 the electron energy losses experienced by a focused electron beam traveling in an aloof trajectory in the vicinity of a model high-index dielectric nanodisk. We show that prominent dips appear in the simulated EEL spectra, and we demonstrate that these dips are associated with the destructive interference between electric and toroidal Cartesian multipoles induced in the disk. In Subsection 3.2.2, we show the far-field optical scattering spectra of the dielectric disks and compare them with the EEL spectra. At the end of Section 3.2, we introduce an analytical model based on temporal coupled-mode theory (TCMT) to describe the anapole dip as the result of the interference produced by two modes excited in the disk. To experimentally access the spectral and spatial information on the anapoles, we performed EELS on fabricated WS_2 nanodisks made from exfoliated multilayer TMDC WS_2 with a high refractive index in the visible and infrared spectral ranges [180–182]. In Subsections 3.3.1 and 3.3.2, we show the fabricated WS_2 nanodisks and discuss the optical properties of multilayer WS_2. We next show in Subsections 3.3.4 the experimental EEL spectra, and compare them with numerical simulations. Finally, in Subsection 3.3.4, we discuss the possibility to spatially map optical anapoles and to control their excitation by placing the electron beam at different positions over the nanodisk, demonstrating the potential of EELS to access these special non-radiating charge-current distributions.

3.2 Theoretical prediction of optical anapoles in EEL spectra

We begin this study by describing the general features appearing in the EEL spectra of a model high-index dielectric nanodisk that can exhibit optical anapole states [183]. Figure 3.2a illustrates a sketch of the system under study: a dielectric disk excited by an electron beam traveling in aloof trajectory close to the disk. We choose a disk of variable radius R_0, thickness $d = 55\,\text{nm}$ and permittivity $\varepsilon_\text{d} = 18$. The electron beam travels with velocity $v = 0.7c$ (200 keV) along the z-axis at a distance $b = 1.1R_0$ with respect to the nanodisk center (impact parameter). We calculate numerically the EEL probability $\Gamma(\omega)$ using the classical dielectric theory discussed in Chapter 1 and Appendix B.

Figure 3.2b shows the calculated $\Gamma(\omega)$ spectra for different nanodisk radius R_0 in the energy range of 0.5 eV to 2.5 eV. The spectra feature a series of peaks (white dotted lines) and dips (gray dashed lines) that monotonously shift to higher energies as the nanodisk radius R_0 reduces from 300 nm to 100 nm. The positions of these peaks and dips do not vary with the electron beam velocity. As we will discuss in Fig. 3.3, these peaks can be associated with the different resonant modes of the nanodisk excited by the electron beam. In the following, we will focus on the underlying physics of the spectral dips and their relationship with the anapole phenomenon. We label these dips as A^E_{ij} based on symmetry reasons that will be explained below.

The anapole phenomenon originates from the destructive interference between the electric and toroidal Cartesian multipole moments inside the nanodisk with identical amplitude and far-field patterns. Due to this destructive interference, the radiation emitted by the disk is suppressed, and thus the anapole phenomenon manifests as a dip in the scattering cross section of the disk. To corroborate that the dips in the EEL spectra are associated with anapole excitation by fast electron beams, we analyze the EEL probability of the 250 nm radius nanodisk (blue line in Fig. 3.2c, where the red dots indicate the spectral dips). To that end, we perform a multipole decomposition of the current density $\mathbf{J}_\text{ind}(\mathbf{r})$ induced by the electron beam in the nanodisk. The induced current density $\mathbf{J}_\text{ind}(\mathbf{r})$ can be described by a series of exact (spherical) multipole moments induced in the disk. In the long-wavelength approximation each multipole moment can be expressed as a superposition of the so-called Cartesian multipole moments [184–186]. For example, the spherical electric

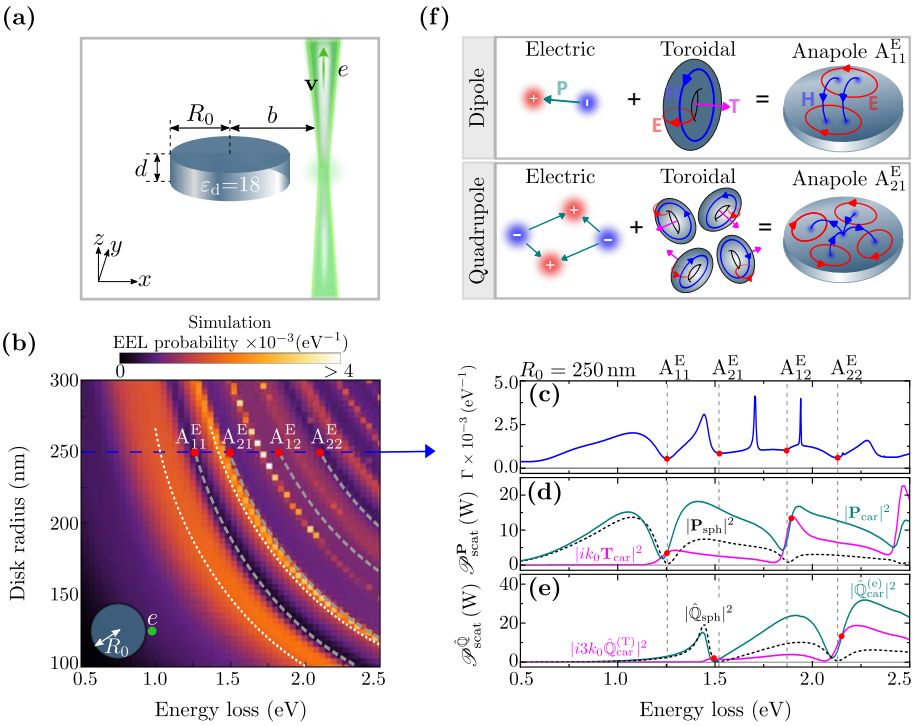

Figure 3.2: Theoretical description of optical anapoles excited by fast electron beams. (a) Sketch of the system under study: a high-index dielectric nanodisk (blue cylinder) with dielectric function $\varepsilon_d = 18$, thickness $d = 55$ nm and radius R_0 excited by a focused electron beam (green ray, e is the elementary charge) traveling along the z-direction with velocity v at a distance b (impact parameter) with respect to the nanodisk center. (b) EEL probability $\Gamma(\omega)$ calculated as a function of both the nanodisk radius R_0 and the energy loss experienced by the electron beam. White dotted lines are guides to the eye and mark the position of the first two peaks in the EEL spectra. Gray dashed lines mark the position of four dips in the EEL spectra and are labeled as A^E_{ij}, according to their symmetry as described in the text. (c) Simulated EEL probability spectrum (blue line) on a nanodisk with $R_0 = 250$ nm. The red dots mark the spectral dip positions. (d) Scattered power of the dipole moments $\mathbf{P}_{\mathrm{sph}}$, $\mathbf{P}_{\mathrm{car}}$ and $\mathbf{T}_{\mathrm{car}}$ induced in the disk with $R_0 = 250$ nm. (e) Scattered power of the quadrupole moments $\hat{\mathbb{Q}}_{\mathrm{sph}}$, $\hat{\mathbb{Q}}^{(e)}_{\mathrm{car}}$ and $\hat{\mathbb{Q}}^{(T)}_{\mathrm{car}}$ induced in the disk with $R_0 = 250$ nm. (f) Sketch of the anapole states formed by the electric and toroidal dipoles and by the electric and toroidal quadrupoles.

dipole moment $\mathbf{P}_{\mathrm{sph}}(\omega)$ is approximated by the following superposition of the electric, $\mathbf{P}_{\mathrm{car}}(\omega)$, and toroidal, $\mathbf{T}_{\mathrm{car}}(\omega)$ Cartesian dipole moments:

$$\mathbf{P}_{\mathrm{sph}}(\omega) \approx \mathbf{P}_{\mathrm{car}}(\omega) + ik_0\mathbf{T}_{\mathrm{car}}(\omega), \tag{3.1}$$

where $k_0 = \omega/c$ is the wavenumber in vacuum. When the electric and toroidal Cartesian dipole moments are equal in magnitude and show opposite phases,

$\mathbf{P}_{\mathrm{car}}(\omega) = -ik_0\mathbf{T}_{\mathrm{car}}(\omega)$, the spherical electric dipole moment $\mathbf{P}_{\mathrm{sph}}(\omega)$ vanishes, suppressing the radiated field. This situation describes the condition for the excitation of an optical anapole [167]. In Appendix D, we provide further details on the calculation of the spherical and Cartesian multipoles as well as on the multipole expansion in the long-wavelength approximation.

To compare the multipole decomposition with the EEL spectrum of the 250 nm disk, we calculate the scattered power from the dipole and quadrupole moments of the induced current density $\mathbf{J}_{\mathrm{ind}}(\mathbf{r})$ (see Appendix D). The scattered power from these multipole orders adequately captures the spectral features of the EEL spectrum across the energy range from 0.5 eV to 1.5 eV. Above 1.5 eV the EEL spectrum reveals additional spectral features that can be reproduced by also considering the scattered power from higher-order multipoles.

Figure 3.2d shows the calculated scattered powers from the spherical electric dipole moment $\mathscr{P}_{\mathrm{scat}}^{\mathbf{P}_{\mathrm{sph}}} \propto |\mathbf{P}_{\mathrm{sph}}(\omega)|^2$ (black dashed line), as well as the Cartesian electric $\mathscr{P}_{\mathrm{scat}}^{\mathbf{P}_{\mathrm{car}}} \propto |\mathbf{P}_{\mathrm{car}}(\omega)|^2$ (green line) and toroidal $\mathscr{P}_{\mathrm{scat}}^{\mathbf{T}_{\mathrm{car}}} \propto |ik_0\mathbf{T}_{\mathrm{car}}(\omega)|^2$ (magenta) dipole moments. The spectrum of $|\mathbf{P}_{\mathrm{sph}}(\omega)|^2$ features a dip at around 1.25 eV marked as $\mathrm{A}_{11}^{\mathrm{E}}$. A direct comparison of the EEL spectrum (Fig. 3.2c) and the spectrum of the scattered power by the spherical dipole moment (black dashed line in Fig. 3.2d) shows that the dip in $|\mathbf{P}_{\mathrm{sph}}(\omega)|^2$ matches the lowest-energy dip in $\Gamma(\omega)$, indicated by the gray dashed lines. In addition, this dip occurs at the energy where the electric and toroidal Cartesian dipole moments induced in the nanodisk show equal magnitude and opposite phase (the intersection of green and magenta lines at $\mathrm{A}_{11}^{\mathrm{E}}$ in Fig. 3.2d). This confirms that the lowest-energy dip in the EEL spectra of the nanodisk is associated with the optical anapole excited by the fast electron beam. We refer to this anapole as the first electric dipole, $\mathrm{A}_{11}^{\mathrm{E}}$, anapole state. We note that the ideal anapole (zero in the EEL probability) is not fully achieved due to higher-order multipolar contributions to the energy loss, and thus, an "attenuated dip" can be observed in the EEL spectra.

Analogously, we can understand the dip at 1.52 eV in the EEL spectrum (marked as $\mathrm{A}_{21}^{\mathrm{E}}$ in Fig. 3.2c) as due to the destructive interference between electric and toroidal quadrupole current distributions with identical far-field patterns [187]. To demonstrate this, we calculate the electric spherical $\hat{\mathbb{Q}}_{\mathrm{sph}}(\omega)$, Cartesian electric $\hat{\mathbb{Q}}_{\mathrm{car}}^{(\mathrm{e})}(\omega)$ and toroidal $\hat{\mathbb{Q}}_{\mathrm{car}}^{(\mathrm{T})}(\omega)$ quadrupole moments of the induced current density $\mathbf{J}_{\mathrm{ind}}(\mathbf{r})$. In the long-wavelength approximation, one finds that the spherical electric quadrupole moment has the following form (see Appendix D):

$$\hat{\mathbb{Q}}_{\mathrm{sph}}(\omega) \approx \hat{\mathbb{Q}}_{\mathrm{car}}^{(\mathrm{e})}(\omega) + 3ik_0\hat{\mathbb{Q}}_{\mathrm{car}}^{((\mathrm{T})}(\omega), \tag{3.2}$$

and thus, the condition for the excitation of electric quadrupole anapole states is $\hat{\mathbb{Q}}_{\mathrm{car}}^{(\mathrm{e})} = -3ik_0\hat{\mathbb{Q}}_{\mathrm{car}}^{(\mathrm{T})}$.

In Fig. 3.2e we show the scattered power from the spherical electric quadrupole moment $\mathscr{P}_{\mathrm{scat}}^{\hat{\mathbb{Q}}_{\mathrm{sph}}} \propto |\hat{\mathbb{Q}}_{\mathrm{sph}}(\omega)|^2$ (black dashed line), Cartesian electric $\mathscr{P}_{\mathrm{scat}}^{\hat{\mathbb{Q}}_{\mathrm{car}}^{(\mathrm{e})}} \propto |\hat{\mathbb{Q}}_{\mathrm{car}}^{(\mathrm{e})}(\omega)|^2$ (green line) and toroidal $\mathscr{P}_{\mathrm{scat}}^{\hat{\mathbb{Q}}_{\mathrm{car}}^{(\mathrm{T})}} \propto |3ik_0\hat{\mathbb{Q}}_{\mathrm{car}}^{(\mathrm{T})}(\omega)|^2$ (magenta line) quadrupole moments. From the green and magenta spectra we clearly see that the Cartesian and toroidal quadrupole moments have the same amplitude but opposite phase at 1.52 eV, which confirms that the dip at 1.52 eV in the EEL spectra corresponds to the excitation of the first electric quadrupole anapole state labeled as $\mathrm{A}_{21}^{\mathrm{E}}$. A schematic representation of the first electric dipole and the first electric quadrupole anapole states is presented in Fig. 3.2f.

The subsequent dips in the EEL spectrum (marked $\mathrm{A}_{12}^{\mathrm{E}}$ and $\mathrm{A}_{22}^{\mathrm{E}}$ in Fig. 3.2c) are associated with the excitation of higher-order anapole states such as the second electric dipole anapole (marked $\mathrm{A}_{12}^{\mathrm{E}}$) and the second electric quadrupole anapole (marked $\mathrm{A}_{22}^{\mathrm{E}}$) states. These dips originate from the destructive interference of the radiation produced by Cartesian electric and higher-order toroidal multipoles excited in the nanodisk [187]. The contribution of these higher-order multipoles is larger at higher energies (shorter wavelengths), and thus the conventional Cartesian multipole decomposition in the long-wavelength approximation fails to describe the spectral positions of $\mathrm{A}_{12}^{\mathrm{E}}$ and $\mathrm{A}_{22}^{\mathrm{E}}$ (compare the position of the red dots and the grey dashed lines above 1.75 eV in Figs. 3.2d and 3.2e). The spherical multipole decomposition, on the other hand, accurately reproduces the dips (anapole states) appearing in the EEL spectra. This allows us to label the j-th dip of the scattered power from the electric spherical 2^i-pole as $\mathrm{A}_{ij}^{\mathrm{E}}$.

The difference in the properties of the different anapole states excited by the fast electron beam can be observed in Fig. 3.3, where we show the spatial field distributions induced in the 250 nm radius disk at the dips marked by the red dots in Fig. 3.3a. Figure 3.3b, for example, shows the amplitude of the total electric field $|\mathbf{E}_{\mathrm{tot}}(\omega)|$ in the xy-plane at the energy of the $\mathrm{A}_{11}^{\mathrm{E}}$ anapole dip (1.255 eV), revealing regions of intense fields inside the nanodisk and two opposite vortices typically found in the optical phenomena involving anapoles. The field distribution of the $\mathrm{A}_{21}^{\mathrm{E}}$ anapole dip (1.52 eV), on the other hand, exhibits two additional vortices compared to the field pattern of the first electric anapole. We attribute this to the quadrupolar distribution of the induced current density inside the disk at 1.52 eV. In addition to the field distributions at the anapole dips, we also show in Fig. 3.3 the field distributions around the disk at the spectral peaks: 1.44 eV and 1.70 eV (marked by the open circles in Fig. 3.3a). We can observe in Fig. 3.3b, modes with 4 and 6 nodes along the azimuthal direction. The electric field of these resonant modes is predominantly confined within the disk, and notably, the number of nodes along the z-direction is zero (see Fig. 3.3c). In contrast, the amplitude of

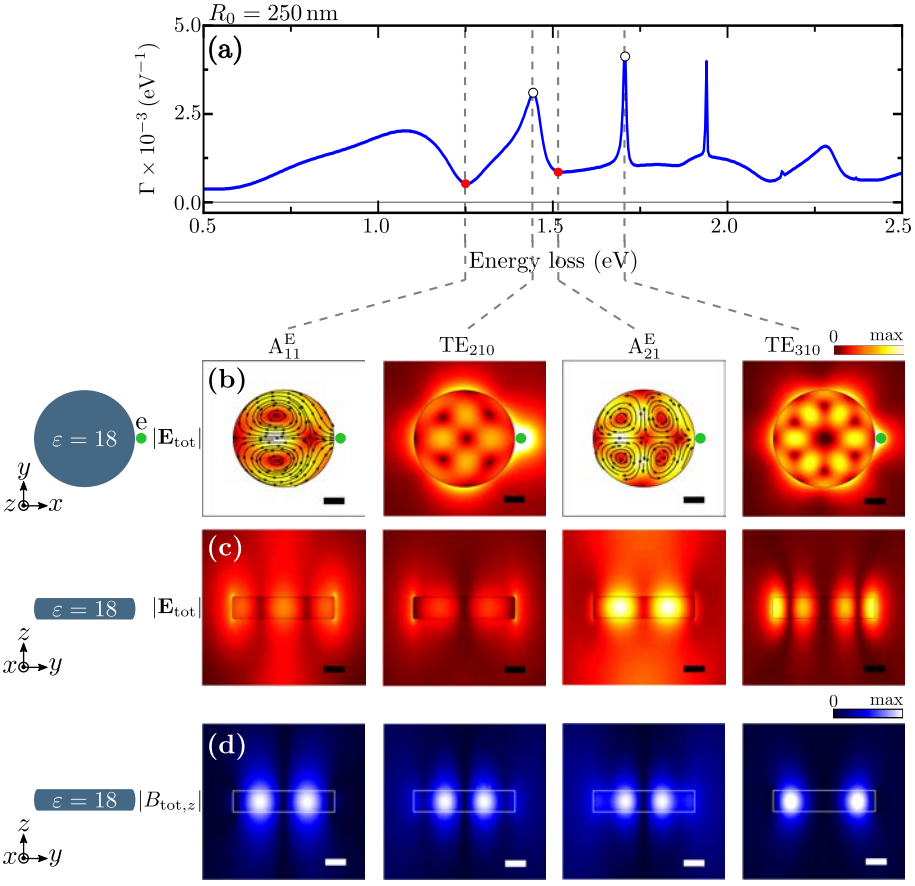

Figure 3.3: Electromagnetic field of the disk modes and optical anapoles.(a) Simulated EEL probability $\Gamma(\omega)$ for a nanodisk with $R_0 = 250\,\text{nm}$ and $d = 55\,\text{nm}$ (same as in Fig. 3.2c). Gray dashed lines mark the first two dips (indicated by the red dots) and the first two peaks (indicated by the open circles) at $(A_{11}^E)\,1.255\,\text{eV}$, $(A_{21}^E)\,1.52\,\text{eV}$ and $(TE_{210})\,1.44\,\text{eV}$, $(TE_{310})\,1.70\,\text{eV}$. The field plots in panel (b) show the amplitude of the total electric field $|\mathbf{E}_{\text{tot}}(\omega)|$ in the xy-plane for the energies marked by the gray dashed lines. Green dots indicate the electron beam position. (c) Same as (b) but for the yz-plane. (d) Same as (c) but showing the amplitude of the z-component of the total magnetic field $|B_{\text{tot},z}(\omega)|$ in the yz-plane. Insets at the left of panels (b), (c) and (d) illustrate top and side views of the nanodisk being probed by the electron beam. The scale bar in panels (b)-(d) is 100 nm. The maximum value at each field plot is (from left to right, top to bottom): $4.2 \times 10^8\,\text{V/m}$, $1.2 \times 10^9\,\text{V/m}$, $4.0 \times 10^8\,\text{V/m}$, $3.0 \times 10^9\,\text{V/m}$, $7.8 \times 10^8\,\text{V/m}$, $2.0 \times 10^9\,\text{V/m}$, $3.7 \times 10^8\,\text{V/m}$, $2.0 \times 10^9\,\text{V/m}$, $4.2\,\text{T}$, $1.6\,\text{T}$, $1.3\,\text{T}$ and $20\,\text{T}$.

the z-component of the total magnetic field, $|B_z^{\text{tot}}(\omega)|$, is different from zero within the disk, as shown in Fig. 3.3d. Consequently, we classified these modes as transverse electric (TE) ones. To label these modes, we use the standard

nomenclature of cylindrical resonator modes [188, 189]: $\mathrm{TE}_{n,k,p}$ where n, k and p indices denote azimuthal, radial and axial wavenumbers, respectively. This analysis confirms that the peaks observed in the EEL spectra are associated with the excitation of different multiple resonant modes in the disk.

3.2.1 Modeling the anapole using TCMT

The anapole is the result of the interference between multiple resonant modes excited by the fast electron beam in the nanodisk [86, 190]. In this subsection, we present an analytical model based on temporal coupled-mode theory (TCMT) that allows to describe the first electric dipole anapole, $\mathrm{A}^{\mathrm{E}}_{11}$, as the result of the far-field interference between two resonant modes of the disk excited by the fast electron beam. The importance of this simple model capable of reproducing the anapole dip in the EEL spectra will be explained in Section 3.3.

As we discussed in Chapter 1, temporal coupled-mode theory (TCMT) is a theoretical formalism that has been widely used to model the scattered and absorbed power of an object when it is illuminated with a monochromatic plane wave [82–86]. One of the key ingredients in TCMT is the expansion of the incident field over a set of appropriate scattering channels. Thus, to apply this formalism to our particular situation of a fast electron interacting with the nanodisk, we express the electric field $\mathbf{E}_{\mathrm{e}}(\mathbf{r};\omega)$ produced by the fast electron as the following sum of incoming and outgoing spherical waves propagating toward and outward the electron beam (for details see Appendix E):

$$\mathbf{E}_{\mathrm{e}}(\mathbf{r};\omega) = \sum_{\ell=0}^{\infty}\sum_{m=-\ell}^{\ell}\left[a^{\mathrm{TE}}_{\ell m}(\omega)\mathbf{E}^{\mathrm{TE},+}_{\ell m}(\mathbf{r};\omega) + a^{\mathrm{TM}}_{\ell m}(\omega)\mathbf{E}^{\mathrm{TM},+}_{\ell m}(\mathbf{r};\omega)\right] + \left[a^{\mathrm{TE}}_{\ell m}(\omega)\mathbf{E}^{\mathrm{TE},-}_{\ell m}(\mathbf{r};\omega) + a^{\mathrm{TM}}_{\ell m}(\omega)\mathbf{E}^{\mathrm{TM},-}_{\ell m}(\mathbf{r};\omega)\right], \tag{3.3}$$

where $a^{q}_{\ell m}(\omega)$ are expansion coefficients determined by Eqs. (E.2)a-(E.2)b and $\mathbf{E}^{q,\pm}_{\ell m}(\mathbf{r};\omega)$ are vector spherical harmonics defined by Eqs. (E.5)-(E.7) and (E.9)-(E.10). Each spherical wave $\mathbf{E}^{q,\pm}_{\ell m}$ defines a scattering channel that can be labeled as $\{q,\ell,m\}$, with q representing the polarization of the field (TM or TE)[1], $\ell = 0,1,2,3,\ldots$ and $m = -\ell,\cdots,\ell$. The scattering of the disk, coming

[1]Note that in Fig. 3.3, we classified the disk modes as transverse electric (TE) or transverse magnetic (TM) depending on whether the z-component of the electric or magnetic field is zero inside the disk. In Eq. (3.3), however, the labels TE or TM denote the components of the electric $\mathbf{E}_{\mathrm{e}}(\mathbf{r};\omega)$ and magnetic $\mathbf{B}_{\mathrm{e}}(\mathbf{r};\omega)$ fields orthogonal to the position vector $\mathbf{r}$. Further details can be found in Appendix E.

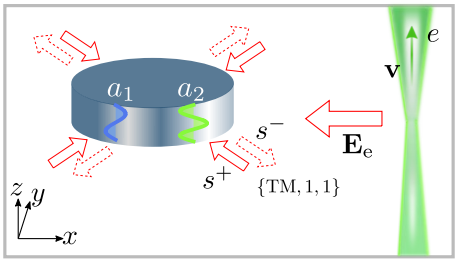

Figure 3.4: Sketch of the two resonant modes being excited by the electron beam. Schematics of the fast electron beam illuminating the nanodisk. Solid arrows represent incoming waves, s^+, toward the disk, whereas dashed arrows represent outgoing waves, s^-, outward the disk. In the schematics the two resonant modes with amplitudes a_1, a_2 are excited by the electron beam. These two resonant modes scatter along the channel $\{\mathrm{TM}, 1, 1\}$ to produce the first electric anapole state $\mathrm{A}^{\mathrm{E}}_{11}$.

from the response to the electromagnetic field of the incident electron beam, couples to the infinite set of scattering channels $\{q, \ell, m\}$ determined by the incident field, as illustrated in Fig. 3.4. The optical anapole characterized by complete suppression of the scattered field by the disk can be modeled as a single-channel scattering problem as we discuss next.

The first electric dipole anapole state, $\mathrm{A}^{\mathrm{E}}_{11}$, originates from the destructive interference of the radiation produced by the Cartesian electric and toroidal dipoles, both of which radiate in the TM, $\ell = 1$ channel [167, 185, 191]. This constrains the $\mathrm{A}^{\mathrm{E}}_{11}$ anapole to occur in three linearly-independent scattering channels: $\{\mathrm{TM}, 1, -1\}$, $\{\mathrm{TM}, 1, 0\}$ and $\{\mathrm{TM}, 1, 1\}$. The Cartesian electric and toroidal dipoles showing the fields of a linearly polarized dipole further constrain the first electric dipole anapole to the $m = \pm 1$ channels which have identical scattering coefficients. To model the $\mathrm{A}^{\mathrm{E}}_{11}$ anapole state excited by the fast electron beam, we thus assume that the scattered field of the nanodisk couples dominantly to the single scattering channel $\{\mathrm{TM}, 1, 1\}$. We then approximate the scattered field of the disk as follows:

$$\mathbf{E}_{\mathrm{scat}}(\mathbf{r}; \omega) \approx b^{\mathrm{TM}}_{11}(\omega)\, \mathbf{E}^{\mathrm{TM},-}_{11}(\mathbf{r}; \omega), \tag{3.4}$$

with $b^{\mathrm{TM}}_{11}(\omega)$ being the amplitude of the scattered field in the $\{\mathrm{TM}, 1, 1\}$ channel. We further assume that the $\mathrm{A}^{\mathrm{E}}_{11}$ anapole is the result of the far-field interference of two resonant modes of the disk radiating in the channel $\{\mathrm{TM}, 1, 1\}$. These resonant modes have amplitudes $a_1(t)$, $a_2(t)$, resonant frequencies ω_1, ω_2 and total decay rates γ_1, γ_2, respectively. Thus, to model

Within TCMT, the two resonant modes excited by the fast electron can be modeled by with an effective 2×2 Hamiltonian, $\hat{\mathbb{H}}_2$. Indeed, the dynamics of

the system is determined by the following equation [192]:

$$\frac{\mathrm{d}\mathbf{A}_2(t)}{\mathrm{d}t} = -i\hat{\mathbb{H}}_2\,\mathbf{A}_2(t) + \mathbf{K}_2\,s^+(t), \tag{3.5}$$

where subindex 2 stands for the dimension of the scattering problem determined by the number of resonant modes in the channel $\{\mathrm{TM},1,1\}$, $\mathbf{A}_2(t) = (a_1(t), a_2(t))^\top$ is the vector with the amplitudes of the two resonant modes of the disk (symbol $\top$ denotes transpose of a matrix). Here the resonance amplitudes are normalized such that $|a_1(t)|^2$, $|a_2(t)|^2$ correspond to the electromagnetic energies of each resonant mode. Notice that Eq. (3.5) has a similar form to Eq. (1.53), but the two resonant modes in this case are coupled to the incoming field (in our case the one produced by the electron beam) $s^+(t)$ in the scattering channel $\{\mathrm{TM},1,1\}$. This coupling to the incoming field is quantified via the vector of radiative coupling coefficients $\mathbf{K}_2 = (\kappa_1,\kappa_2)^\top$. The effective 2×2 Hamiltonian $\hat{\mathbb{H}}_2$ is given by

$$\begin{aligned}\hat{\mathbb{H}}_2 &= \underbrace{\begin{pmatrix}\omega_1 & 0\\ 0 & \omega_2\end{pmatrix}}_{\hat{\Omega}_2} - i\underbrace{\begin{pmatrix}\gamma_1^{\mathrm{abs}}/2 & 0\\ 0 & \gamma_2^{\mathrm{abs}}/2\end{pmatrix}}_{\hat{\Gamma}_2^{\mathrm{abs}}} - i\underbrace{\begin{pmatrix}\gamma_1^{\mathrm{rad}}/2 & \gamma_{12}\\ \gamma_{12} & \gamma_2^{\mathrm{rad}}/2\end{pmatrix}}_{\hat{\Gamma}_2^{\mathrm{rad}}}\\ &= \hat{\Omega}_2 - i\hat{\Gamma}_2,\end{aligned} \tag{3.6}$$

where $\hat{\Gamma}_2 = \hat{\Gamma}_2^{\mathrm{abs}} + \hat{\Gamma}_2^{\mathrm{rad}}$. From Eq. (3.6) one can observe that the matrix $\hat{\mathbb{H}}_2$ has the information of the resonant frequencies ω_1, ω_2, the absorptive decay rates γ_1^{abs}, γ_2^{abs} and the radiative decay rates, γ_1^{rad}, γ_2^{rad} of each resonant mode. The total decay rate is the sum of the absorptive and radiative contributions, $\gamma = \gamma^{\mathrm{abs}} + \gamma^{\mathrm{rad}}$, and determines the linewidth (full width at half-maximum) of the resonance. Matrix elements γ_{12} represent the far-field interference between the two resonant modes [192].

The scattered field of the disk, together with the incident field, produce the following outgoing wave

$$s^-(t) = \mathbf{D}_2\mathbf{A}_2(t) + s^+(t), \tag{3.7}$$

where $\mathbf{D}_2 = (d_1, d_2)$ is a coupling vector and $|s^+(t)|^2$, $|s^-(t)|^2$ are the powers of the incoming and outgoing waves, respectively and the subindex 2 stands for the dimension of the scattering problem. Through the time-to-frequency Fourier transform of Eqs. (3.5) and (3.7), one can find the following steady-state solution for the amplitudes of the two resonant modes

$$\mathbf{A}_2(\omega) = \left[i(\hat{\mathbb{H}}_2 - \omega\hat{\mathbb{I}})\right]^{-1}\mathbf{K}_2\,s^+(\omega), \tag{3.8}$$

and the following expression for the outgoing wave:

$$s^-(\omega) = \mathbf{D}_2\mathbf{A}_2(\omega) + s^+(\omega) = \underbrace{\left[\mathbf{D}_2\left[i(\hat{\mathbb{H}}_2 - \omega\hat{\mathbb{I}})\right]^{-1}\mathbf{K}_2 + 1\right]}_{\hat{\mathbb{S}}(\omega)} s^+(\omega), \tag{3.9}$$

with $\hat{\mathbb{A}}_2(\omega) = \mathcal{F}[\hat{\mathbb{A}}_2(t)]$, $s^{\pm}(\omega) = \mathcal{F}[s^{\pm}(t)]$ and $\mathcal{F}$ is the time-to-frequency Fourier transform (see Appendix A).

Equation (3.9) relates the incoming wave $s^+(\omega)$ and the outgoing wave $s^-(\omega)$ via the scattering matrix $\hat{\mathbb{S}}(\omega)$, which, under our assumption of a single scattering channel, reduces to a single matrix element. Furthermore, the vectors $\mathbf{K}_2$ and $\mathbf{D}_2$ are not independent but instead are related via energy conservation and time-reversal symmetry of the underlying system. We explore such relations in the box presented in the next page, which allows us to write $\gamma_{12} = \sqrt{\gamma_1^{\text{rad}}\gamma_2^{\text{rad}}/4}$ and $\mathbf{K}_2 = \mathbf{D}_2^\top = (\sqrt{\gamma_1^{\text{rad}}}, \sqrt{\gamma_1^{\text{rad}}})^\top$. Substituting the latter expressions into Eqs. (3.8) and (3.9), the vector $\mathbf{A}_2(\omega)$ and the outgoing wave $s^-(\omega)$ can then be rewritten as follows:

$$\mathbf{A}_2(\omega) = \left[i(\hat{\mathbb{H}}_2 - \omega\hat{\mathbb{I}})\right]^{-1}\mathbf{D}_2^\top\, s^+(\omega), \tag{3.10}$$

$$s^-(\omega) = \hat{\mathbb{S}}(\omega)s^+(\omega), \tag{3.11}$$

where the scattering matrix is

$$\hat{\mathbb{S}}(\omega) = \left[\mathbf{D}_2\left[i(\hat{\mathbb{H}}_2 - \omega\hat{\mathbb{I}})\right]^{-1}\mathbf{D}_2^\top + 1\right]. \tag{3.12}$$

In addition, the amplitude of the outgoing wave $s^-(\omega)$ can be expressed as a sum of the contributions of the scattered and the incident fields (Eqs. (3.4) and (3.5)) as: $s^-(\omega) = a_{11}^{\text{TM}}(\omega) + b_{11}^{\text{TM}}(\omega)$. Substituting this last relation into Eq. (3.9), one can deduce that the amplitude of the scattered field $b_{11}^{\text{TM}}(\omega)$ is

$$b_{11}^{\text{TM}}(\omega) = a_{11}^{\text{TM}}(\omega)\left[\hat{\mathbb{S}}(\omega) - 1\right], \tag{3.13}$$

where $s^+(\omega) = a_{11}^{\text{TM}}(\omega)$ is the incoming radiation. Thus, the radiated power by the nanodisk can be calculated as

$$\mathscr{P}_{\text{scat}}(\omega) = |b_{11}^{\text{TM}}(\omega)|^2 = |\hat{\mathbb{S}}(\omega) - 1|^2|\, s^+(\omega)|^2, \tag{3.14}$$

Relationship of $\hat{\Gamma}_2$ with $\mathbf{K}_2$ and $\mathbf{D}_2$

Energy conservation:
In the absence of incident radiation ($s^+(t) = 0$) and with low absorption losses, energy conservation states that the power dissipated by the resonator should be transformed into outgoing waves. This statement can be written mathematically as follows:

$$\frac{\mathrm{d}}{\mathrm{d}t}(\mathbf{A}_2(t)\mathbf{A}_2^\dagger(t)) = -|s^-(t)|^2. \tag{3.15}$$

Substituting Eqs. (3.5) and (3.7) into Eq. (3.15), one finds that energy conservation implies the following condition on vector $\mathbf{D}_2$:

$$\mathbf{D}_2^\dagger \mathbf{D}_2 = 2\hat{\Gamma}_2, \tag{3.16}$$

where the symbol † denotes conjugate transpose of a matrix.

Time-reversal symmetry:
When $s^+(t) = 0$, one finds from Eq. (3.5) that the amplitude of the resonant modes decay exponentially in time as

$$a_j(t) = a_j(0)e^{-i\omega_j t}e^{-\gamma_j t} \quad \text{with} \quad j = 1, 2, \tag{3.17}$$

where $a_j(0)$ are the resonance amplitudes at time $t = 0$. As a result of this decay in time, the outgoing wave produced by the two resonant modes also decays exponentially in time according to the following relation (Eq. (3.7)): $s^-(t) = \mathbf{D}_2\mathbf{A}_2(t) = d_1a_1(0)e^{-i\omega_1 t}e^{-\gamma_1 t} + d_2a_2(0)e^{-i\omega_2 t}e^{-\gamma_2 t}$. If we apply the time-reversal transformation $t \mapsto -t$ to the decay process described before, then the resonator is pumped by the incoming wave $\tilde{s}^+(t) = (s^-(-t))^* = \mathbf{D}_2^*\mathbf{A}_2^*(-t)$ whose amplitude exponentially grows in time. Such an excitation produces resonance amplitudes that also grow exponentially in time, without the outgoing wave. Thus, in the time-reversed case, the amplitudes of the two resonant modes (Eq. (3.17)) transform as $\tilde{a}_j(t) = a_j^*(-t)$ or equivalently as $\tilde{\mathbf{A}}_2(t) = \mathbf{A}_2^*(-t)$, and their dynamics is determined by the following equation (complex conjugate of Eq. (3.5) and change $t \mapsto -t$):

$$\frac{\mathrm{d}\tilde{\mathbf{A}}_2(t)}{\mathrm{d}t} = -i\hat{\mathbb{H}}_2^*\,\tilde{\mathbf{A}}_2(t) - \mathbf{K}_2\,\tilde{s}^+(t). \tag{3.18}$$

Through a time-to-frequency Fourier transform of Eq. (3.18), setting $\omega\hat{\mathbb{I}} = \hat{\Omega}_2 - i\hat{\Gamma}_2$ and using Eqs. (3.7) and (3.16), one finds that time-reversal symmetry implies the following condition:

$$\mathbf{K}_2 = \mathbf{D}_2^\top. \tag{3.19}$$

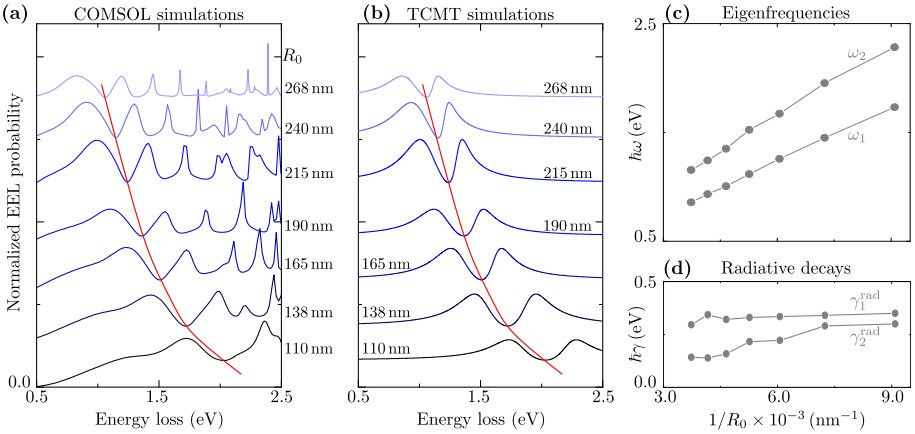

Figure 3.5: COMSOL and TCMT simulations of EEL of the dielectric disks. Electron energy loss spectra obtained from (a) numerical (COMSOL) simulations of high-index dielectric disks and (b) TCMT using Eq. (3.21). The EEL spectra are normalized to the maximum value of $\Gamma(\omega)$ obtained for each radius R_0 and the results are displaced in the vertical axis for clarity. Panels (c) and (d) show the parameters extracted from the TCMT for each case as a function of the inverse radius, $1/R_0$.

whereas the total absorbed power by the nanodisk can be calculated as the sum of the absorbed power by the two resonant modes, that is,

$$\mathscr{P}_{\rm abs}(\omega) = \gamma_1^{\rm abs}|a_1(\omega)|^2 + \gamma_2^{\rm abs}|a_2(\omega)|^2 = 2\,\mathbf{A}_2^\dagger(\omega)\,\Gamma_2^{\rm abs}\,\mathbf{A}_2(\omega). \tag{3.20}$$

Finally, to calculate the electron energy losses within the TCMT formalism, we assume that the energy lost by the electron beam when interacting with the nanodisk is equal to the energy dissipated by the disk either via heating (ohmic losses) or radiation into the far field [193]. Then, the electron energy-loss probability $\Gamma(\omega)$ is proportional to the sum of the scattered and absorbed power (extinction) by the nanodisk excited by the probing electron:

$$\Gamma(\omega) \propto \mathscr{P}_{\rm scat}(\omega)+\mathscr{P}_{\rm abs}(\omega) = |\hat{\mathbb{S}}(\omega)-1|^2|\,s^+(\omega)|^2+2\,\mathbf{A}_2^\dagger(\omega)\,\Gamma_2^{\rm abs}\,\mathbf{A}_2(\omega), \tag{3.21}$$

where the vector $\mathbf{A}_2(\omega)$ and the scattering matrix (a scalar in our case) $\hat{\mathbb{S}}(\omega)$ are determined by Eqs. (3.10)-(3.12).

Once we have developed the coupled-mode theory, we then apply it to reproduce the simulated EEL spectra of the model disks with $\varepsilon = 18$, $d = 70\,$nm and radii $R_0 = 268\,$nm, $240\,$nm, $215\,$nm, $190\,$nm, $165\,$nm, $138\,$nm and $110\,$nm as shown in Fig. 3.5a. In particular, we use Eq. (3.21) to reproduce the simulated EEL spectra and find the eigenfrequencies ω_1, ω_2 and radiative decay rates $\gamma_1^{\rm rad}$, $\gamma_2^{\rm rad}$ of the two resonant modes that produce the first dip in the

simulated EEL spectra. We assume that $\gamma_1^{\text{abs}} = \gamma_1^{\text{abs}} = 0$. The result of this procedure is plotted in Figs. 3.5b-c, where we observe that the spectra obtained within the coupled-mode theory accurately reproduces the first dip appearing in the simulated EEL spectra (highlighted by the red lines in Figs. 3.5a and 3.5b). Note in Figs. 3.5c and 3.5d that the eigenfrequencies and radiative decay rates of the two resonant modes disperse linearly as a function of $1/R_0$. This tendency of the dispersion is in good agreement with the typical linear dispersion of Mie-resonances sustained by high-index dielectric nanodisks [194], corroborating the adequacy of the coupled-mode model to capture the spectral features of our system. In Appendix F, we show in Table F.1 all the parameters obtained from the TCMT plotted in Figs. 3.5c and 3.5d.

3.2.2 Far-field spectroscopy vs EELS

To show the complementary and extra features revealed in EELS as compared to far-field optical spectroscopy in probing anapoles, we compare the EEL spectra of high-index dielectric disks with the far-field optical scattering spectra of the same disks. To that end, we calculate the scattering cross section $\sigma_{\text{scat}}(\omega)$ of the disks shown in Fig. 3.2b illuminated by a linearly-polarized plane wave propagating along the z-axis (illustrated in Fig. 3.6a). The result is shown in Fig. 3.6b and 3.6c (see Appendic B for the details of the numerical simulations). Similar to the EEL spectra $\Gamma(\omega)$, we observe dips in $\sigma_{\text{scat}}(\omega)$ that shift to higher energies as the nanodisk radius R_0 decreases (see gray dashed lines in Fig. 3.6b). By performing a multipole decomposition of the current density $\mathbf{J}_{\text{ind}}(\omega)$ induced in the disk of $R_0 = 250\,\text{nm}$ (see Figs. 3.6d and 3.6e), we can associate these dips (analogue to the discussion of Fig. 3.2) with the excitation of the first (A_{11}^{E}), second (A_{12}^{E}) and third (A_{13}^{E}) electric dipole anapole states, whose field distributions inside the disk are shown in Fig. 3.6f. On the other hand, quadrupolar contributions are negligible in the spectra, as compared to dipolar contributions (Figs. 3.6d and 3.6e), highlighting the advantage of EELS for probing higher-order anapole states.

The possibility to probe optical anapole states with fast electron beams turns EELS into a promising tool for fundamental studies of optical phenomena involving anapoles. In the following section, we present an experimental verification (supported by numerical calculations) of optical anapoles probed using EELS. The TCMT developed in this section will be extremely useful to describe the electromagnetic coupling between anapoles and excitons supported by the WS_2 nanodisks.

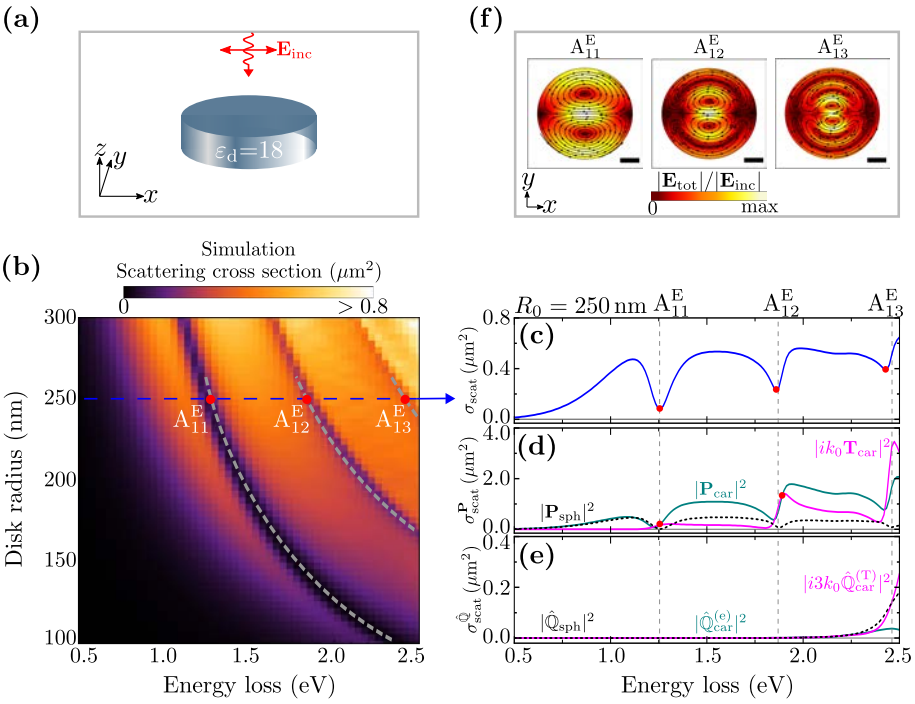

Figure 3.6: Optical anapoles excited by plane wave illumination. (a) A high-index dielectric nanodisk (blue cylinder) is excited by a plane wave ($\mathbf{E}_{\rm inc}$, red arrow) that propagates perpendicular to the top surface of the disk (normal incidence) and is polarized along the x-axis. (b) Simulated scattering cross section $\sigma_{\rm scat}(\omega)$ of the nanodisk calculated as a function of both the disk radius R_0 and the photon energy $\hbar\omega$. Gray dashed lines are guides to the eye and indicate the position of the first three dips in the scattering cross section spectra. (c) $\sigma_{\rm scat}(\omega)$ obtained for the nanodisk with $R_0 = 250\,$nm. The red dots mark the spectral dip positions. (d) Contribution of the scattering cross section of the $\mathbf{P}_{\rm sph}$, $\mathbf{P}_{\rm car}$ and $\mathbf{T}_{\rm car}$ dipole moments induced in the nanodisk with $R_0 = 250\,$nm. (e) Contribution of the scattering cross section of the $\hat{\mathbb{Q}}_{\rm sph}$, $\hat{\mathbb{Q}}^{(e)}_{\rm car}$ and $\hat{\mathbb{Q}}^{(T)}_{\rm car}$ quadrupole moments induced in the nanodisk with $R_0 = 250\,$nm. (f) Amplitude of the total electric field $|\mathbf{E}_{\rm tot}(\omega)|$ inside the disk at the yx-plane, for energies: (A^{E}_{11}) 1.255 eV, (A^{E}_{12}) 1.87 eV and (A^{E}_{31}) 2.46 eV. The scale bar is 100 nm. The field plots are normalized to the amplitude of the incident plane wave $|\mathbf{E}_{\rm inc}|$. In each case, the maximum value of $|\mathbf{E}_{\rm tot}(\omega)|/|\mathbf{E}_{\rm inc}|$ is (from left to right): 3.0, 5.4 and 4.7.

3.3 Optical anapoles in WS_2 nanodisks

To experimental verify the excitation of anapoles using EELS, our collaborators fabricate high-index TMDC WS_2 nanodisks with various radii and performed electron energy loss spectroscopy to spatially resolve their optical behavior. We note that Battulga Munkhbat, under the supervision of Prof. Timur Shegai at Chalmers University of Technology, fabricated the individual WS_2 nanodisks. Andrew Yankovich, on the other hand, has conducted the EELS experiments at Chalmers University of Technology under the supervision of Prof. Eva Olsson. We refer the reader to ref. [195] for specific details on the fabrication procedure and EELS experiments.

3.3.1 Fabrication of WS_2 nanodisks

The WS_2 disks were synthesized by transferring a mechanically exfoliated WS_2 flake onto a 50 nm thick SiN membrane and by performing a combination of e-beam lithography and dry etching. This process enables the creation of donut-shaped etched patterns with isolated nanodisks at their center with selected radii.

Figure 3.7a shows high-angle annular dark-field (HAADF) STEM images of nine WS_2 nanodisks of different size, demonstrating the ability to precisely synthesize isolated nanodisks with controllable radii ranging from around 88 nm to 295 nm. Simultaneously acquired 53° tilted HAADF and secondary electron (SE) STEM images of nanodisks with various radii (Figs. 3.7b-g) reveal the morphology of the nanoresonators and the residual resist material that remains on top of the WS_2 nanodisks after fabrication, as indicated in Fig. 3.7e. High-angle annular dark-field STEM images are dominated by mass-thickness Z-contrast [196], and thus, the brightest regions reveal the position and shape of the WS_2 nanodisks below the primarily low-Z residual resist material. To identify the size and morphology of both the WS_2 nanodisks and the residual material, we use SE image contrast which is sensitive to surface topography [197]. From Figs. 3.7b-g we observe two main features of the WS_2 nanodisks: (i) the edges with small vertically aligned surface variations and (ii) a tapered side surface with larger radii at the base. These variations of the WS_2 nanodisk

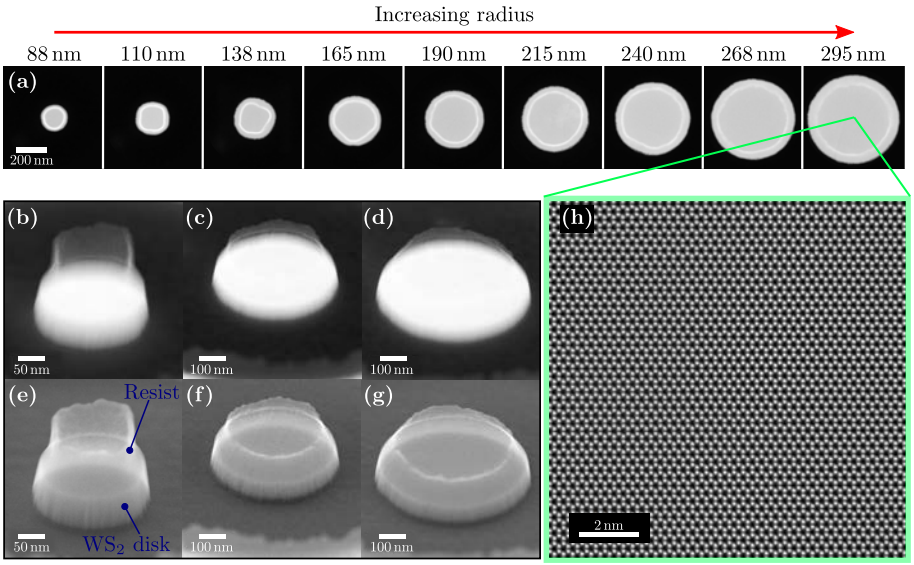

Figure 3.7: Fabrication of WS_2 nanodisks. (a) Plan view HAADF STEM images of nine WS_2 nanodisks with radii ranging from 88 nm to 295 nm. Disk radii are shown at the top of each image and a scale bar of 200 nm stands for all the images. (b)-(d) 53° tilted HAADF STEM images of the nanodisks with radii 110 nm, 240 nm and 295 nm, respectively. (e)-(g) 53° tilted SE STEM images simultaneously acquired of the three nanodisks shown in panels (b)-(d). (h) Atomic resolution HAADF STEM image taken from the center of the largest (295 nm) disk. Images are obtained by Andrew Yankovich at Chalmers University of Technology (Gothenburg, Sweden).

radius are small compared to the average nanodisk radius, and thus modeling our nanodisks as perfect disks is an adequate description of the system. The residual resist could lead to minor shifts in energy of the disk modes, but does not alter the excitation of the nanodisk modes and anapole states. Therefore, the resist has not been included in our model calculations. In Fig. 3.7h we show an atomic-resolution HAADF STEM image from the center of a nanodisk, revealing that the single crystalline atomic structure of the WS_2 flake is preserved after the nanodisk fabrication process.

The thickness of the nanodisk determines its optical response to a probing fast electron, therefore we experimentally measure the disk thickness using three independent methods: EELS, tilted view STEM imaging, and the combination of optical reflectivity and transfer-matrix fitting. As we show in ref. [195], from the three methods, we can estimate a disk thickness of around $d \approx 70$ nm.

3.3.2 Optical properties of WS_2

As sketched in Fig. 3.8a, multilayer tungsten disulfide is a transition metal dichalcogenide material composed of monolayers of W atoms (transition-metal atoms) surrounded in a sandwich structure by S atoms (chalcogen atoms). The stacking of the multiple layers that constitute WS_2 is mediated via van der Waals forces, which produce a uniaxial optical response of the material that can be described by the following dielectric tensor [62]:

$$\hat{\varepsilon}_{WS_2} = \begin{pmatrix} \varepsilon_\perp & 0 & 0 \\ 0 & \varepsilon_\perp & 0 \\ 0 & 0 & \varepsilon_\parallel \end{pmatrix}, \tag{3.22}$$

where we assumed that the stacking direction of the WS_2 layers is along the z-axis. Thus, $\varepsilon_x = \varepsilon_y = \varepsilon_\perp$ is the in-plane component of the permittivity tensor and $\varepsilon_z = \varepsilon_\parallel$ is the out-of-plane component parallel to the optical axis of WS_2 (see Fig. 3.8a).

An interesting property of WS_2 is its ability to support excitons in the visible frequency range. This can be clearly observed in the optical response of this material shown in Fig. 3.8b, where we plot the in- and out-of-plane components of the permittivity tensor of WS_2 obtained from ellipsometry experiments [62]. From the plots, we observe three promiment peaks (labeled as A, B and C) in the visible frequency range associated with the A-, B- and C-excitons in WS_2. For reasons that will become clear in the next subsection, we model the in- and out-of-plane permittivities of WS_2 by a single excitonic excitation in the in-plane direction, and ad a dielectric in the out-of-plane direction, as follows [183]:

$$\varepsilon_\perp = \varepsilon_\infty + f_{ex} \frac{\omega_{ex}^2}{\omega_{ex}^2 - \omega^2 - i\gamma_{ex}\omega}, \tag{3.23}$$

$$\varepsilon_\parallel = 7, \tag{3.24}$$

where $\varepsilon_\infty = 18$ is the high-frequency permittivity, $f_{ex} = 0.4$ is the oscillator strength, $\hbar\omega_{ex} = 1.96\,\text{eV}$ is the exciton frequency and $\hbar\gamma_{ex} = 90\,\text{meV}$ is the exciton damping constant. Note that the model considers only the A-exciton resonance of the WS_2 (see Fig. 3.8c). As we will discuss in the following subsections, the coexistence of excitonic resonances and dispersive anapoles within the same energy range allows these resonant features to couple and hybridize with each other.

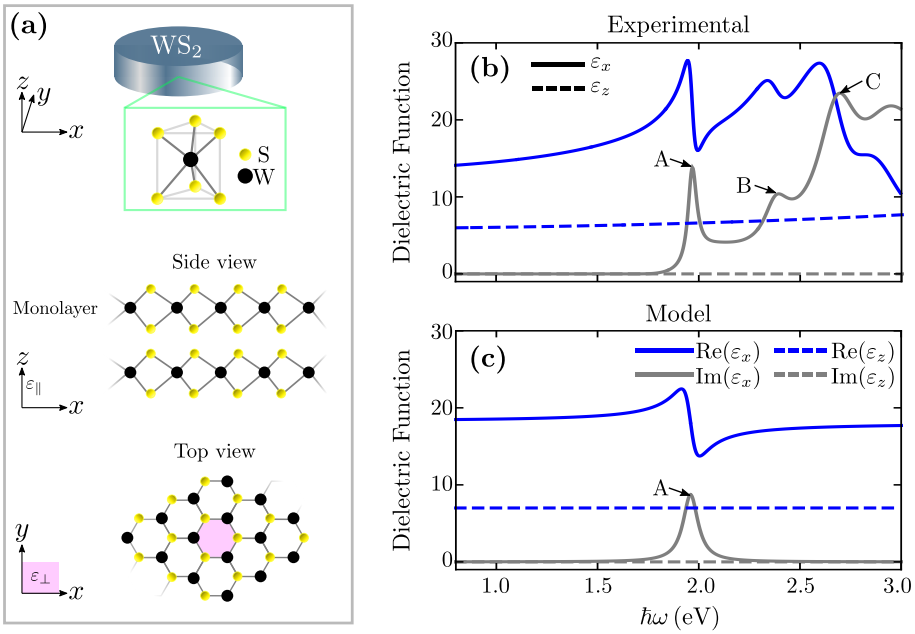

Figure 3.8: Atomic structure and dielectric function of WS_2. (a) Schematic representation of the WS_2 nanodisk and its atomic structure. Below the nanodisk is a sketch of a side and top views of the monolayers that constitute WS_2. (b) Experimental in- and out-of-plane components of the permittivity tensor of WS_2, $\varepsilon_x = \varepsilon_y = \varepsilon_\perp$ (solid lines) and $\varepsilon_z = \varepsilon_\parallel$ (dashed lines), respectively. Blue lines represent real parts and gray lines imaginary parts. The dielectric functions were obtained from ref. [62]. The labels A, B and C indicate the A-, B-, and C-exciton absorption bands of WS_2. (c) Same as (b) but the components of the dielectric function are the ones given by Eqs. 3.23 and 3.24 with a single excitonic excitation in the material.

3.3.3 EELS of WS_2 nanodisks

To experimentally investigate the optical response of WS_2 nanodisks to a fast electron beam, our collaborators performed monochromated STEM EELS experiments using a 200 keV electron beam with less than 1 nm spatial resolution and 20 meV − 40 meV energy resolution. In Fig. 3.9a we show the collected EEL spectra as a function of nanodisk radius as obtained when an aloof electron beam passes outside ($b < R + 5$ nm) the edge of each nanodisk shown in Fig. 3.7a. From the EEL spectra we observe a low-energy loss signal composed of multiple sharp peaks and dips (see Fig. 3.9a). The number of peaks and dips decreases steadily as the disk size is reduced and their position shifts monotonously to higher energies in agreement with our theoretical prediction

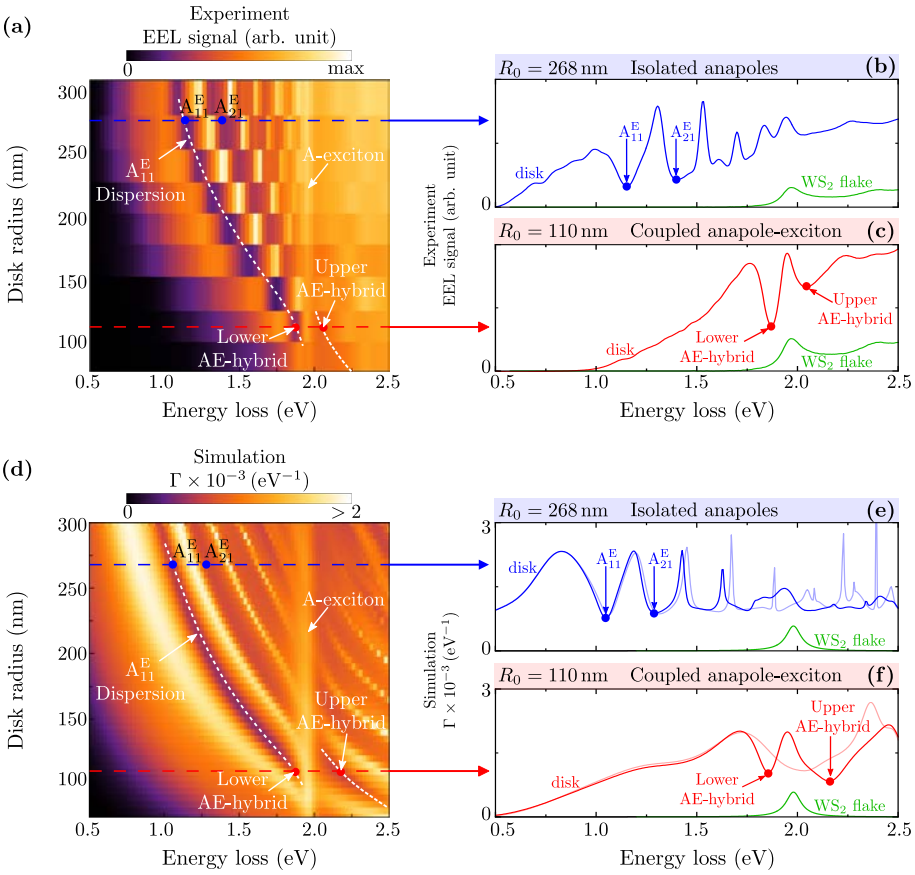

Figure 3.9: Electron energy loss spectra of the WS_2 nanodisks. (a) Experimental EEL spectra of the nine disks displayed in Fig. 3.7(a). Blue solid line in (b) and red solid line in (c) show the EEL spectra for disks with $R_0 = 268$ nm and $R_0 = 110$ nm, respectively. Green lines in panels (b) and (c) show EEL spectra from an unpatterned WS_2 flake. (d) Simulated EEL probability $\Gamma(\omega)$ as a function of both the nanodisk radius R_0 and the energy loss experienced by the electron beam. Blue solid line in (e) and red solid line in (f) show the EEL spectra for disks with $R_0 = 268$ nm and $R_0 = 110$ nm, respectively. Thin blue and thin red spectra correspond to $\Gamma(\omega)$ obtained with disks of artificial permittivity $\varepsilon_d = 18$. Green lines in panels (e) and (f) show calculated $\Gamma(\omega)$ for a WS_2 flake of 70 nm thickness. White dashed lines in panels (a) and (d) are guides to the eye indicating anti-crossing of the A^E_{11} anapole and the A-exciton. Green curves in (b) and (c) were scaled to be consistent with the relatives heights in (e) and (f). Numerical calculations are performed considering that the nanodisk is on top of a 50 nm thick substrate layer characterized by the permittivity of SiN $\varepsilon_{SiN} = 4.1853$. Experimental data are obtained by Andrew Yankovich at Chalmers University of Technology (Gothenburg, Sweden).

(Fig. 3.2b).

All collected EEL spectra of the WS_2 disks exhibit a spectral peak at around

1.95 eV (bright region in Fig. 3.9a), above which the EEL signal dampens and blurs. For a better quantitative comparison, we show in Figs. 3.9b and 3.9c individual experimental EEL spectra of the $R_0 = 268$ nm (blue spectrum) and $R_0 = 110$ nm (red spectrum) nanodisks, respectively. The peak at 1.96 eV is due to the excitation of the A-exciton of WS_2 (see Fig. 3.8b), as identified in the EEL spectrum of an unpatterned WS_2 flake shown by the green line in Figs. 3.9b and 3.9c.

To better understand the measured EEL spectra, we calculate numerically the EEL probability $\Gamma(\omega)$ for WS_2 nanodisks with similar radius ranging from 88 nm to 295 nm and thickness $d = 70$ nm (Fig. 3.9d). In contrast to the numerical simulations shown in Fig. 3.2b, the calculations shown in Figs. 3.9d-f were performed with the permittivity tensor given by Eqs. 3.23 and 3.24, i. e., including the A-exciton resonance of WS_2 (see Fig. 3.8c). The results of these simulations show a good agreement with the experimental spectra in the number, position, and dispersion of peaks and dips across the complete set of disk sizes (compare Figs. 3.8a and 3.8d). The excitation of the A-exciton can be consistently observed both in the experimental and simulated spectra. Above 2 eV, the peaks and dips in the simulated spectra are better resolved than in the experimental spectra, which is due to the excitation of B- and C-exciton resonances in W_2 that were not included in the numerical simulations. Incorporating a single A-exciton resonance into the permittivity tensor of WS_2 (Eqs. (3.23) and (3.24)) allows for clearly identifying the high-energy excitation in the EEL spectra (Fig. 3.9d), and thus, identifying the complex hybridization scheme.

To check whether the dips in the experimental spectra are due to the excitation of optical anapoles, we analyze the EEL signal of the 268 nm radius nanodisk (blue lines in Figs. 3.9e). Both the experimental and simulated EEL spectra show two attenuated dips between 1 eV and 1.5 eV, marked with A^E_{11} and A^E_{21} in Figs. 3.9b and 3.9e. As discussed above in Fig. 3.2, these dips can be associated with the first electric dipole and the first electric quadrupole anapole states excited in the nanodisk. To verify that the dips in this energy range are not caused by the material losses of WS_2, we simulate the EEL spectrum of the model disk with $R_0 = 268$ nm, $d = 70$ nm and artificial permittivity $\varepsilon_d = 18$ mimicking that of WS_2 without the A-exciton resonance (thin blue line in Fig. 3.9e). By comparing the solid and thin blue lines, we can observe that the two lowest-energy dips (marked with A^E_{11} and A^E_{21}) appear nearly at the same energies in both spectra, which confirms that the dips are not caused by material losses of WS_2. The differences between the solid and the thin blue spectra in Fig. 3.9e are a direct consequence of the appearance of the A-exciton resonance at 1.96 eV (identified in the EEL spectrum of a WS_2 flake shown by the green line in Fig. 3.9e). As discussed in Subsection 3.3.2, multilayered WS_2

is a natural anisotropic material, however, the anisotropy in this case does not influence the anapoles excitation, and the spectral response of the disk with isotropic permittivity is nearly identical to that of an anisotropic disk. We also note that in the experiments and simulations, the WS_2 nanodisk is located on top of a SiN substrate. This, however, does not alter the excitation of the anapole states. It slightly redshifts the resonant modes of the nanodisk, causing the anapole dips to appear at lower energies. A detailed analysis of anisotropy and substrate effects in anapoles excitation is reported in the supplementary materials of ref. [195].

Anapole-exciton hybridization

The coexistence of an excitonic resonance and the dispersive anapoles in the same object allows these resonant features to couple and hybridize with each other with different levels of strength as the nanodisk radius R_0 is varied. To explore this aspect, we trace the first electric dipole anapole state upon decreasing the nanodisk radius from 268 nm to 110 nm (white dashed line in Fig. 3.9a and 3.9d) until it reaches the energy of the A-exciton resonance, where a splitting (anti-crossing) of the dip is produced. This behavior is clearly shown in Fig. 3.9f, where we plot the simulated spectrum of the 110 nm disk radius (solid red line, extracted from Fig. 3.9d). For comparison, we also plot the spectrum of the model disk with artificial permittivity $\varepsilon_d = 18$ (thin red line). By comparing the spectra of both type of disks, one can observe that the attenuated anapole dip at 2 eV (thin red line) splits into two dips at 1.86 eV and 2.16 eV in the solid red line. Due to the hybrid nature of these dips, we refer to them as the lower anapole-exciton-hybrid (lower AE-hybrid) and the upper anapole-exciton-hybrid (upper AE-hybrid). We can also see a peak in between the two dips which originates from the excitation of excitons that do not couple to the anapole. The splitting of the dips, together with the anti-crossing feature, are signatures of the coupling between the A_{11}^{E} anapole state and the A-exciton, consistent with previous observations in far-field optical spectroscopy of WS_2 nanodisks [183].

The anti-crossing observed, and fully identified in Fig. 3.9d resembles the typical situation of coupling between an EM mode confined in an optical cavity and a dipolar excitation. As pointed out in Subsection 3.2.1, the anapole, however, is not an EM mode of the disk, but instead is the result of interference between at least two resonant modes excited by the electron beam [86, 190]. To explain the coupling between the A_{11}^{E} anapole and the A-exciton, we thus implement an analytical model of the response of the coupled anapole-exciton system based on temporal coupled mode theory. We extend the TCMT presented in Subsection 3.2.1, and model the anapole-exciton system with an

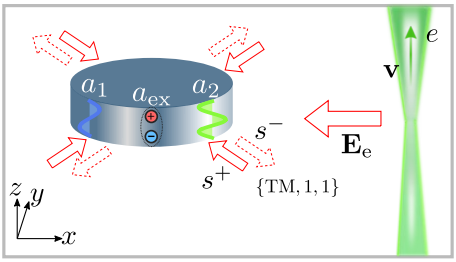

Figure 3.10: Sketch of the anapole-exciton system excited by the electron beam. Solid arrows represent incoming waves s^+ toward the disk, whereas dashed arrows represent outgoing waves s^- outward the disk. In the schematics, the two disk modes with amplitudes a_1, a_2 interact with the exciton with amplitude a_{ex}. The nanodisk scatters along the channel $\{\mathrm{TM}, 1, 1\}$ to produce two anapole-exciton dips.

effective 3×3 Hamiltonian, $\hat{\mathbb{H}}_3$. This contains the eigenfrequencies of two EM modes, whose far-field interference produces the $\mathrm{A}_{11}^{\mathrm{E}}$ anapole dip, coupled to a third non-radiating mode representing the A-exciton of WS_2.

The dynamics of the anapole-exciton coupled system is then determined by the following equation:

$$\frac{\mathrm{d}\mathbf{A}_3(t)}{\mathrm{d}t} = -i\hat{\mathbb{H}}_3\,\mathbf{A}_3(t) + \mathbf{K}_3\,s^+(t), \tag{3.25}$$

where subindex 3 stands for the dimension of the scattering problem, $\mathbf{A}_3(t) = (a_1(t), a_2(t), a_{ex}(t))^\top$ is the vector with the amplitudes of the three modes of the disk, namely the two resonant modes of the disk $a_1(t)$ and $a_2(t)$, and that of the exciton $a_{ex}(t)$. $\mathbf{K}_3 = (\sqrt{\gamma_1^{\mathrm{rad}}}, \sqrt{\gamma_2^{\mathrm{rad}}}, 0)^\top$ is the vector of radiative coupling coefficients to the incoming field (produced by the electron beam), and the effective 3×3 Hamiltonian $\hat{\mathbb{H}}_3$ is given by

$$\begin{aligned}\hat{\mathbb{H}}_3 = &\underbrace{\begin{pmatrix} \omega_1 & 0 & 0 \\ 0 & \omega_2 & 0 \\ 0 & 0 & \omega_{ex} \end{pmatrix}}_{\hat{\Omega}_3} - i\underbrace{\begin{pmatrix} \gamma_1^{\mathrm{abs}}/2 & 0 & 0 \\ 0 & \gamma_2^{\mathrm{abs}}/2 & 0 \\ 0 & 0 & \gamma_{ex}/2 \end{pmatrix}}_{\hat{\Gamma}_3^{\mathrm{abs}}} \\ &- i\underbrace{\begin{pmatrix} \gamma_1^{\mathrm{rad}}/2 & \gamma_{12} & 0 \\ \gamma_{12} & \gamma_2^{\mathrm{rad}}/2 & 0 \\ 0 & 0 & 0 \end{pmatrix}}_{\hat{\Gamma}_3^{\mathrm{rad}}} + \underbrace{\begin{pmatrix} 0 & 0 & g_{1ex} \\ 0 & 0 & g_{2ex} \\ g_{1ex} & g_{2ex} & 0 \end{pmatrix}}_{\hat{\mathbb{G}}_3} \\ &= \hat{\Omega}_3 - i\hat{\Gamma}_3 + \hat{\mathbb{G}}_3,\end{aligned} \tag{3.26}$$

where $\hat{\Gamma}_3 = \hat{\Gamma}_3^{\text{abs}} + \hat{\Gamma}_3^{\text{rad}}$. The parameters $g_{1\text{ex}}$ and $g_{2\text{ex}}$ are the coupling strengths between each of the resonant modes (Subsection 3.2.2) and the A-exciton. We recall that $\gamma_1^{\text{rad}} = \gamma_1^{\text{rad}} = 0$.

Figure 3.10 shows a schematic representation of the two resonant modes coupled to the A-exciton. We can see that the three resonances are excited by the fast electron beam, and the scattered field of the disk, together with the incident illumination, produce the following outgoing wave

$$s^-(t) = \mathbf{K}_3^\top \mathbf{A}_3(t) + s^+(t). \tag{3.27}$$

Through a time-to-frequency Fourier transform of Eqs. (3.25) and (3.27), one can find the following steady-state solution for the amplitudes of the three resonant modes

$$\mathbf{A}_3(\omega) = \left[i(\hat{\mathbb{H}}_3 - \omega\hat{\mathbb{I}}) \right]^{-1} \mathbf{K}_3 \, s^+(\omega), \tag{3.28}$$

with

$$s^-(\omega) = \hat{\mathbb{S}}(\omega) s^+(\omega). \tag{3.29}$$

In this case, the scattering matrix $\hat{\mathbb{S}}(\omega)$ is determined by the following equation:

$$\hat{\mathbb{S}}(\omega) = \left[\mathbf{K}_3^\top \left[i(\hat{\mathbb{H}}_3 - \omega\hat{\mathbb{I}}) \right]^{-1} \mathbf{K}_3^\top + 1 \right], \tag{3.30}$$

and, following Eq. 3.21, we can calculate the electron energy-loss probability $\Gamma(\omega)$ as the sum of the scattered and absorbed power (extinction) by the nanodisk, as:

$$\Gamma(\omega) \propto \mathscr{P}_{\text{scat}}(\omega) + \mathscr{P}_{\text{abs}}(\omega) = |\hat{\mathbb{S}}(\omega) - 1|^2 |\, s^+(\omega)|^2 + 2\, \mathbf{A}_3^\dagger(\omega)\, \Gamma_3^{\text{abs}}\, \mathbf{A}_3(\omega). \tag{3.31}$$

We use this model to reproduce the experimental and simulated EEL spectra of the WS_2 nanodisk (Figs. 3.9a and 3.9d). Specifically, we model the electron energy losses using Eq. 3.31 and find the coupling strengths, $g_{1\text{ex}}$ and $g_{2\text{ex}}$, between each EM mode and the A-exciton resonance. The values of ω_1, ω_2 and γ_1, γ_2 are the same as those obtained in Subsection 3.2.1 (see Figs. 3.5c-d and Table F.1). We next diagonalize the effective 3×3 Hamiltonian $\hat{\mathbb{H}}_3$ (Eq. 3.26) and find the eigenfrequencies of the new hybrid modes. The results obtained with this procedure are shown in Fig. 3.11, where we show in detail the TMCT simulations, eigenfrequencies of the hybrid modes and coupling strengths. From TCMT simulations, we are able to recover the anti-crossing of the hybrid dips, as indicated by the red lines in Figs. 3.11b and 3.11f. More importantly, the analysis reveals a clear anti-crossing between the hybrid modes as one varies the nanodisk radius (see Figs. 3.11c and 3.11g), indicating that

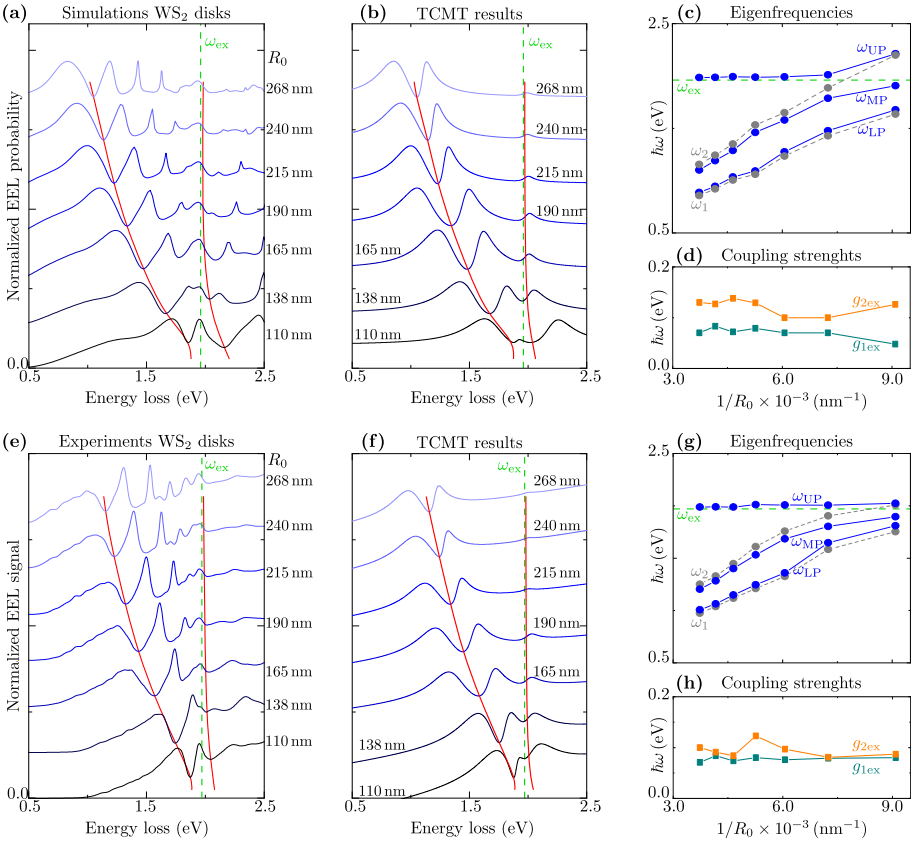

Figure 3.11: Quantitative analysis of the EEL of tungsten disulfide disks by TCMT. Electron energy loss spectra obtained from (a) numerical (COMSOL) simulations of the WS_2 disks and (b) TCMT simulations using Eq. 3.31. Panels (c)-(d) show the parameters extracted from the TCMT results as a function of the inverse radius, $1/R_0$. (e)-(h) show the same analysis as in panels (a)-(d) but for the experimental spectra as a reference. All spectra are normalized to their maximum value obtained for each radius R_0 and the results are displaced in the vertical axis for clarity.

the two electromagnetic modes are strongly coupled to the A-exciton resonance. The two dips that result from the coupling between the two modes and the A-exciton correspond to the lower and upper AE-hybrids.

3.3.4 Real-space mapping of optical anapole states

EELS in STEM shows the ability to acquire spectral information of a sample with subnanometer spatial resolution [10, 17, 198]. Typically, this is achieved by scanning the sample area with the fast electron beam, thus obtaining spectral information of the sample at different beam positions. We apply this capability to spatially resolve the resonant modes and anapoles states excited in the WS_2 disks. To that end, we collect the experimental EEL signal as a function of the position of the fast electron with respect to the nanodisk center (impact parameter b). The cylindrical symmetry of the nanodisk along the z-axis, together with the trajectory of the probing electron beam, yields an EEL signal that depends only on the impact parameter. This allows us to present the spatial distribution of the EEL signals obtained from the WS_2 nanodisks at particular energy loss by a 2D-EEL line profile showing the energy loss as a function of impact parameters for each energy.

Figure 3.12 shows experimental and simulated 2D-EEL line profiles for $R_0 = 268\,\text{nm}$ (Figs. 3.12a and 3.12b) and $R_0 = 110\,\text{nm}$ nanodisks (Figs. 3.12f and 3.12g). The line profiles for the $R_0 = 268\,\text{nm}$ nanodisk reveal a low-loss EEL signal confined to an annular region with a maximum at the edge of the nanodisk (see region between 0.5 eV to 1.5 eV in Figs. 3.12a and Fig. 3.12b). We show in Fig. 3.12e the simulated spectrum for a beam that is close to the nanodisk edge (blue dashed line in Fig. 3.12a). We recognize the A^E_{11} and the A^E_{21} anapole dips at around 1 eV and 1.25 eV, respectively. The electric field distribution inside the nanodisk associated with these energies (see Figs. 3.12c and 3.12d) corroborate the nature of these dips. Interestingly, when the electron beam passes through the nanodisk center ($b = 0$) the EEL signal becomes nearly zero, as shown in Figs. 3.12a and Fig. 3.12b. In this case, the electron beam is not able to efficiently excite the disk modes due to the cylindrical symmetry of the disk, and thus the optical anapoles are also not excited by the electron beam.

Finally, the line profile obtained from the $R_0 = 110\,\text{nm}$ nanodisk reveals an EEL signal that is spatially confined to an annular region from half the disk radius to significantly outside of the nanodisk. The calculated electric field distributions at the spectral dips (around 1.75 eV and 2.25 eV as indicated in Fig. 3.12j) display a clear electric dipole anapole-like field pattern (Figs. 3.12h and 3.12i). These field distributions corroborates that the first electric dipole anapole is hybridized with the A-exciton (bright region around 1.95 eV) to produce the anapole-exciton hybrids. These results open up the possibility to

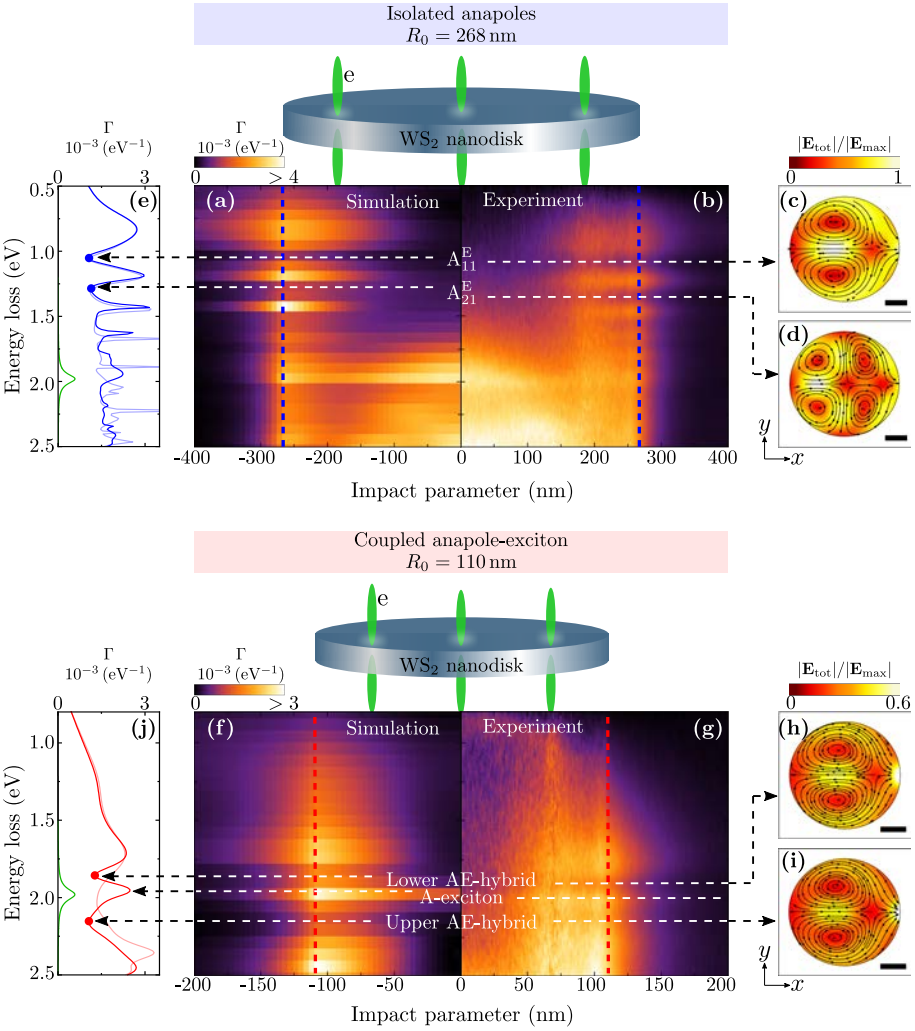

Figure 3.12: Spatially-resolved EEL of WS_2 nanodisks. (a) Simulated and (b) experimental EEL spectra recorded along the impact parameter b of a disk with 268 nm radius as depicted in the schematics above the spectra. Blue dashed lines indicate $b = 268$ nm. White dashed lines indicate the anapoles A^E_{11} (at 1.048 eV) and A^E_{21} (at 1.276 eV). Panels on the right of (b) show the amplitude of the total electric field $|\mathbf{E}_{tot}(\omega)|$ at the xy-plane for the energies (c) 1.048 eV and (d) 1.276 eV. The scale bar is 100 nm and the field plots are normalized to the maximum value $|\mathbf{E}_{max}|$ in each case: (c) 3.2×10^8 V/m and (d) 3.4×10^8 V/m. (e) Simulated $\Gamma(\omega)$ spectra for the WS_2 disk (solid blue line), the model disk with $\varepsilon_d = 18$ (thin blue line) and a WS_2 flake of 70 nm thickness (green line). (f)-(j) same as (a)-(e) but for the $R_0 = 110$ nm nanodisk. The scale bars in panels (h) and (j) are 50 nm. The maximum value $|\mathbf{E}_{max}|$ in each case is: (h) 1.2×10^9 V/m and (j) 1.4×10^9 V/m. For the calculation of $\Gamma(\omega)$, we use an impact parameter equal to $b = 1.05R_0$. Numerical calculations are performed considering that the nanodisk is on top of a 50 nm thick substrate layer characterized by the permittivity of SiN $\varepsilon_{SiN} = 4.1853$. Experimental data are obtained by Andrew Yankovich at Chalmers University of Technology (Gothenburg, Sweden).

explore, in future EELS experiments, systems exhibiting more complex spatial behavior of the isolated anapoles or anapole-exciton hybrids by, for example, breaking the cylindrical symmetry of the system.

3.4 Summary and conclusions

We demonstrate in this chapter that electron energy loss spectroscopy can be applied to probe optical anapole states in high-index dielectric nanoresonators. To that end, we calculate the electron energy-loss probability of high-index dielectric nanodisks and show that the prominent dips in the EEL spectra are associated with the excitation of optical anapoles in the disk. We experimentally verify our theoretical prediction by performing EELS of WS_2 nanodisks and reveal optical anapoles and anapole-exciton hybrid excitation within the same nanoobject. Additionally, we demonstrate that EELS in STEM allows for spatial mapping of WS_2 nanodisk modes, isolated anapoles and anapole-exciton hybrids with subnanometer resolution. By placing the electron beam at specific positions along the WS_2 nanodisk, we can effectively control the modes excitation and thus the formation of the optical anapole.

Our results show that EELS in STEM is a powerful tool to study dark scattering states and their complex interactions with the electronic structure of dielectric materials beyond the possibilities offered by conventional optical techniques. We anticipate that our results will enable new possibilities for studying higher-order and magnetic anapole states in dielectric nanoresonators with subnanometer spatial resolution.

4

Remote near-field spectrocopy of vibrational strong coupling in phononic nanoresonators

We need to be really careful with the loop and how we described it. Really really dangerous criterium.

– Rainer's email (March 03, 2021)

Abstract

In this chapter, we use infrared near-field spectroscopy to study the coupling between the localized modes of PhP nanoresonators made of h-BN and molecular vibrational modes of a semiconductor organic layer. For a most direct probing of the nanoresonator-molecule coupling, we minimize the tip-resonator coupling by employing a non-resonant tip and avoid the direct near-field interaction between tip and molecules by probing the molecule-free part of partially molecule-covered nanoresonators, to which we refer to as remote near-field probing. We obtain spatially and spectrally resolved maps of the hybrid polariton modes, as well as the corresponding coupling strengths, demonstrating vibrational strong coupling (VSC) on a single PhP nanoresonator level. The results discussed in this chapter have been published in the following publication: C. Maciel-Escudero et al. "Remote near-field spectroscopy of vibrational strong coupling between organic molecules and phononic nanoresonators", Nature Communications **13**, 6850 (2022).

4.1 Introduction

Strong coupling between molecular vibrations and infrared photons (vibrational strong coupling, VSC) leads to hybrid light-matter states [70, 199–203]. They offer intriguing possibilities for ultra-sensitive vibrational spectroscopy [88, 204–206] and for modifying chemical reactions [201, 202]. Typically, VSC is achieved with molecules embedded into microcavities, implying large photonic mode volumes and large amounts of molecules, which limits access to quantum phenomena that may be accesible only for nanoscale amounts of molecules or at the level of a few molecules. In this regard, plasmonic infrared resonators are a promising route to achieve VSC at the nanoscale [204, 205] owing to their dramatically reduced mode volumes as compared to microcavities. Alternatively, phonon polaritons (PhP) can be employed for VSC experiments, offering stronger polariton confinement and larger quality factors [88, 206, 207]. Unfortunately, the far-field extinction cross-section of individual PhP nanoresonators [27, 115, 117, 208–213] is extremely small (due to their small size compared to the infrared wavelength), challenging infrared far-field spectroscopy. Further, subradiant dark modes (offering the advantage of longer lifetimes) are difficult to probe by far-field spectroscopy. These problems can be circumvented by accessing modes through nanoscale Fourier transform infrared (nano-FTIR) spectroscopy. As discussed in Chapter 1, this technique employs the strong field concentration at the apex of a metallic probe tip (the near-field probe) [23, 24] to enable near-field spectroscopy and spatial mapping of both bright and dark modes of individual nanoresonators [27, 211].

Nano-FTIR spectroscopy has been employed to study the coupling between molecular vibrations and plasmonic resonators, but the near-field probe itself can couple with the plasmonic resonator and the molecules [204, 214, 215], eventually reaching strong tip-resonator and tip-molecule coupling. Although this coupling may be exploited for on-demand control of VSC, it may challenge the probing of the hybrid polariton modes that are exclusively formed by the nanoresonator-molecule coupling.

In this chapter, we first demonstrate in Section 4.2 that hybrid polariton modes formed by vibrational strong coupling between a single PhP nanoresonator and molecular layer can be studied using nano-FTIR spectroscopy. We minimize the influence of the tip by probing the molecule-free part of partially molecule-covered PhP nanoresonators with a non-resonant metallic tip, which

we refer to as remote near-field probing. In Subsection 4.2.1, we discuss the excitation of higher-order modes in the PhP nanoresonator. In Subsection 4.2.2, we show spatio-spectral near-field mappings of bare and half-molecule-covered h-BN nanoresonators, demonstrating the potential of nano-FTIR spectroscopy for identification of polaritonic modes not accessible by conventional far-field optical techniques. In Section 4.3, we verify the experimental results via comparative numerical simulations, where the near-field probe is modeled by a point-dipole source (representing a non-disturbing near-field probe). We discuss the appearance of a small loop in the trajectory of the complex-valued near-field spectra, and we show that the appearance of this loop is a direct consequence of the coupling between the resonator mode and the molecular vibrational mode. Finally, in Section 4.4, we present a quantitative analysis of experimental and simulated near-field spectra based on the model of two-coupled harmonic oscillators. At the end of this chapter, in Section 4.5, we show numerical simulations where the tip is modeled as a conical structure, and we provide a detailed analysis of its influence on the determination of eigenfrequencies, linewiths, and coupling strengths in the coupled nanoresonator-molecule system. The frequency ω is given in spectroscopic wavenumbers (see Appendix A) throughout this chapter.

4.2 Nano-FTIR spectroscopy of phononic nanoresonators

We motivate our study by the results obtained in the experiment illustrated in Fig. 4.1a, performed by our collaborators at CIC nanoGUNE. Half of a hexagonal boron nitride (h-BN) nanorod is covered with CBP molecules (4, 4′-bis(N-carbazolyl)-1,1′-biphenyl; organic semiconductor) that exhibit a vibrational resonance at $\omega_{\mathrm{CBP}} = 1450\,\mathrm{cm}^{-1}$, as identified from the near-field spectrum of a thin CBP layer shown by the green curve in Figs. 4.1d and 4.1e. The near-field probe, a non-resonant metallic tip [216] of an atomic force microscope, is placed remotely with respect to the molecules at the opposite extremity of the h-BN rod. The tip (oscillating normal to the sample at frequency Ω) concentrates an illuminating broadband infrared laser beam at its apex to a nanoscale near-field spot, which excites phonon polaritons [30, 67, 217] exhibiting Fabry-Perot (FP) resonances [88, 211, 212] on the h-BN nanorod [27]. Figure 4.1b shows a simulation of the second-order FP mode excited by the near field of a dipole (note that this mode is often referred to as a dark mode since it cannot

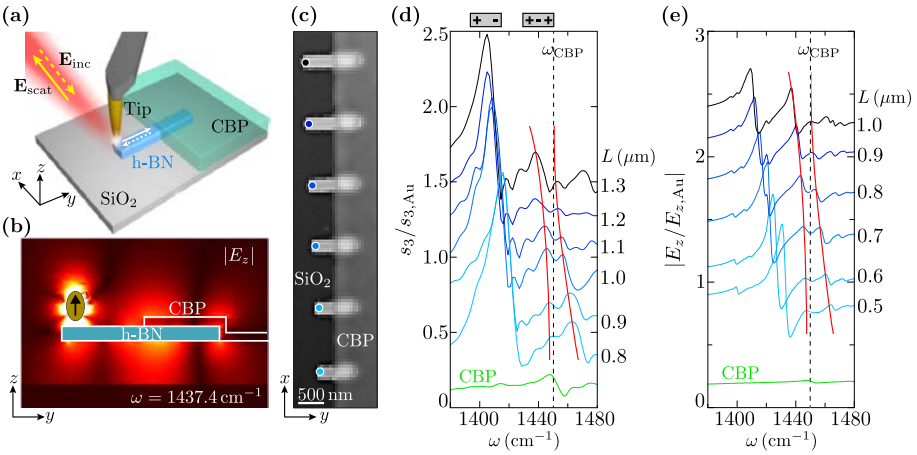

Figure 4.1: Tip-enhanced near-field probing of half molecule-covered h-BN nanoresonators. (a) Illustration of the experiment. (b) Numerical simulation showing the amplitude of the z-component of the electric field at $\omega = 1437\,\mathrm{cm}^{-1}$ around an h-BN nanorod of 1000 nm length, 250 nm width and 87 nm height, whose right half is covered by a 50 nm thick CBP layer. The vertical arrow indicates a point-dipole source mimicking the tip. (c) Topography image of h-BN nanorods (length L, 87 nm height and 250 nm width) that are half covered by a 50 nm thick CBP layer. (d) Experimental nano-FTIR amplitude spectra recorded at the positions marked in panel (c) by dots of the respective color. For better visualization, spectra for $L = 1.0\,\mu$m and $1.3\,\mu$m are scaled by a factor of 0.7. (e) Simulated nano-FTIR amplitude spectra, obtained as described in Section 4.3. We use the nominal experimental values for the width and thickness of the h-BN rods. The lengths L are chosen such that the 2^{nd}-order FP mode tunes across the molecular vibrational resonance of the CBP molecules at $\omega = 1450\,\mathrm{cm}^{-1}$. We attribute the differences between L in the experiment and the simulation to fabrication uncertainties which can produce trapezoid-like rod cross sections [88, 206]. In panels (d) and (e) the green curves show experimental and simulated nano-FTIR amplitude spectra of a 50 nm thick bare CBP layer on a 250 nm thick SiO_2 on Si substrate. Red lines are guides to the eye and mark peak positions. Grey-dashed lines indicate the CBP vibrational resonance at $\omega_{\mathrm{CBP}} = 1450\,\mathrm{cm}^{-1}$ whose linewidth is $6.4\,\mathrm{cm}^{-1}$ (ref. [207]). All spectra are normalized to that obtained on a Au reference surface, and are offset. Experimental data are obtained by Irene Dolado at CIC nanoGUNE (Donostia-San Sebastian).

be excited by far-field illumination due to its zero net electric dipole moment). The coupling between the resonator mode and the layer of molecules, resulting from the strong overlap between the near-field of the resonator mode and the molecules, is probed by recording the tip-scattered field with an asymmetric Fourier transform spectrometer, yielding both near-field amplitude and phase spectra, $s_3(\omega)$ and $\varphi_3(\omega)$, respectively, where the index indicates that the detector signal was demodulated at 3Ω to suppress background signals (Chapter 1).

A topography image of the set of h-BN nanorods of 250 nm width, 87 nm height and different lengths L is shown in Fig. 4.1c, where one can also observe the thin, homogeneous CBP layer of 50 nm thickness covering the right

half of all resonators. The experimental nano-FTIR amplitude spectra (Fig. 4.1d) recorded on the left rod extremity (measurement position marked by blue symbols in Fig. 4.1c) clearly show the resonance peaks of the first- and second-order FP resonances (illustrated by the schematic above the diagram in Fig. 4.1d and verified by the experimental mode pattern shown in Fig. 4.3), which shift to higher frequencies when the nanoresonator length L is reduced from 1300 nm to 800 nm. However, the peak of the second-order mode does not cross the CBP vibrational resonance at $\omega_{\mathrm{CBP}} = 1450\,\mathrm{cm}^{-1}$. Tracing the peak positions (marked by red lines) indeed reveals anti-crossing behavior, indicating that the nanoresonator near field couples with the molecular vibrations of the CBP layer. Most importantly, the nanoresonator-molecule coupling (occurring on the right half of the h-BN nanorods) can be well probed when the tip is placed on the left nanorod extremity, that is several 100 nm away from the molecules, where a direct near-field interaction between tip and molecules can be neglected (note that significant near-field interaction between tip and sample occurs only for distances smaller than the tip apex radius, here about 25 nm). The experimental near-field spectra can be well reproduced by numerical simulations (Fig. 4.1e), where the tip is modeled as a point-dipole source, which are described in more detail in Section 4.3 and Appendix B.

We note that in the experimental spectra (Fig. 4.1d), we observe several smaller peaks, e.g., in the frequency range between $1420\,\mathrm{cm}^{-1}$ and $1440\,\mathrm{cm}^{-1}$. They can be attributed to higher-order PhP modes [206]. In the simulated spectra, where the near-field probe is described by a point dipole source (Fig. 4.1e), these peaks are only partially observed. A much better reproduction of these peaks is obtained in numerical simulations where the near-field probe is modeled by a conical metallic tip, as we discuss in the following subsection.

4.2.1 Higher-order modes in the h-BN resonator

As pointed out above, there are several peaks in the experimental near-field spectra (Fig. 4.1d), which are not observed in the numerical simulations of the amplitude spectra shown in Fig. 4.1e. They can be attributed to higher-order PhP modes. To demonstrate this, we show in Figs. 4.2b the near-field spectrum of a half molecule-covered nanoresonator, whose length is chosen such that the 2^{nd}-order FP resonance is at $1450\,\mathrm{cm}^{-1}$. The tip is modeled as a point-dipole source and the z-component of the electric field, $E_z(\omega)$, is interpreted as the near-field signal (Section 4.3), analogue to the procedure followed to obtain the results in Fig. 4.1e. In the frequency range from $1430\,\mathrm{cm}^{-1}$ to $1441\,\mathrm{cm}^{-1}$ (grey shaded region in Fig. 4.2b) the amplitude spectrum $|E_z(\omega)|$ does not show

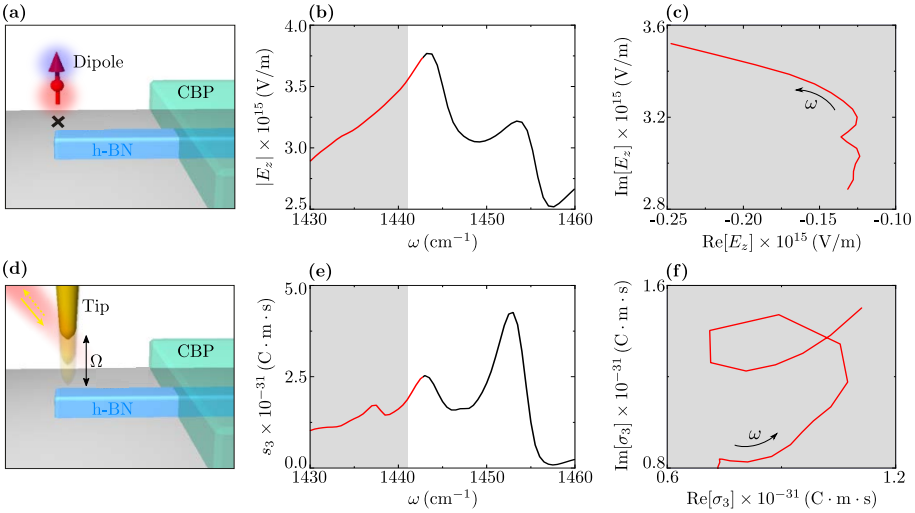

Figure 4.2: Higher-order modes in the h-BN nanoresonator. (a) Schematics showing a point-dipole source above an h-BN nanorod of 840 nm length, 87 nm height and 250 nm width, which is half covered with a 50 nm thick CBP layer. (b) Near-field amplitude below the point dipole (at the position marked by a cross in panel (a)) as a function of frequency ω. The grey shaded region marks the frequency region from 1430 cm^{-1} to 1441 cm^{-1}. (c) Near-field below the point-dipole source, plotted in the complex plane from 1430 cm^{-1} to 1441 cm^{-1}. The arrow indicates increasing frequency. (d) Schematics showing a conical metal tip oscillating above the same h-BN nanoresonator as in (a) at frequency Ω. (e) Amplitude of the 3$^{\mathrm{rd}}$-order demodulated scattered field, $s_3(\omega)$. The grey shaded region marks the frequency region from 1430 cm^{-1} to 1441 cm^{-1}. (f) 3$^{\mathrm{rd}}$-order demodulated scattered field, $\sigma_3(\omega)$, plotted in the complex plane from 1430 cm^{-1} to 1441 cm^{-1}. The arrow indicates increasing frequency. The simulations are performed without considering the SiO_2/Si substrate.

clearly any resonance peak. By plotting $E_z(\omega)$ in the complex plane in the same spectral range (gray shaded region in Fig. 4.2c), however, we can observe a small kink in the complex trajectory, indicating a weakly excited mode.

We repeat the simulation with the tip modeled as a platinum cone (see schematics in Fig. 4.2d) and calculate the complex-valued 3$^{\mathrm{rd}}$-order demodulated scattered field ($\sigma_3(\omega) = s_3(\omega)e^{i\varphi_3(\omega)}$, Figs. 4.2e-f). For simulation details, see Appendix B.2. In contrast to the near-field spectrum obtained with the point-dipole simulation (Fig. 4.2b), we observe a clear peak at around 1437 cm^{-1} in the amplitude spectrum $s_3(\omega)$ (Fig. 4.2e), corresponding to a higher-order PhP mode excited by the tip in the h-BN nanoresonator. As we will show in Sections 4.3 and 4.5, the excitation of a nanoresonator mode corresponds to a loop or a kink when plotting $E_z(\omega)$ or $\sigma_3(\omega)$ in the complex plane, as observed in Fig. 4.2c and 4.2f. Thus, the appearance of the loop when plotting $\sigma_3(\omega)$ in the complex plane indicates that the excitation of this higher-order PhP mode is stronger for the tip being a metal cone rather than a

point-dipole source. For that reason, the peak is observed in the experimental near-field amplitude spectrum (Fig. 4.1d) but not in the simulated near-field amplitude spectrum (Fig. 4.1e).

4.2.2 Near-field mapping of phononic nanoresonators

Remote near-field spectroscopy can be applied for nanoscale spatial mapping of the resonator-molecule coupling via hyperspectral nanoimaging (even for dark modes that are not accessible by far-field spectroscopy). In future, such a possibility could be applied, for example, to study advanced resonator structures where a variety of different resonator modes may coexist and couple with the molecular vibrations. In Fig. 4.3, we show this capability for direct experimental identification of the phononic resonator mode that couples with the molecular layer and to verify that the peak splitting is caused by the presence of the molecules. To that end, we record nano-FTIR amplitude spectra along the principal axis of a bare (Figs. 4.3a and 4.3b) and a half-covered (Figs. 4.3c and 4.3d) h-BN nanoresonator. The length L of the nanoresonators are chosen such that their 2^{nd}-order FP resonance occurs at the molecular vibrational resonance, $\omega_{\text{CBP}} = 1450\,\text{cm}^{-1}$. For each spectral peak, we observe strong near-field oscillations along the principal nanoresonator axis. The number of oscillations increases steadily with increasing frequency, revealing a series of FP modes. The three near-field maxima (in the center and at the two extremities of the nanoresonator) at $1450\,\text{cm}^{-1}$ clearly reveal the 2^{nd}-order (dark) FP mode. More importantly, the 2^{nd}-order FP modal near-field pattern of the half-covered nanoresonator exhibits a small spectral dip at the molecular vibrational resonance of CBP at $1450\,\text{cm}^{-1}$ (dark region in Fig. 4.3d, marked by the green double arrow line) all along the principal resonator axis, which is absent in the hyperspectral linescan of the bare nanoresonator (Fig. 4.3b). For a better quantitative comparison, we show in Fig. 4.3e the nano-FTIR amplitude spectra recorded at the left extremity of the bare and molecule-covered h-BN nanoresonators (positions marked by blue and red dots in Figs. 4.3a and 4.3c respectively). One can clearly observe that the peak of the 1^{st}-order FP mode (far away from the CBP resonance, $\omega_{\text{CBP}} = 1450\,\text{cm}^{-1}$) is nearly the same for both nanoresonators, whereas the peak of the 2^{nd}-order FP mode of the molecule-covered h-BN nanoresonator exhibits a spectral dip at ω_{CBP}, as typically occurs in the coupling between molecular vibrational modes and nanoresonator modes [88, 204, 206, 214].

The spatio-spectral observation presented in Fig. 4.3 demonstrates that the nanoresonator-molecule coupling can in principle be probed at any location

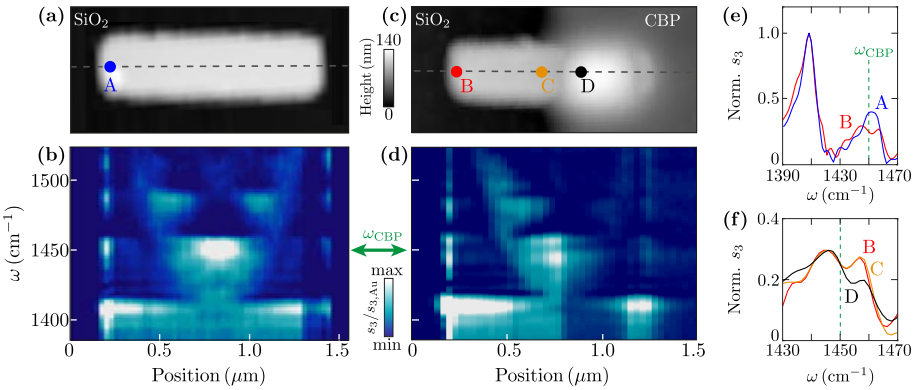

Figure 4.3: Nano-FTIR line scans of bare and half molecule-covered h-BN nanoresonators. (a) Topography image of a bare h-BN nanorod of 1.25 μm length, 110 nm height and 250 nm width. (b) nano-FTIR amplitude spectra recorded along the horizontal dashed black line in panel (a). (c) Topography image of h-BN nanorod of 1.1 μm length, 110 nm height and 250 nm width, which is half covered with a 50 nm thick CBP layer. (d) nano-FTIR amplitude spectra recorded along the horizontal dashed black line in panel (c). (e) nano-FTIR amplitude spectra of the bare (blue) and molecule-covered (red) h-BN nanorod at positions marked by blue and red dots in panels (a) and (c), respectively. Both spectra are normalized to the peak maximum at 1408 cm^{-1}. (f) nano-FTIR amplitude spectra of the molecule-covered h-BN nanorod at positions marked by red, orange and black dots in panel (c). The spectra are normalized to the peak maximum at 1445 cm^{-1}. The vertical green dashed line marks the frequency of the molecular vibrational resonance of CBP. Experimental data are obtained by Irene Dolado at CIC nanoGUNE (Donostia-San Sebastian).

where the nanoresonator mode can be activated by the near-field probe. On the other hand, Fig. 4.3 reveals that the near-field signal on the molecule-covered part of the nanoresonator is strongly reduced due to the increased tip-nanoresonator distance and that the spectral line shape is modified due to the direct near-field interaction between tip and molecules, highlighting the advantages of probing the molecule-free part of the resonator, that is, probing larger near-field signals and reduction of undesirable near-field interaction between tip and molecules. The modification of the line shape is more clearly observed in Fig. 4.3f, which compares spectra recorded on the molecule-free nanoresonator part (B and C) with spectrum D that is recorded on the molecule-covered part. Specifically, we can observe that the spectrum D exhibits an asymmetric line shape and that the dip is shifted to slightly higher frequencies. This asymmetric line shape can be explained as a superposition of the symmetric nano-FTIR spectrum of the molecule-covered nanoresonator (B) and the asymmetric nano-FTIR spectrum of a bare CBP layer (such as the green spectrum in Fig. 4.1) caused by the direct near-field interaction between tip and molecules. The later exhibits a derivative-like spectral line shape, that is, a peak and a dip to

the left and right of the molecular resonance, respectively, which is a typical characteristic of nano-FTIR amplitude spectra of molecular layers [218]. This analysis thus demonstrates the ability of near-field spectroscopy to spatially map the polaritonic modes that result from the nanoresonator-molecule coupling. Furthermore, it confirms that the coupling between the nanoresonator and molecule can be analyzed at any location where the nanoresonator mode is activated by the near-field probe.

4.3 Theoretical description of remote near-field probing of VSC

To understand how the hybrid nanoresonator-molecule modes manifest in the near-field spectra, we first discuss in Fig. 4.4 the results of our numerical simulations where the tip is modeled as a point-dipole source [27, 219] (red arrow in Figs. 4.4a and 4.4d) located above the h-BN resonator. We obtain the complex-valued near-field spectrum by evaluating the vertical (z-) component of the electric field below the dipole (evaluation position marked by a cross in Figs. 4.4a and 4.4d) as a function of frequency, $E_z(\omega)$. Further simulation details are described in Appendix B.2. Importantly, the dipole moment of the source is kept constant and consequently is not modified by the fields of the nanoresonator. This simplified modeling of the tip allows for excluding a potential coupling of the tip with the nanoresonator and the molecules, and thus exclusively reveals the spectral near-field signature of the coupling between the nanoresonator and the molecular vibrations.

Figure 4.4b shows the simulated near-field amplitude spectrum, $|E_z(\omega)|$ (open symbols), of a h-BN nanorod that is half covered with a layer of permittivity $\varepsilon = 2.8$ (corresponding to the permittivity of CBP without the molecular resonance at $1450\,\mathrm{cm}^{-1}$). Its length is chosen such that the 2^{nd}-order FP resonance is at $\omega = 1450\,\mathrm{cm}^{-1}$, which manifests as a single peak in the near-field amplitude spectrum. Repeating the simulation when the h-BN nanorod is half covered by a CBP layer (Fig. 4.4e), the nanoresonator's near-field amplitude peak splits into two peaks (open symbols), which is a consequence of the coupling between the nanoresonator mode and molecular vibrational mode. For quantifying the coupling strength between the h-BN nanoresonator and the molecular vibrations, we fit the simulated near-field spectra by the model of

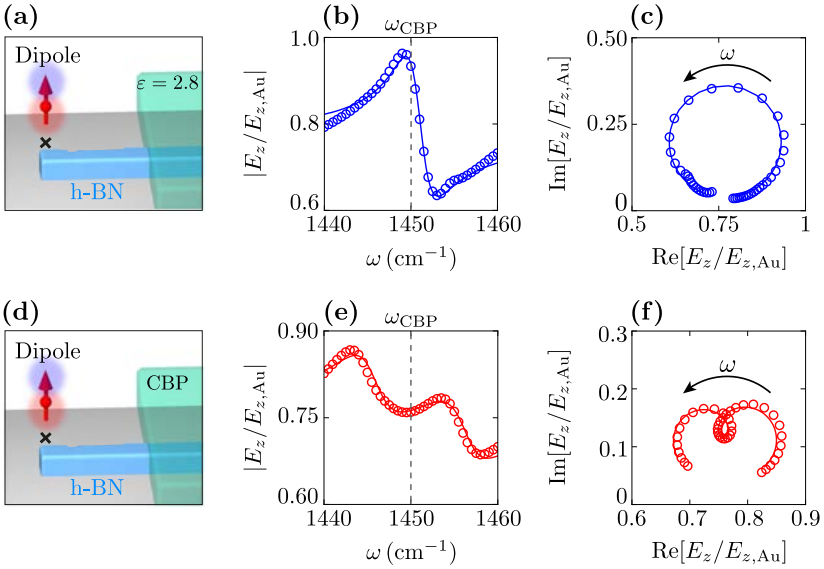

Figure 4.4: Theoretical description of near-field probing of VSC. (a) Simulation geometry, showing a point-dipole source above an h-BN nanorod of 785 nm length, 87 nm height and 250 nm width, which is half covered with a 50 nm thick layer of permittivity $\varepsilon = 2.8$. (b) Electric field amplitude, $|E_z(\omega)|$, below the dipole at the position marked by a cross in panel (a) (normalized to that obtained on a Au reference surface, $|E_z(\omega)/E_{z,\mathrm{Au}}(\omega)|$), as function of frequency ω. (c) Electric field $E_z(\omega)$ below the point-dipole source at the position marked by a cross in panel (a), plotted in the complex plane. The arrow indicates increasing frequency ω. (d) Simulation geometry, showing a point-dipole source above the same h-BN nanorod as in panel (a) but half covered with CBP molecules. (e) Same as panel (b), but the h-BN nanorod is half covered by a 50 nm thick CBP layer. (f) Same as panel (c), but for a half CBP-covered h-BN nanorod. Open symbols in panels (b), (c), (e) and (f) show simulation results. Solid lines show fits obtained with Eqs. (4.2a) and (4.3).

two coupled harmonic oscillators discussed in Chapter 1:

$$\ddot{x}_{\mathrm{PhP}}(t) + \gamma_{\mathrm{PhP}}\dot{x}_{\mathrm{PhP}}(t) + \omega_{\mathrm{PhP}}^2 x_{\mathrm{PhP}}(t) - 2g\dot{x}_{\mathrm{CBP}}(t) = F_{\mathrm{PhP}}(t), \tag{4.1a}$$

$$\ddot{x}_{\mathrm{CBP}}(t) + \gamma_{\mathrm{CBP}}\dot{x}_{\mathrm{CBP}}(t) + \omega_{\mathrm{CBP}}^2 x_{\mathrm{CBP}}(t) + 2g\dot{x}_{\mathrm{PhP}}(t) = F_{\mathrm{CBP}}(t), \tag{4.1b}$$

where $x_{\mathrm{PhP}}(t)$ is associated with the vector potential $\mathbf{A}(t)$ of the PhP mode and $x_{\mathrm{CBP}}(t)$ is associated with the dipole moment $\mathbf{p}_{\mathrm{CBP}}(t)$ induced at the molecular layer [73]. The PhP mode has resonance frequency ω_{PhP} and damping constant γ_{PhP}, and the molecular vibrational mode of CBP has resonance frequency ω_{CBP} and damping constant γ_{CBP}. g is the coupling strength between the two resonators and the dots denote time derivatives. Notice that Eqs. (4.1a)-(4.1b) have similar form to Eq. (1.48a)-(1.48b), but in this situation each oscillator is driven by an effective force $F_{\mathrm{PhP}}(t)$ and $F_{\mathrm{CBP}}(t)$. These effective

forces are proportional to the near fields provided by the tip. In particular, we set $F_{\mathrm{CBP}}(t) = 0$ as in our experiment the near fields of the tip do not act directly on the CBP molecules. Through a time-to-frequency Fourier transform of Eqs. (4.1a) and (4.1b), one can find the following steady-state solutions of the equations above:

$$x_{\mathrm{PhP}}(\omega) = \frac{(\omega_{\mathrm{CBP}}^2 - \omega^2 - i\gamma_{\mathrm{CBP}}\,\omega)\,F_{\mathrm{PhP}}(\omega)}{(\omega_{\mathrm{PhP}}^2 - \omega^2 - i\gamma_{\mathrm{PhP}}\,\omega)(\omega_{\mathrm{CBP}}^2 - \omega^2 - i\gamma_{\mathrm{CBP}}\,\omega) - (2g\omega)^2}, \tag{4.2a}$$

$$x_{\mathrm{CBP}}(\omega) = \frac{(i2g\omega)\,F_{\mathrm{PhP}}(\omega)}{(\omega_{\mathrm{PhP}}^2 - \omega^2 - i\gamma_{\mathrm{PhP}}\,\omega)(\omega_{\mathrm{CBP}}^2 - \omega^2 - i\gamma_{\mathrm{CBP}}\,\omega) - (2g\omega)^2}, \tag{4.2b}$$

with $x_{\mathrm{PhP}}(\omega) = \mathcal{F}[x_{\mathrm{PhP}}(t)]$, $x_{\mathrm{CBP}}(\omega) = \mathcal{F}[x_{\mathrm{CBP}}(t)]$, $F_{\mathrm{PhP}}(\omega) = \mathcal{F}[F_{\mathrm{PhP}}(t)]$ and $\mathcal{F}$ is the time-to-frequency Fourier transform (see Appendix A).

Since $x_{\mathrm{PhP}}(\omega)$ is proportional to the vector potential $\mathbf{A}(\omega)$, and thus to the near field $\mathbf{E}(\omega)$ of the PhP mode, we use Eq. (4.2a) to fit the simulated near-field spectra (Fig. 4.4). Specifically, to perform the fitting, we add a complex-valued offset term $(x_0 + iy_0)$ to $x_{\mathrm{PhP}}(\omega)$, which accounts for the non-polaritonic near-field interaction between the tip and the nanoresonator, i.e.,

$$E_z(\omega) \propto x_{\mathrm{PhP}}(\omega) + x_0 + iy_0, \tag{4.3}$$

and for a most reliable analysis, we perform a complex-valued fitting of the simulated near-field spectra $E_z(\omega) = |E_z(\omega)|e^{i\varphi(\omega)}$, where $|E_z(\omega)|$ and $\varphi(\omega)$ are the amplitude and phase spectra (Fig. 4.4f). Plotting the fits by red solid lines in Figs. 4.4e and 4.4f, we find an excellent agreement with the simulated spectra (red open symbols), which confirms the validity of the two coupled harmonic oscillators model to fit the simulated near-field spectra.

Loop in the near-field spectra

We note that the simulated near-field spectrum of the h-BN nanoresonator in the absence of molecular vibrations yields a nearly circular trajectory in the complex plane (Fig. 4.4c). Interestingly, when the nanoresonator is half covered with CBP molecules, the topology of the trajectory of the complex-valued near-field spectra changes. We find that a small loop appears within the main circular trajectory (Fig. 4.4f) , which reveals the coupling between the PhP resonator mode and the molecular vibrational mode, similar to a recent observation in far-field ellipsometry of excitonic coupling in classical microresonators [77]. The appearance of the loop is not only a mere superposition of two modes, as we show with the following example.

Figures 4.5a-d show a situation where two oscillators are driven by the same force $F_1 = F_2$ (see inset above Fig. 4.5a), which, for example, would correspond

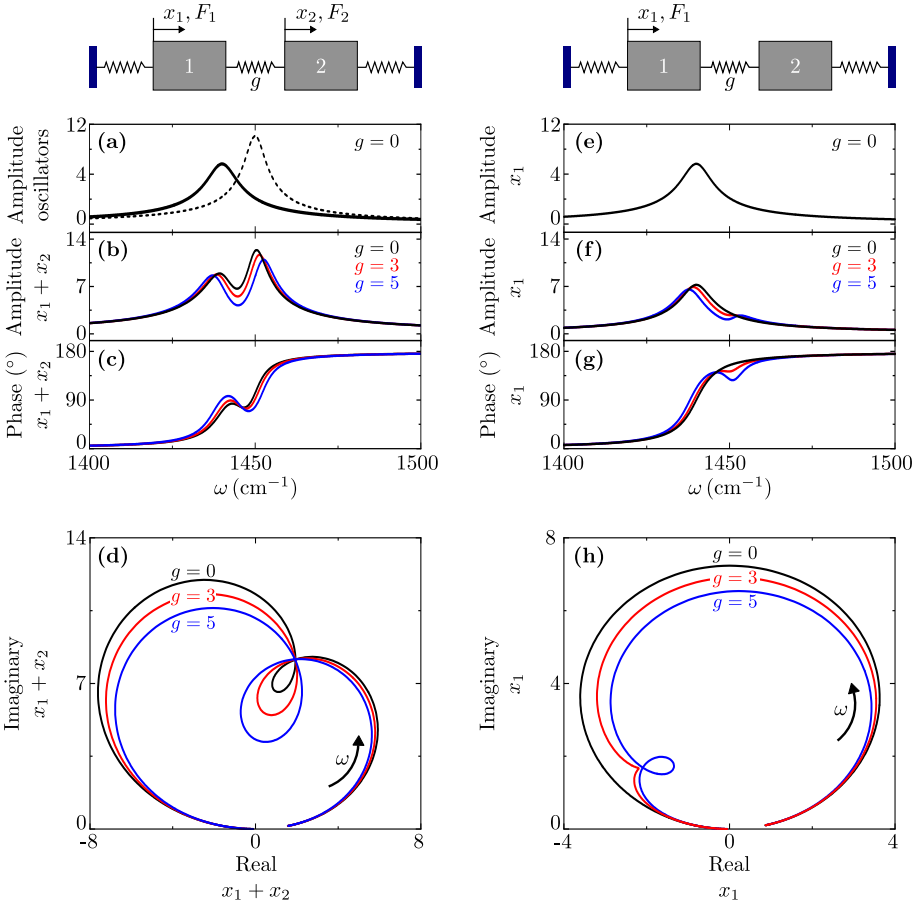

Figure 4.5: Comparison of coupled mechanical oscillators. (a)-(d) Two-coupled oscillators labeled 1 and 2 are driven and thus displaced by distances x_1 and x_2, respectively. The complex-valued oscillation amplitude of the combined displacement $x_1 + x_2$ is analyzed as a function of frequency. (a) Spectra of the oscillation amplitude of two slightly frequency-detuned, uncoupled oscillators. The first oscillator (solid curve) has eigenfrequency $\omega_1 = 1440\,\mathrm{cm}^{-1}$, damping $\gamma_1 = 9.6\,\mathrm{cm}^{-1}$ and driving force $F_1 = 1 \times 10^5\,\mathrm{cm}^{-2}$. The second oscillator (dashed curve) has eigenfrequency $\omega_2 = 1450\,\mathrm{cm}^{-1}$, damping $\gamma_2 = 6.5\,\mathrm{cm}^{-1}$ and driving force $F_2 = 1 \times 10^5\,\mathrm{cm}^{-2}$. (b) Amplitude and (c) phase spectra of $x_1 + x_2$ for three coupling strengths: $g = 0\,\mathrm{cm}^{-1}$ (black line), $3\,\mathrm{cm}^{-1}$ (red line) and $5\,\mathrm{cm}^{-1}$ (blue line). (d) Representation of the spectra of panel (b) and (c) in the complex plane. (e)-(h) Same mechanical oscillators as in (a) with only oscillator 1 driven, and the individual complex-valued oscillation amplitude x_1 is analyzed. (e) Spectrum of the oscillation amplitude of the driven oscillator (solid curve), which has eigenfrequency $\omega_1 = 1440\,\mathrm{cm}^{-1}$, damping $\gamma_1 = 9.6\,\mathrm{cm}^{-1}$ and driving force $F_1 = 1 \times 10^5\,\mathrm{cm}^{-2}$. The second oscillator has eigenfrequency $\omega_2 = 1450\,\mathrm{cm}^{-1}$, damping $\gamma_2 = 6.5\,\mathrm{cm}^{-1}$ and driving force $F_2 = 0\,\mathrm{cm}^{-2}$. (f) Amplitude and (g) phase spectra for the three coupling strengths: $g = 0\,\mathrm{cm}^{-1}$ (black line), $3\,\mathrm{cm}^{-1}$ (red line) and $5\,\mathrm{cm}^{-1}$ (blue line). (h) Representation of the spectra of panel (f) and (g) in the complex plane.

to two molecules with slightly frequency-detuned resonances that are studied by far-field optical spectroscopy. The sum of the dipole moments induced at each molecule, namely the total dipole moment in the system, is proportional to the radiation emitted by the two molecules into the far field. Within the two-coupled harmonic oscillators model, this total dipole moment of the system can be associated with the variable $x_1 + x_2$. By plotting $x_1 + x_2$ in the complex plane for different coupling strengths g, one can observe the appearance of a loop even for $g = 0$ (see Fig. 4.5d). Consequently, the appearance of the loop in this situation does not necessarily indicate coupling between the two oscillators (two molecules), but it might just be the consequence of a mere superposition of two molecular resonances.

Figures 4.5e-h, on the other hand, show the situation in which only one oscillator is driven by the force F_1 (see the inset above Fig. 4.5e), which would correspond to the situation of our experiment. In such a situation, the PhP nanoresonator, illuminated by the tip, generates a near field that can be related to the variable x_1 within the two-coupled oscillator model (Eq. (4.3)). When x_1 is plotted in the complex plane (Fig. 4.5h), it becomes evident that the loop is only present when $g > 0$ (see blue curve). By decreasing the value of g, the loop undergoes a topological transition to a kink (red curve), which already indicates the coupling between the two oscillators. When the oscillators are uncoupled, i. e., $g = 0$, the loop and kink disappear from the trajectory traced in the complex plane by x_1 (black curve). This observation confirms that the appearance of the loop indicates the existence of coupling between the two oscillators. Thus, in our experiments, the appearance of the loop in the complex plane is a consequence of the nanoresonator-molecules coupling.

From this analysis, one can conclude a recipe to establish the existence of coupling in a hybrid system when only one of the elements is driven: when the loop appears in the complex-valued near-field spectra, as shown in Fig. 4.4f, the two elements of the hybrid system are coupled.

4.4 Quantitative analysis of experimental nano-FTIR spectra

We analyze here the experimental near-field spectra (Figs. 4.6a and 4.6b) obtained in Fig. 4.1d. To that end, we first assume that the tip is solely illuminating the nanoresonator (i.e., that it acts like a dipole source with a constant

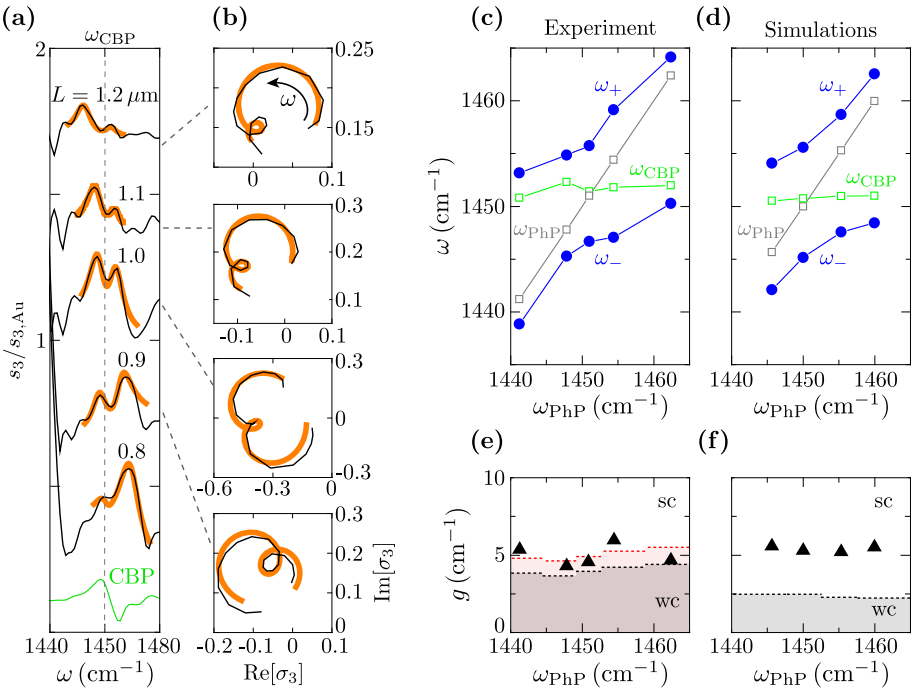

Figure 4.6: Quantitative analysis of nano-FTIR spectra by coupled harmonic oscillator fitting. (a) Black curves show the experimental nano-FTIR amplitude spectra of h-BN nanorods of length L, which are half covered with CBP molecules (same data as in Fig. 4.1d). Orange curves show fits obtained using the coupled harmonic oscillator model. For better visualization, the spectrum for $L = 1\,\mu$m is scaled by a factor of 0.7. (b) Black curves show the complex-valued experimental nano-FTIR spectra, $\sigma_3(\omega) = s_3(\omega)e^{i\varphi_3(\omega)}$, plotted in the complex plane. Orange curves show fits obtained using the coupled harmonic oscillator model. (c) Eigenfrequencies $\omega_\pm$ of the hybrid modes, the nanoresonators´ bare eigenfrequencies ω_{PhP} (grey squares), and bare molecular vibrational eigenfrequency ω_{CBP} (green squares), all of them obtained by fitting of the complex-valued experimental nano-FTIR spectra. (d) Same as panel (c), but obtained by fitting complex-valued simulated near-field spectra of h-BN nanoresonators of length $L = 1.2\,\mu$m to $0.8\,\mu$m, which are half covered by CBP molecules (the corresponding amplitude spectra are shown in Fig. 4.1e). The tip is modeled by a point-dipole source as in Fig. 4.3e. (e) Coupling strength g obtained from the fitting of the experimental and simulated near-field spectra, respectively. Black and red dashed horizontal lines indicate the transition from weak (WC) to strong (SC) coupling defined by $g = (\gamma_{PhP} + \gamma_{CBP})/4$ (Chapter 1) and $g = (\gamma_{PhP} + \gamma_{CBP})/3.23$ (see discussion in Subsection 4.5.2), respectively. Experimental data are obtained by Irene Dolado at CIC nanoGUNE (Donostia-San Sebastian).

dipole moment and, for that reason, it does not need to be modeled as another coupled oscillator). We thus apply the same model of two-coupled harmonic oscillators as for the simulated near-field spectra to fit the experimental spectra. We further assume that the PhP mode is not excited by far-field illumination because it is a dark mode. Figure 4.6b shows the experimental near-field spec-

tra of the half-covered nanoresonators in the complex plane (black lines), as well as the fitting results (orange lines) performed following an identical procedure as the one in Fig. 4.4, to analyse the simulation results. The small loops in the complex plane clearly reveal the coupling between the nanoresonator mode and the molecular vibrational mode, as predicted by the simulations discussed in Section 4.3. We note that the size of the small loop slightly varies in the experimental spectra of the different nanoresonators, which we attribute to variations in the resonators´ quality factor due to fabrication uncertainties. From the fits, we determine for each experimental near-field spectrum (i.e., for each nanoresonator) the coupling strength g, the PhP eigenfrequency ω_{PhP}, and damping γ_{PhP}, the molecular vibrational eigenfrequency ω_{CBP} and damping γ_{CBP} (the fitting values are reported in Appendix G). From these parameters, we can obtain the eigenfrequencies of the new hybrid modes for each nanoresonator, $\omega_{\pm}$, appyling Eq. (1.50) for the nanoresonator-molecules coupled system:

$$\omega_{\pm} = \frac{\omega_{\mathrm{PhP}} + \omega_{\mathrm{CBP}}}{2} - \frac{i}{4}(\gamma_{\mathrm{PhP}} + \gamma_{\mathrm{CBP}}) \pm \frac{1}{2}\sqrt{4g^2 + \left[\Delta\omega - \frac{i}{2}\Delta\gamma\right]^2}, \quad (4.4)$$

with $\Delta\omega = \omega_{\mathrm{PhP}} - \omega_{\mathrm{CBP}}$ being the detuning and $\Delta\gamma = \gamma_{\mathrm{PhP}} - \gamma_{\mathrm{CBP}}$. The eigenfrequencies of the new modes are shown in Fig. 4.6c (blue symbols) as a function of the nanoresonators´ eigenfrequencies ω_{PhP}. We observe a clear anticrossing of the hybrid modes, which indicates strong coupling. To determine the coupling regime for each individual resonator, we mark in Fig. 4.6e the transition from weak to strong coupling, defined by the criterium $g = (\gamma_{\mathrm{PhP}} + \gamma_{\mathrm{CBP}})/4$ (Chapter 1), by black dashed horizontal lines. Interestingly, we find that g is above the black dashed line for all individual resonators, indicating that all of them are strongly coupled with the molecular vibrations.

Importantly, applying the same fitting procedure to the simulated complex-valued near-field spectra (where the tip is modeled as a point-dipole source; see Appendix B.2) yields hybrid eigenmodes (Fig. 4.6d) and coupling strengths (Fig. 4.6f) that match well the experimental results. Since the tip is not involved in the nanoresonator-molecule coupling in the simulations, this quantitative agreement lets us further assume that the coupling between the PhP mode and the molecular vibrational mode in our experiment can be well described with a simple two-coupled harmonic oscillator model, without the need of considering the tip as a third oscillator. Our analysis thus demonstrates the capability of remote near-field spectroscopy to probe the hybrid modes arising from the coupling between a single PhP nanoresonator and nanoscale amounts of organic molecules.

We note that the damping γ_{PhP} obtained from the simulated near-field spectra is a factor of three lower than that obtained from the experimental spec-

tra (see Tables in Appendix G). We explain this finding by PhP scattering and absorption at fabrication-induced irregularities and damage of the h-BN nanorod edges [88, 206], which is not considered in the simulation. Although the damping has only a minor influence on the coupling strength g and on the determination of the hybrid eigenmodes (see Eq. (4.4)), it is a crucial parameter that determines whether a coupled system is in the weak or in the strong coupling regime. Marking the transition from weak to strong coupling in Fig. 4.6f by black horizontal dashed lines (analogue to Fig. 4.6e), we find that it occurs at much lower g for the simulation as compared to experiment, which shows that in simulations we are deeper inside the strong coupling regime than in the experiment.

4.5 Influence of the oscillating tip and signal demodulation

So far, we have not explicitly considered in the simulations that the tip is a long metallic cone, that the tip is oscillating, and that the detector signal is demodulated at higher harmonics of the tip oscillation frequency (Chapter 1). To elucidate the influence and impact of these key features on the spectral mode positions and linewidths, in this section we perform numerical simulations where the tip is modeled as a conical platinum structure of 1 μm length and semispherical apex of 25 nm radius, and signal demodulation are considered (for details of the simulations, we refer the reader to Appendix B.2).

4.5.1 Tip on top of the h-BN nanoresonator

We start with an extended discussion of the near-field spectra obtained for the point-dipole source. Figure 4.7b shows the near-field amplitude spectrum $|E_z(\omega)|$ at 65 nm height above the h-BN resonator (position marked by a cross in Fig. 4.7a). We can clearly observe a strong resonance peak around 1450 cm^{-1} and another much weaker peak around 1455 cm^{-1}. We associate the strong peak with the 2^{nd}-order FP mode [27] discussed in the previous sections and the weaker one to a higher-order PhP mode [206]. The asymmetry of the strong resonance peak we attribute to Fano-like interference [219, 220] between the electric field produced by the (non-resonant) point-dipole source, together with

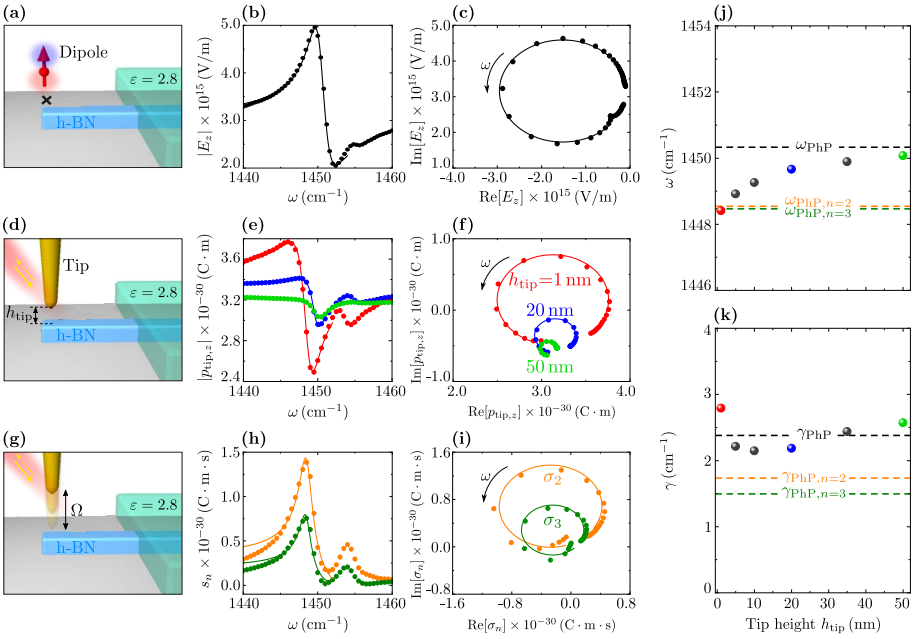

Figure 4.7: Influence of the tip and signal demodulation on the nanoresonator mode. (a) Schematics showing a point-dipole source above an h-BN nanorod half-covered with a layer of permittivity $\varepsilon = 2.8$. (b) Near-field amplitude $|E_z(\omega)|$ below the dipole at the position marked by a cross in panel (a). In the simulations, the point dipole and the evaluation point were located at coordinates $(x = 0, y = -370\,\text{nm}, z = 350\,\text{nm})$ and $(x = 0, y = -370\,\text{nm}, z = 65\,\text{nm})$ respectively. (c) Near-field $E_z(\omega)$ below the dipole source, plotted in the complex plane for frequencies between $1440\,\text{cm}^{-1}$ and $1460\,\text{cm}^{-1}$. The arrow indicates increasing frequency. (d) Schematics of the Pt tip at height h_{tip} above the h-BN nanorod, illuminated with a broadband infrared laser beam. (e) Amplitude of the induced dipole moment $|p_{\text{tip},z}(\omega)|$ at the tip for $h_{\text{tip}} = 1\,\text{nm}$ (red dots), 20 nm (blue dots) and 50 nm (green dots) tip heights above the h-BN nanoresonator. (f) $p_{\text{tip},z}(\omega)$ plotted in the complex plane, from $1440\,\text{cm}^{-1}$ to $1452\,\text{cm}^{-1}$. Same color code as in panel (e). (g) Schematics of the Pt tip oscillating above the h-BN nanoresonator at frequency Ω. (h) Amplitude of the 2^{nd}- and 3^{rd}-order demodulated scattered fields, $s_2(\omega)$ (orange dots) and $s_3(\omega)$ (green dots). (i) $\sigma_2(\omega)$ and $\sigma_3(\omega)$ plotted in the complex plane, from $1440\,\text{cm}^{-1}$ to $1452\,\text{cm}^{-1}$. Dots in panels (h) and (i) are the numerical results obtained by demodulating the complex-valued spectra $p_{\text{tip},z}(\omega)$. Dots in panels (b), (c), (e) and (f) are the numerical results obtained from simulations. Solid lines represent fits using Eq. (4.5). We fit the spectra between $1440\,\text{cm}^{-1}$ and $1452\,\text{cm}^{-1}$. (j) Eigenfrequency and (k) damping of the 2^{nd}-order FP resonance, ω_{PhP} and γ_{PhP}, for different tip heights h_{tip}. Black dashed lines show the fitting values obtained from panel (c). Orange and green dashed lines show the fitting values obtained from panel (i). Dots show the fitting values obtained from fitting the spectra of the induced dipole moment $p_{\text{tip},z}(\omega)$ at different tip height $h_{\text{tip}} = 1\,\text{nm}$ (red dot), 20 nm (blue dot), 50 nm (green dot) and 5 nm, 10 nm and 35 nm (grey dots). In all numerical calculations, we use a h-BN nanorod of 840 nm length, 87 nm height and 250 nm width, which is half covered with a 50 nm thick layer of permittivity $\varepsilon = 2.8$. The calculation are performed without considering the SiO_2/Si substrate.

the non-polaritonic near field of the resonator, and the resonant near field of the 2$^{\text{nd}}$-order FP mode. For a better understanding of the FP resonance, we plot the spectrum $E_z(\omega)$ in the complex plane (Fig. 4.7c) where the 2$^{\text{nd}}$-order FP resonance and the Fano interference manifests as a circular trajectory with an offset, which is the typical signature of a harmonic oscillator [221].

We next discuss the near-field spectra when a conical Pt tip is placed at different heights above the left nanoresonator extremity (illustrated in Fig. 4.7d). To that end, we calculate the dipole moment $p_{\text{tip},z}(\omega)$ induced at the tip. This can be associated to the tip-scattered field and thus to the near-field spectra, as discussed in Chapter 1 and in Appendix B. For this calculation, we employ the same nanorod dimensions ($840 \times 250 \times 87\,\text{nm}^3$) as the one used for the point-dipole calculations (Figs. 4.7b-c). The amplitude spectra $|p_{\text{tip},z}(\omega)|$ for three different tip heights $h_{\text{tip}} = 1\,\text{nm}$ (red dots), 20 nm (blue dots) and 50 nm (green dot) are shown in Fig. 4.7e. From the red spectra, we recognize a strong peak at $1446\,\text{cm}^{-1}$ and weaker one at $1453\,\text{cm}^{-1}$, which are redshifted $4\,\text{cm}^{-1}$ and $2\,\text{cm}^{-1}$ as compared to the near-field spectra obtained with the point-dipole source (Fig. 4.7b). We attribute these spectral peak shifts to the electromagnetic loading of the h-BN nanoresonator by the Pt tip, as we show below by fitting the spectral line shapes. As in the point-dipole calculation, the Fano spectral line shape is the result of the interference between the dipole moment $p_{0,z}(\omega)$ induced at the Pt tip by the incident illumination and the dipole moment $p_{\text{NF},z}(\omega)$ induced at the tip by the near fields of the h-BN nanoresonator. We further find that (i) the peak positions blueshift with increasing height h_{tip} and (ii) the magnitude of $p_{\text{tip},z}(\omega)$ close to the peak (around $1446\,\text{cm}^{-1}$) is reduced as the tip height is increased. The decrease of $|p_{\text{tip},z}(\omega)|$ can be observed in Fig. 4.7f, where we plot $p_{\text{tip},z}(\omega)$ in the complex plane for the three tip heights ($h_{\text{tip}} = 1\,\text{nm}$, 201 nm and 50 nm). We clearly see that the radius of curvature of the circular trajectories is decreased (compare red, blue and green curves) as h_{tip} is increased meaning a reduction of $|p_{\text{tip},z}(\omega)|$.

To calculate the demodulated scattered field $\sigma_n(\omega)$, we vary the tip height (illustrated in Fig. 4.7g) in the simulations and then follow the procedure explained in Appendix B to demodulate the simulated signal. In Fig. 4.7h, we show the amplitude of the 2$^{\text{nd}}$- and 3$^{\text{rd}}$-order demodulated scattered fields, $s_2(\omega)$ (orange dots) and $s_3(\omega)$ (green dots), respectively. We observe the 2$^{\text{nd}}$-order PhP FP peak around $1448\,\text{cm}^{-1}$ and the weak higher-order mode peak at $1454\,\text{cm}^{-1}$. As typical in s-SNOM and nano-FTIR spectroscopy, the amplitude of $\sigma_n(\omega)$ decreases with increasing demodulation order n. We also observe that the resonance peaks remain asymmetric, which we attribute to the interference between the nanoresonator modes and the near field produced by the non-resonant near-fields of the h-BN resonator. For completeness, we plot in Fig. 4.7i $\sigma_2(\omega)$ (orange dots) and $\sigma_3(\omega)$ (green dots) in the complex plane, where

we see the circular trajectory representing the 2nd-order PhP FP mode.

To obtain the eigenfrequency and damping constant of the 2nd-order PhP FP mode, we perform a complex-valued fitting (see solid lines in Figs. 4.7b, c, e, f, h and i) to the spectra shown in Fig. 4.7. We fit the following three spectra: (i) the near-field $E_z(\omega)$ for the point-dipole simulation, (ii) the dipole moment $p_{\mathrm{tip},z}(\omega)$ induced at the Pt tip at different tip heights and (iii) the second, $\sigma_2(\omega)$, and third order, $\sigma_3(\omega)$, demodulated scattered fields. As mentioned in Section 4.3, $x_{\mathrm{PhP}}(\omega)$ is proportional to the near-field $E_z(\omega)$. Thus, the complex-valued fittings shown in Fig. 4.7 are performed using Eqs. (4.2a) and (4.3), i. e., the following relation

$$E_z(\omega) \propto \frac{F_{\mathrm{PhP}}(\omega)}{\omega_{\mathrm{PhP}}^2 - \omega^2 - i\gamma_{\mathrm{PhP}}\omega} + x_0 + iy_0, \tag{4.5}$$

where we assume that $g = 0$ because in these simulations the CBP layer is substituted by a medium with permittivity $\varepsilon = 2.8$, as illustrated in Figs. 4.7a ,d and g.

Figure 4.7j shows the values of ω_{PhP} extracted from the fittings. As a reference, we first fit (solid line in Fig. 4.7c) the near-field spectrum $E_z(\omega)$ obtained from the point-dipole calculation (dots in Fig. 4.7c). The fitting value $\omega_{\mathrm{PhP}} = 1450.3\,\mathrm{cm}^{-1}$ is indicated in Fig. 4.7j by a black dashed line. We next fit (solid lines) the complex spectra $p_{\mathrm{tip},z}(\omega)$ for different tip heights (dots in Fig. 4.7f) obtained from the simulation of the Pt tip on top of the resonator. The values of ω_{PhP} are represented in Fig. 4.7j by the dots. When the tip is far from the nanoresonator, we find that ω_{PhP} is close to the fitting value extracted from the $E_z(\omega)$ spectrum (compare the black dashed line and the green dot). When the height h_{tip} of the tip above the nanoresonator is reduced, ω_{PhP} shifts to lower frequencies, which can be explained by the loading of the nanoresonator by the metallic tip. Fitting the 2nd- and 3rd-order demodulated scattered field spectra, $\sigma_2(\omega)$ and $\sigma_3(\omega)$ (dots in Fig. 4.7i), respectively, we find the same value of ω_{PhP} for both demodulation orders. The fitting values are $\omega_{\mathrm{PhP},n=2} = \omega_{\mathrm{PhP},n=3} = 1448.5\,\mathrm{cm}^{-1}$, which are indicated by orange and green dashed lines in Fig. 4.7j. Notice that $\omega_{\mathrm{PhP},n=2}$ and $\omega_{\mathrm{PhP},n=3}$ are only $2\,\mathrm{cm}^{-1}$ shifted with respect to the fitting value obtained from the $E_z(\omega)$ spectrum.

From the fittings we also extract the damping constant γ_{PhP} (Fig. 4.7k). As a reference, we first show the fitting value extracted from the near-field spectrum $E_z(\omega)$ (shown in Fig. 4.7c). The fitting value $\gamma_{\mathrm{PhP}} = 2.4\,\mathrm{cm}^{-1}$ is indicated in Fig. 4.7k by a black dashed line. We next show the fitting values extracted from the complex spectra $p_{\mathrm{tip},z}(\omega)$ for different tip heights (Fig. 4.7f) obtained from the simulation of the Pt tip on top of the resonator. The fitting values

of γ_{PhP} are represented in Fig. 4.7k by the dots. We find fitting values within the range between $2.1\,\mathrm{cm}^{-1}$ and $2.8\,\mathrm{cm}^{-1}$, which differ at most $0.4\,\mathrm{cm}^{-1}$ with respect to the fitting value obtained from the $E_z(\omega)$ spectrum. Fitting the 2^{nd}- and 3^{rd}-order demodulated scattered field spectra, $\sigma_2(\omega)$ and $\sigma_3(\omega)$ (shown in Fig. 4.7i), respectively, we find a smaller damping constant compared to that obtained by fitting the non-demodulated spectrum of $p_{\mathrm{tip},z}(\omega)$. The fitting values are $\gamma_{\mathrm{PhP},n=2} = 1.7\,\mathrm{cm}^{-1}$ ($0.6\,\mathrm{cm}^{-1}$ shifted with respect to the fitting value obtained from the $E_z(\omega)$ spectrum) for $\sigma_2(\omega)$ spectrum and $\gamma_{\mathrm{PhP},n=3} = 1.5\,\mathrm{cm}^{-1}$ ($0.9\,\mathrm{cm}^{-1}$ shifted with respect to the fitting value obtained from the $E_z(\omega)$ spectrum) for $\sigma_3(\omega)$ spectrum. In Fig. 4.7k, these values are indicated by the orange and green dashed lines respectively.

From these findings, we conclude that the Pt tip on top of the h-BN nanoresonator leads to negligible resonance shift, and the damping constant obtained by fitting the different non-demodulated spectra (Fig. 4.7c and 4.7f) reveals small variations for the 2^{nd}-order PhP FP resonance. Alternatively, when applying a simple harmonic oscillator model to fit the demodulated scattered field spectra, the resulting damping constants are systematically underestimated. Consequently, caution is necessary during the derivation of damping constants from the fitting process applied to nano-FTIR spectra.

4.5.2 Tip on top of the h-BN nanoresonator covered with CBP

In this subsection, we analyze the influence of the metallic tip on top of the nanoresonator that is half covered with molecules. To that end, we show the simulated near-field spectra when the metallic tip is placed on the left extremity of a h-BN nanoresonator ($840\times250\times87\,\mathrm{nm}^3$, same dimensions as the ones used for the calculations shown in Fig. 4.7), whose right half is covered by a 50 nm thick CBP layer. The length of the nanorod is chosen such that the 2^{nd}-order PhP FP resonance is approximately tuned to the CBP molecular resonance at $\omega_{\mathrm{CBP}} = 1450\,\mathrm{cm}^{-1}$. For comparison, we first show the results obtained for the tip being mimicked by a point-dipole source (illustrated in Fig. 4.8a).

We begin our analysis by discussing the near-field spectra obtained for the point-dipole source. Figure 4.8b shows the near-field amplitude spectrum $|E_z(\omega)|$ below the point-dipole source at 65 nm height above the h-BN nanoresonator (position marked by a cross in Fig. 4.8a). By comparing the near-field spectra shown in Figs. 4.7b and 4.8b, we observe that the amplitude peak of the 2^{nd}-order PhP FP resonance splits into two peaks, one around $1443.5\,\mathrm{cm}^{-1}$ and the other one around $1453.5\,\mathrm{cm}^{-1}$. The splitting is a consequence of the

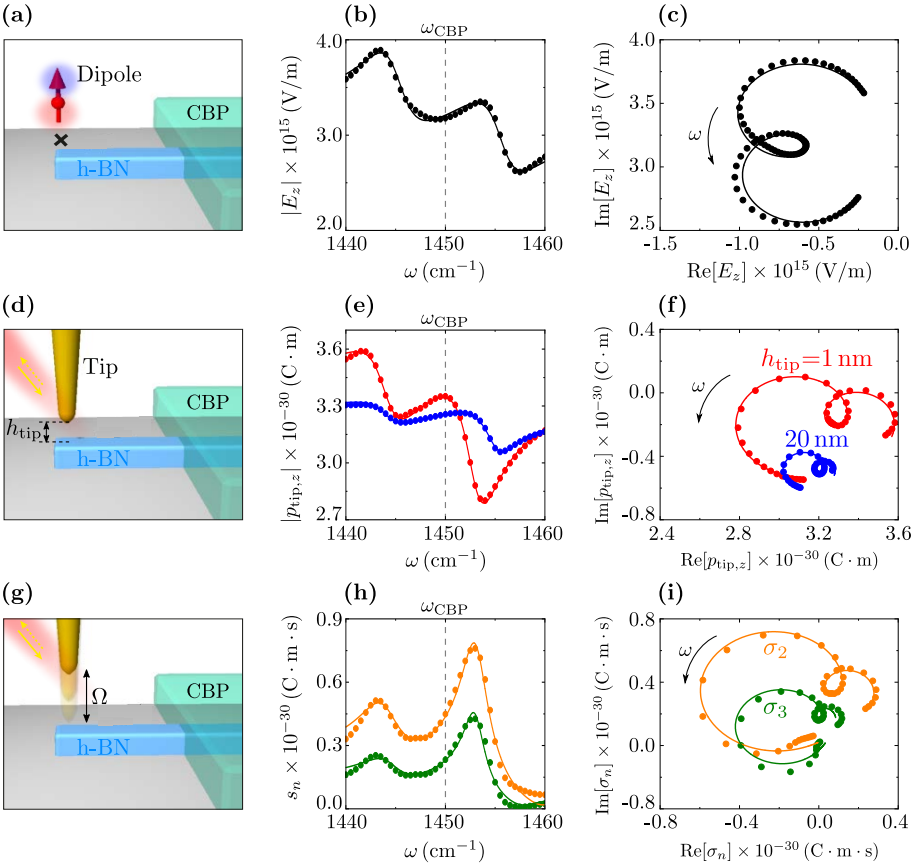

Figure 4.8: Influence of the tip and signal demodulation on the nanoresonator-molecule coupled system. (a) Schematics showing a point-dipole source above an h-BN nanorod half-covered by a CBP molecular layer. (b) Near-field amplitude $|E_z(\omega)|$ below the dipole at the position marked by a cross in panel (a). In the simulations, the point dipole and the evaluation point where located at coordinates ($x = 0, y = -370\,\mathrm{nm}, z = 350\,\mathrm{nm}$) and ($x = 0, y = -370\,\mathrm{nm}, z = 65\,\mathrm{nm}$) respectively. (c) Near-field $E_z(\omega)$ below the point-dipole source, plotted in the complex plane for the frequency range between $1440\,\mathrm{cm}^{-1}$ and $1460\,\mathrm{cm}^{-1}$. The arrow indicates increasing frequency. (d) Schematics of a Pt tip at height h_{tip} above a h-BN nanorod, illuminated with a broadband infrared laser beam. (e) Amplitude of the induced dipole moment $p_{\mathrm{tip},z}(\omega)$ calculated for 1 nm (red line) and 20 nm (blue line) tip height. (f) $p_{\mathrm{tip},z}(\omega)$ plotted in the complex plane for the frequency range between $1440\,\mathrm{cm}^{-1}$ and $1460\,\mathrm{cm}^{-1}$. The color code is the same as the one used in panel (e). The arrow indicates increasing frequency. (g) Schematics of a Pt tip oscillating on top of a h-BN nanoresonator at frequency Ω. (h) Amplitude of the 2$^{\mathrm{nd}}$- and 3$^{\mathrm{rd}}$-order demodulated scattered fields, $s_2(\omega)$ (orange dots) and $s_3(\omega)$ (green dots). (i) $\sigma_2(\omega)$ and $\sigma_3(\omega)$ plotted in the complex plane for the frequencies between $1440\,\mathrm{cm}^{-1}$ and $1460\,\mathrm{cm}^{-1}$. The arrow indicates increasing frequency. Dots in panels (h) and (i) are the numerical results obtained by demodulating the complex-valued spectra $p_{\mathrm{tip},z}(\omega)$. Dots in panels (b), (c), (e) and (f) are the numerical results obtained from simulations. Solid lines represent fits using Eqs. (4.2a) and (4.3). The fittings were performed in the frequency range between $1440\,\mathrm{cm}^{-1}$ and $1460\,\mathrm{cm}^{-1}$. In all numerical calculations we use a nanorod of 840 nm length, 87 nm height and 250 nm width. The calculation are performed without considering the SiO_2/Si substrate.

coupling between the nanoresonator mode and molecular vibrational mode. For a better understanding of the nanoresonator-molecule coupling, we plot in Fig. 4.8c the spectrum $E_z(\omega)$ in the complex plane, where one can identify the appearance of a small loop (compare Figs. 4.7c and 4.8c). As discussed in Section 4.3, the appearance of this loop is a consequence of the nanoresonator mode being coupled to the molecular vibrational mode.

We next discuss the near-field spectra when a conical Pt tip is placed at different heights above the left nanoresonator extremity (illustrated in Fig. 4.8d). To that end, we calculate the dipole moment $p_{\mathrm{tip},z}(\omega)$ induced at the tip as described in Appendix B.2. The amplitude spectra $|p_{\mathrm{tip},z}(\omega)|$ for two different tip heights $h_{\mathrm{tip}} = 1\,\mathrm{nm}$ (red dots) and $20\,\mathrm{nm}$ (blue dots) are shown in Fig. 4.8e. From the red spectra, we recognize two peaks, one at $1442\,\mathrm{cm}^{-1}$ and one at $1450\,\mathrm{cm}^{-1}$, which are shifted $1.5\,\mathrm{cm}^{-1}$ and $3.5\,\mathrm{cm}^{-1}$ as compared to the near-field spectra obtained with the point-dipole source (Fig. 4.8b). These spectral peak shifts are attributed to the electromagnetic loading of the h-BN nanoresonator by the Pt tip, which we verify below by fitting the spectra with the Eq. (4.3). Similarly to the point-dipole calculation shown in Fig. 4.8b, the appearance of two peaks and one dip around ω_{CBP} in the $|p_{\mathrm{tip},z}(\omega)|$ spectrum is the result of the coupling between the nanoresonator and molecular vibrational modes. We further find that the position of the peaks blueshift with increasing height h_{tip}. By plotting $p_{\mathrm{tip},z}(\omega)$ in the complex plane (see Fig. 4.8f), we again observe a small loop indicating the nanoresonator-molecule coupling.

To calculate the demodulated scattered field, we vary the tip height (illustrated in Fig. 4.8g) in the simulations and then follow the procedure explained in Appendix B.2. In Fig. 4.8h, we show the amplitude of the 2^{nd}- and 3^{rd}-order demodulated scattered fields, $s_2(\omega)$ (orange dots) and $s_3(\omega)$ (green dots), respectively. We also observe the two peaks, one around $1443\,\mathrm{cm}^{-1}$ and the other one around $1453\,\mathrm{cm}^{-1}$. For completeness, we plot in Fig. 4.8i the demodulated scattered fields $\sigma_2(\omega)$ and $\sigma_3(\omega)$ in the complex plane, where one can see the formation of the characteristic loop indicating coupling.

To obtain the eigenfrequencies and damping constants of the hybrid modes, we perform a complex-valued fitting (see solid lines in Figs. 4.8b, c, e, f, h and i) to the spectra shown in Figs. 4.8b and 4.8e (dots). Using Eqs. (4.2a) and (4.3), we fit the following three spectra: (i) the near- field $E_z(\omega)$ for the point-dipole simulation, (ii) the dipole moment $p_{\mathrm{tip},z}(\omega)$ induced at the Pt tip at different tip heights and (iii) the second, $\sigma_2(\omega)$, and third order, $\sigma_3(\omega)$, demodulated scattered fields.

Figures 4.9a-b show the values of ω_{PhP} and ω_{CBP} extracted from the fittings in Fig. 4.8. As a reference, we first fit (solid line in Fig. 4.8c) the near-field spectrum $E_z(\omega)$ obtained from the point-dipole calculation (dots in Fig. 4.8c). The fitting values are $\omega_{\mathrm{PhP}} = 1450.2\,\mathrm{cm}^{-1}$ and $\omega_{\mathrm{CBP}} = 1450.3\,\mathrm{cm}^{-1}$

indicated in Figs. 4.9a-b by the black dashed lines. We next fit (solid lines in 4.8f) the complex-valued spectra $p_{\mathrm{tip},z}(\omega)$ (dots in Fig. 4.8f) obtained from the simulation of the Pt tip on top of the resonator that is half covered with the CBP layer. The values of ω_{PhP} and ω_{CBP} are represented in Figs. 4.9a-b by the dots. When the tip is far from the nanoresonator, we find that ω_{PhP} and ω_{CBP} are close to the fitting values extracted from the $E_z(\omega)$ spectrum (compare the black dashed lines and the grey dots at $h_{\mathrm{tip}} = 35\,\mathrm{nm}$ in Figs. 4.9a, c). When the height h_{tip} of the tip above the nanoresonator is reduced, ω_{PhP} and ω_{CBP} shift to lower frequencies due to an increase of the electromagnetic loading of the h-BN nanoresonator by the Pt tip. Fitting the 2$^{\mathrm{nd}}$- and 3$^{\mathrm{rd}}$-order demodulated scattered field spectra, $\sigma_2(\omega)$ and $\sigma_3(\omega)$ (shown in Fig. 4.8i), respectively, one can find the following fitting values: $\omega_{\mathrm{PhP},n=2} = 1449.8\,\mathrm{cm}^{-1}$, $\omega_{\mathrm{PhP},n=3} = 1450.3\,\mathrm{cm}^{-1}$, indicated by the orange and green dashed lines in Fig. 4.9a, and $\omega_{\mathrm{CBP},n=2} = 1447.3\,\mathrm{cm}^{-1}$, $\omega_{\mathrm{CBP},n=3} = 1447\,\mathrm{cm}^{-1}$, indicated by the orange and green dashed lines in Fig. 4.9b. Notice that $\omega_{\mathrm{PhP},n=2}$ and $\omega_{\mathrm{PhP},n=3}$ differ at most $0.4\,\mathrm{cm}^{-1}$ with respect to the fitting value obtained from the $E_z(\omega)$ spectrum. On the other hand, the fitting values $\omega_{\mathrm{CBP},n=2}$ and $\omega_{\mathrm{CBP},n=3}$ differ at most $3.5\,\mathrm{cm}^{-1}$ with respect to the fitting value obtained from the $E_z(\omega)$ spectrum.

From the fittings, one can also extract the damping constants γ_{PhP} and γ_{CBP}, which are plotted in Figs. 4.9c-d. As a reference, we first show the fitting value extracted from the near-field spectra $E_z(\omega)$ (Fig. 4.8c). The fitting values $\gamma_{\mathrm{PhP}} = 2.3\,\mathrm{cm}^{-1}$ and $\gamma_{\mathrm{CBP}} = 7.6\,\mathrm{cm}^{-1}$ are indicated in Figs. 4.9c-d by a black dashed line. The sum of the damping constants extracted from the near-field spectra $E_z(\omega)$ is $\gamma_{\mathrm{PhP}} + \gamma_{\mathrm{CBP}} = 9.9\,\mathrm{cm}^{-1}$. We next show the fitting values extracted from the complex spectra $p_{\mathrm{tip},z}(\omega)$ (Fig. 4.8f) obtained from the simulation of the Pt tip on top of the resonator. The fitting values of γ_{PhP} and γ_{CBP} are represented in Figs. 4.9c-d by the dots. We find fitting values for γ_{PhP} and γ_{CBP} within the ranges of $2.5\,\mathrm{cm}^{-1}$ to $3.0\,\mathrm{cm}^{-1}$ and $5.3\,\mathrm{cm}^{-1}$ to $7.0\,\mathrm{cm}^{-1}$, respectively, which differ at most $2.3\,\mathrm{cm}^{-1}$ from the fitting values obtained from the $E_z(\omega)$ spectrum. Thus, the sum of the damping constants lies within the range of $7.8\,\mathrm{cm}^{-1}$ to $10.0\,\mathrm{cm}^{-1}$ which differ from the value $\gamma_{\mathrm{PhP}} + \gamma_{\mathrm{CBP}} = 9.9\,\mathrm{cm}^{-1}$ by $2.1\,\mathrm{cm}^{-1}$ (21%). Fitting the demodulated scattered fields spectra $\sigma_2(\omega)$ and $\sigma_3(\omega)$ (Fig. 4.8i), we find a smaller damping constant for γ_{PhP} than that obtained by fitting the non-demodulated spectrum of $p_{\mathrm{tip},z}(\omega)$. In Fig. 4.9c, we indicate the value of $\gamma_{\mathrm{PhP},n=2}$ by an orange dashed line and the value of $\gamma_{\mathrm{PhP},n=3}$ by a green dashed line ($\gamma_{\mathrm{PhP},n=2} = \gamma_{\mathrm{PhP},n=3} = 0.4\,\mathrm{cm}^{-1}$). Additionally, the damping constants of the CBP oscillator are plotted in Fig. 4.9d by the orange and green dashed lines, respectively ($\gamma_{\mathrm{CBP},n=2} = 6.7\,\mathrm{cm}^{-1}$ and $\gamma_{\mathrm{CBP},n=3} = 5.9\,\mathrm{cm}^{-1}$). We find that the sum of the damping constants $\gamma_{\mathrm{PhP},n=2} + \gamma_{\mathrm{PhP},n=2} = 7.1\,\mathrm{cm}^{-1}$ and $\gamma_{\mathrm{PhP},n=3} + \gamma_{\mathrm{CBP},n=3} = 6.3\,\mathrm{cm}^{-1}$ differ

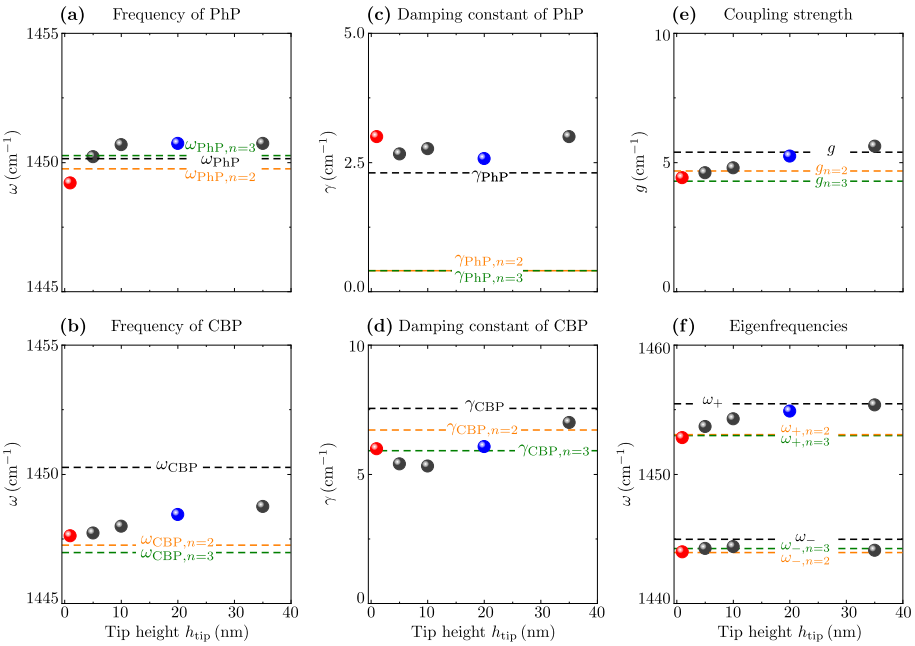

Figure 4.9: Fitting values obtained from the fits shown in Fig. 4.8. Fitting values of (a) eigenfrequency of the 2nd-order FP resonance ω_{PhP}, (b) eigenfrequency of CBP molecular resonance ω_{CBP}, (c) damping constant of the 2nd-order FP resonance, γ_{PhP}, (d) CBP damping constant, γ_{CBP}, (e) coupling strength g, and (f) eigenfrequencies of the coupled system, $\omega_{\pm}$, as a function of the tip height h_{tip}. The fittings were performed using Eq. (4.3). The eigenfrequencies $\omega_{\pm}$ were obtained with Eq. (4.4). Black dashed lines represent the fitting values obtained from the spectra plotted in Fig. 4.8c. Orange and green dashed lines represent the fitting values obtained from the spectra plotted in Fig. 4.8i. Dots represent the fitting values obtained from the spectra of $p_{tip,z}(\omega)$ at different tip heights $h_{tip} = 1\,\text{nm}$ (red dot), 20 nm (blue dot) and 5 nm, 10 nm and 35 nm (grey dots).

from the value $\gamma_{PhP} + \gamma_{CBP} = 9.9\,\text{cm}^{-1}$ around $2.8\,\text{cm}^{-1}$ (28%) and $3.6\,\text{cm}^{-1}$ (36%), respectively. These modifications of the sum of the damping constants obtained from the demodulated spectra can be summarized as $\gamma_{PhP} + \gamma_{CBP} = 1.39 \times (\gamma_{PhP,n=2} + \gamma_{CBP,n=2})$ and $\gamma_{PhP} + \gamma_{CBP} = 1.56 \times (\gamma_{PhP,n=3} + \gamma_{CBP,n=3})$.

In addition, we extract from the fits the coupling strength g and then use Eq. (4.4) to calculate the eigenfrequencies $\omega_{\pm}$. The results are shown in Figs. 4.9e-f. When the tip is far from the nanoresonator, we find that g extracted from the $p_{tip,z}(\omega)$ spectra is close to the fitting value $g = 5.4\,\text{cm}^{-1}$ extracted from the $E_z(\omega)$ spectrum (compare the black dashed line and the grey dots at $h_{tip} = 35\,\text{nm}$ in Fig. 4.9e). We find fitting values for g within the range of $4.4\,\text{cm}^{-1}$ to $5.7\,\text{cm}^{-1}$, which differ at most $1\,\text{cm}^{-1}$ (19%) from the fitting values

obtained from the $E_z(\omega)$ spectrum. Fitting the 2$^{\text{nd}}$- and 3$^{\text{rd}}$-order demodulated scattered field spectra, $\sigma_2(\omega)$ and $\sigma_3(\omega)$ (shown in Fig. 4.8i), respectively, we find coupling strength values of $g_{n=2} = 4.7\,\text{cm}^{-1}$ and $g_{n=3} = 4.3\,\text{cm}^{-1}$, which differ at most $1.1\,\text{cm}^{-1}$ (21%) from the fitting value obtained from the $E_z(\omega)$ spectrum, leading to the following relation: $g = 1.26 \times g_{n=3}$. Furthermore, we find similar values for the eigenfrequencies ω_+ and ω_- obtained from the $E_z(\omega)$ spectrum (Fig. 4.8c), from the $p_{\text{tip},z}(\omega)$ spectra (Fig. 4.8f) and from $\sigma_2(\omega)$ and $\sigma_3(\omega)$ spectra (Fig. 4.8i). The values of the eigenfrequencies $\omega_\pm$ are plotted in Fig. 4.9f. The black dashed lines represents the values obtained from the $E_z(\omega)$ spectrum, the color dots represent the values obtained from the $p_{\text{tip},z}(\omega)$ spectra, and, the orange and green dashed lines represent the values obtained $\sigma_2(\omega)$ and $\sigma_3(\omega)$. By comparing the values, it be inferred that $\omega_\pm$ exhibit small variations.

The analysis presented in this subsection can be summarized as follows. We first applied the two-coupled harmonic oscillator model (same as the one used in Fig. 4.4) to fit the simulated near-field spectra where the tip is modeled as a metal cone but without considering the tip oscillation and signal demodulation. Compared to the fitting parameters obtained from the unperturbed molecule-covered resonator spectra (obtained from the point-dipole simulations), we find that the presence of the metallic tip yields negligible spectral shifts of the bare h-BN nanoresonator mode and the hybrid polariton modes ($< 3\,\text{cm}^{-1}$), a negligible change of the sum of damping parameters, $\gamma_{\text{PhP}} + \gamma_{\text{CBP}}$, and only a slight reduction of the coupling strength by a factor ~ 1.26. In a second simulation, we additionally implemented tip oscillation and signal demodulation. Fitting of the simulated spectra yields nearly the same coupling strengths and mode positions as in the previous case. However, for the sum of the damping parameters, $\gamma_{\text{PhP}} + \gamma_{\text{CBP}}$, we obtain values that are reduced by a factor of ~ 1.56 as compared to the results obtained from the simulations where the tip is modeled as a point-dipole source. Since the presence of the tip, its oscillation and signal demodulation can yield significantly different values for g and $\gamma_{\text{PhP}} + \gamma_{\text{CBP}}$, we re-evaluate the coupling regime obtained in the experiment (Fig. 4.6e) according to the following modified condition to establish strong coupling,

$$\frac{1.26 \times g}{1.56 \times (\gamma_{\text{PhP}} + \gamma_{\text{CBP}})} > 0.25 \;\text{ or equivalently }\; \frac{g}{\gamma_{\text{PhP}} + \gamma_{\text{CBP}}} > 0.31, \tag{4.6}$$

where g and $\gamma_{\text{PhP}} + \gamma_{\text{CBP}}$ are the parameters (listed in Table G.2 of Appendix G) obtained by fitting the experimental near-field spectra. Under this modified condition, we find that two of the nanoresonators (length $L = 1.2\,\mu\text{m}$ and $L = 0.9\,\mu\text{m}$) satisfy the strong coupling criteria, whereas the other nanores-

onators are at the onset to strong coupling. The transition from weak to strong coupling according to this re-evaluation is marked in Fig. 4.6e by red dashed horizontal lines. Since the modified condition for evaluating the coupling regime is more conservative than the original one ($g/(\gamma_{\mathrm{PhP}} + \gamma_{\mathrm{CBP}}) > 0.25$), the transition occurs in Fig. 4.6e at larger g values. We note that the factors used to re-evaluate the coupling regime are specific for our nano-FTIR experiment and may change for different tip oscillation amplitudes or signal demodulation orders.

4.6 Summary and conclusions

We have demonstrated in this chapter that infrared near-field spectroscopy can be applied for nanoscale spatial mapping of strong coupling between molecular vibrational modes and resonating dark PhP modes. To that end, we introduce the concept of remote near-field probing with a non-resonant tip, where the tip and molecules are spatially separated such that the direct near-field interaction between tip and molecules is avoided. Such minimal-invasive probing offers the advantage that the hybrid nanoresonator-molecule modes and coupling strengths can be determined within the model of two coupled harmonic oscillators without considering the tip as a third oscillator, which significantly simplifies the coupling analysis and increases its robustness. On the other hand, numerical simulations of remote near-field spectroscopy including the metal tip, its oscillation and signal demodulation reveal that damping parameters may be underestimated when tip oscillation and signal demodulation are not properly considered to describe the near-field spectra through a coupled harmonic oscillator model. Since near-field spectroscopy is available in the wide spectral range between visible and terahertz frequencies, we envision remote near-field probing studies of strong coupling of different plasmonic and phononic resonators (which apart from h-BN, could be made, for example, from V_2O_5 or α-MoO_3 that cover various infrared frequency ranges) with molecular vibrations or excitons in various resonator geometries. The possibility to probe dark modes and spatially control the selective excitation and probing of coexisting modes could pave the way to explore strong coupling configurations that are not easily accessible by far-field spectroscopy.

Outlook and conclusions

This thesis aims at studying polartions using fast electron beams and near-field optical probes. In particular, we analyze three different samples: (i) phonon polaritons in bulk and semi-infinite surfaces of h-BN (Chapter 2), (ii) anapoles and excitons interplay in WS_2 nanodisks with high-refractive index (Chapter 3), and (iii) h-BN phononic nanoresonator-CBP molecules coupling (Chapter 4). In the following, we summarize the main findings in each chapter and discuss possible avenues for future investigation:

- In Chapter 2, we analyze in detail the excitation of phonon polaritons in hexagonal boron nitride using fast electron beams. We consider two different situations: when the electron travels through the bulk of h-BN and when it travels in vacuum above a semi-infinite h-BN surface. In the first situation, we show that the fast probing electron couples to volume phonon polaritons when traveling either parallel or at an angle α relative to the h-BN optical axis. We demonstrate that the excitation of these polaritonic modes strongly depends on the electron velocity v and the angle α between the trajectory of the fast electron and the h-BN optical axis. Additionally, we demonstrate that Dyakonov surface phonon polaritons can be induced by a fast electron traveling above the h-BN surface. A remarkable feature is the capability of fast electrons traveling in an aloof trajectory to excite volume polaritons in h-BN. From a detailed mode analysis, we show that the electron beam transfers a specific momentum to polaritons excited in h-BN. This momentum transfer determines the properties of the excited phonon polaritons and thus controls their phase and group velocities, as well as their propagation direction.

  Although we study the specific uniaxial material, h-BN, the results presented in this chapter can be generalized to other uniaxial polaritonic materials, such as $PdCoO_2$, for instance. Considering the significant advancements in the investigation of polaritons excited in biaxial materials, we believe that the theoretical framework introduced here can be extended to this kind of materials and may provide a further understanding of the properties of polaritons excited in α-MoO_3 or V_2O_5. It is also worth mentioning that one of the key findings in this chapter is that polaritonic waves in h-BN can be controlled through variations of two degrees of freedom: the electron velocity v and the angle of its trajectory α with respect to the h-BN optical axis. A natural next step involves systematically varying these parameters to explore whether the disper-

sion relation of hyperbolic polaritonic waves can be reconstructed using EELS.

- In Chapter 3, we demonstrate that electron energy loss spectroscopy can be applied to probe optical anapole states in high-index dielectric nanoresonators. We show that the prominent dips appearing in the EEL spectra of high-index dielectric disks are associated with the excitation of optical anapoles in the disk. We provide an analytical model based on temporal coupled-mode theory (TCMT) that allows us to describe the first electric dipole anapole as the result of the far-field interference between two resonant modes of the disk excited by the fast electron beam. We experimentally verify our theoretical predictions by performing EELS of WS_2 nanodisks by our collaborators at Chalmers University of Technology (Sweden), and reveal optical anapoles and anapole-exciton hybrid excitation within the same nanoobject. By extending the TCMT model and consider the A-exciton of WS_2, we are able to model the optical response of the coupled anapole-exciton system with an effective 3×3 Hamiltonian which allows us to calculate the eigenfrequencies of the new hybrid modes. We find a clear anti-crossing of these eigenfrequencies as one varies the nanodisk radius, indicating that the two resonant modes that model the anapole are strongly coupled to the A-exciton. Additionally, we demonstrate that EELS in STEM allows for spatial mapping of WS_2 nanodisk modes, isolated anapoles and anapole-exciton hybrids with subnanometer resolution. By placing the electron beam at specific positions along the WS_2 nanodisk, we can effectively control the modes excitation and thus the formation of the optical anapoles.

  The results shown in this chapter help to understand the properties of dielectric anapole excitation by fast electron beams as well as to unveil the details of anapole-exicton coupling in a compact nanoconfiguration. Furthermore, we demonstrate that EELS in STEM is a powerful tool to study dark scattering states appearing in dielectric materials beyond the possibilities offered by conventional optical techniques. Considering the rapid progress of the field of high-refractive index dielectric materials, we envision that our results will enable new possibilities for studying dielectric modes, higher-order and magnetic anapole states in dielectric nanoresonators with subnanometer spatial resolution. Future work could be directed towards understanding the excitation of optical anapoles for different electron trajectories or in more complicated geometries that are not cylindrically symmetric.

- In Chapter 4, we demonstrate that infrared near-field spectroscopy can be applied for nanoscale spatial mapping of strong coupling between molec-

ular layers and single phonon polariton nanoresonators. We introduce the concept of remote near-field probing with a non-resonant tip, where the tip and molecules are spatially separated so that the direct near-field interaction between the tip and molecules is avoided. This methodology offers the advantage that the hybrid nanoresonator and molecular vibrational modes and coupling strengths can be determined using the model of two coupled harmonic oscillators without considering the tip as a third oscillator. We verify this approach via numerical simulation, where we model the tip as a point-dipole source and find the appearance of a loop in the complex-valued near-field spectra of the nanoresonator half-covered with molecules, which is an indicator of the nanoresonator-molecules coupling. Finally, by performing a numerical simulation where we model the tip as a metallic conical structure made of platinum, including its oscillation and signal demodulation. We find that the damping parameters of the constituents (molecular vibrations and phononic resonances) may be underestimated when tip oscillation and signal demodulation are not considered in the fitting of the near-field spectra with a coupled harmonic oscillator model.

An intriguing finding in this chapter is the appearance of the loop and the topology change of complex-valued trajectories of the near field spectrum when the nanoresonator is coupled to the molecular layer. We believe that this feature (the loop) may become an interesting means for characterizing coupling phenomena, and thus, provides a promising complementary tool for coupling examination. Additional investigation on this aspect could be focused on the development of a two-coupled oscillator model that incorporates the impact of demodulating the near-field signal.

We hope that our findings will be of importance and interest to the nanophotonics research community working on anisotropic polaritonic media, high-index dielectric structures, and strongly coupled systems. Our results clearly demonstrate the potential applications of electron and near-field spectroscopy to provide unique information about the rich near-field optical response of strongly coupled nanophotonic systems.

Appendices

A

Units and conventions

We use the International System (SI) of units for the equations presented in this thesis. The physical quantities are reported in units typically employed in EEL and near-field spectroscopy. For example, in Chapters 1-3 we report the amount of energy loss $\hbar\omega$ in eV, whereas in Chapter 4, we report the near-field spectra as a function of spectrocopic wavenumbers $\omega(\mathrm{cm}^{-}1)$. The latter can be easily transformed to angular frequency using to the following relation:

$$\omega(\mathrm{cm}^{-1}) = \frac{\omega(\mathrm{rad/s})}{2\pi c}. \tag{A.1}$$

In Chapter 3, we report the electron energy-loss probability $\Gamma(\omega)$ in units of eV^{-1}. Notice that $\Gamma(\omega)$ as defined by Eq. (1.59) has dimensions of time (units of seconds in SI), and thus, to obtain $\Gamma(\omega)$ in dimensions of 1/Energy one has to divide Eq. (1.59) by the reduced Planck's contant, that is,

$$\Gamma[1/\mathrm{Energy}] = \frac{\Gamma[\mathrm{time}]}{\hbar}. \tag{A.2}$$

Additionally, in this thesis, we follow ref. [31] and define the Fourier transform as

$$\mathbf{F}(\mathbf{k};\omega) := \mathscr{F}\{\mathbf{F}(\mathbf{r};t)\} = \int_{-\infty}^{\infty} \mathrm{d}t\, e^{i\omega t} \int_{\mathbb{R}^3} \mathrm{d}^3\mathbf{r}\, e^{-i\mathbf{k}\cdot\mathbf{r}}\, \mathbf{F}(\mathbf{r};t), \tag{A.3}$$

and its inverse as

$$\mathbf{F}(\mathbf{r};t) := \mathscr{F}^{-1}(\mathbf{k};\omega)\} = \frac{1}{(2\pi)^4} \int_{-\infty}^{\infty} \mathrm{d}\omega\, e^{-i\omega t} \int_{\mathbb{K}^3} \mathrm{d}^3\mathbf{k}\, e^{i\mathbf{k}\cdot\mathbf{r}}\, \mathbf{F}(\mathbf{k};\omega), \tag{A.4}$$

where $\mathbf{F}$ is a smooth vector field, $\mathscr{F}$ is the Fourier transform, $\mathbb{R}^3$ stands for the Euclidean space and $\mathbb{K}^3$ stands for the reciprocal space. Following this convention, the spatial and temporal derivatives of $\mathbf{F}(\mathbf{r};t)$ can be Fourier transformed

using the following relations:

$$\frac{\partial}{\partial x_i}\mathbf{F}(x_i;t) \rightarrow ik_i\mathbf{F}(k_i;t) \;\text{ with }\; x_i \in \{x,y,z\},\; k_i \in \{k_x,k_y,k_z\}, \tag{A.5a}$$

$$\text{and }\; \frac{\partial}{\partial t}\mathbf{F}(\mathbf{r};t) \rightarrow -i\omega\mathbf{F}(\mathbf{r};\omega). \tag{A.5b}$$

When only the time domain is transformed to the frequency domain while preserving the spatial coordinates, we refer to the Fourier transform as the time-to-frequency Fourier transform and define it as follows:

$$\mathbf{F}(\mathbf{r};\omega) := \mathcal{F}\{\mathbf{F}(\mathbf{r};t)\} = \int_{-\infty}^{\infty} \mathrm{d}t\, e^{i\omega t}\, \mathbf{F}(\mathbf{r};t), \tag{A.6}$$

and its inverse as:

$$\mathbf{F}(\mathbf{r};t) := \mathcal{F}^{-1}\{\mathbf{F}(\mathbf{r};\omega)\} = \frac{1}{2\pi}\int_{-\infty}^{\infty} \mathrm{d}\omega\, e^{-i\omega t}\, \mathbf{F}(\mathbf{r};\omega). \tag{A.7}$$

B

Numerical implementation of Maxwell's equations: Finite Element Method (FEM)

As we discussed in Chapter 1, the differential form of Maxwell's equations consists of a set of four coupled partial differential equations that relate, at each spatial position $\mathbf{r}$ and time t, the total electric $\mathbf{E}_{\text{tot}}(\mathbf{r};t)$ and magnetic $\mathbf{B}_{\text{tot}}(\mathbf{r};t)$ fields to the charge and current density distributions, $\rho(\mathbf{r};t)$ and $\mathbf{J}(\mathbf{r};t)$, respectively. For arbitrary-geometric objects, with a specific material (that is, for specific $\rho(\mathbf{r};t)$ and $\mathbf{J}(\mathbf{r};t)$), interacting with EM waves, it is not always possible to find analytical solutions to Maxwell's equations and thus numerical methods need to be employed in order to find their solutions. Among these numerical techniques, one can use the finite difference method (FDM) or the finite element method (FEM) which are well known numerical techniques based on discretization of the spatial and time domains. The FDM solves Maxwell's equations by approximating the derivatives with finite differences [222–224], whereas the FEM uses variational methods and trial functions to find an approximate solution to the differential equations [225–227] .

In this thesis, we use the FEM in the frequency domain to solve Maxwell's equations and perform the numerical simulations. Particularly, we use FEM as implemented in the Radio Frequency Module of the commercial software COMSOL Multiphysics [228]. In the following sections, we describe a methodology to calculate the EEL probability $\Gamma(\omega)$ and to model the nano-FTIR signal using COMSOL Multiphysics.

B.1 EEL probability within COMSOL simulation box

For an arbitrary geometric nanostructure with specific dielectric function $\varepsilon(\omega)$, we performed numerical simulations using the 3D simulation domain in the Cartesian coordinate system (x, y, z). The simulation domain consists of a nanostructure and a line current along the z-axis, which models the probing electron traveling in the z-direction. The complete system (probing electron and nanostructure) is embedded in a homogeneous box (simulation box) filled with air of depth, width and height equal to L_{PML}. We applied perfectly matched layers (PML) for the boundaries of the simulation box to ensure numerical convergence and to attenuate the reflection of EM waves at the boundaries of the box. Typically, we set the size of the PML box, L_{PML}, to be 12 or 15 times larger than the size of the nanostructure with a thickness equal to $d_{\mathrm{PML}} = 0.1 \times L_{\mathrm{PML}}$. We show in Fig. B.1a a representative example of a 3D simulation domain, where the nanostructure is a spherical Al nanoparticle close to an electron beam traveling in aloof trajectory (see blue vertical line in Fig. B.1a). The Al sphere has radius $a = 75\,\mathrm{nm}$ and dielectric function $\varepsilon_{\mathrm{Al}}(\omega)$ which is characterized by the Drude–Sommerfeld–Lorentz model given by Eq. (1.14), with parameters $\hbar\omega_p = 15.2\,\mathrm{eV}$, $\hbar\gamma = 0.15\,\mathrm{eV}$ and $\varepsilon_\infty = 1$. The vertical line that models the electron beam carries a current $I(\omega) = -I_0 e^{i\omega z/v}$, where $I_0 = 1\,\mathrm{A}$, ω is the angular frequency and $v = 0.7c$ is the velocity of the electron. The length of the line current is equal to L_{PML} and is located at a distance $b = 100\,\mathrm{nm}$ (impact parameter) with respect to the center of the sphere (see Fig. B.1b). In order to solve Maxwell's equations in the simulation domain, we discretize (mesh) all the structures using free tetrahedral elements as depicted in Fig. B.1c. The maximum element size in the mesh is set to be less than $\lambda_{\mathrm{min}}/10$, with λ_{min} the minimum wavelength involved in the simulation. The area of the PML is meshed by $5 - 10$ Swept layers. Once all the structures within the simulation domain are meshed, we then solve Maxwell's equations and find the total EM field at each spatial point in the domain. This allow us to calculate the energy losses using the classical dielectric theory (for details see Chapter 1) as we discuss next.

To calculate the EEL probability $\Gamma(\omega)$, we assume that the induced electric field, $\mathbf{E}_{\mathrm{ind}}(\mathbf{r};\omega)$, coming from the response of the nanostructure to the incident electromagnetic field of the electron beam, acts back on the beam, causing an

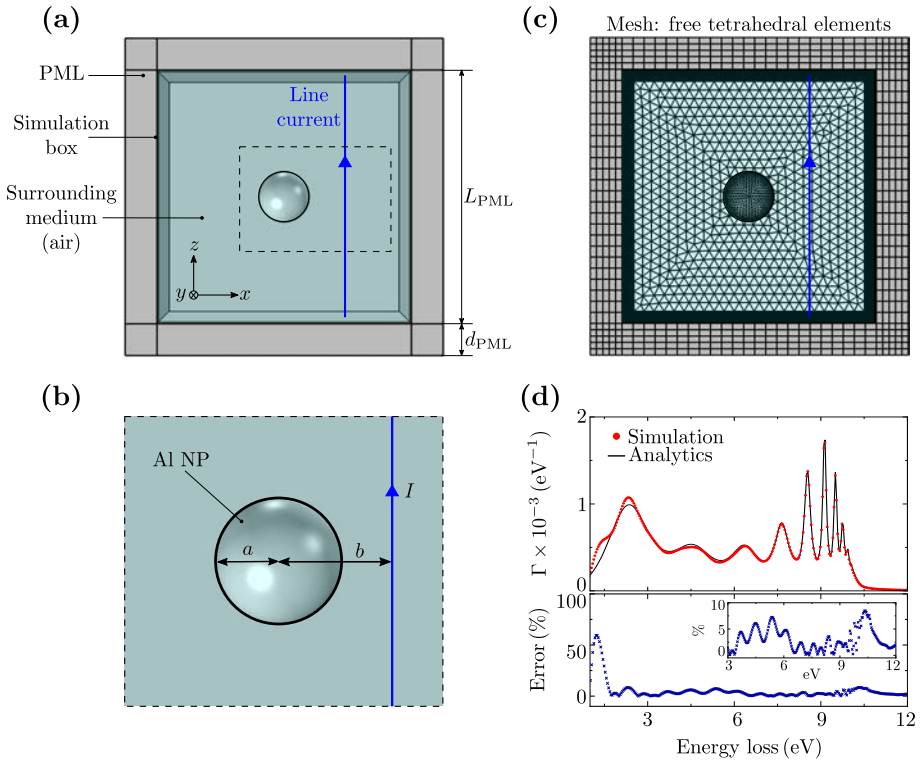

Figure B.1: Comparison of analytical and numerical calculation of EEL probability. (a) Sketch of the simulation domain under study. The sphere centered at the origin represents an Al spherical nanoparticle with a dielectric function characterized by Eq. (1.14) and a radius $a = 75\,\mathrm{nm}$. The blue vertical line represents the probing electron beam traveling along the z-direction at a distance $b = 100\,\mathrm{nm}$ with respect to the center of the spherical nanoparticle. The particle and line are embedded in air (light green region). The gray rectangular box represents the PML. (b) Zoom of panel (a) around the region marked by the dashed lines. (c) Image of the simulation domain containing the mesh used to solve Maxwell's equations. The top panel in (d) shows the simulated EEL spectra obtained with COMSOL Multyphisycs (red dots) and the analytical solution (black line), whereas the bottom panel shows the relative error between the two calculations.

energy loss which reveals the energy and strength of the excitation induced in the nanostructure. Following Eq. (1.59), the EEL probability $\Gamma(\omega)$ of the electron beam to lose an energy $\hbar\omega$ is given by

$$\Gamma(\omega) = \frac{e^2}{\pi\hbar\omega I_0} \int_{-L_{\mathrm{PML}}/2}^{L_{\mathrm{PML}}/2} \mathrm{d}z\, \mathrm{Re}[E_{\mathrm{ind},z}(x_{\mathrm{e}}, y_{\mathrm{e}}, z; \omega)\, e^{-i\omega z/v}], \tag{B.1}$$

where $E_{\mathrm{ind},z}(\mathbf{r};\omega)$ is the z-component of the electromagnetic field induced by the nanostructure and $E_{\mathrm{ind},z}(\mathbf{r};\omega)$ is evaluated along the trajectory of the elec-

tron beam $\mathbf{r}_e(t) = (x_e = b, y_e = 0, z = vt)$. As mentioned above, the electron beam is modeled in numerical simulations as a vertical line with current $I(\omega) = -I_0 e^{i\omega z/v}$. Thus, to obtain Eq. (B.1) from Eq. (1.59), we change $E_{\mathrm{ind},z}(\mathbf{r}_e;\omega) \mapsto eE_{\mathrm{ind},z}(\mathbf{r}_e;\omega)/I_0$. In practice, to calculate $E_{\mathrm{ind},z}(\mathbf{r};\omega)$ around the nanostructure, we performed the simulation for each frequency ω twice: one simulation considering the nanostructure with its characteristic dielectric function $\varepsilon(\omega)$ and another simulation considering the nanostructure with permittivity $\varepsilon(\omega) = 1$, while maintaining the same mesh in all domains. Their difference yields $E_{\mathrm{ind},z}(\mathbf{r})$, which can be integrated along the electron beam trajectory to find $\Gamma(\omega)$ (Eq. (B.1)).

We show in the top panel of Fig. B.1d the simulated EEL spectra (red dots) obtained for the aloof electron beam traveling close to the Al spherical nanoparticle. One can clearly recognize in the spectra different peaks associated with the LSPP resonances excited at the particle. For comparison, we also calculate the EEL probability following the analytical theory for the interaction of spherical nanoparticles with fast electron beams reported in refs. [8, 229–231]. The results obtained with this theory are shown by the black line in Fig. B.1d, where one can see the good agreement between both the numerical (COMSOL) and the analytical calculations. The relative error between both calculations is less than 10% for energies between $1.5\,\mathrm{eV} - 12\,\mathrm{eV}$ (see bottom panel in Fig. B.1d). For lower energies, the numerical simulation deviates from the analytical solution by up to 60%. This deviation can be reduced by refining the mesh of the simulation domain. From this analysis we can conclude that modeling the fast electron as a line current and solving Maxwell's equation with FEM is adequate to reproduce the classical interaction of nanoparticles with fast electron beams.

B.2 Tip-scattered field within COMSOL simulation box and demodulation

To perform the numerical simulations shown in Chapter 4, we use the Radio Frequency Module of COMSOL Multiphysics software and model the h-BN nanoresonators as rectangular structures of $w = 250\,\mathrm{nm}$ width (along the x-direction), $d = 87\,\mathrm{nm}$ thickness (along the z-direction) and variable length L (along the y-direction). The resonators are on top of a 250 nm thick layer characterized by the permittivity of $\varepsilon_{\mathrm{SiO_2}}(\omega)$, which is on top of a Si substrate (see Fig. B.2a). The CBP layer is modeled as a 50 nm thick layer covering half

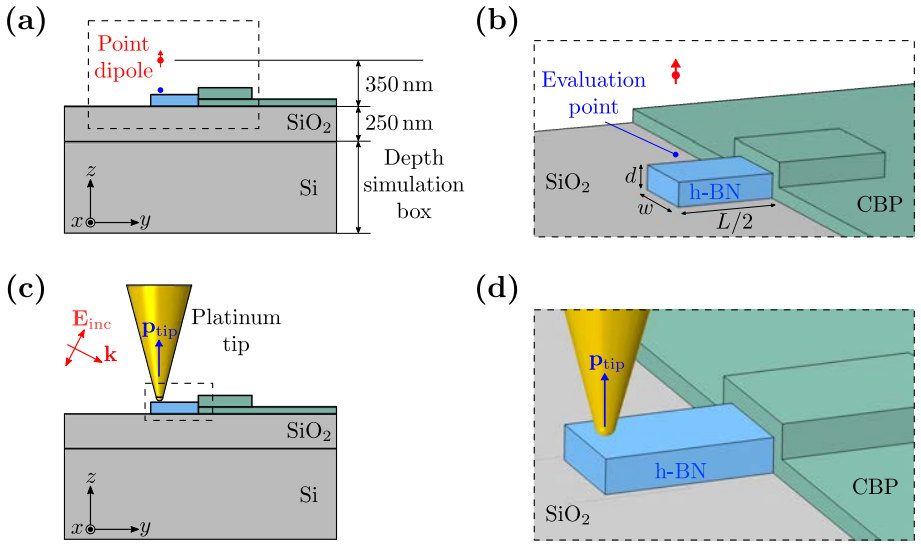

Figure B.2: Numerical simulations of nanoscale spectroscopy of phononic resonators. (a) Sketch of the simulation domain under study. The two grey boxes from top to bottom represent the SiO_2/Si substrate, and the blue-green structure on top of the SiO_2 substrate represents the h-BN rod half (blue box) covered with the CBP layer (green layer). The vertical red arrow represents the point-dipole source, whereas the blue circle indicates the spatial position where the electric field is evaluated (evaluation point). (b) Zoom of panel (a) in 3D perspective around the region marked by the dashed lines. (c) Sketch of the same simulation domain show in panel (a), where a conical structure (yellow cone) made of platinum models the nano-FTIR tip instead of a point-dipole source. The p-polarized incident illumination (red arrows), together with the the tip-resonator near-field interaction induces a net dipole moment $\mathbf{p}_{\text{tip}}$ at the tip (vertical blue arrow). (d) Zoom in 3D of panel (c) around the region marked by the dashed lines.

the length of the h-BN nanorod. We model the nano-FTIR tip as a point-dipole source and also as a conical platinum structure, as explained below.

B.2.1 Tip modeled as a point-dipole source

To obtain the numerical results shown in Figs. 4.1e, 4.2b-c, and 4.4, we model the tip as a point-dipole source (red arrow in Figs. B.2a,b) oriented perpendicularly to the substrate (along the z-direction). This model assumes that the elongated tip in the experiment is oriented perpendicularly (z-direction) to the h-BN nanorod and is illuminated by p-polarized light. The experimental signal detected in the far-field ($E_{\text{scat}}(\omega)$) is approximated by the vertical component of the electric near-field ($E_z(\omega)$) at an evaluation point (blue circle

in Figs. B.2a,b) below the point-dipole source. In all the calculations, the point-dipole source and the evaluation points are located at coordinates ($x = 0, y = -L/2 + 50\,\text{nm}, z = 350\,\text{nm}$) and ($x = 0, y = -L/2 + 50\,\text{nm}, z = 65\,\text{nm}$), respectively. We set the origin ($x = 0, y = 0, z = 0$) in the middle of the top surface of the nanorod. The CBP layer covers the nanorod for $y > 0$.

To ensure numerical convergence of the simulated near-field spectra, the complete structure (point-dipole source, h-BN nanorod and CBP layer) is located in a homogeneous rectangular box (filled with air) of $8 \times w$ width, $25 \times d$ depth and $4 \times L$ length (see Fig. B.2b where we define the parameters w, d and L). We use perfectly matched layers (PML) for the boundaries of the simulation box and free triangular elements for the nanorod mesh and free tetrahedral elements for all other structures.

B.2.2 Tip modeled as a Pt conical structure

To perform the numerical simulations shown in Figs. 4.2e, f, 4.7 and 4.8, we model the probing tip as a conical platinum structure of 1 μm length with a 16° half angle and semispherical apex of 25 nm radius. The symmetry axis of the tip is parallel to the z-direction (perpendicular to the nanoresonator surface, see Figs. B.2c, d). The h-BN nanoresonator and the CBP molecular layer are modeled in an analogous way to the configuration described above. In addition, the simulations with the metallic tip were performed using the scattering problem approach (implemented in the Radio Frequency Module of COMSOL Multiphysics), which allows us to distinguish between the incident illumination (background field, E_{inc}), and the scattered field (relative field, $\mathbf{E}_{\text{scat}}$). The incident illumination E_{inc} is defined as a p-polarized plane wave, incident at the tip apex, with and angle of 60° relative to the symmetry axis of the tip.

The illuminated tip interacts with the nanorod via the near fields around the tip apex. This interaction results predominantly in a net vertical dipole moment induced along the conical structure, $\mathbf{p}_{\text{tip}}(\omega) = p_{\text{tip},z}(\omega)\hat{\mathbf{z}}$ (blue arrow in Figs. B.2c, d). Thus, the tip-scattered field $E_{\text{scat}}(\omega)$ can be interpreted as the radiation emitted by this net dipole, which is proportional to $p_{\text{tip},z}(\omega)$. The latter is calculated as the first moment of the surface charge density induced along the tip, $\rho_s(\omega)$. The tip-scattered field $E_{\text{scat}}(\omega)$ can thus be related to $\rho_s(\omega)$ according to the following equation

$$E_{\text{scat}}(\omega) \propto p_{\text{tip},z}(\omega) = \int_S \mathrm{d}^2\mathbf{r}\, z\rho_s(\omega) \tag{B.2}$$

where $\mathrm{d}^2\mathbf{r}$ is the surface element with outward normal unit vector $\hat{\mathbf{n}}$, z is the vertical position, $\rho_s(\omega) = \varepsilon_0[\mathbf{E}^{\mathrm{out}}(S;\omega) - \mathbf{E}^{\mathrm{in}}(S;\omega)] \cdot \hat{\mathbf{n}}$ and $\mathbf{E}^{\mathrm{out}}(S;\omega)$ ($\mathbf{E}^{\mathrm{in}}(S;\omega)$) is the total electric field outside (inside) the tip surface at each point. The integration in Eq. (B.2) is performed along the complete surface S of the tip. To determine $E_{\mathrm{scat}}(\omega)$), we consider only the z-component of the induced dipole moment because $p_{\mathrm{tip},x}(\omega)$ and $p_{\mathrm{tip},y}(\omega)$ components are relatively small as the tip is strongly elongated in the z-direction.

For simplicity and to reduce the numerical calculation time, the simulations with the Pt tip are performed without considering the SiO_2/Si substrate. In all the simulations the tip-surface apex is located at coordinates ($x = 0, y = -L/2 + 50\,\mathrm{nm}, z = h_{\mathrm{tip}}$) where h_{tip} is the height between the tip apex and the h-BN nanorod top surface. We set the origin ($x = 0, y = 0, z = 0$) in the middle of the top surface of the h-BN nanorod. In addition, we calculate the surface charge density $\rho_s(\omega)$ using only the electric field outside the tip, that is $\rho_s(\omega) = \varepsilon_0\mathbf{E}^{\mathrm{out}}(S;\omega)\cdot\hat{\mathbf{n}}$. This approximation is justified by the high reflectivity of platinum at the frequency range between $1400\,\mathrm{cm}^{-1}$ and $1500\,\mathrm{cm}^{-1}$. As a consequence, the electric field inside the platinum tip is close to zero, as we have verified. The material permittivities are provided in ref. [232].

To ensure numerical convergence of the calculated induced dipole moment $p_{\mathrm{tip},z}(\omega)$, the mesh of the Pt tip is chosen extremely fine with a maximum element size of 60 nm, mainly in upper surface elements of the tip, far from the apex. In addition, the complete structure (Pt tip, h-BN nanorod and CBP layer) is located in a homogeneous rectangular box (filled with air) of $4.2 \times 3.75 \times 4.35\,\mu\mathrm{m}^3$ size. We use PML for the boundaries of the simulation box and free triangular elements for the nanorod mesh and free tetrahedral elements for all other structures.

Signal demodulation

To suppress background scattering signals in the experiment, the tip is oscillating normal to the surface, i.e. the distance between tip and sample is modulated. Consequently, the tip-scattered field is modulated at an oscillation frequency, Ω, and its harmonics. To consider tip modulation and signal demodulation in our simulations, we apply the following procedure:

1. We calculate the induced dipole moment $p_{\mathrm{tip},z}(\omega)$ (Eq. (B.2)) for different tip heights $h_{\mathrm{tip}} = 1\,\mathrm{nm}$, 2 nm, 3 nm, 4 nm, 5 nm, 6 nm, 7 nm, 8 nm, 9 nm, 10 nm, 15 nm, 20 nm, 25 nm, 30 nm, 35 nm, 40 nm, 45 nm and 50 nm. We define the tip height as the minimum distance between the tip apex and the nanorod surface. For each simulation we only vary h_{tip} and leave constant the rest of the parameters.

2. We interpolate $p_{\mathrm{tip},z}(\omega)$ and assume the tip height to be a harmonic function of time (Eq. (**??**)):

$$h_{\mathrm{tip}}(t) = h_0 + A[1 - \cos(\Omega t)], \tag{B.3}$$

where $A = (h_{\mathrm{tip}}^{\mathrm{max}} - h_{\mathrm{tip}}^{\mathrm{min}})/2$ is the tapping amplitude with $h_{\mathrm{tip}}^{\mathrm{min}}$ and $h_{\mathrm{tip}}^{\mathrm{max}}$ being the minimum and maximum tip heights used in the simulations. To closely reproduce experimental parameters, we use a tapping frequency of $\Omega = 265.55\,\mathrm{kHz}$.

3. The n^{th}-order demodulated scattered field is proportional to $\sigma_n(\omega) = s_n(\omega)e^{i\varphi_n(\omega)}$, which is obtained by calculating the n^{th} Fourier coefficient of the induced dipole moment:

$$\sigma_n(\omega) \propto p_{\mathrm{tip},n}(\omega) = \int_0^T \mathrm{d}t\, p_{\mathrm{tip},z}\left(h_{\mathrm{tip}}(t);\omega\right) e^{in\Omega t}, \tag{B.4}$$

where $T = 2\pi/\Omega$ is the period of oscillation of the tip. In practice, the Fourier transform of $p_{\mathrm{tip},z}(h_{\mathrm{tip}}(t);\omega)$ is performed using the Fourier package of Wolfram Mathematica software.

B.3 Cross sections and electric energy

In this thesis, we use the following expressions to calculate the scattering cross section σ_{scat}, absorption cross section σ_{abs} and electric energy E_e of a nanoparticle with permittivity $\varepsilon(\omega)$ illuminated by an incident plane wave with electric field $\mathbf{E}_{\mathrm{inc}}$:

$$\sigma_{\mathrm{scat}} = \frac{1}{S_0}\oint_A \mathrm{d}^2\mathbf{r}\,\langle \mathbf{S}_{\mathrm{scat}}(\mathbf{r})\rangle_t \cdot \hat{\mathbf{n}}, \tag{B.5a}$$

$$\sigma_{\mathrm{abs}} = \frac{1}{S_0}\int_V \mathrm{d}^3\mathbf{r}\,\mathrm{Re}\left[\mathbf{J}_{\mathrm{ind}}^*(\mathbf{r})\cdot\mathbf{E}_{\mathrm{tot}}(\mathbf{r})\right], \tag{B.5b}$$

$$E_e = \frac{1}{4}\int_V \mathrm{d}^3\mathbf{r}\,\mathbf{E}_{\mathrm{tot}}(\mathbf{r})\cdot\mathbf{D}^*(\mathbf{r}), \tag{B.5c}$$

where $S_0 = |\mathbf{E}_{\mathrm{inc}}|^2/(2Z_0)$, $|\mathbf{E}_{\mathrm{inc}}|$ is the amplitude of the incident plane wave and Z_0 is the impedance of vacuum. $\langle \mathbf{S}_{\mathrm{scat}}(\mathbf{r})\rangle_t = \mathrm{Re}[\mathbf{E}_{\mathrm{scat}}(\mathbf{r})\times\mathbf{B}_{\mathrm{scat}}^*(\mathbf{r})]/(2\mu_0)$ is the expression for the time-averaged Poynting's vector with $\mathbf{E}_{\mathrm{scat}}(\mathbf{r})$ and

$\mathbf{B}_{\mathrm{scat}}(\mathbf{r})$ the electric and magnetic fields scattered by the nanoparticle. $\mathbf{J}_{\mathrm{ind}}(\mathbf{r})$ is the induced current density inside the nanoparticle, $\mathbf{E}_{\mathrm{tot}}(\mathbf{r})$ is the total electric field given by the sum of the incident plus the induced electric field in the nanoparticle and $\mathbf{D}(\mathbf{r})$ is the electric displacement field. The integration in Eq. (B.5a) is performed along the complete surface A of a sphere (enclosing the nanoparticle) with surface element $\mathrm{d}^2\mathbf{r}$ and outward normal unit vector $\hat{\mathbf{n}}$, whereas the integrations in Eqs. (B.5b) and (B.5c) are performed over the complete volume V of the nanoparticle with volume element $\mathrm{d}^3\mathbf{r}$. Note that in Eqs. (B.5a)-(B.5c) we assume that all fields and sources have a harmonic dependence on time (see Appendix A).

C

Induced electromagnetic field for an electron trajectory above the surface of an uniaxial anisotropic semi-infinite medium

In this appendix, we calculate the induced electromagnetic field $\mathbf{E}^{\mathrm{I}}_{\mathrm{ind}}(\mathbf{r};\omega)$ when the electron is traveling above the surface of an anisotropic media. We solve the following wave equation (derived from Maxwell's equations) satisfied by the total electric field [31]

$$\nabla^2\mathbf{E}_{\mathrm{tot}}(\mathbf{r};t) - \mu_0\varepsilon_0\frac{\partial^2}{\partial t^2}[\hat{\varepsilon}\,\mathbf{E}_{\mathrm{tot}}(\mathbf{r};t)] = \mu_0\frac{\partial}{\partial t}\mathbf{J}_{\mathrm{e}}(\mathbf{r};t) + \nabla[\nabla\cdot\mathbf{E}_{\mathrm{tot}}(\mathbf{r};t)], \quad \text{(C.1)}$$

where ε_0 and μ_0 stand for the vacuum permittivity and permeability, respectively, and $\mathbf{J}_{\mathrm{e}}(\mathbf{r};t) = \rho_{\mathrm{e}}(\mathbf{r};t)\mathbf{v} = -e\delta(x-b,0,z-vt)(0,0,v)$ is the current density corresponding to the electron traveling with velocity $\mathbf{v} = v\hat{\mathbf{z}}$ and impact parameter b. We show in Fig. 2.13 of Chapter 2 a schematics of the considered geometry.

By Fourier transforming Eq. (C.1) with respect to the variables y, z and t and solving for the electric field separately outside (label I) and inside (label II) the anisotropic medium, we obtain the following solutions for the components of the total electric field

$$E^{\mathrm{I}}_{\mathrm{tot},x}(x,k_y,k_z;\omega) = B_{\mathrm{I}}\,e^{-\kappa_{\mathrm{I}}x} - \frac{\pi e}{\varepsilon_0}\mathrm{sign}(x-b)\delta(\omega-k_zv)e^{-\kappa_{\mathrm{I}}|x-b|}, \quad \text{(C.2a)}$$

$$E^{\mathrm{I}}_{\mathrm{tot},y}(x,k_y,k_z;\omega) = D_{\mathrm{I}}\,e^{-\kappa_{\mathrm{I}}x} + i\frac{\pi e}{\varepsilon_0}\frac{k_y}{\kappa_{\mathrm{I}}}\delta(\omega-k_zv)e^{-\kappa_{\mathrm{I}}|x-b|}, \quad \text{(C.2b)}$$

$$E^{\mathrm{I}}_{\mathrm{tot},z}(x,k_y,k_z;\omega) = G_{\mathrm{I}}\,e^{-\kappa_{\mathrm{I}}x} + i\frac{\pi e}{\varepsilon_0}\frac{k_z-\frac{\omega}{c^2}v}{\kappa_{\mathrm{I}}}\delta(\omega-k_zv)e^{-\kappa_{\mathrm{I}}|x-b|}, \quad \text{(C.2c)}$$

$$E^{\mathrm{II}}_{\mathrm{tot},x}(x,k_y,k_z;\omega) = A_{\mathrm{II}}e^{\kappa^o_{\mathrm{II}}x} - iF^{\mathrm{II}}\frac{k_z\kappa^e_{\mathrm{II}}}{(\kappa^o_{\mathrm{II}})^2-k_y^2}e^{\kappa^e_{\mathrm{II}}x}, \quad \text{(C.2d)}$$

$$E^{\rm II}_{{\rm tot},y}(x,k_y,k_z;\omega) = C_{\rm II}e^{\kappa^o_{\rm II}x} + F_{\rm II}\frac{k_yk_z}{(\kappa^o_{\rm II})^2-k_y^2}e^{\kappa^e_{\rm II}x}, \tag{C.2e}$$

$$E^{\rm II}_{{\rm tot},z}(x,k_y,k_z;\omega) = F_{\rm II}e^{\kappa^e_{\rm II}x}, \tag{C.2f}$$

where

$$\kappa_{\rm I}^2 = k_y^2+k_z^2-\frac{\omega^2}{c^2},\ (\kappa^e_{\rm II})^2 = k_y^2+\frac{\varepsilon_\parallel}{\varepsilon_\perp}\left(k_z^2-\frac{\omega^2}{c^2}\varepsilon_\perp\right)$$
$$\text{and}\quad (\kappa^o_{\rm II})^2 = k_y^2+k_z^2-\varepsilon_\perp\frac{\omega^2}{c^2}. \tag{C.3}$$

The coefficients $A_{\rm II}, B_{\rm I}, C_{\rm II}, D_{\rm I}, F_{\rm II}$ and $G_{\rm I}$ can be found from the application of the standard boundary conditions for the field at the interface ($x=0$) between both media, that is,

$$\begin{aligned} &E^{\rm II}_y|_{x=0} = E^{\rm I}_y|_{x=0}, \qquad E^{\rm II}_z|_{x=0} = E^{\rm I}_z|_{x=0}, \\ &\varepsilon_\perp E^{\rm II}_x|_{x=0} = E^{\rm I}_x|_{x=0}, \end{aligned} \tag{C.4}$$

together with the Gauss law and the boundary conditions for the magnetic field. From these conditions one finds the following linear system of equations:

$$\hat{\mathbb{M}}\mathbf{x} = \mathbf{b}, \tag{C.5}$$

with

$$\hat{\mathbb{M}} = \begin{pmatrix} -\varepsilon_\perp & 1 & 0 & 0 & i\varepsilon_\perp k_z\kappa^e_{\rm II}/[(\kappa^o_{\rm II})^2-k_y^2] & 0 \\ 0 & 0 & -1 & 1 & -k_yk_z/[(\kappa^o_{\rm II})^2-k_y^2] & 0 \\ 0 & 0 & 0 & 0 & -1 & 1 \\ -k_z & k_z & 0 & 0 & -i\kappa^e_{\rm II}[1-k_z^2/((\kappa^o_{\rm II})^2-k_y^2)] & -i\kappa_{\rm I} \\ k_y & -k_y & i\kappa^o_{\rm II} & i\kappa_{\rm I} & 0 & 0 \\ \varepsilon_\perp\kappa^o_{\rm II} & 0 & i\varepsilon_\perp k_y & 0 & 0 & 0 \end{pmatrix},$$

and

$$\mathbf{x} = \begin{pmatrix} A_{\rm II} \\ B_{\rm I} \\ C_{\rm II} \\ D_{\rm I} \\ F_{\rm II} \\ G_{\rm I} \end{pmatrix}, \qquad \mathbf{b} = -\frac{2\pi e\delta(\omega-k_zv)e^{-\kappa_{\rm I}b}}{2\varepsilon_0}\begin{pmatrix} 1 \\ ik_y/\kappa_{\rm I} \\ ik_z/\kappa_{\rm I}-i\omega v/(c^2\kappa_{\rm I}) \\ \omega v/c^2 \\ 0 \\ 0 \end{pmatrix}.$$

By solving the above linear system of equations, one further finds that each

coefficient in Eqs. (C.2a)-(C.2f) can be expressed as

$$A_{\mathrm{II}} = \tilde{\rho}\, a_{\mathrm{II}}, \quad B_{\mathrm{I}} = \tilde{\rho}\, b_{\mathrm{I}}, \quad C_{\mathrm{II}} = \tilde{\rho}\, c_{\mathrm{II}}$$
$$D_{\mathrm{I}} = \tilde{\rho}\, d_{\mathrm{I}}, \quad F_{\mathrm{II}} = \tilde{\rho} f_{\mathrm{II}}, \quad G_{\mathrm{I}} = \tilde{\rho} g_{\mathrm{I}},$$

with $\tilde{\rho} = -2\pi e\delta(\omega - k_z v)e^{-\kappa_{\mathrm{I}} b}/\varepsilon_0$. Thus, we obtain that the induced electric fields in vacuum (labeled as I) and in h-BN (labeled as II) are given by (Eqs. (C.2a)-(C.2f))

$$\mathbf{E}^{\mathrm{I}}_{\mathrm{ind}}(x, k_y, k_z; \omega) = (b_{\mathrm{I}}, d_{\mathrm{I}}, g_{\mathrm{I}})\, \tilde{\rho}\, e^{-\kappa_{\mathrm{I}} x}, \tag{C.6a}$$
$$\mathbf{E}^{\mathrm{II}}_{\mathrm{ind}}(x, k_y, k_z; \omega) = (a_{\mathrm{II}}, c_{\mathrm{II}}, 0)\, \tilde{\rho}\, e^{\kappa^o_{\mathrm{II}} x} \tag{C.6b}$$
$$+ \left(-i\frac{k_z \kappa^e_{\mathrm{II}}}{(\kappa^o_{\mathrm{II}})^2 - k_y^2}, \frac{k_z k_y}{(\kappa^o_{\mathrm{II}})^2 - k_y^2}, 1 \right) \tilde{\rho}\, \mathrm{f}_{\mathrm{II}}\, e^{\kappa^e_{\mathrm{II}} x}.$$

To obtain Eqs. (2.34) and (2.35) presented in Chapter 2, one can substitute Eq. (C.6a) into Eqs (2.7) and find the following expression for the EEL probability $\Gamma^{\mathrm{surf}}(\omega)$:

$$\Gamma_{\mathrm{surf}}(\omega) = \frac{e}{\pi\hbar\omega} \mathrm{Re}\left[\mathbf{E}^{\mathrm{I}}_{\mathrm{ind}}(\mathbf{r}_{\mathrm{e}}; \omega) \cdot \hat{\mathbf{z}}\, e^{-i\omega t_{\mathrm{e}}}\right] = \int_0^{k_y^c} \mathrm{d}k_y\, P_{\mathrm{surf}}(k_y; \omega), \tag{C.7}$$

with $\hbar k_y^c$ the maximum momentum of the electrons that can pass through the collection aperture of the detector in the y-direction, and

$$P_{\mathrm{surf}}(k_y; \omega) = -\frac{e^2}{\pi^2 \varepsilon_0 \hbar\omega v} \mathrm{Re}\left[g_{\mathrm{I}} e^{-2\kappa_{\mathrm{I}} b}\right]\Big|_{k_z = \omega/v}, \tag{C.8}$$

where $\hbar k_z = \hbar\omega/v$ is the momentum transferred by the electron to the polaritons along the beam trajectory.

D

Multipole decomposition of the induced current density

In Chapter 3, we show both the electric spherical and Cartesian multipole moments induced in the nanodisks by the probing electron beam. These multipole moments were calculated using the standard expressions reported in Refs. [185, 233]. In this appendix, we present the close expressions for the spherical electric dipole $\mathbf{P}_{\rm sph}(\omega)$ and the spherical electric quadrupole $\hat{\mathbb{Q}}_{\rm sph}(\omega)$ moments. We also show that in the long-wavelength limit approximation, electric spherical dipole and quadrupole moments are a combination of Cartesian electric and toroidal multipole moments.

D.1 Electric dipole

We calculate the electric spherical dipole moment $\mathbf{P}_{\rm sph}(\omega)$ in the nanodisk using the following expression [185]

$$\mathbf{P}_{\rm sph}(\omega) = -\frac{1}{i\omega}\int_V \mathrm{d}^3\mathbf{r}\left\{\mathbf{J}_{\rm ind}\, j_0(k_0 r) + \frac{k_0^2}{2}\left[3(\mathbf{r}\cdot\mathbf{J}_{\rm ind})\mathbf{r} - r^2\mathbf{J}_{\rm ind}\right]\frac{j_2(k_0 r)}{(k_0 r)^2}\right\}. \tag{D.1}$$

Here the integral extends over the whole volume V of the nanodisk with volume element $\mathrm{d}^3\mathbf{r}$, $j_\ell(x)$ is the spherical Bessel function of the first kind of order ℓ, r is the magnitude of the position vector $\mathbf{r} = (x, y, z)$ and $\mathbf{J}_{\rm ind} = \mathbf{J}_{\rm ind}(\mathbf{r})$ is the induced current density distribution in the nanodisk.

In the long-wavelength limit approximation ($k_0 r \ll 1$) the spatial size of

$\mathbf{J}_{\rm ind}(\mathbf{r})$ is much smaller than the wavelength of the electromagnetic field, and thus one can expand the spherical Bessel functions $j_0(k_0 r)$, $j_2(k_0 r)$ using the small argument limit [31]

$$j_0(k_0 r) \approx 1 - \frac{(k_0 r)^2}{6}, \tag{D.2}$$

$$j_2(k_0 r) \approx \frac{(k_0 r)^2}{15}. \tag{D.3}$$

By substituting Eqs. D.2 and D.3 into Eq. D.1, we can obtain the following expression for the electric spherical dipole moment in the long-wavelength limit:

$$\begin{aligned}\mathbf{P}_{\rm sph}^{k_0 r \ll 1}(\omega) \approx & -\frac{1}{i\omega}\int_V \mathrm{d}^3\mathbf{r}\left\{\mathbf{J}_{\rm ind}\left[1-\frac{(k_0 r)^2}{6}\right]+\frac{k_0^2}{2}\left[3(\mathbf{r}\cdot\mathbf{J}_{\rm ind})\mathbf{r}-\right.\right. \\ & \left.\left.-r^2\mathbf{J}_{\rm ind}\right]\frac{(k_0 r)^2}{15(k_0 r)^2}\right\} \\ \approx & \underbrace{-\frac{1}{i\omega}\int_V \mathrm{d}^3\mathbf{r}\,\mathbf{J}_{\rm ind}}_{\mathbf{P}_{\rm car}(\omega)} + ik_0 \underbrace{\left\{\frac{1}{10c}\int_V \mathrm{d}^3 r\,\left[(\mathbf{r}\cdot\mathbf{J}_{\rm ind})\mathbf{r}-2r^2\mathbf{J}_{\rm ind}\right]\right\}}_{\mathbf{T}_{\rm car}(\omega)},\end{aligned} \tag{D.4}$$

where one recognizes from the last equality the conventional expressions of Cartesian electric and toroidal dipole moments [233]. From this analysis, we conclude that in the long-wavelength approximation the electric spherical dipole moment $\mathbf{P}_{\rm sph}(\omega)$ is determined by the sum of Cartesian electric $\mathbf{P}_{\rm car}(\omega)$ and toroidal $\mathbf{T}_{\rm car}(\omega)$ dipole moments as:

$$\mathbf{P}_{\rm sph}^{k_0 r \ll 1}(\omega) \approx \mathbf{P}_{\rm car}(\omega) + ik_0 \mathbf{T}_{\rm car}(\omega). \tag{D.5}$$

D.2 Electric quadrupole

To calculate the electric spherical quadrupole moment $\hat{\mathbb{Q}}_{\rm sph}(\omega)$ induced in the nanodisk, we use the following expression [185]:

$$\hat{\mathbb{Q}}_{\text{sph}}(\omega) = -\frac{3}{i\omega}\int_V \mathrm{d}^3\mathbf{r}\left\{\left[3(\mathbf{r}\otimes\mathbf{J}_{\text{ind}}+\mathbf{J}_{\text{ind}}\otimes\mathbf{r})-2(\mathbf{r}\cdot\mathbf{J}_{\text{ind}})\hat{\mathbb{I}}\right]\frac{j_1(k_0r)}{k_0r}+\right. \tag{D.6}$$
$$+2k_0^2\left[5\mathbf{r}\otimes\mathbf{r}(\mathbf{r}\cdot\mathbf{J}_{\text{ind}})-(\mathbf{r}\otimes\mathbf{J}_{\text{ind}}+\mathbf{J}_{\text{ind}}\otimes\mathbf{r})r^2-\right.$$
$$\left.\left.-r^2(\mathbf{r}\cdot\mathbf{J}_{\text{ind}})\hat{\mathbb{I}}\right]\frac{j_3(k_0r)}{(k_0r)^3}\right\},$$

with $\hat{\mathbb{I}}$ being the identity tensor and $\otimes$ the tensor product. In the long-wavelength approximation, one can expand the spherical Bessel functions $j_1(k_0r)$, $j_3(k_0r)$ as [31]

$$j_1(k_0r) \approx \frac{k_0r}{3} - \frac{(k_0r)^3}{30}, \tag{D.7}$$
$$j_3(k_0r) \approx \frac{(k_0r)^3}{105}, \tag{D.8}$$

and substituting Eqs. D.7 and D.8 into Eq. D.6 one finds that

$$\hat{\mathbb{Q}}_{\text{sph}}^{k_0r\ll1}(\omega) \approx -\frac{3}{i\omega}\int_V \mathrm{d}^3\mathbf{r}\left\{\left[3(\mathbf{r}\otimes\mathbf{J}_{\text{ind}}+\mathbf{J}_{\text{ind}}\otimes\mathbf{r})-2(\mathbf{r}\cdot\mathbf{J}_{\text{ind}})\hat{\mathbb{I}}\right]\times\right.$$
$$\times\frac{1}{k_0r}\left[\frac{k_0r}{3}-\frac{(k_0r)^3}{30}\right]+2k_0^2\left[5\mathbf{r}\otimes\mathbf{r}(\mathbf{r}\cdot\mathbf{J}_{\text{ind}})-(\mathbf{r}\otimes\mathbf{J}_{\text{ind}}+\mathbf{J}_{\text{ind}}\otimes\mathbf{r})r^2-\right.$$
$$\left.\left.-r^2(\mathbf{r}\cdot\mathbf{J}_{\text{ind}})\hat{\mathbb{I}}\right]\frac{(k_0r)^3}{105(k_0r)^3}\right\} \tag{D.9}$$
$$\approx \underbrace{-\frac{1}{i\omega}\int_V \mathrm{d}^3\mathbf{r}\left[3(\mathbf{r}\otimes\mathbf{J}_{\text{ind}}+\mathbf{J}_{\text{ind}}\otimes\mathbf{r})-2(\mathbf{r}\cdot\mathbf{J}_{\text{ind}})\hat{\mathbb{I}}\right]}_{\hat{\mathbb{Q}}_{\text{car}}^{(\text{e})}(\omega)}$$
$$+i3k_0\underbrace{\left\{\frac{1}{42c}\int_V \mathrm{d}^3\mathbf{r}\left[4\mathbf{r}\mathbf{r}(\mathbf{r}\cdot\mathbf{J}_{\text{ind}})-5r^2(\mathbf{r}\mathbf{J}_{\text{ind}}+\mathbf{J}_{\text{ind}}\mathbf{r})+2r^2(\mathbf{r}\cdot\mathbf{J}_{\text{ind}})\hat{\mathbb{I}}\right]\right\}}_{\hat{\mathbb{Q}}_{\text{car}}^{(\text{T})}(\omega)},$$

where $\hat{\mathbb{Q}}^{(\text{e})}(\omega)$ and $\hat{\mathbb{Q}}^{(\text{T})}(\omega)$ are the conventional electric Cartesian and toroidal quadrupole moments [233], respectively. Thus, in the long-wavelength approximation electric spherical quadrupole moment $\hat{\mathbb{Q}}_{\text{sph}}(\omega)$ is determined by the sum of Cartesian electric $\hat{\mathbb{Q}}_{\text{car}}^{(\text{e})}(\omega)$ and toroidal $\hat{\mathbb{Q}}_{\text{car}}^{(\text{T})}(\omega)$ quadrupole moments as:

$$\hat{\mathbb{Q}}_{\text{sph}}^{k_0r\ll1}(\omega) \approx \hat{\mathbb{Q}}_{\text{car}}^{(\text{e})}(\omega) + i3k_0\hat{\mathbb{Q}}_{\text{car}}^{(\text{T})}(\omega). \tag{D.10}$$

In our numerical simulations using COMSOL, we calculate the multipole

moments $\mathbf{P}_{\rm sph}(\omega)$, $\mathbf{P}_{\rm car}(\omega)$, $\mathbf{T}_{\rm car}(\omega)$, $\hat{\mathbb{Q}}_{\rm sph}(\omega)$, $\hat{\mathbb{Q}}^{\rm (e)}_{\rm car}(\omega)$ and $\hat{\mathbb{Q}}^{\rm (T)}_{\rm car}(\omega)$ induced in the nanodisk by applying the following procedure:

(i) We calculate the total electric field $\mathbf{E}_{\rm tot}(\mathbf{r})$ inside the nanodisk.

(ii) We next calculate the induced current density as $\mathbf{J}_{\rm ind}(\mathbf{r}) = -i\omega\varepsilon_0(\varepsilon - 1)\mathbf{E}_{\rm tot}(\mathbf{r})$ and perform the volume integrals (Eqs. D.1, D.4, D.6 and D.10) with functions predefined in COMSOL Multiphysics software.

D.3 Contributions of the multipoles to the scattered power and cross section

From the multipole moments induced in the nanodisk, one can obtain the scattered power by the disk, $\mathscr{P}_{\rm scat}(\omega)$, using the following expression [185, 234]:

$$\begin{aligned}\mathscr{P}_{\rm scat}(\omega) &= \mathscr{P}^{\mathbf{P}_{\rm sph}}_{\rm scat}(\omega) + \mathscr{P}^{\hat{\mathbb{Q}}_{\rm sph}}_{\rm scat}(\omega) + \mathscr{P}^{\mathbf{m}_{\rm sph}}_{\rm scat}(\omega) + \cdots, \qquad \text{(D.11)}\\ &= \frac{k_0^4 c}{12\pi\varepsilon_0}\left[|\mathbf{P}_{\rm sph}(\omega)|^2 + \frac{k_0^2}{120}\left|\hat{\mathbb{Q}}_{\rm sph}(\omega)\right|^2 + \left|\frac{\mathbf{m}_{\rm sph}(\omega)}{c}\right|^2 + \cdots\right],\end{aligned}$$

where

$$\mathscr{P}^{\mathbf{P}_{\rm sph}}_{\rm scat}(\omega) = \frac{k_0^4 c}{12\pi\varepsilon_0}|\mathbf{P}_{\rm sph}(\omega)|^2, \qquad \text{(D.12)}$$

$$\mathscr{P}^{\hat{\mathbb{Q}}_{\rm sph}}_{\rm scat}(\omega) = \frac{k_0^6 c}{1440\pi\varepsilon_0}\left|\hat{\mathbb{Q}}_{\rm sph}(\omega)\right|^2 \text{ and} \qquad \text{(D.13)}$$

$$\mathscr{P}^{\mathbf{m}_{\rm sph}}_{\rm scat}(\omega) = \frac{k_0^4 c}{12\pi\varepsilon_0}\left|\frac{\mathbf{m}_{\rm sph}(\omega)}{c}\right|^2, \qquad \text{(D.14)}$$

are the scattered powers from the spherical electric dipole, spherical electric quadrupole, and spherical magnetic dipole moments, respectively. The scattered powers of higher-order electric and magnetic multipoles are implicitly indicated by the three dots in Eq. D.11. In this thesis, however, we focus on the electric dipole and electric quadrupole multipole contributions, as they serve to explain most of the phenomenology involved in our systems.

As discussed in the previous sections, in the long-wavelength approximation, spherical electric dipole and quadrupoles can be expressed in terms of Cartesian multipoles (Eqs. D.5 and D.10). Thus, to obtain the scattered power from

Cartesian multipoles, we substitute Eqs. D.1 and D.5 into Eq. D.11 and find that

$$\mathscr{P}_{\text{scat}}^{k_0 r \ll 1}(\omega) \approx \frac{k_0^4 c}{12\pi\varepsilon_0}\left[\left|\mathbf{P}_{\text{car}}(\omega) + ik_0\mathbf{T}_{\text{car}}(\omega)\right|^2 + \right. \tag{D.15}$$
$$\left. + \frac{k_0^2}{120}\left|\hat{\mathbb{Q}}_{\text{car}}^{(\text{e})}(\omega) + i3k_0\hat{\mathbb{Q}}_{\text{car}}^{(\text{T})}(\omega)\right|^2 + \cdots\right],$$

where one identifies the the following expressions:

$$\mathscr{P}_{\text{scat}}^{\mathbf{P}_{\text{car}}}(\omega) = \frac{k_0^4 c}{12\pi\varepsilon_0}\left|\mathbf{P}_{\text{car}}(\omega)\right|^2, \tag{D.16}$$

$$\mathscr{P}_{\text{scat}}^{\mathbf{T}_{\text{car}}}(\omega) = \frac{k_0^4 c}{12\pi\varepsilon_0}\left|ik_0\mathbf{T}_{\text{car}}(\omega)\right|^2, \tag{D.17}$$

$$\mathscr{P}_{\text{scat}}^{\hat{\mathbb{Q}}_{\text{car}}^{(\text{e})}}(\omega) = \frac{k_0^6 c}{1440\pi\varepsilon_0}\left|\hat{\mathbb{Q}}_{\text{car}}^{(\text{e})}(\omega)\right|^2 \text{ and} \tag{D.18}$$

$$\mathscr{P}_{\text{scat}}^{\hat{\mathbb{Q}}_{\text{car}}^{(\text{T})}}(\omega) = \frac{k_0^6 c}{1440\pi\varepsilon_0}\left|i3k_0\hat{\mathbb{Q}}_{\text{car}}^{(\text{T})}(\omega)\right|^2. \tag{D.19}$$

The partial scattering cross sections of the disk shown in Figs. 3.6d and 3.6e in Chapter 3 were calculated as

$$\sigma_{\text{scat}}(\omega) = \frac{1}{S_0}\mathscr{P}_{\text{scat}}(\omega) = \frac{1}{S_0}\mathscr{P}_{\text{scat}}^{\mathbf{P}_{\text{sph}}}(\omega) + \frac{1}{S_0}\mathscr{P}_{\text{scat}}^{\hat{\mathbb{Q}}_{\text{sph}}}(\omega) + \frac{1}{S_0}\mathscr{P}_{\text{scat}}^{\mathbf{m}_{\text{sph}}}(\omega) + \cdots \tag{D.20}$$
$$= \sigma_{\text{scat}}^{\mathbf{P}_{\text{sph}}}(\omega) + \sigma_{\text{scat}}^{\hat{\mathbb{Q}}_{\text{sph}}}(\omega) + \sigma_{\text{scat}}^{\mathbf{m}_{\text{sph}}}(\omega) + \cdots,$$

where $S_0 = |\mathbf{E}_{\text{inc}}|^2/(2Z_0)$ and $|\mathbf{E}_{\text{inc}}| = 1\,\text{V/m}$ is the amplitude of the incident plane wave.

E

Spherical decomposition of the EM field produced by a fast electron

In this appendix, we show that the electric field, $\mathbf{E}_{\mathrm{e}}(\mathbf{r};\omega)$, produced by a fast electron beam traveling in vacuum can be decomposed into a sum of incoming and outgoing spherical waves propagating toward and outward the electron beam, respectively.

We consider an electron traveling in vacuum along the z-axis, with impact parameter b and velocity v (see Fig. 3.2a). This fast electron produces a broadband electromagnetic field that can be expressed on the basis of vector spherical harmonics as follows [8, 229, 231]:

$$\mathbf{E}_{\mathrm{e}}(\mathbf{r};\omega) = \sum_{\ell=0}^{\infty}\sum_{m=-\ell}^{\ell} a_{\ell m}^{\mathrm{TE}}(\omega)\,\mathbf{E}_{\ell m}^{\mathrm{TE}}(\mathbf{r};\omega) + a_{\ell m}^{\mathrm{TM}}(\omega)\,\mathbf{E}_{\ell m}^{\mathrm{TM}}(\mathbf{r};\omega), \tag{E.1a}$$

$$\mathbf{B}_{\mathrm{e}}(\mathbf{r};\omega) = \sum_{\ell=0}^{\infty}\sum_{m=-\ell}^{\ell} a_{\ell m}^{\mathrm{TE}}(\omega)\,\mathbf{B}_{\ell m}^{\mathrm{TE}}(\mathbf{r};\omega) + a_{\ell m}^{\mathrm{TM}}(\omega)\,\mathbf{B}_{\ell m}^{\mathrm{TM}}(\mathbf{r};\omega) \tag{E.1b}$$

where

$$a_{\ell m}^{\mathrm{TE}}(\omega) = -i\frac{ev}{\varepsilon_0}\frac{m}{\sqrt{\ell(\ell+1)}}\frac{\omega}{c^2}\phi_{\ell m}^{\mathrm{TE}}(\omega), \tag{E.2a}$$

$$a_{\ell m}^{\mathrm{TM}}(\omega) = \frac{ev}{c\varepsilon_0}\frac{1}{\sqrt{\ell(\ell+1)}}\phi_{\ell m}^{\mathrm{TM}}(\omega), \tag{E.2b}$$

and the overlap integrals $\phi_{\ell m}^{\mathrm{TM}}(\omega)$ and $\phi_{\ell m}^{\mathrm{TE}}(\omega)$ are determined as:

$$\phi_{\ell m}^{\mathrm{TE}}(\omega) = \frac{4\pi k_0}{v} i \int_{-\infty}^{\infty} \mathrm{d}z\, e^{i\omega z/v} h_{\ell}^{(1)}(k_0 r_{\mathrm{e}}) Y_{\ell m}^{*}(\theta_{\mathrm{e}},\phi_{\mathrm{e}}), \tag{E.3a}$$

$$\phi^{\mathrm{TM}}_{\ell m}(\omega) = c_{\ell m}\, e^{-i\phi_{\mathrm{e}}} \left(\frac{\partial}{\partial b} - \frac{i}{b}\frac{\partial}{\partial \phi_{\mathrm{e}}} \right) \phi^{\mathrm{TE}}_{\ell m-1}(\omega) \tag{E.3b}$$
$$- d_{\ell m}\, e^{i\phi_{\mathrm{e}}} \left(\frac{\partial}{\partial b} + \frac{i}{b}\frac{\partial}{\partial \phi_{\mathrm{e}}} \right) \phi^{\mathrm{TE}}_{\ell m+1}(\omega).$$

Here $h^{(1)}_{\ell}(x)$ is the spherical Hankel function of the first kind of order ℓ, $Y_{\ell m}(\theta,\phi)$ is the scalar spherical harmonics, the variables $(r_{\mathrm{e}}, \phi_{\mathrm{e}}, \theta_{\mathrm{e}})$ are the spherical coordinates of the electron beam trajectory $\mathbf{r}_{\mathrm{e}}(t) = (x_{\mathrm{e}} = b, y_{\mathrm{e}} = 0, z = vt)$ and

$$c_{\ell m} = \sqrt{\ell(\ell+1) - m(m-1)}, \tag{E.4a}$$
$$d_{\ell m} = \sqrt{\ell(\ell+1) - m(m+1)}. \tag{E.4b}$$

In Eq. (E.1), the fields vectors $\mathbf{E}^{\mathrm{TE}}_{\ell m}(\mathbf{r};\omega)$, $\mathbf{E}^{\mathrm{TM}}_{\ell m}(\mathbf{r};\omega)$, $\mathbf{B}^{\mathrm{TE}}_{\ell m}(\mathbf{r};\omega)$ and $\mathbf{B}^{\mathrm{TM}}_{\ell m}(\mathbf{r};\omega)$ are defined according to the standard vector spherical harmonics relations [31]:

$$\mathbf{E}^{\mathrm{TE}}_{\ell m}(\mathbf{r};\omega) = -c\mathbf{B}^{\mathrm{TM}}_{\ell m}(\mathbf{r};\omega) = j_{\ell}(k_0 r)\mathbf{X}_{\ell m}(\theta,\phi), \tag{E.5}$$
$$\mathbf{E}^{\mathrm{TM}}_{\ell m}(\mathbf{r};\omega) = c\mathbf{B}^{\mathrm{TE}}_{\ell m}(\mathbf{r};\omega) = -\frac{i}{k_0}\nabla \times \left[j_{\ell}(k_0 r)\mathbf{X}_{\ell m}(\theta,\phi) \right], \tag{E.6}$$
$$\mathbf{X}_{\ell m}(\theta,\phi) = \frac{1}{\sqrt{\ell(\ell+1)}}\mathbf{L}\left[Y_{\ell m}(\theta,\varphi) \right], \tag{E.7}$$

where $\mathbf{L} = -i(\mathbf{r}\times\nabla)$ is the angular momentum operator. It is worth mentioning that labels TE (transverse electric) and TM (transverse magnetic) denote the components of the fields that are transverse to the position vector $\mathbf{r}$. More specifically, by applying the relationship $\mathbf{r}\cdot\mathbf{X}_{\ell m} = 0$ to Eq. (E.5), one can derive that $\mathbf{r}\cdot\mathbf{E}^{\mathrm{TE}}_{\ell m}(\mathbf{r};\omega) = \mathbf{r}\cdot\mathbf{B}^{\mathrm{TM}}_{\ell m}(\mathbf{r};\omega) = 0$. For this reason, we label these field components as TE or TM, respectively.

By expressing the spherical Bessel function $j_{\ell}(k_0 r)$ as [235]

$$j_{\ell}(k_0 r) = \frac{1}{2}\left[h^{(1)}(k_0 r) + h^{(2)}(k_0 r) \right], \tag{E.8}$$

with $h^{(2)}_{\ell}(x)$ being the spherical Hankel function of the second kind of order ℓ, one finds that the fields vectors $\mathbf{E}^{\mathrm{TE}}_{\ell m}(\mathbf{r};\omega)$ and $\mathbf{E}^{\mathrm{TM}}_{\ell m}(\mathbf{r};\omega)$ (Eqs. (E.5) and (E.6)) can be written as the following equally weighted superposition of incoming (+) and outgoing (-) spherical waves:

$$\mathbf{E}^{\mathrm{TE}}_{\ell m}(\mathbf{r};\omega) = \underbrace{\frac{h^{(1)}(k_0 r)}{2}\mathbf{X}_{\ell m}(\theta,\phi)}_{\mathbf{E}^{\mathrm{TE},+}_{\ell m}} + \underbrace{\frac{h^{(2)}(k_0 r)}{2}\mathbf{X}_{\ell m}(\theta,\phi)}_{\mathbf{E}^{\mathrm{TE},-}_{\ell m}}, \tag{E.9}$$

and

$$\mathbf{E}_{\ell m}^{\mathrm{TM}}(\mathbf{r};\omega) = \underbrace{-\frac{i}{2k_0}\nabla\times\left[h_\ell^{(1)}(k_0 r)\mathbf{X}_{\ell m}(\theta,\phi)\right]}_{\mathbf{E}_{\ell m}^{\mathrm{TM},+}} \underbrace{-\frac{i}{2k_0}\nabla\times\left[h_\ell^{(2)}(k_0 r)\mathbf{X}_{\ell m}(\theta,\phi)\right]}_{\mathbf{E}_{\ell m}^{\mathrm{TM},-}}. \tag{E.10}$$

Substituting Eqs. (E.9) and (E.10) into Eq. (E.1a), one further finds that the electric field $\mathbf{E}_{\mathrm{e}}(\mathbf{r};\omega)$ can be described as incoming and outgoing waves (propagating toward and outward the electron beam):

$$\mathbf{E}_{\mathrm{e}}(\mathbf{r};\omega) = \sum_{\ell=0}^{\infty}\sum_{m=-\ell}^{\ell} a_{\ell m}^{\mathrm{TE}}(\omega)\left[\mathbf{E}_{\ell m}^{\mathrm{TE},+}(\mathbf{r};\omega)+\mathbf{E}_{\ell m}^{\mathrm{TE},-}(\mathbf{r};\omega)\right]+ a_{\ell m}^{\mathrm{TM}}(\omega)\left[\mathbf{E}_{\ell m}^{\mathrm{TM},+}(\mathbf{r};\omega)+\mathbf{E}_{\ell m}^{\mathrm{TM},-}(\mathbf{r};\omega)\right]. \tag{E.11}$$

Here, one can assume that each TM or TE polarization together with the pair $\{\ell, m\}$ correspond to a distinct scattering channel labeled as $\{q, \ell, m\}$ with q representing the polarization of the field. This assumption provides a convenient tool to calculate the scattered power of an object interacting with a fast electron beam. For example, one can calculate the power carried by the outgoing spherical waves (Eq. (E.11)) by summing the radiated power along each scattering channel:

$$\mathscr{P}_{\mathrm{scat}}^{\mathrm{e}}(\omega) = \frac{1}{8ck_0^2}\sum_{\ell=0}^{\infty}\sum_{m=-\ell}^{\ell}\left(\left|a_{\ell m}^{\mathrm{TE}}(\omega)\right|^2+\left|a_{\ell m}^{\mathrm{TM}}(\omega)\right|^2\right). \tag{E.12}$$

As we discuss in Chapter 3 (see Sections 3.2.2 and 3.3.3), the decomposition of the electric field $\mathbf{E}_{\mathrm{e}}(\mathbf{r};\omega)$ in different scattering channels plays an important role in the description of the anapole dip using temporal coupled-mode theory.

F

Parameters obtained from the TCMT results

In this appendix, we show all parameters obtained from the TCMT results presented in Chapter 3.

R_0 (nm)	ω_1 (eV)	γ_1^{rad} (eV)	ω_2 (eV)	γ_2^{rad} (eV)
110	1.73	0.35	2.28	0.30
138	1.45	0.34	1.95	0.29
165	1.26	0.33	1.67	0.22
190	1.12	0.33	1.52	0.22
215	1.01	0.32	1.35	0.16
240	0.93	0.34	1.24	0.14
268	0.86	0.30	1.15	0.14

Table F.1: Values of eigenfrequencies and radiative decays of the two resonant modes. Parameters obtained within TCMT (Eq. 3.21) to reproduce the simulated EEL spectra of the high-index dielectric disks shown in Fig. 3.5a. These parameters are plotted in Figs. 3.5c-d.

R_0 (nm)	ω_1 (eV)	γ_1^{rad} (eV)	$g_{1\mathrm{ex}}$ (meV)	ω_2 (eV)	γ_2^{rad} (eV)	$g_{2\mathrm{ex}}$ (meV)	ω_{LP} (eV)	ω_{MP} (eV)	ω_{UP} (eV)
110	1.64	0.36	48	2.20	0.30	126	1.68	1.91	2.21
138	1.43	0.34	70	1.89	0.29	100	1.48	1.79	2.01
165	1.24	0.33	70	1.65	0.22	100	1.27	1.58	1.99
190	1.06	0.33	79	1.53	0.22	129	1.09	1.46	1.99
215	1.01	0.32	72	1.35	0.16	138	1.03	1.29	1.99
240	0.92	0.34	83	1.24	0.14	127	0.94	1.19	1.99
268	0.86	0.30	70	1.15	0.14	130	0.89	1.10	1.98

Table F.2: Values of eigenfrequencies, radiative decays and coupling strengths obtained to reproduce the COMSOL simulations. Parameters obtained within TCMT to reproduce the simulated EEL spectra of the WS_2 disks shown in Figs. 3.9d and 3.11f. These parameters are plotted in Figs. 3.11c-d.

R_0 (nm)	ω_1 (eV)	γ_1^{rad} (eV)	$g_{1\mathrm{ex}}$ (meV)	ω_2 (eV)	γ_2^{rad} (eV)	$g_{2\mathrm{ex}}$ (meV)	ω_{LP} (eV)	ω_{MP} (eV)	ω_{UP} (eV)
110	1.75	0.36	80	2.01	0.30	87	1.81	1.90	2.02
138	1.58	0.34	79	1.90	0.29	81	1.65	1.80	2.01
165	1.33	0.33	76	1.76	0.22	97	1.36	1.68	2.01
190	1.21	0.33	80	1.61	0.22	123	1.25	1.53	2.01
215	1.12	0.32	74	1.45	0.16	84	1.15	1.40	1.99
240	1.04	0.34	84	1.33	0.14	91	1.06	1.28	1.99
268	0.97	0.30	71	1.25	0.14	100	1.01	1.20	1.99

Table F.3: Values of eigenfrequencies, radiative decays and coupling strengths obtained to reproduce the experimental EEL spectra. Parameters obtained to reproduce within TCMT the experimental EEL spectra of the WS_2 disks shown in Figs. 3.9a and 3.11e. These parameters are plotted in Figs. 3.11g-h.

G

Parameters obtained by fitting experimental and simulated near-field spectra

In this appendix, we show all fitting parameters, obtained for the simulated and experimental near-field spectra presented in Chapter 4.

L (μm)	ω_{PhP} (cm^{-1})	γ_{PhP} (cm^{-1})	ω_{CBP} (cm^{-2})	γ_{CBP} (cm^{-1})	g (cm^{-1})
0.9	1445.6	3.0	1450.5	7.0	5.5
0.8	1450.0	3.0	1450.7	7.0	5.3
0.7	1455.2	3.0	1450.9	6.4	5.2
0.6	1459.9	3.1	1451.0	6.0	5.5

Table G.1: Parameters obtained by fitting the simulated complex-valued near-field spectra. Parameters obtained by fitting the simulated near-field spectra shown in Fig. 4.1e with the two-coupled harmonic oscillator model.

L (μm)	ω_{PhP} (cm^{-1})	γ_{PhP} (cm^{-1})	ω_{CBP} (cm^{-2})	γ_{CBP} (cm^{-1})	g (cm^{-1})
1.2	1441.2	9.4	1450.8	6.0	5.4
1.1	1447.8	8.9	1452.3	6.0	4.3
1.0	1451.0	8.8	1451.4	7.0	4.6
0.9	1454.4	10.2	1451.8	6.6	6.0
0.8	1462.4	10.7	1452.0	7.0	4.7

Table G.2: Parameters obtained by fitting the experimental complex-valued near-field spectra. Parameters obtained by fitting the experimental near-field spectra shown in Figs. 4.1d and 4.6a with the two-coupled harmonic oscillator model.

List of Publications

The contents of this thesis are based on the following publications:

1. **C. Maciel-Escudero**, A. Konečná, R. Hillenbrand and J. Aizpurua. "Probing and steering bulk and surface phonon polaritons in uniaxial materials using fast electrons: hexagonal boron nitride", Phys. Rev. B **102**, 115431 (2020).

2. I. Dolado*, **C. Maciel-Escudero***, E. Nikulina, E. Modin, F. Calavalle, S. Chen, A. Bylinkin, F. Javier Alfaro-Mozaz, J. Li, J. H. Edgar, F. Casanova, S. Vélez, L. E. Hueso, R. Esteban, J. Aizpurua and R. Hillenbrand. "Remote near-field spectroscopy of vibrational strong coupling between organic molecules and phononic nanoresonators" Nat. Commun. **13**, 6850 (2022). (*Equally contributed)

3. **C. Maciel-Escudero***, A. B. Yankovich*, B. Munkhbat, D. G. Baranov, R. Hillenbrand, E. Olsson, J. Aizpurua and T. O. Shegai. "Probing optical anapoles with fast electron beams". Accepted in Nat. Commun., arxiv preprint: arXiv:2304.01018. (*Equally contributed)

Other relevant publications that are not included in the text:

4. **C. Maciel-Escudero** and A. Reyes-Coronado. "Electromagnetic fields produced by a swift electron: A source of white light", Wave Motion **86**, 137-149 (2019).

5. C. Chen, S. Chen, R. P. S. M. Lobo, **C. Maciel-Escudero**, M. Lewin, T. Taubner, W. Xiong, M. Xu, X. Zhang, X. Miao, P. Li and R. Hillenbrand. "Terahertz Nanoimaging and Nanospectroscopy of Chalcogenide Phase-Change Materials", ACS Photonics **7**, 3499-3506 (2020).

6. J. Castrejón-Figueroa, J. A. Castellanos-Reyes, **C. Maciel-Escudero**, A. Reyes-Coronado and R. G. Barrera. "Time-dependent forces between a swift electron and a small nanoparticle within the dipole approximation", Phys. Rev. B **103**, 155413 (2021).

7. S. Chen, P. L. Leng, A. Konečná, E. Modin, M. Gutierrez-Amigo, E. Vicentini, B. Marín-García, M. Barra-Burillo, I. Niehues, **C. Maciel-Escudero**, C. Y. Xie, L. E. Hueso, E. Artacho, J. Aizpurua, I. Errea, M. G. Vergniory, A. Chuvilin, F. X. Xiu and R. Hillenbrand. "Real-space observation of ultraconfined in-plane anisotropic acoustic terahertz plasmon polaritons", Nat. Mater., 1476-1122 (2023).

8. A. Nodar, R. Esteban, **C. Maciel-Escudero**, J. Lasa-Alonso, J. Aizpurua and G. Molina-Terriza. "Preservation and destruction of the purity of two-photon states in the interaction with a nanoscatterer". Under review, arxiv preprint: arXiv:2211.14244.

9. J. Lasa-Alonso, C. Devescovi, **C. Maciel-Escudero**, A. García-Etxarri and G. Molina-Terriza. "On the origin of the Kerker phenomena". Under review, arxiv preprint: arXiv:2306.12762.

10. D. Virmani, **C. Maciel-Escudero**, R. Hillenbrand and M. Schnell. "Prediction and experimental verification of antenna-enhanced molecular scattering". Under review.

11. S. Yoon*, **C. Maciel-Escudero***, J. Mok Ok, Seoung-Hun Kang, H. Seong Jeon, B. Kang, C. Sohn, M. Yoon, J. Kim, A. Seo, R. Hillenbrand, J. Aizpurua, A. R. Lupini and H. Nyung Lee. "Observation of resonating hyperbolic plasmon polaritons in metallic delafossite $PdCoO_2$". In preparation. (*Equally contributed).

List of Symbols

a	Radius of a sphere
$\mathbf{A}$	Vector potential
a_0	Bohr radius
b	Impact parameter
$\mathbf{B}$	Magnetic field
c	Speed of light in vacuum
d	Thickness of a structure
$\mathbf{D}$	Electric displacement field
e	Elementary charge
E	Energy
$\mathbf{E}$	Electric field
$\mathscr{F}$	Fourier transform
$\mathcal{F}$	Time-to-frequency Fourier transform
g	Coupling strength
G_0	Scalar Green's function
$\hat{\mathbb{G}}$	Green's tensor
h_{tip}	Tip-sample distance
$h_\ell^{(1)}$	Spherical Hankel function of the first kind of order ℓ
$h_\ell^{(2)}$	Spherical Hankel function of the second kind of order ℓ
$\hbar$	Reduced Planck's constant
$\hat{\mathbb{I}}$	Identity tensor
j_ℓ	Spherical Bessel function of the first kind of order ℓ
$\mathbf{J}$	Current density
k_0	Magnitude of the wavevector in vacuum
$\mathbf{k}$	Wavevector of a wave
K_n	Modified Bessel function of the second kind of order n
$\mathbb{K}^3$	Reciprocal space
L	Length of a structure
$\mathbf{L}$	Angular momentum operator
m_{e}	Rest mass of the electron
$\mathbf{M}$	Magnetization
n_0	Number of dipoles per unit volume

$\mathbf{p}_\mathrm{e}$	Linear momentum of the electron
$\mathbf{p}$	Dipole moment
P	Momentum-resolved energy loss probability
$\mathbf{P}$	Dipole moment/Macroscopic Polarization
$\mathscr{P}$	Power
$\hat{\mathbb{Q}}$	Quadrupole moment
$\mathbf{r}$	Position vector
R_0	Radius of a disk
$\mathbb{R}^3$	Euclidean space
s_n	Amplitude of the n^{th}-order demodulated signal
$\mathbf{S}$	Poynting's vector
t	Time
$\mathbf{T}$	Toroidal moment
$\mathbf{v}$	Velocity of the electron
$\mathbf{v}_g$	Group velocity of a wave
$\mathbf{v}_p$	Phase velocity of a wave
V	Volume of a structure
w	Width of a structure
$Y_{\ell m}$	Scalar spherical harmonics
Z_0	Impedance of vacuum
x,y,z	Components of the Cartesian coordinate system
R,ϕ,z	Components of the cylindrical coordinate system
r,ϕ,θ	Components of the spherical coordinate system
γ	Damping constant or decay rate
γ_L	Lorentz factor
Γ	Electron energy-loss probability
Γ'	Electron energy-loss probability per unit length
δ	Dirac delta function
ε	Relative permittivity or dielectric function
ε_0	Permittivity of free space
$\hat{\varepsilon}$	Permittivity tensor
λ	Wavelength of a wave
μ_0	Permeability of free space
ν	Spectroscopic wavenumber
ρ	Volume charge density
ρ_s	Surface charge density
σ_n	Complex n^{th}-order demodulated signal
τ	Lifetime
φ_n	Phase of the n^{th}-order demodulated signal
χ	Electric susceptibility
$\hat{\chi}$	Electric susceptibility tensor
ω	Angular frequency
ω_TO, ω_LO	Transverse and longitudinal optical phonon frequencies
ω_p	Plasma frequency
Ω	Tip oscillation

Ω_{R}	Mode splitting
$\parallel$	Parallel (longitudinal) to a direction
$\perp$	Perpendicular (transverse) to a direction
$\dagger$	Conjugate transpose
$\top$	Transpose
$\otimes$	Tensor product
$\langle\,\rangle_t$	Time average

List of Abbreviations

AFM	Atomic Force Microscope
Al	Aluminium
Au	Gold
CBP	4, 4′-bis(N-carbazolyl)-1,1′-biphenyl
ED	Electric Dipole
EEL(S)	Electron Energy Loss (Spectroscopy)
EM	Electromagnetic
EQ	Electric Quadrupole
FDM	Finite Difference Method
FEM	Finite Element Method
FP	Fabry-Perot
FTIR	Fourier Transformed Infrared Spectroscopy
FWHM	Full Width at Half Maximum
h-BN	Hexagonal Boron Nitride
HAADF	High-Angle Annular Dark-Field
IR	Infrared
LO	Longitudinal Optical
LSP	Localized Surface Plasmon
LSPP	Localized Surface Plasmon Polariton
LSPh	Localized Surface Phonon
LSPhP	Localized Surface Phonon Polariton
MoS_2	Molybdenum Disulfide
nano-FTIR	Nanoscale Fourier Transform Infrared Spectroscopy
$PdCoO_2$	Palladium-based Delafossite
PhP	Phonon Polariton
PML	Perfectly Matched Layers
PP	Plasmon Polariton
Pt	Platinum
SC	Strong Coupling
Si	Silicon
SiC	Silicon Carbide
SiO_2	Silicon Dioxide

SPh	Surface Phonon
SPhP	Surface Phonon Polariton
SP	Surface Plasmon
SPP	Surface Plasmon Polariton
STEM	Scanning Transmission Electron Microscopy
(s)-SNOM	(Scattering-type) Scanning Near-field Optical Microscopy
QNM	Quasinormal Mode
TCMT	Temporal Coupled Mode Theory
TE	Transverse Electric
TM	Transverse Magnetic
TMDC	Transition Metal Dichalcogenide
TO	Transverse Optical
$\mathbf{V_2O_5}$	Vanadium Pentoxide
VSC	Vibrational Strong Coupling
WC	Weak Coupling
$\mathbf{WS_2}$	Tungsten Disulfide
α-$\mathbf{MoO_3}$	α-Molybdenum Trioxide

List of Figures

List of Tables

Bibliography

[1] E. Abbe, "Beiträge zur theorie des mikroskops und der mikroskopischen wahrnehmung," Archiv f. Mikros. Anatomie **9**, 413–468 (1873).

[2] Rayleigh, "Xv. on the theory of optical images, with special reference to the microscope," The London, Edinburgh, and Dublin Philosophical Magazine and Journal of Science **42**, 167–195 (1896).

[3] D L Mills and E Burstein, "Polaritons: the electromagnetic modes of media," Rep. Pog. Phys. **37**, 817 (1974).

[4] D. N. Basov, M. M. Fogler, and F. J. García de Abajo, "Polaritons in van der waals materials," Science **354**, aag1992 (2016).

[5] Shuming Nie and Steven R. Emory, "Probing single molecules and single nanoparticles by surface-enhanced raman scattering," Science **275**, 1102–1106 (1997).

[6] Martti Kauranen and Anatoly V. Zayats, "Nonlinear plasmonics," Nat. Photonics **6**, 1749–4893 (2012).

[7] Urcan Guler, Justus C. Ndukaife, Gururaj V. Naik, A. G. Agwu Nnanna, Alexander V. Kildishev, Vladimir M. Shalaev, and Alexandra Boltasseva, "Local heating with lithographically fabricated plasmonic titanium nitride nanoparticles," Nano Letters **13**, 6078–6083 (2013).

[8] F. J. García De Abajo, "Optical excitations in electron microscopy," Rev. Mod. Phys. **82**, 209–275 (2010).

[9] Albert Polman, Mathieu Kociak, and F. J. García de Abajo, "Electron-beam spectroscopy for nanophotonics," Nat. Mater. **18**, 1159–1171 (2019).

[10] Jaysen Nelayah, Mathieu Kociak, Odile Stéphan, F. Javier García de Abajo, Marcel Tencè, Luc Henrard, Dario Taverna, Isabel Pastoriza-

Santos, Luis M. Liz-Marzán, and Christian Colliex, "Mapping surface plasmons on a single metallic nanoparticle," Nat. Phys. **3**, 348–353 (2007).

[11] Franz-Philipp Schmidt, Harald Ditlbacher, Ulrich Hohenester, Andreas Hohenau, Ferdinand Hofer, and Joachim R. Krenn, "Dark plasmonic breathing modes in silver nanodisks," Nano Lett. **12**, 5780–5783 (2012).

[12] Andrew B. Yankovich, Ruggero Verre, Erik Olsèn abd Anton E. O. Persson, Viet Trinh, Gudrun Dovner, Mikael Käll, and Eva Olsson, "Multidimensional hybridization of dark surface plasmons," ACS Nano **11**, 4265–4274 (2017).

[13] Yueying Wu, Guoliang Li, and Jon P. Camden, "Probing nanoparticle plasmons with electron energy loss spectroscopy," Chemical Reviews **118**, 2994–3031 (2018).

[14] Luiz H. G. Tizei, Yung-Chang Lin, Masaki Mukai, Hidetaka Sawada, Ang-Yu Lu, Lain-Jong Li, Koji Kimoto, and Kazu Suenaga, "Exciton mapping at subwavelength scales in two-dimensional materials," Phys. Rev. Lett. **114**, 107601 (2015).

[15] Surong Guo, Nahid Talebi, Alfredo Campos, Mathieu Kociak, and Peter A. van Aken, "Radiation of dynamic toroidal moments," ACS Photonics **6**, 467–474 (2019).

[16] Duncan T. L. Alexander, Valentin Flauraud, and Frank Demming-Janssen, "Near-field mapping of photonic eigenmodes in patterned silicon nanocavities by electron energy-loss spectroscopy," ACS Nano **15**, 16501–16514 (2021).

[17] Mathieu Kociak and Javier García de Abajo, "Nanoscale mapping of plasmons, photons, and excitons," MRS Bulletin **37**, 39–46 (2012).

[18] Andrea Konečná, Tomáš Neuman, Javier Aizpurua, and Rainer Hillenbrand, "Surface-enhanced molecular electron energy loss spectroscopy," ACS Nano **12**, 4775–4786 (2018).

[19] Andrew B. Yankovich, Battulga Munkhbat, Denis G. Baranov, Jorge Cuadra, Erik Olsén, Hugo Lourenço-Martins, Luiz H. G. Tizei, Mathieu Kociak, Eva Olsson, and Timur Shegai, "Visualizing spatial variations of plasmon-exciton polaritons at the nanoscale using electron microscopy," Nano Lett. **19**, 8171–8181 (2019).

[20] Ora Bitton, Satyendra Nath Gupta, Lothar Houben, Michal Kvapil, Vlastimil Křápek, Tomáš Šikola, and Gilad Haran, "Vacuum rabi splitting of

a dark plasmonic cavity mode revealed by fast electrons," Nat. Commun. **11**, 487 (2020).

[21] Luiz H. G. Tizei, Vahagn Mkhitaryan, Hugo Lourenço-Martins, Leonardo Scarabelli, Kenji Watanabe, Takashi Taniguchi, Marcel Tencé, Jean-Denis Blazit, Xiaoyan Li, Alexandre Gloter, Alberto Zobelli, Franz-Philipp Schmidt, Luis M. Liz-Marzán, F. Javier García de Abajo, Odile Stéphan, and Mathieu Kociak, "Tailored nanoscale plasmon-enhanced vibrational electron spectroscopy," Nano Lett. **2**, 2973–2979 (2020).

[22] Maureen J. Lagos, Philip E. Batson, Zihan Lyu, and Ulrich Hohenester, "Imaging strongly coupled plasmon–phonon modes in mid-infrared double antennas," ACS Photonics **8**, 1293–1300 (2021).

[23] Keilmann Fritz and Hillenbrand Rainer, "Near-field microscopy by elastic light scattering from a tip," Phil. Trans. R. Soc. A. **362**, 787–805 (2004).

[24] Xinzhong Chen, Debo Hu, Ryan Mescall, Guanjun You, D. N. Basov, Qing Dai, and Mengkun Liu, "Modern scattering-type scanning near-field optical microscopy for advanced material research," Advanced Materials **31**, 1804774 (2019).

[25] A.V. Zayats and D. Richards, *Nano-optics and Near-field Optical Microscopy*, Artech House nanoscale science and engineering series (Artech House, 2009).

[26] Tomáš Neuman, Pablo Alonso-González, Aitzol Garcia-Etxarri, Martin Schnell, Rainer Hillenbrand, and Javier Aizpurua, "Mapping the near fields of plasmonic nanoantennas by scattering-type scanning near-field optical microscopy," Laser & Photonics Reviews **9**, 637–649 (2015).

[27] F. J. Alfaro-Mozaz, P. Alonso-González, S. Vélez, I. Dolado, M. Autore, S. Mastel, F. Casanova, L. E. Hueso, P. Li, A. Y. Nikitin, and R. Hillenbrand, "Nanoimaging of resonating hyperbolic polaritons in linear boron nitride antennas," Nat. Commun. **8**, 15624 (2017).

[28] Jianing Chen, Michela Badioli, Pablo Alonso-González, Sukosin Thongrattanasiri, Florian Huth, Johann Osmond, Marko Spasenović, Alba Centeno, Amaia Pesquera, Philippe Godignon, Amaia Zurutuza Elorza, Nicolas Camara, F. Javier García de Abajo, Rainer Hillenbrand, and Frank H. L. Koppens, "Optical nano-imaging of gate-tunable graphene plasmons," Nature **487**, 77—-81 (2012).

[29] Z. Fei, A. S. Rodin, G. O. Andreev, W. Bao, A. S. McLeod, M. Wagner, L. M. Zhang, Z. Zhao, M. Thiemens, G. Dominguez, M. M. Fogler,

A. H. Castro Neto, C. N. Lau, F. Keilmann, and D. N. Basov, "Gate-tuning of graphene plasmons revealed by infrared nano-imaging," Nature **487**, 1476–4687 (2012).

[30] S. Dai, Z. Fei, Q. Ma, A. S. Rodin, M. Wagner, A. S. McLeod, M. K. Liu, W. Gannett, W. Regan, K. Watanabe, T. Taniguchi, M. Thiemens, G. Dominguez, A. H. Castro Neto, A. Zettl, F. Keilmann, P. Jarillo-Herrero, M. M. Fogler, and D. N. Basov, "Tunable phonon polaritons in atomically thin van der waals crystals of boron nitride," Science **343**, 1125–1129 (2014).

[31] John David Jackson, *Classical Electrodynamics*, 3rd ed. (John Wiley & Sons, Inc, United States, 1999).

[32] Lukas Novotny and Bert Hecht, *Principles of Nano-Optics*, 2nd ed. (Cambridge University Press, New York, 2012).

[33] Andrew Zangwill, *Modern Electrodynamics* (Cambridge University Press, 2012).

[34] S. R. de Groot and L. G. Suttorp, *Foundations of electrodynamics* (Noord-Hollandsche U.M Amsterdam, 1972).

[35] Henri Benist, Jean-Jacques Greffet, and Phillippe Lalanne, *Introduction to Nanophotonics* (Oxford University Press, 2022).

[36] A. M. Fox, *Optical Properties of Solids*, Oxford master series in condensed matter physics (Oxford University Press, 2001).

[37] P. Drude, "Zur elektronentheorie der metalle," Annalen der Physik **306**, 566–613 (1900).

[38] N. W. Ashcroft and N.D. Mermin, *Solid State Physics*, HRW international editions (Holt, Rinehart and Winston, 1976).

[39] D. Pines, *Elementary Excitations in Solids* (CRC Press, 1999).

[40] D. Bohm and E. P. Gross, "Theory of plasma oscillations. A. Origin of medium-like behavior," Phys. Rev. **75**, 1851–1864 (1949).

[41] David Bohm and David Pines, "A collective description of electron interactions. I. Magnetic interactions," Phys. Rev. **82**, 625–634 (1951).

[42] David Pines and David Bohm, "A collective description of electron interactions: II. Collective vs individual particle aspects of the interactions," Phys. Rev. **85**, 338–353 (1952).

[43] H. Ehrenreich, H. R. Philipp, and B. Segall, "Optical properties of aluminum," Phys. Rev. **132**, 1918–1928 (1963).

[44] C. Kittel, *Introduction to Solid State Physics*, eighth ed. (John Wiley & Sons, 2005).

[45] P. Yu and M. Cardona, *Fundamentals of Semiconductors: Physics and Materials Properties*, Graduate Texts in Physics (Springer Berlin Heidelberg, 2010).

[46] E. D. Palik, *Handbook of Optical Constants of Solids* (Academic Press, 1998).

[47] Ruben Esteban, Javier Aizpurua, and Garnett W Bryant, "Strong coupling of single emitters interacting with phononic infrared antennae," New Journal of Physics **16**, 013052 (2014).

[48] V. Klimov, *Nanoplasmonics*, 1st ed. (Jenny Stanford Publishing, 2013).

[49] J. M. Pitarke, V. M. Silkin, E. V. Chulkov, and P. M. Echenique, "Theory of surface plasmons and surface-plasmon polaritons," Rep. Prog. Phys. **70**, 1 (2006).

[50] H. Raether, *Surface Plasmons on Smooth and Rough Surfaces and on Gratings*, 1st ed. (Springer Berlin, Heidelberg, 2006).

[51] Stefan A. Maier, *Plasmonics: Fundamentals and Applications*, 1st ed. (Springer New York, NY, 2007).

[52] U. Hohenester, *Nano and Quantum Optics: An Introduction to Basic Principles and Theory*, Graduate Texts in Physics (Springer International Publishing, 2019).

[53] C. M. Escudero, *Linear momentum transfer from swift electrons to small metallic nanoparticles: dipole approximation*, Master's thesis, Universidad Nacional Autónoma de México (2017).

[54] A. B. Aizpurua, *Quantum many-body effects in the optoelectronic response of plasmonic nanostructures and their coupling to quantum emitters*, Ph.D. thesis, Universidad del País Vasco (2022).

[55] Jens Dorfmüller, Ralf Vogelgesang, R. Thomas Weitz, Carsten Rockstuhl, Christoph Etrich, Thomas Pertsch, Falk Lederer, and Klaus Kern, "Fabry-pérot resonances in one-dimensional plasmonic nanostructures," Nano Letters **9**, 2372–2377 (2009).

[56] Cecilia Noguez, "Surface plasmons on metal nanoparticles: the influence of shape and physical environment," The Journal of Physical Chemistry C **111**, 3806–3819 (2007).

[57] Olivia Nicoletti, Francisco de la Peña, Rowan K. Leary, Daniel J. Holland, Caterina Ducati, and Paul A. Midgley, "Three-dimensional imaging of localized surface plasmon resonances of metal nanoparticles," Nature **502**, 1476–4687 (2013).

[58] Sean M. Collins, "Dispersion characteristics of face modes in ionic-crystal and plasmonic-metal nanoparticles," Phys. Rev. B **97**, 245422 (2018).

[59] Shuiyan Cao, Mario Zapata-Herrera, Alfredo Campos, Eric Le Moal, Sylvie Marguet, Gérald Dujardin, Mathieu Kociak, Javier Aizpurua, Andrei G. Borisov, and Elizabeth Boer-Duchemin, "Probing the radiative electromagnetic local density of states in nanostructures with a scanning tunneling microscope," ACS Photonics **7**, 1280–1289 (2020).

[60] Max Born, Emil Wolf, A. B. Bhatia, P. C. Clemmow, D. Gabor, A. R. Stokes, A. M. Taylor, P. A. Wayman, and W. L. Wilcock, *Principles of Optics: Electromagnetic Theory of Propagation, Interference and Diffraction of Light*, 7th ed. (Cambridge University Press, 1999).

[61] C. C. Homes, S. Khim, and A. P. Mackenzie, "Perfect separation of intraband and interband excitations in $pdcoo_2$," Phys. Rev. B **99**, 195127 (2019).

[62] Battulga Munkhbat, Piotr Wróbel, Tomasz J. Antosiewicz, and Timur O. Shegai, "Optical constants of several multilayer transition metal dichalcogenides measured by spectroscopic ellipsometry in the 300–1700 nm range: High index, anisotropy, and hyperbolicity," ACS Photonics **9**, 2398–2407 (2022).

[63] G. A. Ermolaev, D. V. Grudinin, Y. V. Stebunov, K. V. Voronin, V. G. Kravets, J. Duan, A. B. Mazitov, G. I. Tselikov, A. Bylinkin, D. I. Yakubovsky, S. M. Novikov, D. G. Baranov, A. Y. Nikitin, I. A. Kruglov, T. Shegai, P. Alonso-González, A. N. Grigorenko, A. V. Arsenin, K. S. Novoselov, and V. S. Volkov, "Giant optical anisotropy in transition metal dichalcogenides for next-generation photonics," Nat. Commun. **12** (2021), 10.1038/s41467-021-21139-x.

[64] Joshua D. Caldwell, Igor Aharonovich, Guillaume Cassabois, James H. Edgar, Bernard Gil, and D. N. Basov, "Photonics with hexagonal boron nitride," Nat. Rev. Mater **4**, 552 (2019).

[65] Simon Vassant, Jean-Paul Hugonin, and Jean-Jacques Greffet, "Quasi-confined enz mode in an anisotropic uniaxial thin slab," Opt. Express **27**, 12317–12335 (2019).

[66] Gonzalo Álvarez-Pérez, Kirill V. Voronin, Valentyn S. Volkov, Pablo Alonso-González, and Alexey Y. Nikitin, "Analytical approximations for the dispersion of electromagnetic modes in slabs of biaxial crystals," Phys. Rev. B **100**, 235408 (2019).

[67] Edward Yoxall, Martin Schnell, Alexey Y. Nikitin, Oihana Txoperena, Achim Woessner, Mark B. Lundeberg, Félix Hueso Luis E. Casanova, Frank H. L. Koppens, and Rainer Hillenbrand, "Direct observation of ultraslow hyperbolic polariton propagation with negative phase velocity," Nat. Photon. **9**, 674–678 (2015).

[68] Andrea Konečná, *Theoretical description of low-energy excitations in naostructures as probed by fast electrons*, Ph.D. thesis, Universidad del País Vasco (2019).

[69] James A. Hutchison, Tal Schwartz, Cyriaque Genet, Eloïse Devaux, and Thomas W. Ebbesen, "Modifying chemical landscapes by coupling to vacuum fields," Angew. Chem. Int. Ed. **51**, 1592–1596 (2012).

[70] Francisco J. Garcia-Vidal, Cristiano Ciuti, and Thomas W. Ebbesen, "Manipulating matter by strong coupling to vacuum fields," Science **373**, eabd0336 (2021).

[71] Yuto Ashida, Ata ç İmamoğlu, Jérôme Faist, Dieter Jaksch, Andrea Cavalleri, and Eugene Demler, "Quantum electrodynamic control of matter: Cavity-enhanced ferroelectric phase transition," Phys. Rev. X **10**, 041027 (2020).

[72] Kati Stranius, Manuel Hertzog, and Karl Börjesson, "Selective manipulation of electronically excited states through strong light-matter interactions," Nat. Commun. **9**, 2273 (2018).

[73] U. M. Caballero, *Quantum-mechanical study of optical excitations in nanoscale systems: first-principles description of plasmons, tunneling-induced light emission and ultrastrong light-matter interaction*, Ph.D. thesis, Universidad del País Vasco (2023).

[74] Xiaohua Wu, Stephen K. Gray, and Matthew Pelton, "Quantum-dot-induced transparency in a nanoscale plasmonic resonator," Opt. Express **18**, 23633–23645 (2010).

[75] Matthew Pelton, S. David Storm, and Haixu Leng, "Strong coupling of emitters to single plasmonic nanoparticles: exciton-induced transparency and rabi splitting," Nanoscale **11**, 14540–14552 (2019).

[76] V. Savona, L.C. Andreani, P. Schwendimann, and A. Quattropani, "Quantum well excitons in semiconductor microcavities: Unified treatment of weak and strong coupling regimes," Solid State Communications **93**, 733–739 (1995).

[77] Philip A. Thomas, Wai Jue Tan, Henry A. Fernandez, and William L. Barnes, "A new signature for strong light–matter coupling using spectroscopic ellipsometry," Nano Letters **20**, 6412–6419 (2020).

[78] G. Khitrova, H. M. Gibbs, M. Kira, S. W. Koch, and A. Scherer, "Vacuum rabi splitting in semiconductors," Nat. Phys. **2**, 1745–2481 (2007).

[79] P Törmä and W L Barnes, "Strong coupling between surface plasmon polaritons and emitters: a review," Reports on Progress in Physics **78**, 013901 (2014).

[80] Denis G. Baranov, Martin Wersäll, Jorge Cuadra, Tomasz J. Antosiewicz, and Timur Shegai, "Novel nanostructures and materials for strong light–matter interactions," ACS Photonics **5**, 24–42 (2018).

[81] E. M. Purcell, H. C. Torrey, and R. V. Pound, "Resonance absorption by nuclear magnetic moments in a solid," Phys. Rev. **69**, 37–38 (1946).

[82] Hermann A. Haus, *Waves and Fields in Optoelectronics* (Prentice Hall: Englewood Cliffs, New Jersey, 1984).

[83] Shanhui Fan, Wonjoo Suh, and J. D. Joannopoulos, "Temporal coupled-mode theory for the fano resonance in optical resonators," J. Opt. Soc. Am. A **20**, 569–572 (2003).

[84] Rafif E. Hamam, Aristeidis Karalis, J. D. Joannopoulos, and Marin Soljačić, "Coupled-mode theory for general free-space resonant scattering of waves," Phys. Rev. A **75**, 053801 (2007).

[85] Zhichao Ruan and Shanhui Fan, "Temporal coupled-mode theory for light scattering by an arbitrarily shaped object supporting a single resonance," Phys. Rev. A **85**, 043828 (2012).

[86] Chia Wei Hsu, Brendan G. DeLacy, Steven G. Johnson, John D. Joannopoulos, and Marin Soljačić, "Theoretical criteria for scattering dark states in nanostructured particles," Nano Lett. **14**, 2783–2788 (2014).

[87] Filippo Alpeggiani, Nikhil Parappurath, Ewold Verhagen, and L. Kuipers, "Quasinormal-mode expansion of the scattering matrix," Phys. Rev. X **7**, 021035 (2017).

[88] Marta Autore, Peining Li, Irene Dolado, Francisco J. Alfaro-Mozaz, Ruben Esteban, Ainhoa Atxabal, Fèlix Casanova, Luis E. Hueso, Pablo Alonso-González, Javier Aizpurua, Alexey Y. Nikitin, Saül Vélez, and Rainer Hillenbrand, "Boron nitride nanoresonators for phonon-enhanced molecular vibrational spectroscopy at the strong coupling limit," Light Sci. Appl. **7**, 2047–7538 (2018).

[89] Stephen J. Pennycook and Peter D. Nellist, *Scanning Transmission Electron Microscopy* (Springer, New York, 2011).

[90] Stephen J. Pennycook, Maria Varela, Andrew R. Lupini, Mark P. Oxley, and Matthew F. Chisholm, "Atomic-resolution spectroscopic imaging: past, present and future," Journal of Electron Microscopy **58**, 87–97 (2009).

[91] O. L. Krivanek, T.C. Lovejoy, and N. Dellby, "Aberration-corrected stem for atomic-resolution imaging and analysis," Journal of Microscopy **259**, 165–172 (2015).

[92] R.F. Egerton, *Electron Energy-Loss Spectroscopy in the Electron Microscope*, 3rd ed. (Springer New York, 2011).

[93] C. Maciel-Escudero and A. Reyes-Coronado, "Electromagnetic fields produced by a swift electron: A source of white light," Wave Motion **86**, 137–149 (2019).

[94] P. A. Cherenkov, "Visible light from clear liquids under the action of gamma radiation," Compt. Rend. Acad. Sci. URSS **2**, 451–454 (1934).

[95] P. A. Cherenkov, "Visible radiation produced by electrons moving in a medium with velocities exceeding that of light," Phys. Rev. **52**, 378–379 (1937).

[96] I. M. Frank and I. E. Tamm, "Coherent visible radiation of fast electrons passing through matter," Compt. Rend. Acad. Sci. URSS **14**, 109–114 (1937).

[97] Ig. Tamm, "Radiation emitted by uniformly moving electrons," in *Selected Papers*, edited by Boris M. Bolotovskii, Victor Ya. Frenkel, and Rudolf Peierls (Springer Berlin Heidelberg, Berlin, Heidelberg, 1991) pp. 37–53.

[98] A. A. Lucas and E. Kartheuser, "Energy-loss spectrum of fast electrons in a dielectric slab. i. nonretarded losses and cherenkov bulk loss," Phys. Rev. B **1**, 3588–3598 (1970).

[99] C. H. Chen and J. Silcox, "Calculations of the electron-energy-loss probability in thin uniaxial crystals at oblique incidence," Phys. Rev. B **20**, 3605–3614 (1979).

[100] Vitalii L Ginzburg, "Radiation by uniformly moving sources (vavilov–cherenkov effect, transition radiation, and other phenomena)," Phys.-Usp.+ **39**, 973 (1996).

[101] Nahid Talebi, *Near-Field-Mediated Photon-Electron Interactions* (Sprimger, Switzerland, 2019).

[102] Gonzalo Álvarez Pérez, Thomas G. Folland, Ion Errea, Javier Taboada-Gutiérrez, Jiahua Duan, Javier Martín-Sánchez, Ana I. F. Tresguerres-Mata, Joseph R. Matson, Andrei Bylinkin, Mingze He, Weiliang Ma, Qiaoliang Bao, José Ignacio Martín, Joshua D. Caldwell, Alexey Y. Nikitin, and Pablo Alonso-González, "Infrared permittivity of the biaxial van der waals semiconductor α-moo$_3$ from near- and far-field correlative studies," Advanced Materials **32**, 1908176 (2020).

[103] S. Chen, P. L. Leng, A. Konečná, E. Modin, M. Gutierrez-Amigo, E. Vicentini, B. Martín-García, M. Barra-Burillo, I. Niehues, C. Maciel Escudero, X. Y. Xie, L. E. Hueso, E. Artacho, J. Aizpurua, I. Errea, M. G. Vergniory, A. Chuvilin, F. X. Xiu, and R. Hillenbrand, "Real-space observation of ultraconfined in-plane anisotropic acoustic terahertz plasmon polaritons," Nature Materials **22**, 860–866 (2023).

[104] Nenad Ocelic, Andreas Huber, and Rainer Hillenbrand, "Pseudoheterodyne detection for background-free near-field spectroscopy," Applied Physics Letters **89**, 101124 (2006).

[105] Sergiu Amarie, Thomas Ganz, and Fritz Keilmann, "Mid-infrared near-field spectroscopy," Opt. Express **17**, 21794–21801 (2009).

[106] Florian Huth, Alexander Govyadinov, Sergiu Amarie, Wiwat Nuansing, Fritz Keilmann, and Rainer Hillenbrand, "Nano-ftir absorption spectroscopy of molecular fingerprints at 20 nm spatial resolution," Nano Letters **12**, 3973–3978 (2012).

[107] Jin Sun, P. Scott Carney, and John C. Schotland, "Strong tip effects in near-field scanning optical tomography," Journal of Applied Physics **102**, 103103 (2007).

[108] Bradley Deutsch, Rainer Hillenbrand, and Lukas Novotny, "Visualizing the optical interaction tensor of a gold nanoparticle pair," Nano Letters **10**, 652–656 (2010).

[109] Rémi Carminati and John C. Schotland, *Principles of Scattering and Transport of Light* (Cambridge University Press, 2021).

[110] C. Tai, IEEE Antennas, Propagation Society, IEEE Microwave Theory, and Techniques Society, *Dyadic Green Functions in Electromagnetic Theory*, IEEE Press Publication Series (IEEE Press, 1994).

[111] Liesbeth Venema, Bart Verberck, Iulia Georgescu, Giacomo Prando, Elsa Couderc, Silvia Milana, Maria Maragkou, Lina Persechini, Giulia Pacchioni, and Luke Fleet, "The quasiparticle zoo," Nat. Phys. **12**, 1085–1089 (2016).

[112] R. Hillenbrand, T. Taubner, and F. Keilmann, "Phonon-enhanced light–matter interaction at the nanometre scale," Nature **418**, 159–162 (2002).

[113] T. G. Folland, L. Nordin, D. Wasserman, and J. D. Caldwell, "Probing polaritons in the mid- to far-infrared," J. Appl. Phys. **125**, 191102 (2019).

[114] Zubin Jacob, "Hyperbolic phonon–polaritons," Nat. Mater. **13**, 1081–1083 (2014).

[115] Joshua D. Caldwell, Lucas Lindsay, Vincenzo Giannini, Igor Vurgaftman, Thomas L. Reinecke, Stefan A. Maier, and Orest J. Glembocki, "Low-loss, infrared and terahertz nanophotonics using surface phonon polaritons," Nanophotonics **4**, 44–68 (2015).

[116] Tony Low, Andrey Chaves, Joshua D. Caldwell, Anshuman Kumar, Nicholas X. Fang, Phaedon Avouris, Tony F. Heinz, Francisco Guinea, Luis Martin-Moreno, and Frank Koppens, "Polaritons in layered two-dimensional materials," Nat. Mater. **16**, 182–194 (2017).

[117] Joshua D. Caldwell, Andrey V. Kretinin, Yiguo Chen, Vincenzo Giannini, Michael M. Fogler, Yan Francescato, Chase T. Ellis, Joseph G. Tischler, Colin R. Woods, Alexander J. Giles, Minghui Hong, Kenji Watanabe, Takashi Taniguchi, Stefan A. Maier, and Kostya S. Novoselov, "Sub-diffractional volume-confined polaritons in the natural hyperbolic material hexagonal boron nitride," Nat. Commun. **5**, 5221 (2014).

[118] Zhiwen Shi, Hans A. Bechtel, Samuel Berweger, Yinghui Sun, Bo Zeng, Chenhao Jin, Henry Chang, Michael C. Martin, Markus B. Raschke,

and Feng Wang, "Amplitude- and phase-resolved nanospectral imaging of phonon polaritons in hexagonal boron nitride," ACS Photonics **2**, 790–796 (2015).

[119] Leonid Gilburd, Kris S. Kim, Kevin Ho, Daniel Trajanoski, Aniket Maiti, Duncan Halverson, Sissi de Beer, and Gilbert C. Walker, "Hexagonal boron nitride self-launches hyperbolic phonon polaritons," J. Phys. Chem. Lett. **8**, 2158–2162 (2017).

[120] Antonio Ambrosio, Michele Tamagnone, Kundan Chaudhary, Philip Jauregui, Luis A.and Kim, William L. Wilson, and Federico Capasso, "Selective excitation and imaging of ultraslow phonon polaritons in thin hexagonal boron nitride crystals," Light-Sci. Appl. **7**, 27 (2018).

[121] Joshua D. Caldwell and Kostya S. Novoselov, "Mid-infrared nanophotonics," Nat. Mater. **14**, 364—366 (2015).

[122] Ondrej L. Krivanek, Tracy C. Lovejoy, Niklas Dellby, Toshihiro Aoki, R. W. Carpenter, Peter Rez, Emmanuel Soignard, Jiangtao Zhu, Philip E. Batson, Maureen J. Lagos, Ray F. Egerton, and Peter A. Crozier, "Vibrational spectroscopy in the electron microscope," Nature **514**, 209—212 (2014).

[123] Alexander A. Govyadinov, Andrea Konečná, Andrey Chuvilin, Saül Vélez, Irene Dolado, Alexey Y. Nikitin, Sergei Lopatin, Fèlix Casanova, Luis E. Hueso, Javier Aizpurua, and Rainer Hillenbrand, "Probing low-energy hyperbolic polaritons in van der waals crystals with an electron microscope," Nat. Commun. **8**, 95 (2017).

[124] Fredrik S. Hage, Rebecca J. Nicholls, Jonathan R. Yates, Dougal G. McCulloch, Tracy C. Lovejoy, Niklas Dellby, Ondrej L. Krivanek, Keith Refson, and Quentin M. Ramasse, "Nanoscale momentum-resolved vibrational spectroscopy," Science Advances **4**, eaar7495 (2018).

[125] Alexander Poddubny, Ivan Iorsh, Pavel Belov, and Yuri Kivshar, "Hyperbolic metamaterials," Nat. Photonics **7**, 948—957 (2013).

[126] Abdullah Eroglu, *Wave Propagation and Radiation in Gyrotropic and Anisotropic Media*, 1st ed. (Springer New York, NY, New York, 2010).

[127] Andrey S. Potemkin, Alexander N. Poddubny, Pavel A. Belov, and Yuri S. Kivshar, "Green function for hyperbolic media," Phys. Rev. A **86**, 023848 (2012).

[128] Weng Cho Chew, *Waves and Fields in Inhomogeneous Media*, 1st ed. (IEEE Press, New York, 1995).

[129] F. J. García de Abajo and M. Kociak, "Probing the photonic local density of states with electron energy loss spectroscopy," Phys. Rev. Lett. **100**, 106804 (2008).

[130] Robert E. Collin, *Field Theory of Guided Waves*, 2nd ed. (IEEE Press, New York, 1991).

[131] Leopold B. Felsen and Nathan Marcuvitz, *Radiation and Scattering of Waves* (Wiley, New York, 1994).

[132] Sergey N. Galyamin and Andrey V. Tyukhtin, "Electromagnetic field of a charge traveling into an anisotropic medium," Phys. Rev. E **84**, 056608 (2011).

[133] L. D. Landau and E. M. Lifshitz, *Electrodynamics of continuous media*, 2nd ed. (Pergamon Press, New York, 1984).

[134] Amnon Yariv and Pochi Yeh, *Optical Waves in Crystals* (Wiley, New York, 1983).

[135] Jin Tao, Qi Jie Wang, Jingjing Zhang, and Yu Luo, "Reverse surface-polariton cherenkov radiation," Sci. Rep. **6**, 30704 (2016).

[136] Jin Tao, Lin Wu, Guoxing Zheng, and Shaohua Yu, "Cherenkov polaritonic radiation in a natural hyperbolic material," Carbon **150**, 136–141 (2019).

[137] V. N. Neelavathi, R. H. Ritchie, and W. Brandt, "Bound electron states in the wake of swift ions in solids," Phys. Rev. Lett. **34**, 560–560 (1975).

[138] P. M. Echenique, R. H. Ritchie, and Werner Brandt, "Spatial excitation patterns induced by swift ions in condensed matter," Phys. Rev. B **20**, 2567–2580 (1979).

[139] R. H. Ritchie, P. M. Echenique, W. Brandt, and G. Basbas, "Plasmons, wakes and clusters," IEEE T. Nucl. Sci. **26**, 1001–1005 (1979).

[140] F. J. García de Abajo and P. M. Echenique, "Wake potential in the vicinity of a surface," Phys. Rev. B **46**, 2663–2675 (1992).

[141] Fang Liu, Long Xiao, Yu Ye, Mengxuan Wang, Kaiyu Cui, Xue Feng, Wei Zhang, and Yidong Huang, "Integrated cherenkov radiation emitter eliminating the electron velocity threshold," Nat. Photon. **11**, 289–292 (2017).

[142] David E. Fernandes, Stanislav I. Maslovski, and Mário G. Silveirinha, "Cherenkov emission in a nanowire material," Phys. Rev. B **85**, 155107 (2012).

[143] Primož Rebernik Ribič and Rudolf Podgornik, "Interaction of a point charge with the surface of a uniaxial dielectric," Europhys. Lett. **102**, 24001 (2013).

[144] M. I. D'yakonov, "New type of electromagnetic wave propagating at an interface," Zh. Eksp. Teor. Fiz. **94**, 119 (1988), [Sov. Phys.–JETP **67**, 4 (1988)].

[145] Osamu Takayama, Lucian-Cornel Crasovan, Steffen Kjær Johansen, Dumitru Mihalache, David Artigas, and Lluis Torner, "Dyakonov surface waves: A review," Electromagnetics **28**, 126–145 (2008).

[146] Nahid Talebi, *Topological Hyperbolic and Dirac Plasmons. In Reviews in Plasmonics 2017* (Springer, Switzerland, 2019).

[147] P. Li, I. Dolado, F. J. Alfaro-Mozaz, A. Yu. Nikitin, F. Casanova, L. E. Hueso, S. Vélez, and R. Hillenbrand, "Optical nanoimaging of hyperbolic surface polaritons at the edges of van der waals materials," Nano Lett. **17**, 228–235 (2017).

[148] Nahid Talebi, Cigdem Ozsoy-Keskinbora, Hadj M. Benia, Klaus Kern, Christoph T. Koch, and Peter A. van Aken, "Wedge dyakonov waves and dyakonov plasmons in topological insulator bi2se3 probed by electron beams," ACS Nano **10**, 6988–6994 (2016).

[149] E. Cojocaru, "Comparative analysis of dyakonov hybrid surface waves at dielectric-elliptic and dielectric-hyperbolic media interfaces," J. Opt. Soc. Am. B **31**, 2558–2564 (2014).

[150] B Zhu, G Ren, Y Gao, Q Wang, C Wan, J Wang, and S Jian, "Dyakonov surface waves at the interface between hexagonal-boron-nitride and isotropic material," J. Opt. **18**, 125006 (2016).

[151] Arseniy I. Kuznetsov, Andrey E. Miroshnichenko, Mark L. Brongersma, Yuri S. Kivshar, and Boris Luk'yanchuk, "Optically resonant dielectric nanostructures," Science **354**, aag2472 (2016).

[152] Isabelle Staude and Jörg Schilling, "Metamaterial-inspired silicon nanophotonics," Nat. Photon. **11**, 274–284 (2017).

[153] Kirill Koshelev, Sergey Kruk, Elizaveta Melik-Gaykazyan, Jae-Hyuck Choi, Andrey Bogdanov, Hong-Gyu Park, and Yuri Kivshar, "Subwavelength dielectric resonators for nonlinear nanophotonics," Science **367**, 288–292 (2020).

[154] Kirill Koshelev and Yuri Kivshar, "Dielectric resonant metaphotonics," ACS Photonics **8**, 102–112 (2021).

[155] Jacob B. Khurgin, "Expanding the photonic palette: Exploring high index materials," ACS Photonics **9**, 743–751 (2022).

[156] Yuri Kivshar, "The rise of mie-tronics," Nano Letters **22**, 3513–3515 (2022).

[157] Battulga Munkhbat, Betül Küçüköz, Denis G. Baranov, Tomasz J. Antosiewicz, and Timur O. Shegai, "Nanostructured transition metal dichalcogenide multilayers for advanced nanophotonics," Laser & Photonics Reviews **17**, 2200057 (2023).

[158] Yuri Kivshar and Andrey Miroshnichenko, "Meta-optics with mie resonances," Opt. Photon. News **28**, 24–31 (2017).

[159] Anastasiia Zalogina, Luca Carletti, Anton Rudenko, Jerome V. Moloney, Aditya Tripathi, Hoo-Cheol Lee, Ilya Shadrivov, Hong-Gyu Park, Yuri Kivshar, and Sergey S. Kruk, "High-harmonic generation from a subwavelength dielectric resonator," Science Advances **9**, eadg2655 (2023).

[160] M. Nieto-Vesperinas, R. Gomez-Medina, and J. J. Saenz, "Angle-suppressed scattering and optical forces on submicrometer dielectric particles," J. Opt. Soc. Am. A **28**, 54–60 (2011).

[161] Boris S. Luk'yanchuk, Nikolai V. Voshchinnikov, Ramón Paniagua-Domínguez, and Arseniy I. Kuznetsov, "Optimum forward light scattering by spherical and spheroidal dielectric nanoparticles with high refractive index," ACS Photonics **2**, 993–999 (2015).

[162] Maxim R. Shcherbakov, Dragomir N. Neshev, Ben Hopkins, Alexander S. Shorokhov, Isabelle Staude, Elizaveta V. Melik-Gaykazyan, Manuel Decker, Alexander A. Ezhov, Andrey E. Miroshnichenko, Igal Brener, Andrey A. Fedyanin, and Yuri S. Kivshar, "Enhanced third-harmonic generation in silicon nanoparticles driven by magnetic response," Nano Letters **14**, 6488–6492 (2014).

[163] Ia B Zel'Dovich, "Electromagnetic interaction with parity violation," Sov. Phys. JETP **6**, 1184–1186 (1958).

[164] V. M. Dubovik and V. V. Tugushev, "Toroid moments in electrodynamics and solid-state physics," Phys. Rep. **187**, 145–202 (1990).

[165] G. N. Afanasiev and Yu P. Stepanovsky, "The electromagnetic field of elementary time-dependent toroidal sources," J. Phys. A: Math. Gen. **28**, 4565–4580 (1995).

[166] Vassili A Fedotov, AV Rogacheva, Vassili Savinov, Din Ping Tsai, and Nikolay I Zheludev, "Resonant transparency and non-trivial non-radiating excitations in toroidal metamaterials," Sci. Rep. **3**, 2967 (2013).

[167] Andrey E. Miroshnichenko, Andrey B. Evlyukhin, Ye Feng Yu, Reuben M. Bakker, Arkadi Chipouline, Arseniy I. Kuznetsov, Boris Luk'yanchuk, Boris N. Chichkov, and Yuri S. Kivshar, "Nonradiating anapole modes in dielectric nanoparticles," Nat. Commun. **6**, 8069 (2015).

[168] Kseniia V. Baryshnikova, Daria A. Smirnova, Boris S. Luk'yanchuk, and Yuri S. Kivshar, "Optical anapoles: Concepts and applications," Adv. Opt. Mater. **7**, 1801350 (2019).

[169] V. Savinov, N. Papasimakis, D. P. Tsai, and N. I. Zheludev, "Optical anapoles," Commun. Phys. **2**, 69 (2019).

[170] Kirill Koshelev, Gael Favraud, Andrey Bogdanov, Yuri Kivshar, and Andrea Fratalocchi, "Nonradiating photonics with resonant dielectric nanostructures," Nanophotonics **8**, 725–745 (2019).

[171] Vladimir A. Zenin, Andrey B. Evlyukhin, Sergey M. Novikov, Yuanqing Yang, Radu Malureanu, Andrei V. Lavrinenko, Boris N. Chichkov, and Sergey I. Bozhevolnyi, "Direct amplitude-phase near-field observation of higher-order anapole states," Nano Lett. **17**, 7152–7159 (2017).

[172] Yuanqing Yang and Sergey I. Bozhevolnyi, "Nonradiating anapole states in nanophotonics: from fundamentals to applications," Nanotechnology **30**, 204001 (2019).

[173] Gustavo Grinblat, Yi Li, Michael P. Nielsen, Rupert F. Oulton, and Stefan A. Maier, "Enhanced third harmonic generation in single germanium nanodisks excited at the anapole mode," Nano Lett. **16**, 4635–4640 (2016).

[174] Lei Xu, Mohsen Rahmani, Khosro Zangeneh Kamali, Aristeidis Lamprianidis, Lavinia Ghirardini, Jürgen Sautter, Rocio Camacho-Morales, Haitao Chen, Matthew Parry, Isabelle Staude, *et al.*, "Boosting third-harmonic generation by a mirror-enhanced anapole resonator," Light Sci. Appl. **7**, 44 (2018).

[175] Gustavo Grinblat, Yi Li, Michael P Nielsen, Rupert F Oulton, and Stefan A Maier, "Degenerate four-wave mixing in a multiresonant germanium nanodisk," ACS Photonics **4**, 2144–2149 (2017).

[176] Denis G Baranov, Ruggero Verre, Pawel Karpinski, and Mikael Käll, "Anapole-enhanced intrinsic raman scattering from silicon nanodisks," ACS Photonics **5**, 2730–2736 (2018).

[177] Thomas D Green, Denis G Baranov, Battulga Munkhbat, Ruggero Verre, Timur Shegai, and Mikael Käll, "Optical material anisotropy in high-index transition metal dichalcogenide mie nanoresonators," Optica **7**, 680–686 (2020).

[178] Tianyue Zhang, Ying Che, Kai Chen, Jian Xu, Yi Xu, Te Wen, Guowei Lu, Xiaowei Liu, Bin Wang, Xiaoxuan Xu, *et al.*, "Anapole mediated giant photothermal nonlinearity in nanostructured silicon," Nature communications **11**, 3027 (2020).

[179] Aitzol García-Etxarri, Isabel Romero, F. Javier García de Abajo, Rainer Hillenbrand, and Javier Aizpurua, "Influence of the tip in near-field imaging of nanoparticle plasmonic modes: Weak and strong coupling regimes," Phys. Rev. B **79**, 125439 (2009).

[180] Sebastian Busschaert, René Reimann, Moritz Cavigelli, Ronja Khelifa, Achint Jain, and Lukas Novotny, "Transition metal dichalcogenide resonators for second harmonic signal enhancement," ACS Photonics **7**, 2482–2488 (2020).

[181] Haonan Ling, Renjie Li, and Artur R. Davoyan, "All van der waals integrated nanophotonics with bulk transition metal dichalcogenides," ACS Photonics **8**, 721–730 (2021).

[182] Lujun Huang, Alex Krasnok, Andrea Alú, Yiling Yu, Dragomir Neshev, and Andrey E Miroshnichenko, "Enhanced light–matter interaction in two-dimensional transition metal dichalcogenides," Rep. Prog. Phys. **85**, 046401 (2022).

[183] Ruggero Verre, Denis G. Baranov, Battulga Munkhbat, Jorge Cuadra, Mikael Käll, and Timur Shegai, "Transition metal dichalcogenide nanodisks as high-index dielectric mie nanoresonators," Nat. Nanotechnol. **14**, 679–683 (2019).

[184] Ivan Fernandez-Corbaton, Stefan Nanz, Rasoul Alaee, and Carsten Rockstuhl, "Exact dipolar moments of a localized electric current distribution," Opt. Express **23**, 33044–33064 (2015).

[185] Rasoul Alaee, Carsten Rockstuhl, and I. Fernandez-Corbaton, "An electromagnetic multipole expansion beyond the long-wavelength approximation," Opt. Commun. **407**, 17–21 (2018).

[186] Rasoul Alaee, Carsten Rockstuhl, and Ivan Fernandez-Corbaton, "Exact multipolar decompositions with applications in nanophotonics," Adv. Opt. Mater. **7**, 1800783 (2019).

[187] Egor A Gurvitz, Konstantin S Ladutenko, Pavel A Dergachev, Andrey B Evlyukhin, Andrey E Miroshnichenko, and Alexander S Shalin, "The high-order toroidal moments and anapole states in all-dielectric photonics," Laser Photonics Rev. **13**, 1800266 (2019).

[188] Keqian Zhang and Dejie Li, *Electromagnetic Theory for Microwaves and Optoelectronics*, 2nd ed. (Springer, New York, 1998).

[189] Andrey A. Bogdanov, Kirill L. Koshelev, Polina V. Kapitanova, Mikhail V. Rybin, Sergey A. Gladyshev, Zarina F. Sadrieva, Kirill B. Samusev, Yuri S. Kivshar, and Mikhail F. Limonov, "Bound states in the continuum and fano resonances in the strong mode coupling regime," Adv. Photonics **1**, 016001 (2019).

[190] Francesco Monticone, Dimitrios Sounas, Alex Krasnok, and Andrea Alú, "Can a nonradiating mode be externally excited? nonscattering states versus embedded eigenstates," ACS Photonics **6**, 3108–3114 (2019).

[191] P Grahn, A Shevchenko, and M Kaivola, "Electromagnetic multipole theory for optical nanomaterials," New J. Phys. **14**, 093033 (2012).

[192] Wonjoo Suh, Zheng Wang, and Shanhui Fan, "Temporal coupled-mode theory and the presence of non-orthogonal modes in lossless multimode cavities," IEEE J. Quantum Elect. **40**, 1511–1518 (2004).

[193] Gabriel D. Bernasconi, Jérémy Butet, Valentin Flauraud, Duncan Alexander, Juergen Brugger, and Olivier J. F. Martin, "Where does energy go in electron energy loss spectroscopy of nanostructures?" ACS Photonics **4**, 156–164 (2017).

[194] Jon A Schuller and Mark L Brongersma, "General properties of dielectric optical antennas," Opt. Express **17**, 24084–24095 (2009).

[195] Carlos Maciel-Escudero, Andrew B. Yankovich, Battulga Munkhbat, Denis G. Baranov, Rainer Hillenbrand, Eva Olsson, Javier Aizpurua, and Timur O. Shegai, "Probing optical anapoles with fast electron beams," (2023), arXiv:2304.01018 .

[196] Stephen J. Pennycook and Peter D. Nellist, *Scanning Transmission Electron Microscopy* (Springer, New York, 2011).

[197] Y Zhu, H Inada, K Nakamura, and J Wall, "Imaging single atoms using secondary electrons with an aberration-corrected electron microscope," Nat. Mater. **8**, 808–812 (2009).

[198] Michel Bosman, Vicki J Keast, Masashi Watanabe, Abbas I Maaroof, and Michael B Cortie, "Mapping surface plasmons at the nanometre scale with an electron beam," Nanotechnology **18**, 165505 (2007).

[199] A. Shalabney, J. George, J. Hutchison, G. Pupillo, C. Genet, and T. W. Ebbesen, "Coherent coupling of molecular resonators with a microcavity mode," Nat. Commun. **6**, 5981 (2015).

[200] Jino George, Atef Shalabney, James A. Hutchison, Cyriaque Genet, and Thomas W. Ebbesen, "Liquid-phase vibrational strong coupling," The Journal of Physical Chemistry Letters **6**, 1027–1031 (2015).

[201] A. Thomas, J. George, A. Shalabney, M. Dryzhakov, S. J. Varma, J. Moran, T. Chervy, X. Zhong, E. Devaux, C. Genet, J. A. Hutchison, and T. W. Ebbesen, "Ground-state chemical reactivity under vibrational coupling to the vacuum electromagnetic field," Angew. Chem. Int. Ed. Engl. **55**, 11462–11466 (2016).

[202] A. Thomas, L. Lethuillier-Karl, K. Nagarajan, R. M. A. Vergauwe, J. George, T. Chervy, A. Shalabney, E. Devaux, C. Genet, J. Moran, and T. W. Ebbesen, "Tilting a ground-state reactivity landscape by vibrational strong coupling," Science **363**, 615–619 (2019).

[203] R. M. A. Vergauwe, A. Thomas, K. Nagarajan, A. Shalabney, J. George, T. Chervy, M. Seidel, E. Devaux, V. Torbeev, and T. W. Ebbesen, "Modification of enzyme activity by vibrational strong coupling of water," Angew. Chem. Int. Ed. Engl. **58**, 15324–15328 (2019).

[204] Brian T. O'Callahan, Mario Hentschel, Markus B. Raschke, Patrick Z. El-Khoury, and A. Scott Lea, "Ultrasensitive tip- and antenna-enhanced infrared nanoscopy of protein complexes," The Journal of Physical Chemistry C **123**, 17505–17509 (2019).

[205] Govind Dayal, Ikki Morichika, and Satoshi Ashihara, "Vibrational strong coupling in subwavelength nanogap patch antenna at the single resonator level," The Journal of Physical Chemistry Letters **12**, 3171–3175 (2021).

[206] Marta Autore, Irene Dolado, Peining Li, Ruben Esteban, Francisco Javier Alfaro-Mozaz, Ainhoa Atxabal, Song Liu, James H. Edgar, Saül Vélez, Fèlix Casanova, Luis E. Hueso, Javier Aizpurua, and Rainer Hillenbrand, "Enhanced light–matter interaction in 10b monoisotopic boron nitride infrared nanoresonators," Advanced Optical Materials **9**, 2001958 (2021).

[207] Andrei Bylinkin, Martin Schnell, Marta Autore, Francesco Calavalle, Peining Li, Javier Taboada-Gutièrrez, Song Liu, James H. Edgar, Fèlix Casanova, Luis E. Hueso, Pablo Alonso-Gonzalez, Alexey Y. Nikitin, and Rainer Hillenbrand, "Real-space observation of vibrational strong coupling between propagating phonon polaritons and organic molecules," Nat. Photonics (2021), 10.1038/s41566-020-00725-3.

[208] Tao Wang, Peining Li, Benedikt Hauer, Dmitry N. Chigrin, and Thomas Taubner, "Optical properties of single infrared resonant circular microcavities for surface phonon polaritons," Nano Letters **13**, 5051–5055 (2013).

[209] Joshua D. Caldwell, Orest J. Glembocki, Yan Francescato, Nicholas Sharac, Vincenzo Giannini, Francisco J. Bezares, James P. Long, Jeffrey C. Owrutsky, Igor Vurgaftman, Joseph G. Tischler, Virginia D. Wheeler, Nabil D. Bassim, Loretta M. Shirey, Richard Kasica, and Stefan A. Maier, "Low-loss, extreme subdiffraction photon confinement via silicon carbide localized surface phonon polariton resonators," Nano Letters **13**, 3690–3697 (2013).

[210] Tao Wang, Peining Li, Dmitry N. Chigrin, Alexander J. Giles, Francisco J. Bezares, Orest J. Glembocki, Joshua D. Caldwell, and Thomas Taubner, "Phonon-polaritonic bowtie nanoantennas: Controlling infrared thermal radiation at the nanoscale," ACS Photonics **4**, 1753–1760 (2017).

[211] Michele Tamagnone, Antonio Ambrosio, Kundan Chaudhary, Luis A. Jauregui, Philip Kim, William L. Wilson, and Federico Capasso, "Ultraconfined mid-infrared resonant phonon polaritons in van der waals nanostructures," Science Advances **4**, eaat7189 (2018).

[212] Jiahua Duan, Francisco Javier Alfaro-Mozaz, Javier Taboada-Gutiérrez, Irene Dolado, Gonzalo Álvarez Pérez, Elena Titova, Andrei Bylinkin, Ana Isabel F. Tresguerres-Mata, Javier Martín-Sánchez, Song Liu, James H. Edgar, Denis A. Bandurin, Pablo Jarillo-Herrero, Rainer Hillenbrand, Alexey Y. Nikitin, and Pablo Alonso-González, "Active and passive tuning of ultranarrow resonances in polaritonic nanoantennas," Advanced Materials **34**, 2104954 (2022).

[213] Shang-Jie Yu, Yue Jiang, John A. Roberts, Markus A. Huber, Helen Yao, Xinjian Shi, Hans A. Bechtel, Stephanie N. Gilbert Corder, Tony F. Heinz, Xiaolin Zheng, and Jonathan A. Fan, "Ultrahigh-quality infrared polaritonic resonators based on bottom-up-synthesized van der waals nanoribbons," ACS Nano **16**, 3027–3035 (2022).

[214] Eric A. Muller, Benjamin Pollard, Hans A. Bechtel, Ronen Adato, Dordaneh Etezadi, Hatice Altug, and Markus B. Raschke, "Nanoimaging and control of molecular vibrations through electromagnetically induced scattering reaching the strong coupling regime," ACS Photonics **5**, 3594–3600 (2018).

[215] Bernd Metzger, Eric Muller, Jun Nishida, Benjamin Pollard, Mario Hentschel, and Markus B. Raschke, "Purcell-enhanced spontaneous emission of molecular vibrations," Phys. Rev. Lett. **123**, 153001 (2019).

[216] Florian Huth, Andrey Chuvilin, Martin Schnell, Iban Amenabar, Roman Krutokhvostov, Sergei Lopatin, and Rainer Hillenbrand, "Resonant antenna probes for tip-enhanced infrared near-field microscopy," Nano Letters **13**, 1065–1072 (2013).

[217] Alexander J. Giles, Siyuan Dai, Igor Vurgaftman, Timothy Hoffman, Song Liu, Lucas Lindsay, Chase T. Ellis, Nathanael Assefa, Ioannis Chatzakis, Thomas L. Reinecke, Joseph G. Tischler, Michael M. Fogler, J. H. Edgar, D. N. Basov, and Joshua D. Caldwell, "Ultralow-loss polaritons in isotopically pure boron nitride," Nature Materials (2018), 10.1038/nmat5047.

[218] Stefan Mastel, Alexander A. Govyadinov, Thales V. A. G. de Oliveira, Iban Amenabar, and Rainer Hillenbrand, "Nanoscale-resolved chemical identification of thin organic films using infrared near-field spectroscopy and standard Fourier transform infrared references," Applied Physics Letters **106**, 023113 (2015).

[219] A. Y. Nikitin, P. Alonso-González, S. Vélez, S. Mastel, A. Centeno, A. Pesquera, A. Zurutuza, F. Casanova, L. E. Hueso, F. H. L. Koppens, and R. Hillenbrand, "Real-space mapping of tailored sheet and edge plasmons in graphene nanoresonators," Nature Photonics **10** (2016), 10.1038/nphoton.2016.44.

[220] Andrey E. Miroshnichenko, Sergej Flach, and Yuri S. Kivshar, "Fano resonances in nanoscale structures," Rev. Mod. Phys. **82**, 2257–2298 (2010).

[221] Martin Jurna, Erik T. Garbacik, Jeroen P. Korterik, Jennifer L. Herek, Cees Otto, and Herman L. Offerhaus, "Visualizing resonances in the

complex plane with vibrational phase contrast coherent anti-stokes raman scattering," Analytical Chemistry **82**, 7656–7659 (2010).

[222] Kane Yee, "Numerical solution of initial boundary value problems involving maxwell's equations in isotropic media," IEEE Transactions on Antennas and Propagation **14**, 302–307 (1966).

[223] Allen Taflove, "Review of the formulation and applications of the finite-difference time-domain method for numerical modeling of electromagnetic wave interactions with arbitrary structures," Wave Motion **10**, 547–582 (1988).

[224] Allen Taflove and S. Hagness, *Computational Electrodynamics: The Finite-Difference Time-Domain Method, 3rd edition*, Vol. 2062 (2005).

[225] Peter P. Silvester and Ronald L. Ferrari, *Finite Elements for Electrical Engineers*, 3rd ed. (Cambridge University Press, 1996).

[226] Jian-Ming Jin, *The Finite Element Method in Electromagnetics* (Wiley, 2002).

[227] Peter Monk, *Finite Element Methods for Maxwell's Equations* (Oxford University Press, 2003).

[228] "COMSOL Multiphysics v. 5.5. www.comsol.com. COMSOL AB, Stockholm, Sweden," .

[229] F. J. García de Abajo, "Relativistic energy loss and induced photon emission in the interaction of a dielectric sphere with an external electron beam," Phys. Rev. B **59**, 3095–3107 (1999).

[230] Saskia Fiedler, P. Elli Stamatopoulou, Artyom Assadillayev, Christian Wolff, Hiroshi Sugimoto, Minoru Fujii, N. Asger Mortensen, Søren Raza, and Christos Tserkezis, "Disentangling cathodoluminescence spectra in nanophotonics: Particle eigenmodes vs transition radiation," Nano Letters **22**, 2320–2327 (2022).

[231] P. Elli Stamatopoulou, Wenhua Zhao, Álvaro Rodríguez Echarri, N. Asger Mortensen, Kurt Busch, Christos Tserkezis, and Christian Wolff, "Electron beams traversing spherical nanoparticles: analytic and numerical treatment," (2023), arXiv:2309.00918 .

[232] Irene Dolado, Carlos Maciel-Escudero, Elizaveta Nikulina, Evgenii Modin, Francesco Calavalle, Shu Chen, Andrei Bylinkin, Francisco Javier Alfaro-Mozaz, Jiahan Li, James H. Edgar, Fèlix Casanova, Saül Vélez,

Luis E. Hueso, Ruben Esteban, Javier Aizpurua, and Rainer Hillenbrand, "Remote near-field spectroscopy of vibrational strong coupling between organic molecules and phononic nanoresonators," Nature Communications **13**, 6850 (2022).

[233] Nahid Talebi, Surong Guo, and Peter A. van Aken, "Theory and applications of toroidal moments in electrodynamics: their emergence, characteristics, and technological relevance," Nanophotonics **7**, 93–110 (2018).

[234] E. E. Radescu and G. Vaman, "Exact calculation of the angular momentum loss, recoil force, and radiation intensity for an arbitrary source in terms of electric, magnetic, and toroid multipoles," Phys. Rev. E **65**, 046609 (2002).

[235] Milton Abramowitz and Irene A. Stegun, *Handbook of Mathematical Functions: With Formulas, Graphs, and Mathematical Tables*, 10th ed. (National Bureau of Standards Applied Mathematics Series 55, 1972).